UNIVERSITY OF LONDON

# A HIGH-RESOLUTION MULTIPROXY LATE NEOGENE PALAEOCLIMATE RECORD FROM GUAYMAS BASIN, GULF OF CALIFORNIA

by

**Heather Cheshire**

**Thesis submitted in fulfilment of the requirements for the degree of Doctor of Philosophy**

**Department of Earth Sciences**
**University College London**



**October 2007**





ProQuest LLC
789 East Eisenhower Parkway
P.O. Box 1346
Ann Arbor, MI 48106-1346

University of London Doctor of Philosophy

# A high-resolution multiproxy Late Neogene palaeoclimate record from Guaymas Basin, Gulf of California

## Abstract

The annual migration of the North Pacific Subtropical High, fuelled by tropical heat and moisture – derived partly from the Atlantic - drives seasonal coastal upwelling and, importantly, transports heat into the mid-latitudes. Interannual to orbital cyclicity affects eastern North Pacific climate by varying the relative strengths/interactions of the Subtropical High and the Aleutian Subpolar Low. In modern Guaymas Basin - situated at the wet/dry subtropical divide – dry-season diatom productivity alternates with wet-season terrestrial flux, and pre-formed low-oxygen intermediate waters ensure varve deposition. High-resolution logging of ~75% laminated, ~63 m, continuous piston core MD02-2515 and companion ~6 m kasten core MD02-2517 has identified eight sediment fabric types, six of which are laminated with systematic variations in relative lamina thickness and presence/absence of sub-laminae. Based on observed climate and supported by climate proxies provided by continuous X-ray fluorescence, colour, magnetic susceptibility, sediment density, biogenic silica, carbon and microfossil analyses, the sediment fabric types have been interpreted as the result of climatic/oceanographic conditions produced by variations in the strength of the North Pacific Subtropical High and the extent of its migration. Varve thickness, $\delta^{18}O$ stratigraphy and correlation with the $\delta^{13}C$ stratigraphy of nearby radiocarbon dated core JPC-56 (Keigwin, 2002) gives an age range of ~0-36,000 Years. Systematic variations in the predominance of one or more sediment types reveal precessional forcing, which drives a ~5000-year oscillation of millennial- and centennial-scale wet/dry cycles, the former are associated with June/December perihelion, the latter with March/September perihelion. Between ~34-11,000 yr BP there are significant non-laminated intervals every ~5000 years. This study indicates that the Trade Winds are confined close to the equator during the glacial. This breaks the hydrological link between the Atlantic and Pacific and reduces dysoxia in coastal waters.

**CONTENTS** **Page**

# LIST OF FIGURES

## LIST OF TABLES



## LIST OF ABBREVIATIONS

| | |
|---|---|
| NPSH | North Pacific Subtropical High |
| ASL | Aleutian Subpolar Low |
| ITCZ | Inter Tropical Convergence Zone |
| GB | Guaymas Basin |
| SBB | Santa Barbara Basin |
| GoC | Gulf of California |
| CC | California Current |
| HC | Humboldt Current |
| LGM | Last Glacial Maximum |
| SST | Sea surface temperature |
| kyr BP | 1000s of years Before Present |
| m bsf | metres below seafloor |
| cps | counts per second |
| eg | for example |
| ie | that is |
| cf | compare |
| pers. comm. | personal communication |

## Acknowledgments

Firstly, I would like to thank Professor Jürgen Thurow, my supervisor, for his encouragement and patience, and for giving me this great project.

Many thanks to the Department of Earth Sciences, UCL, for funding me, and to my many friends there for encouraging me, and generally having faith that I would deliver.

Thanks to all the people who have helped me with data-gathering. To Jürgen, Ivon Balut and everyone onboard the *Marion Dufresne* in June, 2002, for getting the cores. To Sandra Nederbragt for the stable isotope analysis and the digital images. To Ursula Röhl, Frank Lamy, Walter Hale and Alex Wuelbers, in Bremen, for help with the continuous XRF scan. To Guy Rothwell and Belinda Alker in the core repository in Southampton. To Tony Osborn in the Wolfson Laboratory, UCL, for his work on the carbon and biogenic silica analyses. To Professor Hans-Jürgen Brumsack, in Oldenburg, for XRF analysis. To Raja Ganeshram, in Edinburgh, for the AMS TOC.

Many thanks to my friend and sometime fellow-PhD, Ian Bailey, for sticking to it through the good times and the bad, and for much good advice, sympathy and beer.

Lastly, but never least, many, many thanks to Rachael for giving me a home when the funding ran out. Also, many, many thanks to Rachael and Duncan for lifelong friendship and encouragement.

# Chapter 1 Introduction

## 1.1 Rationale

Ongoing concerns about global climate warming make it essential to fully understand the Earth's climate system – the interactions between the atmosphere, the oceans, and the cryosphere. In particular, we need to know why and how drastic climate change occurs and what its long-term effects will be, so we can prepare ourselves against them. One of the keys ways to understand climate systems is to study the past. The past is important because the norm during the 100,000-year climate cycles of the past 450,000 years is very different to the climate of the prolonged interglacial we are currently living in. Glacial climate is a complex pattern of cold, dry stadials alternating with relatively warm ~1000-year long interstadials. Interglacials are singular occurrences within each cycle and each one is different in some respect to all of the others. By constructing highly detailed records on long timescales in areas sensitive to alterations in global heat transport, it becomes possible to understand the processes of ancient climates and to grasp in what ways they function differently to modern observable climate.

Palaeoclimate records of the highest possible resolution come from marine sites with exceptionally high sedimentation rates (1 m per 1000 years or more), where the local combination of atmospheric and oceanic processes drives a seasonality that results in distinct compositional changes in the sediment (Kemp, 1996). If productivity is high and the bathymetry of the site restricts the circulation of oxygenated bottom waters, there is potential for enhanced preservation and long, virtually undisturbed sequences of seasonal laminations are laid down. Guaymas Basin, Gulf of California, in the southeastern North Pacific (Figure 1.1), fulfils all these criteria.

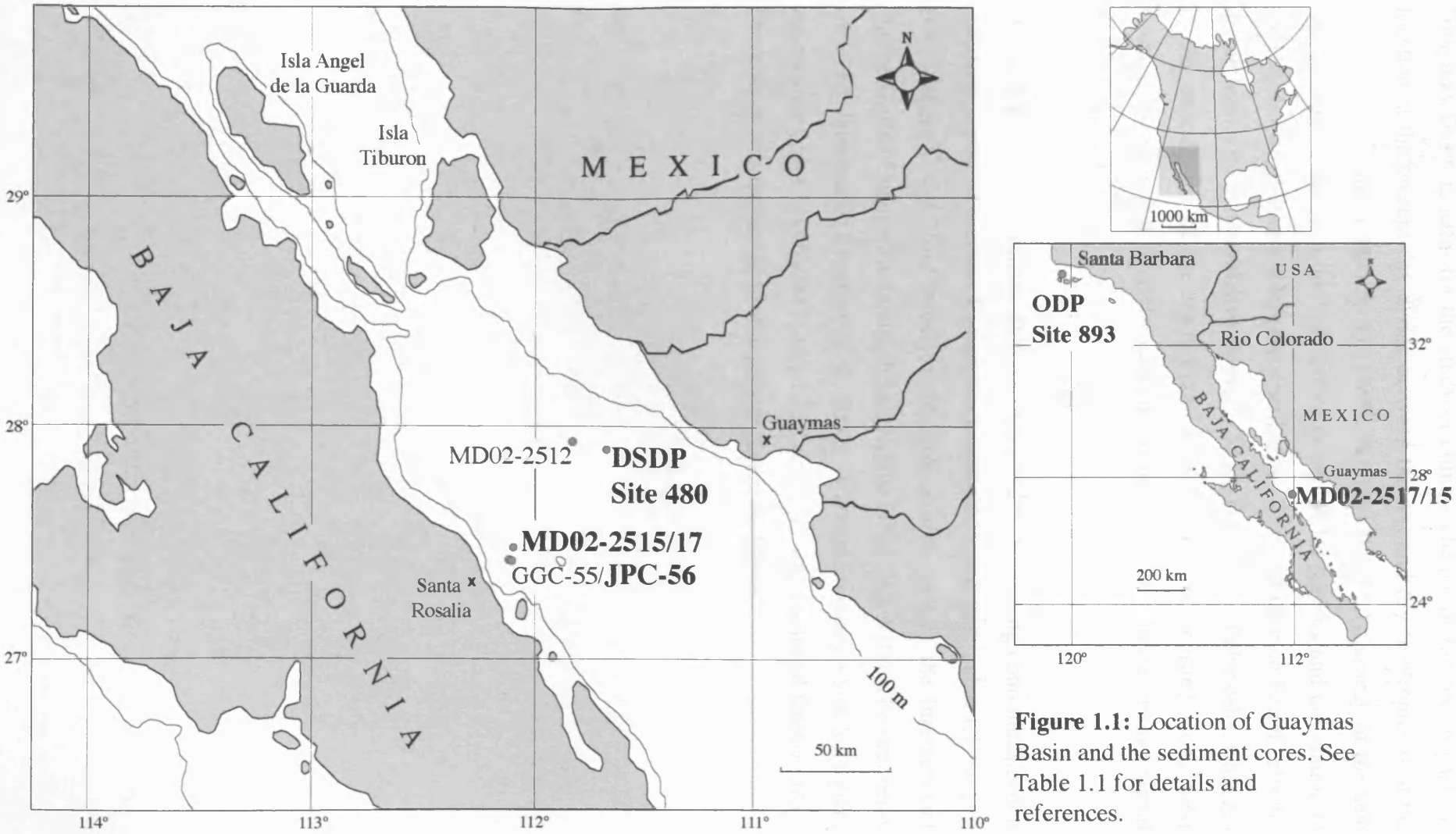


**Figure 1.1:** Location of Guaymas Basin and the sediment cores. See Table 1.1 for details and references.

Guaymas Basin is ideal for the study of climate change of the recent past. Its location at the present-day divide between the wet and dry Subtropics is at the interface between the Hadley and Ferrel climate cells. The majority of the heat the Earth receives from the Sun arrives in equatorial regions and circulation in the Hadley cells initiates its global distribution. The mid-latitude Ferrel cells are driven indirectly by the relative strengths of the Hadley and Polar cells. Changes in the interactions of the Hadley and Ferrel cells are recorded along their boundary at sites that have the capacity to preserve the climate change signal within their sediment.

In June 2002, the RV *Marion Dufresne* retrieved a ~63 m-long continuous piston core from western Guaymas Basin (core MD02-2515; Fig. 1.1; Table 1.1) on Leg 164, Marges Ouest Nord America (MONA) cruise, part of the International Marine Global Change Study eighth programme (IMAGES VIII). The sediments are ~75% laminated (Beaufort *et al.*, 2002). A complementary ~6 m-long giant kasten core (core MD02-2517; Fig 1.1; Table 1.1) was retrieved from nearby. This core is also laminated for the greater part of its length.

| CORE | LOCATION | DEPTH (m) | SEDIMENT (m) | REFERENCES |
|---|---|---|---|---|
| **MD02-2515** | 27°29.01'N, 112°04.64'W | 881 | 62.58 | Beaufort *et al.* (2002); Cheshire *et al.* (2005) |
| **MD02-2517** | 27°29.10'N, 112°04.46'W | 888 | 5.97 | Beaufort *et al.* (2002) |
| **JPC-56** | 27°28.16'N, 112°06.26'W | 818 | 19.12 | Sancetta (1995); Pike & Kemp (1996; 1997; 1999); Pride *et al.* (1999); Barron *et al.* (2005); Keigwin (2002); |
| **GGC-55** | 27°28.22'N, 112°6.33'W | 820 | 0.3 | Pride *et al.* (1999); Keigwin (2002); Barron *et al.* (2005) |
| **DSDP Site 480** | 27°54.10'N, 111°39.34'W | 655 | 150 | Schrader *et al.* (1980); Kelts & Niemitz (1982); Keigwin & Jones (1990); Simoneit (1991); Barron *et al.* (2004) |
| **MD02-2512** | 27°56.07'N 111°46.45'W | 477 | 47.79 | Beaufort *et al.* (2002); Cheshire *et al.* (2005) |
| **ODP Site 893** (Santa Barbara Basin) | 34°17.25'N, 120.02.02'W | 576 | 180 | Soutar & Crill (1977); Kennett *et al.* (1994); Kennett & Ingram (1995); Behl & Kennett (1996); Cannariato & Kennett (1999); Hendy & Kennett (1999); Hendy *et al.* (2002); Hendy & Kennett (2003) |

**Table 1.1:** Details of the sediment cores recovered from Guaymas Basin and Santa Barbara Basin. See Fig. 1.1 for locations.

### 1.1.1 The Subtropical High-pressure systems

The forcing mechanism controlling sedimentation in Guaymas Basin at all frequencies up to and including orbital cycles is the North Pacific Subtropical High (Cheshire *et al.*, 2005; Appendix I; Goni *et al.*, 2006). At present, climate scientists are not much interested in the Subtropical Highs; they are, reports Grotjahn (2004), 'little studied and incompletely understood'. However, the circumstantial evidence from modern observations and palaeorecords is compelling: these high-pressure systems, which are permanently present north and south of the equator on the eastern sides of the ocean basins, are important atmospheric heat transport agents. Ocean circulation, the world's principal heat transport agent, is to a large extent driven by atomspheric circulation.

The circulation of the Hadley cells (Figures 1.2 & 1.3) is principally fuelled by sensible heat from equatorial insolation, with a secondary source provided by latent heat. The warm, moist, low-pressure equatorial air mass rises and travels polewards. It sinks as it cools, but is continually buoyed up by heat released from condensing water vapour. The air mass subsides when it runs out of latent heat (over the continents, this is the Subtropical wet/dry divide) and the remaining sensible heat is shed into the Ferrel cell (Barry & Chorley, 2003).

At the zone of subsidence, the by now cool, dry, high-pressure air begins to return to the equatorial low-pressure zone. This airflow - the Trade Winds - is deflected towards the west by the Coriolis effect. In the Subtropics, the Trade Winds blow from the northeast in the northern hemisphere and from the southeast in the southern hemisphere; they converge at ~5°N in an equatorial band called the Inter Tropical Convergence Zone (ITCZ). The ITCZ is the thermal equator and is located north of the geographic equator because the greater amount of landmasses in the northern hemisphere makes the meridional (equator-to-pole) temperature gradient less steep than that of the southern hemisphere. The Trade Winds evaporate the ocean surface as they blow across it and this water vapour forms the majority of that lofted by convection at the ITCZ (Barry & Chorley, 2003).

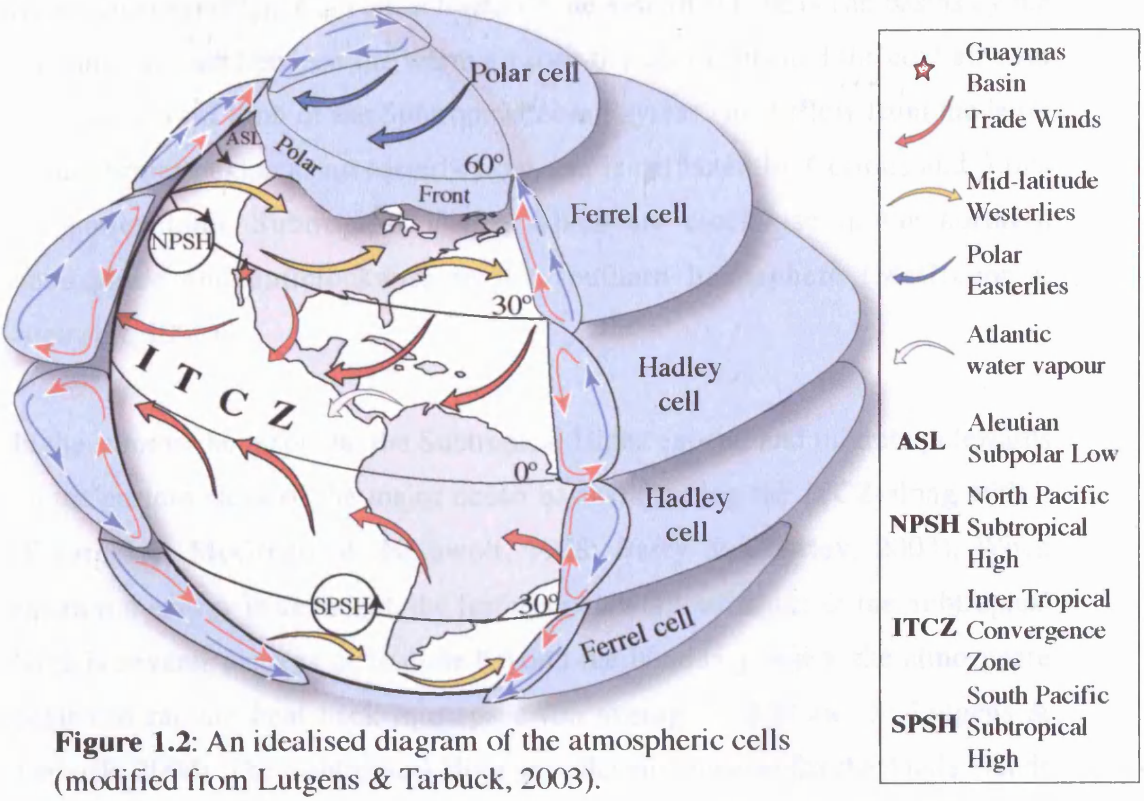


**Figure 1.2**: An idealised diagram of the atmospheric cells (modified from Lutgens & Tarbuck, 2003).

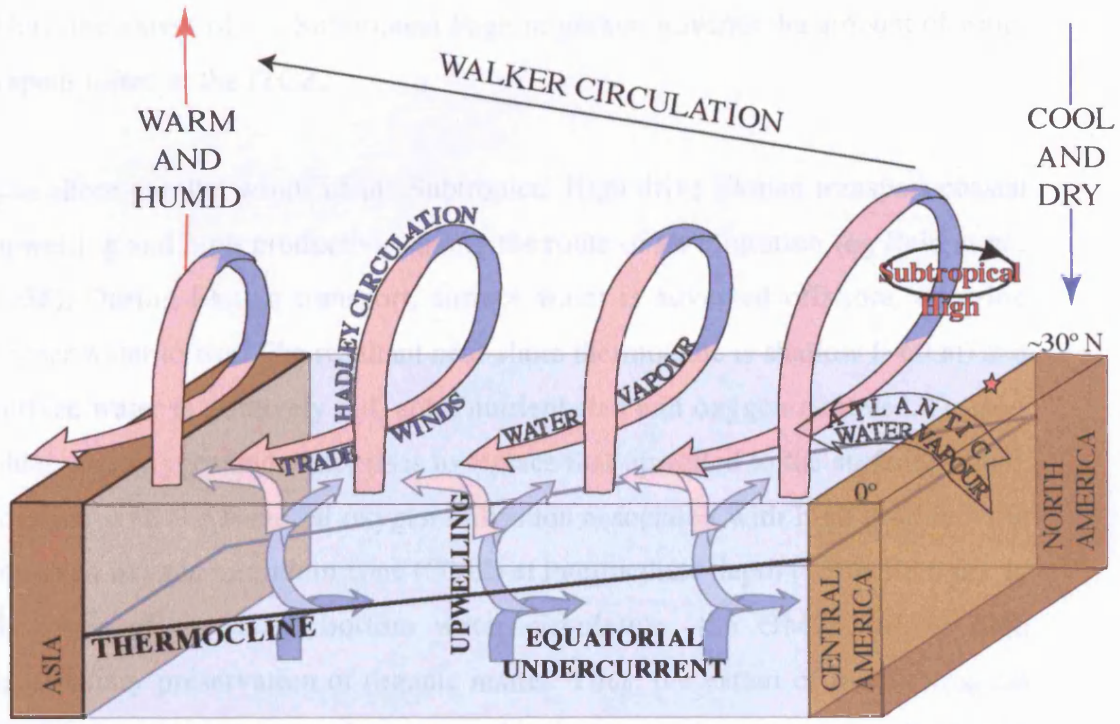


**Figure 1.3:** A schematic diagram of Hadley cell circulation and equatorial upwelling in the North Pacific.

Subtropical subsidence is concentrated on the eastern side of ocean basins by the pressure contrast between the warm air over the continents and the cold air over the equatorward limb of the Subtropical ocean gyres. The airflow from the latter to the former begins as an easterly flow, but is deflected by Coriolis and forms the anticyclonic Subtropical Highs, which are clockwise in the northern hemisphere and anticlockwise in the southern hemisphere (McGregor & Nieuwolt, 1998).

In the summer hemisphere, the Subtropical Highs expand and migrate polewards on the eastern sides of the major ocean basins, drawing the ITCZ along with it (Figure 1.4; McGregor & Nieuwolt, 1998; Barry & Chorley, 2003). When equatorial energy is abundant, the furthest poleward influence of the Subtropical High is several degrees of latitude beyond the boundary where the atmosphere begins to radiate heat back into space (on average ~38°N and S; Lutgens & Tarbuck, 2004). The Subtropical High provides the impetus for the Trade Winds (which are either light or non-existent over the continents), and its location at any time of the year is their poleward limit (Barry & Chorley, 2003; Figure 1.4). Thus, the extent of the Subtropical High migration governs the amount of water vapour lofted at the ITCZ.

The shore-parallel winds of the Subtropical High drive Ekman transport coastal upwelling and high productivity along the route of its migration (eg Reid *et al.*, 1958). During Ekman transport, surface water is advected offshore, allowing deeper water to rise. The resultant near-shore thermocline is shallow (~60 m) and surface water is relatively old, cold, nutrient-rich and oxygen-depleted. Deeper, older, less oxygenated water rises to replace that upwelled to the surface, which, together with the bacterial oxygen utilisation associated with high productivity, forms an oxygen minimum zone (OMZ) at intermediate depth (~500-1000 m). In locations of restricted bottom water circulation, the OMZ ensures high sedimentary preservation of organic matter. Thus, the extent of the Subtropical High migration governs the geographical extent of coastal upwelling, the strength of the OMZ and the age of subthermocline water. The sub-thermocline

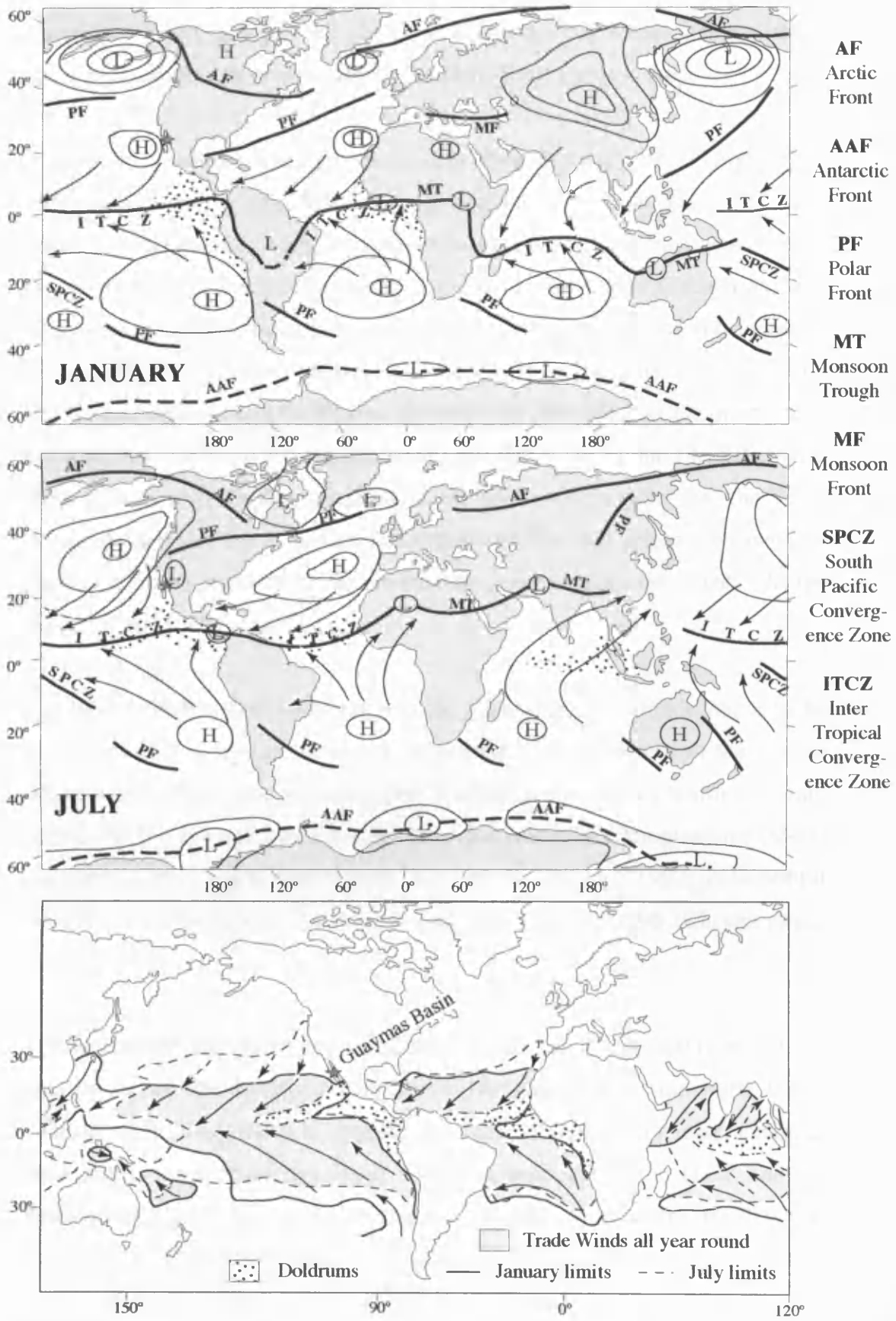


**AF** Arctic Front

**AAF** Antarctic Front

**PF** Polar Front

**MT** Monsoon Trough

**MF** Monsoon Front

**SPCZ** South Pacific Convergence Zone

**ITCZ** Inter Tropical Convergence Zone

**Figure 1.4:** (Top & centre) Modern seasonal migrations of atmospheric pressure cells and climate fronts. (Bottom) The Trade Winds. [Figures adapted from Barry & Chorley, 2003.]

waters flow freely into the Gulf of California (section 2.6) where they are further deoxygenated by high productivity in Guaymas Basin (section 2.8).

Water vapour - an important greenhouse gas (Pierrehumbert, 1999) - and surface water, transported by the Trade Winds, pile up on the western side of the ocean basins. In the Pacific, water transport creates a basin-wide east-west sloping thermocline, while water vapour transport creates the Walker Circulation, with high humidity and convection in the west, and low humidity and subsidence in the east (Fig 1.3). El Niño-Southern Oscillation (ENSO) events, with a cyclicity of 3-8 years, occur when the Walker Circulation is disrupted. At the inception of an event, the climate model of Clement *et al.* (1999) shows that the Subtropical High retreats towards the equator. Climate observations show that the Trade Winds slacken and warm surface water flows west to east across the equatorial Pacific; in the eastern Pacific the thermocline deepens and productivity falls (eg Bigg, 2003).

The 1997-1998 ENSO event began with the weakening of the Trade Winds in the eastern Pacific in late 1996. Shortly afterwards, sea level rose in the eastern equatorial Pacific, while surface waters warmed and remained warm until mid May 1998. In June and July 1997, sea level and sea surface temperatures (SSTs) rose along the central Californian Margin. By August 1997, chlorophyll concentrations were low and remained so until October 1998 (Chavez *et al.*, 2002).

The worldwide effects of modern ENSO events (eg Bigg, 2003) reveal the importance of the Pacific's contribution to global heat transport. When Subtropical High migration is curtailed, the Trade Winds affect a lesser extent of the ocean, consequently less water vapour is available at the ITCZ and the Subtropical Highs are further weakened. It takes months for Hadley cell circulation to return to normal.

ENSO events are not the only way in which Subtropical circulation affects global climate. The modern North Atlantic Trade Winds blow across the Caribbean Sea

(Fig. 1.4) and water vapour is transported across the narrow Isthmus of Panama at the rate of ~0.4 Sv (Weaver *et al.*, 1999; Sverdrup = $10^6$ $m^3s^{-1}$). This provides an additional source of energy for the Pacific Subtropical Highs. More importantly, the transport of water vapour from the North Atlantic to the Pacific decreases the salinity of the latter and increases the salinity of the former. This has an important impact on global thermohaline circulation. Deep water is not formed in the high latitudes of the modern North Pacific because its relatively fresh surface waters never become dense enough to sink, while it is formed in the modern North Atlantic when the dense, high salinity Gulf Stream waters undergo intense cooling at ~70°N. The sensitivity of the glacial North Atlantic to changes in its heat and salinity budget is well known (eg Broecker, 1990; Broecker *et al.*, 1990).

### 1.1.2 The North Pacific Subtropical High

Since 1949 the Californian Co-operative Oceanic Fisheries Investigations (CalCOFI) have been collecting monthly data and have collated historical data from around the North Pacific. The first CalCOFI annual progress report reviews the basic facts: that fish populations exploit phytoplankton blooms and that blooms occur in response to seasonal wind-driven upwelling (Manar *et al.*, 1950). An early review of the California Current System (Reid *et al.*, 1958) reports that the 'high pressure cell off California' is strongest in summer, weakest in winter and its northwest alongshore winds drive upwelling through the spring/summer season from Baja California in the south to Cape Flattery in the north. The CalCOFI reports frequently detail seasons when the fish stocks did not materialise when and where they had the year before because the North Pacific Subtropical High behaved in an 'irregular' manner (eg Reid, 1960).

The US Fish and Wildlife Service commissioned a report on the habitat of the marbled murrelet - a seabird endangered by commerical logging activities - which includes a comprehensive review of observed coastal oceanic and atmospheric processes (McShane *et al.*, 2004). This review states that seasonal coastal upwelling, driven by the North Pacific Subtropical High, starts in February/March at ~23°N. The upwelling cell moves progressively northwards,

reaching ~48°N in July, and then it returns to its starting point. The upwelling brings nutrient-rich waters to the surface, fuelling phytoplankton blooms which are exploited by fish and other wildlife. The ENSO years, in which this phenomenon does not occur, have a large impact on local climate, ecology and economy (eg Mantua *et al.*, 1997; Stapp *et al.*, 1999; Sanchez-Velasco *et al.*, 2002; Chavez *et al.*, 2003; McShane *et al.*, 2004).

Many palaeoceanographers and palaeoclimatologists recognise that the North Pacific Subtropical High is the forcing mechanism for seasonal upwelling along the North American western seaboard (eg Doose, *et al.*, 1997; Gardner *et al.*, 1997; Hendy & Kennett, 1999; Herbert, *et al.*, 2001; Hendy *et al.*, 2002; Kienast *et al.*, 2002; Hendy & Kennett, 2003; Dean *et al.*, 2004; Dean *et al.*, 2006). However, not all sites have the same potential either for greatly enhanced phytoplankton productivity or for enhanced preservation (section 2.8), consequently, not all workers in the eastern North Pacific are studying upwelling parameters and the over-arching significance of North Pacific Subtropical High migration is not explicitly recognised in palaeoclimate records.

### 1.1.3 Intra-annual cycles

The mountains on either side of the Gulf of California (see Figure 2.1) channel the northwesterly winds of the North Pacific Subtropical High along the axis of the basin (section 2.6). There is a strong winter/spring upwelling cell on the eastern side of Guaymas Basin which extends across the full width of the Gulf (eg Hamman *et al.*, 1988; Bray & Robles, 1991; Lluch-Cota, 2000). When the high-pressure cell moves on, the winds die down and a stratified water column develops. The combination of the strong seasonal contrast, very high productivity and low-oxygen subthermocline waters results in the deposition of annually laminated sediment (varves).

Jumbo Piston Core 56 (core JPC-56; Fig. 1.1, Table 1.1) from western Guaymas Basin (sections 1.3 & 2.7) was recovered in 1990 by the R/V *Atlantis II*. It has been the subject of intensive study (Sancetta, 1995; Pike & Kemp, 1996; 1997; 1999; Pride *et al.*, 1999; Keigwin, 2002; Barron *et al.*, 2005). Pike (1996) and

Pike & Kemp (1996; 1997; 1999), using Back Scattered Electron Imagery (BSEI), examine the sediment fabric of ~300 Holocene varves from core JPC-56. They demonstrate variability in the type of varve deposited - essentially, the presence/absence of sub-laminae, and the relative thickness of the diatomaceous and terrigenous laminae - and they attribute this to environmental changes in the strength of upwelling. Their work illustrates the exceptional sensitivity of the depositional system to intra-annual climate change.

### 1.1.4 Interannual cycles

During the 1997-98 ENSO event, the deeper-than-normal thermocline and less nutrient-enrichment resulted in a poor harvest for the sardine fisheries in Guaymas Basin (Lluch-Cota, 2000; Sanchez-Velasco *et al.*, 2002). The high precipitation rates of 1997 resulted in the unusual success of fauna and flora on the normally arid islands of the northern Gulf (Stapp *et al.*, 1999). Sediment-trap data from the 1991-92 event reveal that coccolithophore production increased at the expense of the normal dominance of diatoms (Ziveri & Thunell, 2000) and that, instead of one or two diatom blooms in Guaymas Basin, there were a series of short blooms (Sancetta, 1995). Baumgartner & Christiansen (1985) find a correlation between ENSO events and the sedimentation pattern in modern Guaymas Basin.

### 1.1.5 Interdecadal and centennial cycles

The Pacific Decadal Oscillation (PDO) has been identified by Zhang *et al.* (1997), Mantua *et al.* (1997) and Mantua & Hare (2002). Fluctuations in North Pacific sea level pressure and sea surface temperature (SST) closely parallel each other throughout the 20th century with a ~25-year cyclicity. Peak-to-trough is 12-14 years; peak-to-peak is 25-30 years (Mantua & Hare, 2002).

When the PDO is in its positive phase, Washington and British Columbia have hotter, more settled summers (ie the North Pacific Subtropical High is persistently further north than average), while Alaska has higher than average rainfall all year round (ie the Aleutian Subpolar Low is centred further north than average; Mantua & Hare, 2002). In the negative phase, the Aleutian Subpolar

Low dominates the North Pacific and there is wetter-than-average climate in the mid-latitudes of the North Pacific.

In Guaymas Basin, Dean *et al.* (2004) have found ~20-year cycles in the deposition of titanium (a component of terrigenous flux; eg Peterson *et al.*, 2000a) that match the positive phases of the PDO during the last 180 years and show that, during these phases, the Basin experiences higher than average summer rainfall. A Pacific-wide 25-year variation in anchovy and sardine stocks has been observed (Chavez *et al.* 2003). Since anchovies require cold SSTs during breeding, while sardines need warmer SSTs (Holmgren-Urba & Baumgartner, 1993), the inference is that the forcing mechanism is the PDO. The annually laminated sediments of two sites in the migration path of the North Pacific Subtropical High have been used to decode the cycles. Holmgren-Urba & Baumgartner (1993) reconstruct fish populations over the last 250 years (from fish scales in box-cores taken in Guaymas Basin) and find interdecadal covarience between anchovies and sardines. A 1700-year record from Santa Barbara Basin (Baumgartner *et al.*, 1992) reveals longer-term cyclicity: anchovy populations vary in 100-year cycles while sardines vary in 250-year cycles.

### 1.1.6 Millennial cycles

Santa Barbara Basin (Soutar & Crill, 1977; Kennett *et al.*, 1994; Kennett & Ingram, 1995; Behl & Kennett, 1996; Cannariato & Kennett, 1999; Hendy & Kennett, 1999; Hendy *et al.*, 2002; Hendy & Kennett, 2003; Robert, 2004; Nederbragt & Thurow, 2005) is a restricted, silled basin of the California Borderlands (Fig. 1.1; Table 1.1). A core from Ocean Drilling Program, Leg 146, Site 893 (Kennett *et al.*, 1994) records a series of ~1000-year interstadial events of the past 60,000 years during which the sediment is fully varved. A bioturbation index has been constructed which shows that during stadials the sediment is heavily bioturbated or homogeneous (Behl & Kennett, 1996). The varved intervals have been either radiocarbon-dated or matched to the SPECMAP oxygen isotope record (Martinson *et al.*, 1987) and correlate with Dansgaard-Oeschger warm events of the North Atlantic (Dansgaard *et al.*, 1993)

in the oxygen-isotope record of the ice core from the Greenland Ice Sheet Project 2 (GISP2; eg Stuiver & Grootes, 2000).

Kennett & Ingram (1995), following earlier work of Keigwin (1987), Keigwin & Jones (1990) and Keigwin *et al.* (1992), propose that during stadials better ventilation of North Pacific Intermediate Water (NPIW, section 2.6) allows bioturbation in Santa Barbara Basin. Correlation with the GISP2 record indicates synchroneity of events at mid- and high-latitudes.

An atmospheric teleconnection is proposed whereby forcing in the northern North Pacific drives cycles in NPIW flux (Behl & Kennett, 1996; Nederbragt & Thurow, 2005). The differences between paired benthic and planktonic foraminifera give younger ages for bottom waters during stadials (Kennett & Ingram, 1995; their Figure 1a), which is inferred as higher NPIW flux. Nederbragt & Thurow (2005) trace the millennial-scale cycles through the Holocene and link them to aridity and wind-stress caused by high-latitude atmospheric forcing. Conversely, Hendy & Kennett (1999) and Hendy *et al.* (2002) propose that reorganisation of North Pacific atmospheric circulation during the glacial forces changes in deposition at ODP Site 893. Hendy & Kennett (2003) link the cyclical variability of secondary productivity and SSTs to tropical forcing and propose Trade Wind strength as the forcing mechanism.

### 1.1.7 Orbital cycles

Milankovitch cycles - driven by interactions of the Sun, the Planets and the Moon - affect the geometry of Earth's orbit and modify the geographic distribution of incoming solar radiation. The precession cycle (~20,000 years) is the major orbital influence in the eastern North Pacific. Robert (2004) finds that rainfall in Santa Barbara Basin (ODP Site 893) is linked to maxima and minima of precession. The climate model of Clement *et al* (1999) tests the sensitivity of the tropical Pacific to changes in the distribution of insolation forced by precession. The results show that, although the mean annual change in insolation is close to zero, when there is a seasonal boost in late summer/early autumn, the eastern North Pacific responds by shifting the North Pacific Subtropical High

and the ITCZ northwards. The Trade Winds are intensified and a La Niña state is initiated across the Pacific Basin. According to the model, which was run under Milankovitch parameters for the last 150,000 years, when there is anomalous cooling at this time of year, the response in the eastern North Pacific is an equatorward movement of the North Pacific Subtropical High and the ITCZ. This is the immediate cause of El Niño-like conditions.

It has been proposed that the North Pacific Subtropical High operates differently during glacials (Hendy & Kennett, 1999; Hendy *et al.*, 2002; Cheshire *et al.*, 2005) and glacial climate in the equatorial Pacific has been compared to permanent El Niño-like conditions (Koutavas *et al.*, 2002). The details of this are discussed in Section 2.5.

## 1.2 Previous palaeoclimate records from Guaymas Basin

The potential of Guaymas Basin sediments for highly detailed records has been demonstrated by Pike & Kemp (1996; 1997; 1999) (section 1.1.3), but to date the potential for long palaeoclimate records has never been fully investigated.

In 1979, eastern Guaymas Basin was cored on Leg 64 of the Deep Sea Drilling Project (DSDP Site 480; Fig. 1.1; Table 1.1), using the then newly developed hydraulic piston corer. Recovery was only 80% and there are gaps and disturbances at the top and bottom of each of the 31 core sections (Schrader *et al.*, 1980). Potentially, the core has a 250,000-year record (Schrader *et al.*, 1980), but because of the lack of accurate dates, only the top 20 m of the 152 m of sediment recovered has been fully utilised (Keigwin & Jones, 1990). Using this section of the core, Keigwin & Jones (1990) investigate deglacial climate oscillations and ventilation history; Barron *et al.* (2004) unravel the palaeoceanography of the last 15,000 years using diatom and silicoflagellate assemblage and sediment geochemistry.

A palaeoclimate record of the last 20,000 years has been constructed from gravity core GGC-55 and core JPC-56 (Fig. 1.1, Table 1.1). Sancetta (1995) uses samples from core JPC-56 in conjunction with sediment trap data. She

establishes the seasonal diatom assemblage and uses it to assess environmental conditions from the Late Glacial to the mid-Holocene. Pride *et al.* (1999) reconstruct productivity and redox conditions using stable nitrogen isotopes ($\delta^{15}N$) and biogenic silica. Keigwin (2002) studies palaeoceanography and ventilation history using stable oxygen and carbon isotopes ($\delta^{18}O$ and $\delta^{13}C$) from paired benthic and planktonic foraminifera, and radiogenic carbon isotope ($\delta^{14}C$) data which is compared to paired foraminiferal data from the Sea of Okhotsk, a likely source of glacial NPIW. Barron *et al.* (2005) use diatom and silicoflagellate abundance and assemblage together with geochemistry to construct the palaeoceanographic history of the last 15,000 years.

Schrader *et al.* (1980) report alternations throughout the last ~250,000 years of rhythmically laminated couplets of diatomaceous ooze and muddy diatomaceous ooze with intervals of homogeneous muddy diatomaceous ooze in DSDP Site 480. Simoneit (1991) finds higher concentrations of perylene ($C_{20}H_{12}$; an indicator of oxygen-depletion) in the homogeneous intervals of this core, suggesting that the homogeneity is not the result of bioturbation. The glacial periods contain many intervals of homogeneous sediment, while the interglacials are continuously laminated. The Holocene is represented by 10 m of laminated sediment (ie sedimentation rate is in the order of 1 m per 1000 years).

The studies of the last 25 years (Table 1.2) reveal the climate history of the Late Glacial and the Holocene in Guaymas Basin. The sediments of the North American Last Glacial Maximum (LGM; Dyke *et al.*, 2002), ~16,000 Calendar years before present (16 kyr BP), are homogeneous. Keigwin (2002) shows that there is little evidence of younger LGM bottom waters in either western Guaymas Basin or the Sea of Okhotsk, indicating that neither higher NPIW production nor a more proximal source for it is the cause of higher ventilation in Guaymas Basin. Productivity indicators at the LGM at site JPC-56 are low compared to the present (Sancetta, 1995; Pride *et al.*, 1999), suggesting that upwelling intensity is lower. Homogeneous sediment continues until ~15.5 kyr BP on both sides of Guaymas Basin. After this, the sediment is laminated to the base of the Younger Dryas event at ~12.5 kyr BP (Keigwin, 2002; Barron *et al.*,

2004; 2005). Low productivity continues in western Guaymas Basin from ~16 to ~15 kyr BP, while eastern Guaymas Basin has productivity levels comparable to the present throughout the Bølling-Alleröd warm period (~15-12.5 kyr BP; Barron *et al.*, 2004; 2005). The Younger Dryas event, which is a 1500-year interval of glacial conditions in the circum-North Atlantic (eg Mangerud *et al.*, 1974) and cooler, drier conditions in many other locations around the world (eg Rodbell, 2000), is represented in Guaymas Basin by a short interval of homogeneous sediment. During this interval, there is a reduction in both biogenic silica and the numbers of winter/spring upwelling species (Sancetta, 1995; Pride *et al.*, 1999; Barron *et al.*, 2004; 2005), suggesting a lower intensity of winter upwelling than at present. Laminated sediments return at the beginning of the Holocene (~10 kyr BP), a time when the decline of terrigenous proxies (Barron *et al.*, 2004) suggests an arid climate similar to that of modern Guaymas Basin. Winter productivity is high compared to the present, but the spring diatom bloom is negligible (Sancetta, 1995). Barron *et al.* (2004; 2005) suggest that productivity is high due to intensification of winter winds and a longer than present upwelling season. With the exception of a brief peak of upwelling indicators at ~8.2 kyr BP (Barron *et al.*, 2004) these conditions continue until ~6 kyr BP when tropical diatom species make an abrupt return, suggesting periodic ENSO events (Barron *et al.*, 2004) and a warming in the Gulf (Barron *et al.*, 2005). After ~5.6 kyr BP, Barron *et al.* (2005) find a steady decrease in biogenic silica in western Guaymas Basin, suggesting a decline in diatom productivity. This decline coincides with an increase in coccolith calcium carbonate. These changes do not occur in eastern Guaymas Basin. Sedimentation rates increase during the latest Holocene, indicating a less arid climate; the productivity increases at this time, reported by Pride *et al.* (1999) and Barron *et al.* (2004; 2005), may reflect a rise in river-borne nutrients.

## 1.3 Objectives

The principal objective of this study has been to construct a high-resolution climate record from Guaymas Basin sediment fabric and geochemical composition. The record tests the hypothesis that changes in the migration pattern of the North Pacific Subtropical High - which are driven primarily by solar radiation in the tropics and modified by high latitude feedbacks - has significant local, regional and global effects on climate on all timescales up to and including orbital cycles.

# Chapter 2 Background

## 2.1 Introduction

Driven by the annual migration of the North Pacific Subtropical High, the unique climate and hydrography of the eastern North Pacific have made the Gulf of California a very productive fishing ground. The fisheries are the basis of the prosperity of the region and this economic dependence has generated much research into the parameters of modern climate. Of crucial importance to research into past climates, the interaction of the surface currents with the bathymetry of Guaymas Basin ensures a very high rate of primary productivity that enhances the preservation of each season's sedimentary products.

## 2.2 Formation of the Gulf of California and its modern tectonic regime

The Gulf of California (the 'Gulf') is a semi-enclosed, marginal sea of the eastern North Pacific, lying between Baja California and mainland Mexico. It is ~1100 km long and up to 150 km wide. Figure 2.1 shows the structure of the Gulf.

The opening of the Proto-Gulf of California began in the Late Miocene, ~10 million years ago, when east-west crustal spreading and basin-and-range faulting occurred (Ledesma-Vazquez & Johnson, 2001). Between ~5-6 Myr ago, spreading at the East Pacific Rise caused the transform fault between the Pacific and North American plates to 'jump' from the subduction trench on the Pacific coast of Baja California into the spreading centre in the Proto-Gulf (Lonsdale, 1989). The relative motion of the plates was oblique to the new shear zone and this initiated the San Andreas Fault system and the present-day transtensional strike-slip regime (Einsele, 1992). Baja California has been transferred from the North American to the Pacific Plate and is being pushed northwestwards at the rate of ~6.3 cm per year (Lonsdale, 1989; de la Lanza-Espino & Soto, 1999). The movement is accommodated along transform faults parallel to the Gulf axis, such as the 1500 m deep Ballenas Channel, and at spreading centres perpendicular to the axis (Einsele, 1992).

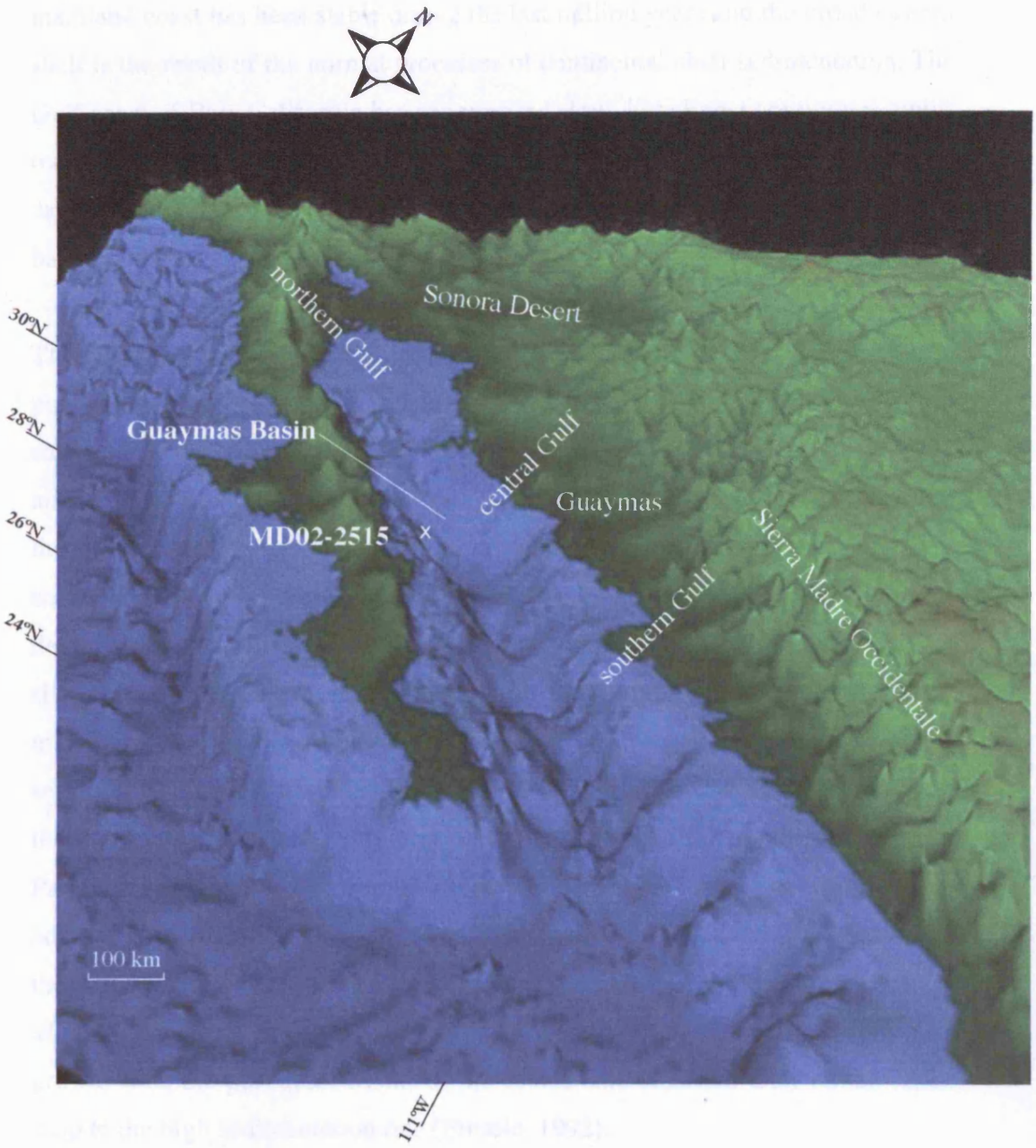


**Figure 2.1:** The topography of the Gulf of California.

[Map from NASA/Goddard Space Flight Center]

Figure 2.2 shows the modern bathymetry of the Gulf and the nearshore Pacific coast of Baja California, and a schematic of the modern fault system affecting the area. The 100-m contour (red) approximates to the glacial coastline. The mainland coast has been stable during the last million years and the broad eastern shelf is the result of the normal processes of continental shelf sedimentation. The Gulf coast of Baja California has experienced slow, but almost continuous, uplift over the last 100,000 years, related to volcano-tectonic events in the La Reforma caldera (Lonsdale, 1989), as a result, the western shelf is very narrow and the bathymetry is steep.

The transtensional regime has led to the development of a series of *en echelon* pull-apart basins (Figs. 2.1 & 2.2; Lonsdale, 1989; Einsele, 1992) and small earthquakes are very common in the Gulf itself (Gorsline *et al.*, 2000). The pull-apart basins are separated by sills that are progressively higher from the mouth of the Gulf northwestwards (eg Bray, 1988; Ripa, 1997). South of ~29°N, the southern and central Gulf, are separated from the northern Gulf by the ~500 m deep Salsipuedes Sill (Figs. 2.1 & 2.9; Bray, 1988; Bray & Robles, 1991). The sills south of ~29°N are not high enough to isolate any of the basins from the major oceanographic processes. Instead, they form restricted basins subject to sediment focusing (Lonsdale, 1989; Einsele, 1992). There is less movement on the older transform faults in the northern Gulf than on those close to the East Pacific Rise. This fact, in combination with the modern arid conditions of the adjacent Sonora Desert (section 2.6) and an abundance of fluvial sediments from the Rio Colorado (before its damming in the mid-20$^{th}$ Century; Kowalewski *et al.*, 2000), has resulted in basin infilling (Einsele, 1992). Because of their fast growth-rate, the pull-apart basins of the central and southern Gulf remain open despite the high sedimentation rate (Einsele, 1992).

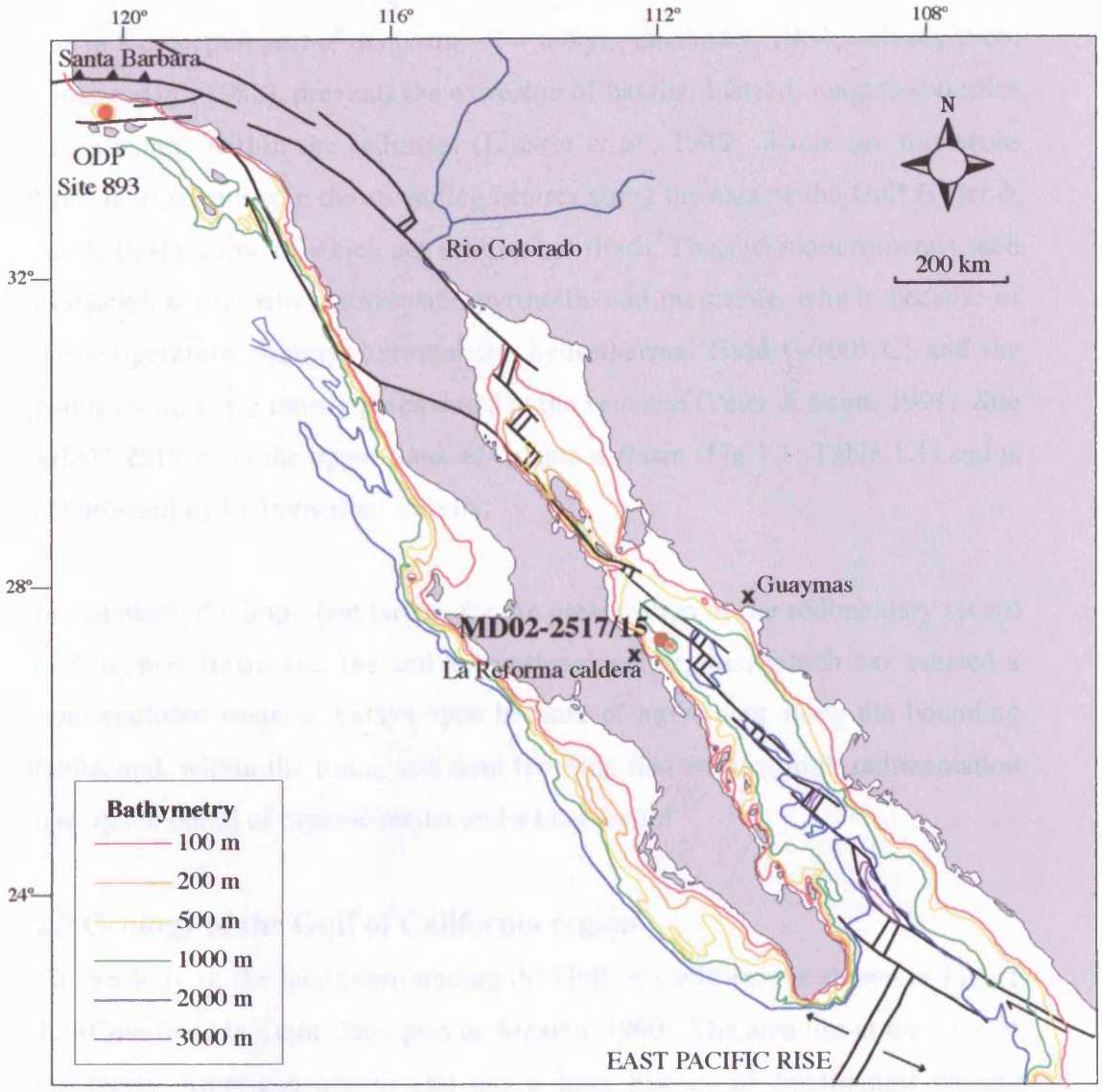


**Figure 2.2:** Modern bathymetry of the Gulf of California and the Pacific coast of Baja California (data from British Oceanographic Centre) and a schematic of the modern active fault system (after Humphreys & Weldon, 1991). The 100 m contour (red) approximates to the coastline during the glacial.

Guaymas Basin is the largest of the pull-apart basins (Figs. 2.1 & 2.2). It is located in the central Gulf immediately south of the Salsipuedes Sill and has an area of ~240 x 60 km. At ~2000 m depth, there are two sub-parallel spreading centres, oriented northeast-southwest (Lonsdale, 1989). The rapid sedimentation rate in the deepest part of the basin, ~1-4 m/kyr (van Andel, 1964; Calvert, 1966; Curray *et al.*, 1982), prevents the extrusion of basalts. Instead, magma solidifies as intrusions within the sediment (Einsele *et al.*, 1980). There are numerous hydrothermal spires in the spreading centres along the axis of the Gulf (Peter & Scott, 1991), some of which are venting hot fluids. These contain minerals such as calcite, barite, silica, stevensite, pyrrhotite and marcasite, which, because of the temperature contrast between the hydrothermal fluid (~300° C) and the bottom waters, are mostly precipitated at the vent site (Peter & Scott, 1991). Site MD02-2515 is on the upper flank of Guaymas Basin (Fig 1.1; Table 1.1) and is not affected by hydrothermal activity.

In summary, the important factors for the preservation of the sedimentary record of Guaymas Basin are: the active transtensional regime, which has created a semi-enclosed basin that stays open because of movement along the bounding faults, and, within the basin, sediment focusing that ensures high sedimentation rate, quick burial of organic matter and a long record.

## 2.3 Geology of the Gulf of California region

The geology of the lands surrounding the Gulf of California is shown in Figure 2.3 (Comité de la Carta Geologíca de México, 1960). The area lies at the edge of the North American craton and has a long history of continental margin sedimentation (Lonsdale, 1989). Only small areas of the older rocks are exposed, most are covered by igneous rocks of Mesozoic and younger age.

Apart from a small area of Palaeozoic metamorphic rocks, the geology of Baja California consists of Mesozoic intrusive igneous rocks overlain by Palaeogene lavas with small amounts of Mesozoic and Palaeogene clastic rocks. Isla Angel de la Guarda (Fig. 1.1) is part of this igneous province, but is separated from it by the Ballenas Channel (Lonsdale, 1989; Bray & Robles, 1991). At the latitude

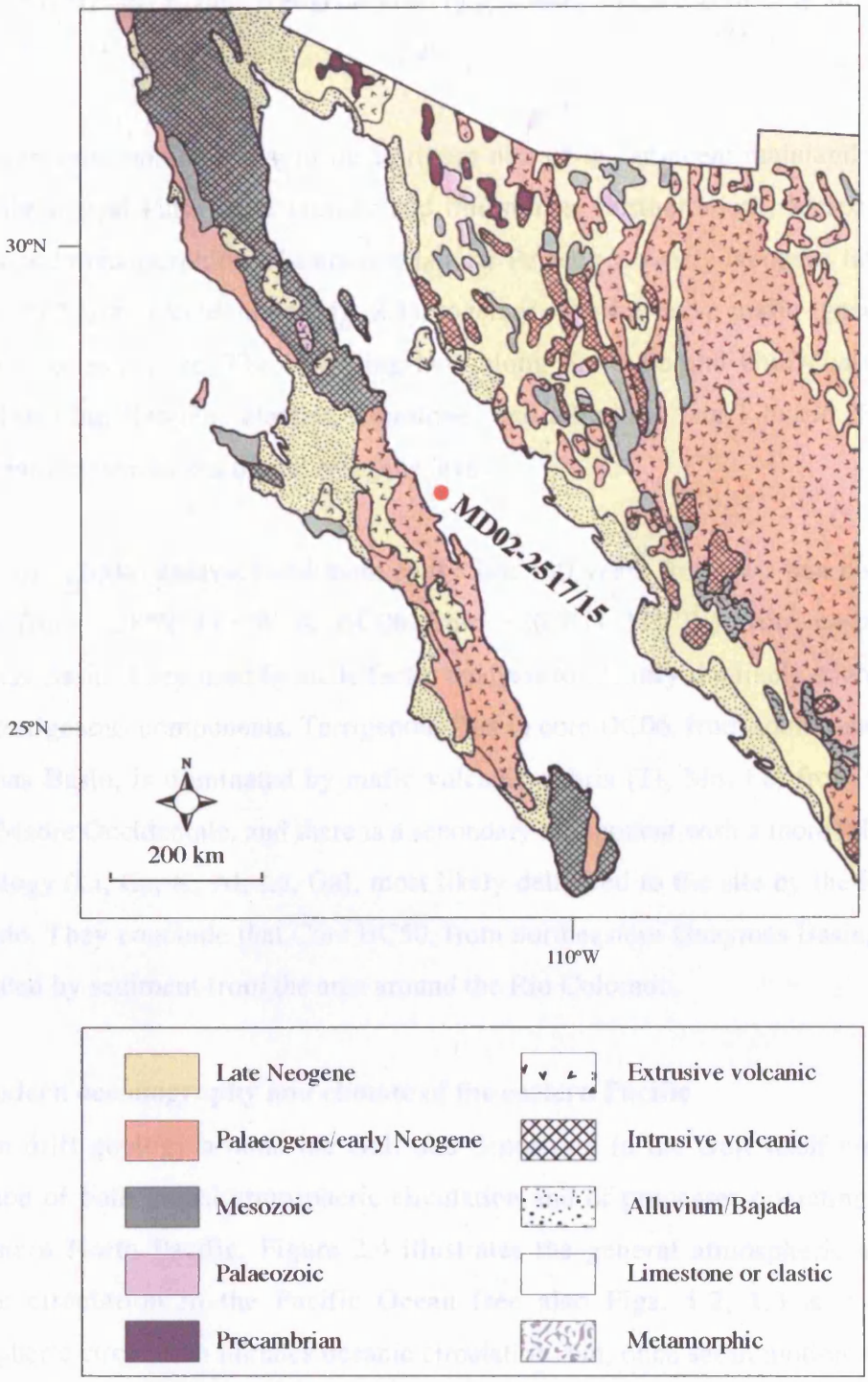


**Figure 2.3:** Geology of Baja California and northwestern Mexico.

[Courtesy of the Perry-Castañada Library Map Collection, University of Texas]

of Site MD02-2515, late Neogene alluvium covers the western side of the peninsula.

The oldest outcropping rocks in the northern part of the adjacent mainland are Precambrian and Palaeozoic clastics and limestones. Further south, Mesozoic clastics and metamorphic rocks are overlain by Palaeogene/early Neogene lavas (the Sierra Madre Occidentale, Fig. 2.1), together with intrusive mafic igneous rocks of the same age. The low-lying land along the mainland Gulf coast is formed of Late Neogene clastics, limestones and alluvium. Isla Tiburon (Fig. 1.1) is entirely composed of late Neogene lavas.

Dean *et al.* (2004) analysed sediment of the last 180 years from two box cores (BC50 from ~28°N 111°W & BC06 from ~26.7°N 110°W) from eastern Guaymas Basin. They used Q-mode factor analysis to identify the likely sources of the terrigenous components. Terrigenous flux in core BC06, from southeastern Guaymas Basin, is dominated by mafic volcanic debris (Ti, Mn, Fe) from the Sierra Madre Occidentale, and there is a secondary component with a more felsic mineralogy (Li, Ce, K, Al, La, Ga), most likely delivered to the site by the Rio Colorado. They conclude that Core BC50, from northeastern Guaymas Basin, is dominated by sediment from the area around the Rio Colorado.

## 2.4 Modern oceanography and climate of the eastern Pacific

Modern drift geology around the Gulf and deposition in the Gulf itself are a reflection of both global atmospheric circulation and of processes operating in the eastern North Pacific. Figure 2.4 illustrates the general atmospheric and oceanic circulation in the Pacific Ocean (see also Figs. 1.2, 1.3 & 1.4). Atmospheric circulation initiates oceanic circulation, but, once set in motion, the physical and thermal inertia of the ocean tends to make its circulation self-perpetuating and this has a feedback into atmospheric processes (Barry & Chorley, 2003).

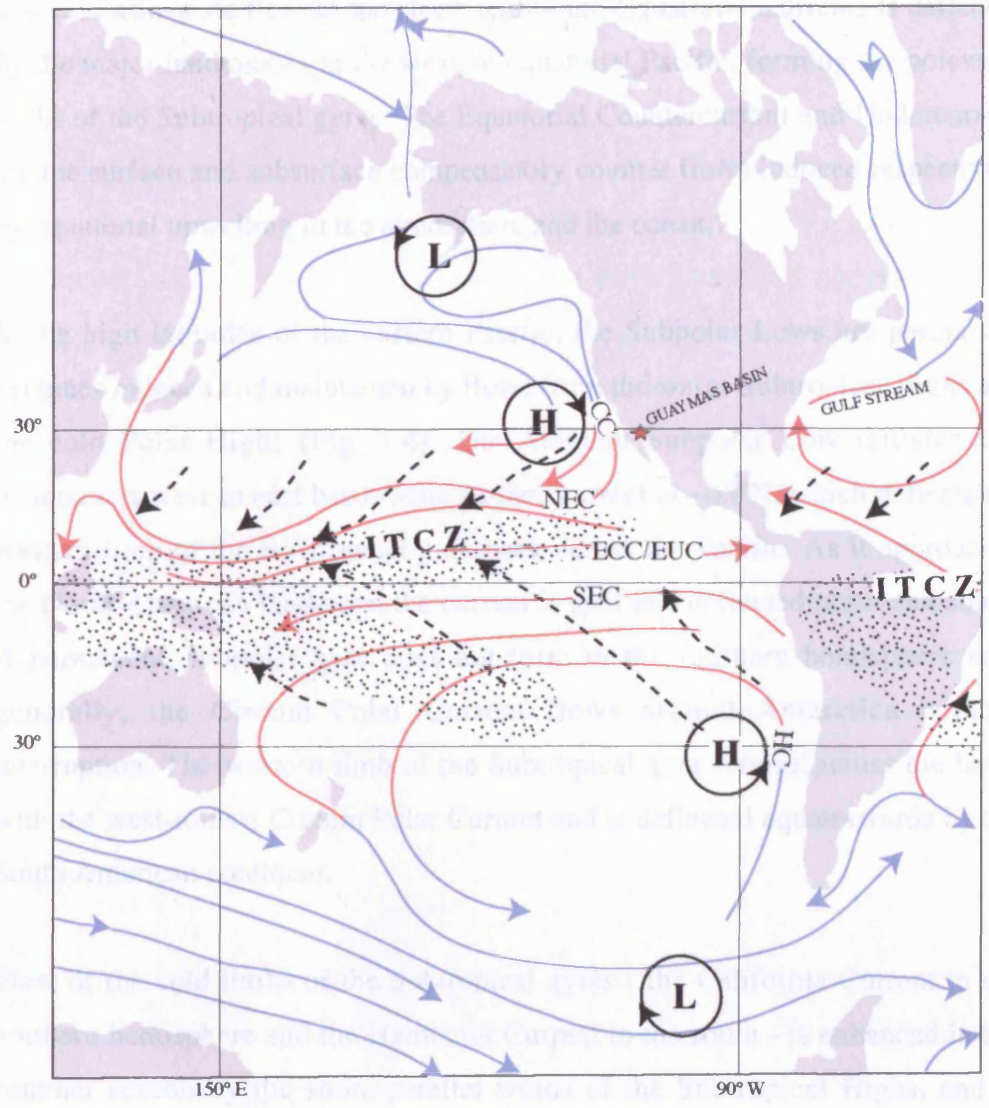


**Figure 2.4:** The general atmospheric and oceanic circulation of the Pacific.
[adapted from Barry & Chorley (2003)]

Initiated and sustained by the Subtropical Highs and the Trade Winds, the east-to-west basin-wide flow of the North and South Equatorial Currents is deflected by the major landmasses in the western equatorial Pacific, forming the poleward limbs of the Subtropical gyres. The Equatorial Countercurrent and Undercurrent are the surface and subsurface compensatory counter flows induced respectively by equatorial upwelling in the atmosphere and the ocean.

In the high latitudes of the eastern Pacific, the Subpolar Lows are permanent cyclones induced and maintained by flows from the warm Subtropical Highs and the cold Polar Highs (Fig. 1.4). The Aleutian Subpolar Low initiates and maintains a west-to east basin-wide surface current at ~45°N, which deflects the western limb of the Subtropical gyre back across the Pacific. As it approaches the North American landmass, the current is split and deflected north and south. A permanent Subpolar gyre does not form in the southern hemisphere and, generally, the Circum Polar Current flows around Antarctica without interruption. The western limb of the Subtropical gyre returns across the basin with the west-to-east Circum Polar Current and is deflected equatorwards by the South American continent.

Flow of the cold limbs of the Subtropical gyres - the California Current in the northern hemisphere and the Humboldt Current in the south - is enhanced in the summer season by the shore-parallel winds of the Subtropical Highs, and is associated with coastal upwelling from late February to July in the north and August to January in the south. Flow in the poleward eastern limb of the North Pacific Subpolar gyre is seasonally enhanced by the shore-parallel winds of the Aleutian Subpolar Low and is associated with coastal downwelling from early autumn to winter (McShane *et al.*, 2004).

There is rainfall all year round in the Tropics of the eastern Pacific. In the Subtropics (~20-30°N and S), rainfall occurs in summer in the wake of the poleward migration of the Subtropical High. Between ~30-50°N and S, the wet season is winter, with rain brought by the Subpolar Lows. Coastal fog, associated with the upwelling season, ameliorates the climate of southern California (eg

McShane *et al.*, 2004), northern Chile and Peru, which would otherwise be as arid as the adjacent continental interiors. Polewards of ~45°N and S, there is precipitation almost all year round.

It is a logical deduction to suggest that if the migration range of the Subtropical Highs is less than at present, the influence of the Subpolar Lows increases. The Subtropical wet/dry divide will shift towards the equator and regions, such as Guaymas Basin, which currently have a winter dry season, will have a wet winter season and the dry upwelling season will be in summer.

**2.5 Glacial climates in the eastern Pacific and the Americas**

A review of glacial to interglacial climate records in the eastern Pacific and the Americas reveals a symmetrical pattern of changes that strongly indicates a substantial, systematic reorganisation of atmospheric and oceanic circulation. To illustrate the pattern of change, Figure 2.5 presents a snapshot of climate of the Americas at the LGM (relative to the present) using data from the papers discussed below. The list of references used (see Appendix IV) is representative, but by no means exhaustive.

There is no consensus as to what is controlling the observed glacial to interglacial changes. However, I propose that restriction of Subtropical High migration during the glacial is responsible for most, if not all, of the effects described here. Restricted migration of the Subtropical Highs means that the Trade Winds affect a lesser extent of the ocean, resulting in less equatorial water vapour (which further weakens the Subtropical Highs) and a deeper coastal thermocline/nutricline. Expanded Subpolar Lows means that there is more coastal downwelling and well-ventilated intermediate waters.

Along the North American margin during the Late Glacial, there were systematic north-south variations that are consistent with the annual migration of the North Pacific Subtropical High gradually extending into its full interglacial range. Immediately prior to the LGM at ~42°N the Aleutian Subpolar Low dominated climate along the margin, which forced an expansion of the Subpolar ocean gyre.

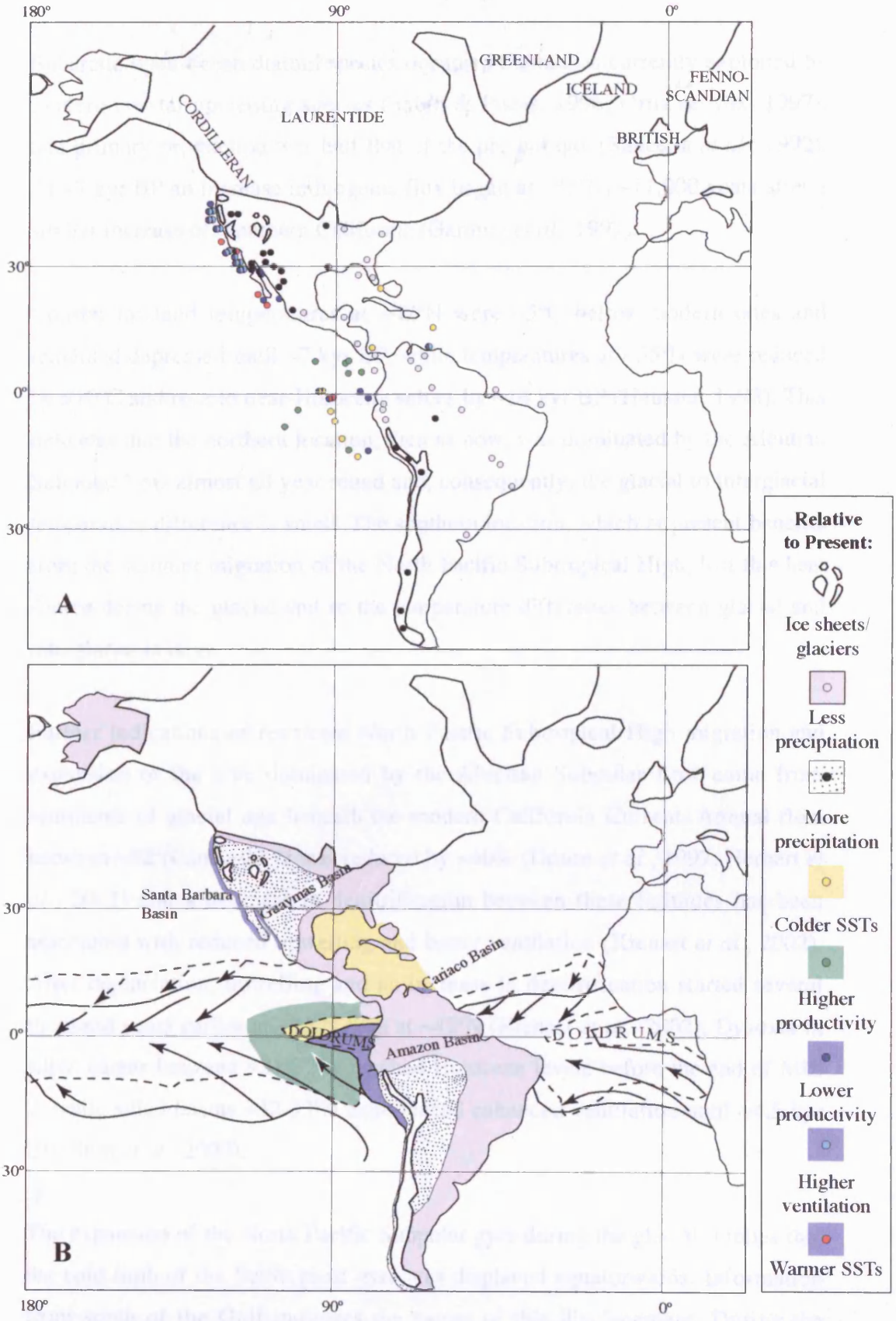


**Figure 2.5:** A snapshot of the climate and oceanography at the LGM.
**A:** For locations and references, see Appendix IV.
**B:** A synthesis of the data in A. Dashed lines are Trade Wind limits in July, solid lines in January. Atlantic Trade Wind limits are an extrapolation.

Subarctic open-ocean diatom species occupied the niches currently exploited by modern coastal upwelling species (Sabin & Pisias, 1996; Ortiz & Mix, 1997), and primary production was half that of the present day (Sancetta *et al.*, 1992). At ~7 kyr BP an increase in biogenic flux began at ~38°N, ~11,000 years after a similar increase off southern California (Gardner *et al.*, 1997).

Coastal lowland temperatures at ~42°N were ~5°C below modern ones and remained depressed until ~7 kyr BP, while temperatures at ~35°N were reduced by >10°C and rose to near-Holocene values by ~14 kyr BP (Heusser, 1998). This indicates that the northern location, then as now, was dominated by the Aleutian Subpolar Low almost all year round and, consequently, the glacial to interglacial temperature difference is small. The southern location, which at present benefits from the summer migration of the North Pacific Subtropical High, lost this heat source during the glacial and so the temperature difference between glacial and interglacial is large.

Further indications of restricted North Pacific Subtropical High migration and expansion of the area dominated by the Aleutian Subpolar Low come from sediments of glacial age beneath the modern California Current. Annual flow between ~42°N and ~23°N was reduced by ~40% (Doose *et al.*, 1997; Herbert *et al.*, 2001) and a decrease in denitrification between these latitudes has been associated with reduced upwelling and better ventilation (Kienast *et al.*, 2002). After deglaciation, upwelling and an increase in denitrification started several thousand years earlier at ~23°N than at ~42°N (Kienast *et al.*, 2002). Dysoxia in silled basins between ~31-32°N reached Holocene levels before the end of MIS 2, while silled basins ~32-33°N experienced enhanced ventilation until ~4.5 kyr BP (Stott *et al.*, 2000).

The expansion of the North Pacific Subpolar gyre during the glacial implies that the cold limb of the Subtropical gyre was displaced equatorwards. Information from south of the Gulf indicates the extent of this displacement. During the coldest phases of the last glacial, there was drastically reduced marine primary productivity at ~24°N at the southern tip of Baja California, (van Geen *et al.*,

2003; Ortiz *et al.*, 2004) and at ~22°N, off central mainland Mexico (Ganeshram & Pedersen, 1998); during interstadials, productivity was comparable to the present. Marine sites between ~5°-3°N 88°-87°W record increased upwelling and higher productivity during the glacial than at present (Pedersen *et al.* 1991; Loubere, 2002). These sites are presently in the Doldrums - the ITCZ in the lee of the continents where the Trade Winds, receiving no impetus from the Subtropical Highs, are light (Barry & Chorley, 2003; Fig. 1.4). The glacial change in productivity at these sites suggests that the North Pacific Subtropical High and the 'California Current' were shifted well south of their interglacial range.

Marine sites at ~90° W immediately north and south of the equator, presently affected by the southeast Trade Winds, record lower productivity than present (Lea *et al.*, 2000; Loubere, 2002; Koutavas *et al.*, 2002), suggesting that the glacial Doldrums were located at the equator. The westward extent of the glacial Doldrums can be estimated from SST records. At ~2°N 90°W there were higher-than-present SSTs (Lea *et al.*, 2000), while at ~1°S and ~100 km to the east SSTs were lower (Koutavas *et al.*, 2002). Lea *et al.* (2006) show that SSTs at ~2°N were colder than present during stadials for the last ~135,000 years, that colder SSTs developed ~3000 years ahead of ice volume, and that SST variations have a ~1000-year cyclicity. They conclude that atmospheric forcing was responsible for large-scale climate change in the eastern equatorial Pacific.

Andreason & Ravelo (1997) and Loubere (2002) investigated several sites ~500-1000 km off Peru and found higher productivity and/or colder SSTs at all sites to the west, while sites to the east show lower productivity and/or warmer SSTs. This suggests that, while the Trade Winds were stronger than present over the open ocean, the South Pacific Subtropical High had a restricted migration and the geographical extent of coastal upwelling was reduced. Colder SSTs ~500 km offshore between ~8°-20°S, suggest that there was a shallowing of the thermocline and compression of the climate zones north and south of the equator (Andreason & Ravelo, 1997).

Although the atmosphere was globally more dynamic and much drier during glacials than at present (Harrison *et al.*, 2001), not all regions of the Americas were drier than now. One of the consequences of expanding the Subpolar Lows and restricting the migration of the Subtropical Highs is an equatorward shift of the dry Subtropics. This is evident from the change in glacial precipitation patterns over the southwest of both Americas (Fig. 2.5).

Some areas of North America that are presently desert or semi-desert were not arid during the glacial. Southwestern North America and Baja California experienced much wetter climate than at present (eg van Devender, 1990a & b; Reheis, 1999; Betancourt *et al.* 2001; Metcalfe *et al.*, 2002; Holmgren *et al.*, 2003; Oviatt *et al.*, 2003). Rainfall in Baja California and New Mexico (Lozano-Garcia *et al.*, 2002; Rhode, 2002; Menking *et al.*, 2004) was double that of the present day and runoff was ~18% of annual precipitation. The phenomenon of the glacial pluvial lakes of southwest North America is well known (eg Smith & Street-Perrott, 1984). Tchakerian & Lancaster (2002) find that 100 pluvial lakes existed during the glacial in the Mojave Desert and the western Great Basin, and that lake level changes correlate with large-scale atmospheric controls. The climate model of Hostetler *et al.* (1994) indicates that the evaporation potential of pluvial Lakes Bonneville and Lahontan constituted a positive feedback that reinforced the re-organised atmospheric circulation. Williams (2002) suggests that in this area the lower albedo and higher evapotranspiration from the greater treecover contributed a positive feedback. Trees grew in areas of northern Baja California that are currently arid (Lozano-Garcia *et al.*, 2002; Rhode, 2002). Jackson *et al.* (2000 and refs) find that immediately north of the Gulf the higher rainfall anomaly increased abruptly towards the west, with ~20% more precipitation than present at ~30°N 90°W, and ~50% more at ~30°N 91°W.

Eastern and northeastern North America were drier than present. Williams (2002 and refs) suggests that lower temperatures, precipitation and atmospheric $CO_2$ in southeastern North America caused less dense treecover and that this, in turn, contributed to the drying out of the atmosphere through higher albedo and lower evapotranspiration. Jackson *et al.* (2000 and refs) find that aridity increased in

severity from southeast to northwest: rainfall in Florida was ~20% less than today and ~60% less in Wisconsin.

This east-west glacial precipitation anomaly is also evident in Central and South America. At present, the ITCZ affects the climate of all parts of Central America, but during the LGM lake records show that sites west of ~95°W were wetter than at present (Watts & Bradbury, 1982), while sites east of this were drier (Bradbury, 1989; Martin, 1964; Leyden *et al.*, 1993; Bush & Colinvaux, 1990). In South America, a higher than present precipitation rate fed the growth of glaciers and ice caps over the southern and central Andes (Hulton *et al.*, 2002; Hajdas *et al.*, 2003; Moreno & Leon, 2003). Prieto (2000) attributes drought in southeastern South America to the greater than present rain shadow effect. Climate was wetter than present in the centre of the continent (van der Hammen & Absy, 1994; Hansen & Rodbell, 1995; Klein *et al.*, 1999; de Freitas *et al.*, 2001; Seltzer *et al.*, 2002), while eastern central South America was drier than at present (Behling & Lichte, 1997; Salgado-Labouriau *et al.*, 1998; Arz *et al.*, 1998).

At present, the southeast Atlantic Trade Winds deliver year-round moisture to the Amazon Basin and the migration of the ITCZ into the summer hemisphere (Fig. 1.4) ensures that rainfall is distributed to the continent immediately north and south of the equator (Hastenrath, 2002). During the glacial, climate north of the Amazon Basin was drier than at present (van Geel & van der Hammen 1973; Bradbury *et al.*, 1981; Leyden, 1985; Colinvaux *et al.*, 1997; Behling & Hooghiemstra, 1998; Rodbell *et al.*, 1999; Colinvaux & de Olivera, 2000; McCulloch *et al.*, 2000). Colinvaux & de Olivera (2000), reviewing the last glacial palaeoclimate records of the Amazon Basin, conclude that the basin was completely forested throughout, but seasonal tree types were more predominant than at present, indicating that there was a wet and a dry season, similar to that occurring in modern northern Venezuela. Benway *et al.* (2006) and Leduc *et al.* (2007) find that salinity in the Eastern Pacific Warm Pool (ie the Doldrums) increased during the glacial, suggesting that the Atlantic Trade Winds were displaced southwards.

Modern Cariaco Basin, northern Venezuela, is a restricted basin with a sill depth of ~200 m. Its climate consists of a dry winter upwelling season, when the North Atlantic Trade Winds blow across the Caribbean Sea, and a non-upwelling summer season, when the zone of Trade Wind intensity moves northwards allowing the rains of the ITCZ to affect the basin (Peterson *et al.*, 2000b; Fig. 1.4). At ODP Site 1002, high productivity and the restricted setting result in bottom water anoxia and the preservation of the sedimentary products of the contrasting seasons as varves (eg Peterson & Haug, 2006). The Bølling-Alleröd/Holocene is fully varved (Peterson *et al.*, 2000b) and L* (light/dark reflectance) values show a remarkable correspondence with the GISP2 oxygen isotope record (Peterson *et al.*, 2000a; Haug *et al.*, 2001; Haug *et al.*, 2003). During the glacial, the sediment is intermittently laminated. The massive intervals have been attributed to the isolation of the basin during sea level lowstands (Overpeck *et al.*, 1989; Peterson *et al.*, 2000b), when only surface water was able to enter the basin. Low terrigenous flux is attributed to the failure of the ITCZ summer migration (Peterson *et al*, 2000b; Yarincik *et al.*, 2000), which caused aridity in northern Venezuela (Peterson & Haug, 2006). The colder than present glacial SSTs in the Caribbean and the Gulf of Mexico, reported by Emiliani *et al.* (1975), Guilderson (1994), Lea *et al.* (2003), Kameo *et al.* (2004) and many others, can be interpreted as the result of the equatorward displacement of the Trade Wind zone.

## 2.6 Modern climate of the Gulf of California and adjacent areas

Figure 2.6 presents the modern climate of the Gulf of California. The Gulf south of ~27°N is in the wet Subtropics where yearly precipitation exceeds evaporation. Most of the Gulf is in the dry Subtropics where evaporation exceeds precipitation (McGregor & Nieuwolt, 1998). South of ~28°N, the Sierra Madre Occidentale has a steppe climate, as do the mountainous regions in southern Baja California. The other Gulf coasts, and the southern half of Baja California, have a desert climate. All have an average annual temperature >18° C. The Pacific coast of northern Baja California, depending on its elevation, has a desert or steppe climate with an average annual temperature <18° C.

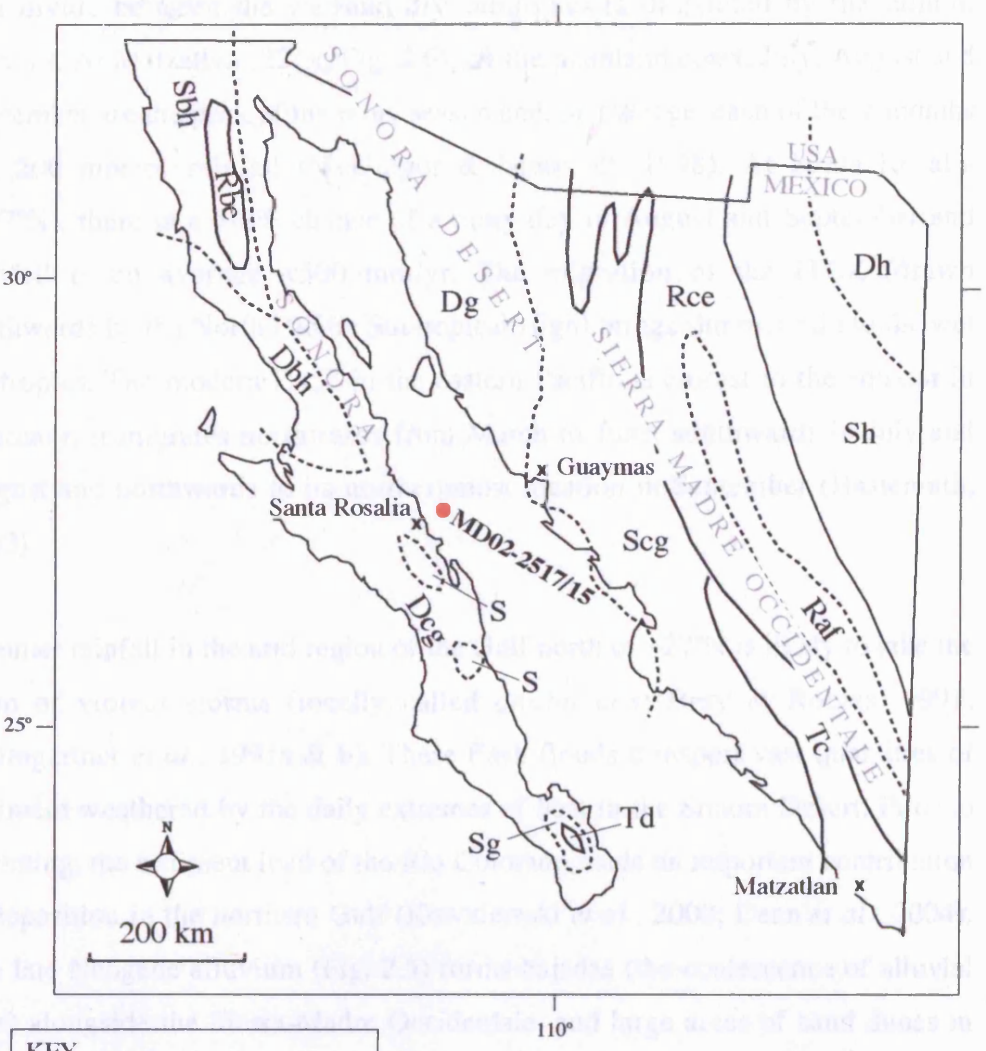


| KEY | |
|---|---|
| **T** | Tropical, rainy, no cool season |
| **S** | Steppe |
| **D** | Desert |
| **R** | Rainy, mild winters |
| **a** | No dry season |
| **b** | Winter wet season |
| **c** | Winter dry season |
| **d** | Max. rainfall autumn, dry winters |
| **e** | Hot summers, average T >22°C |
| **f** | Cool summers, average T <22°C |
| **g** | Average annual T >18°C |
| **h** | Average annual T <18°C |

**Figure 2.6:** Modern climate in northwestern Mexico.

[Courtesy of the Perry-Castañada Library Map Collection, University of Texas]

The divide between the wet and dry subtropics is illustrated by the rainfall patterns. At Matzatlán (22°N; Fig. 2.6), on the mainland coast, July, August and September are the peak of the rainy season and, on average, each of these months has 200 mm of rainfall (McGregor & Nieuwolt, 1998). At Santa Rosalia (~27°N), there is a 5-8% chance of a rainy day in August and September and rainfall is on average <500 mm/yr. The migration of the ITCZ (drawn northwards by the North Pacific Subtropical High) brings summer rain to the wet subtropics. The modern ITCZ in the eastern Pacific is closest to the equator in February, it migrates northwards from March to June, southwards in July and August and northwards to its northernmost location in September (Hastenrath, 2002).

Summer rainfall in the arid region of the Gulf north of ~27°N is likely to take the form of violent storms (locally called *chubascos*; Bray & Robles, 1991; Baumgartner *et al.*, 1991a & b). These flash floods transport vast quantities of sediment weathered by the daily extremes of heat in the Sonora Desert. Prior to damming, the sediment load of the Rio Colorado made an important contribution to deposition in the northern Gulf (Kowalewski *et al.*, 2000; Dean *et al.*, 2004). The late Neogene alluvium (Fig. 2.5) forms bajadas (the coalescence of alluvial fans) alongside the Sierra Madre Occidentale, and large areas of sand dunes in the Sonora Desert. This reflects rapid weathering and mass transport in the harsh environment.

The seasonal wind pattern in the Gulf most quoted in the literature is a yearly monsoonal reversal with strong northwesterlies in winter and light southeasterlies in summer (eg Roden, 1958; Hales, 1972; Alvarez-Borrego, 1983; Merrifield & Winant, 1989; Badon-Dangon, *et al.*, 1991; Pride *et al.*, 1999; Dean *et al.*, 2004; Barron *et al.*, 2005). However, according to Pares-Sierra *et al.* (2003) the monsoonal pattern is based on only a few observations from coastal stations and even fewer over the sea. The symmetrical monsoonal reversal does occur, but only in the upper winds (Douglas *et al.*, 1993).

Pares-Sierra *et al.* (2003) base their assessment of the wind pattern on satellite-derived data (NSCAT and Quickscat) collected between 1996 and 2002. Wave heights are measured and then surface roughness is related to wind speed using a computer model. Their results are shown in Figure 2.7. The strongest winds are northwesterlies blowing in December, January and February. These months show the greatest magnitude variations in wind strength during the year. Weaker northwesterlies prevail during March, April and May, and these are weakest along the mainland coast. In June, July and August, the winds are weak northwesterlies in the northern Gulf, turning to westerlies along the mainland coast and in the southeastern Gulf. Southerlies are occasionally experienced along the east coast in the southern Gulf. Winter conditions return to the Gulf from north to south.

Although the North Pacific Subtropical High is not named by Pares-Sierra *et al.* (2003) as the forcing mechanism of the seasonal wind pattern, the observed variations are consistent with its migration pattern. Particularly telling is the strengthening of the winds from north to south during late autumn and variability in magnitude of winter winds (cf the North Pacific Subtropical High moving southwards in late November to its midwinter location and then its passage northwards in late February).

The data of Pares-Sierra *et al.* (2003), suggest that the summer low-pressure cell over the Sonora Desert (see Fig. 1.4; Pride *et al.*, 1999; Dean *et al.*, 2004) is likely to be responsible for the light westerlies (Fig. 2.7, June-July-August). Light winds and strong heating result in a stratified water column (eg Badon-Dangon *et al.*, 1991; Sancetta, 1995, Pride *et al.*, 1999). Kemp *et al.* (2000) associate the low-nutrient summer stratification with slow-growing diatom species.

Arid southwestern North America is one of the principal dust sources of the modern world (Harrison *et al.*, 2001). Locally, fine-grained material is lofted from the floor of the Sonora Desert and deposited either where the wind dies down or as particles in rainfall (Baba *et al.* 1991a & b; Baumgartner *et al.*,

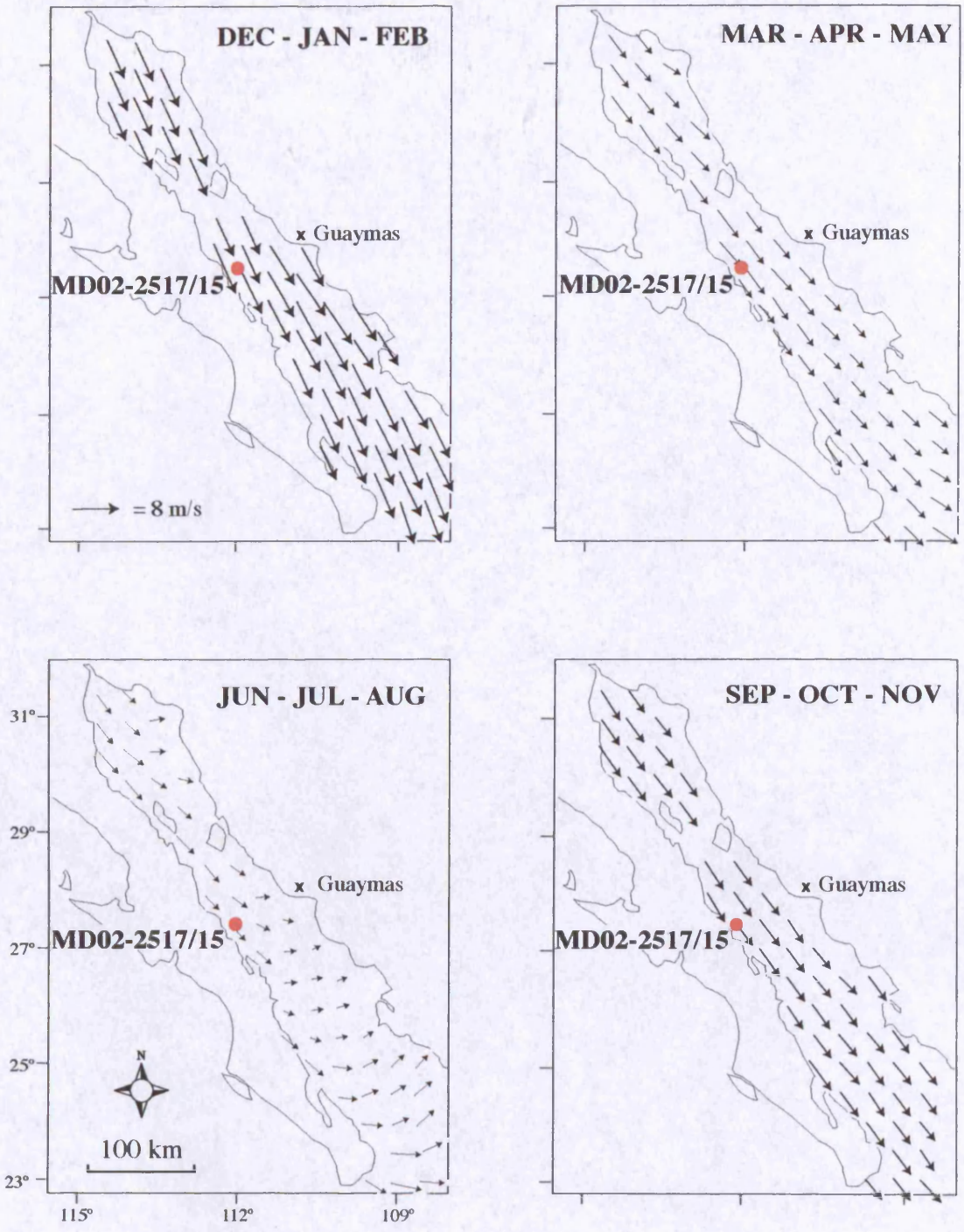


**Figure 2.7:** Seasonal surface wind patterns (adapted from Pares-Sierra *et al.*, 2003). Wind strength during Dec-Jan-Feb is very variable.
[Size of arrow reflects strength of wind]

1991b). Baba *et al.* (1991b) demonstrate that the mid-20th century damming of the rivers that drain into eastern Guaymas Basin has made no difference either to the type or the amount of sediment deposited, and they conclude that modern deposition of the silt-rich dark laminae is aeolian. These findings are based on the analysis of sediment predominantly from the 20th century; Baba *et al.* (1991b) analyse sediment from the last two centuries in order to demonstrate the type of deposition before and after damming. While it is probably safe to extend this hypothesis to the rest of the Holocene, it is unlikely that deposition during the glacial was dominated by aeolian flux. The increased rate of rainfall in the North American southwest and in Central America during the glacial (Section 2.5) suggests that the Sonora Desert was vegetated then and, therefore, could not be a source of aeolian flux to Guaymas Basin.

Gibbard & Lewin (2002) present a model of the development of fluvial behaviour during a glacial-interglacial cycle. Although their work is based on lowland British river sediments, the analogy can be extended to river systems elsewhere such as the Rio Colorado, which has a large catchment area (Fig. 2.2 shows only part of it) and discharges directly into the northern Gulf. Three major fluvial behavioural modes occur: fine-sediment-dominated and meandering during the interglacial; an incision mode during sea level fall in the early glacial; braided and gravel-dominated during the full glacial (Gibbard & Lewin, 2002). During the first of these modes, the majority of the fluvial sediment is deposited in the lower reaches of the river (the highstand wedge of sequence stratigraphy). Before 20th Century damming, the Holocene Colorado fine-grained sediments were trapped in the northern Gulf. In the second fluvial mode, the highstand wedge is incised and the reworked sediments are deposited on the seafloor as a prograding fan. With a 100-m fall of sea level, the mouth of the Colorado would have been ~100 km closer to Site MD02-2517/2515 (Fig. 2.2) and the fine-grained sediments of the northern Gulf, re-worked during incision, would have been deposited where the waters are relatively deep south of the Salsipuedes Sill. In the third fluvial mode, because of its high energy, no sediment is deposited in the river, it is all deposited in the ocean as the lowstand fan. Fluvial sediment load is high during the third mode because of high weathering and erosion rates.

The high precipitation rate in the Rio Colorado catchment area during the glacial (section 2.5) indicates that fluvial sediment load acquired via runoff was high.

During the glacial, between a quarter and a third of the northern Gulf would have been exposed (Fig. 2.2) and most likely vegetated, as would the shelf on the eastern side of Guaymas Basin, and therefore were unlikely to have been a dust source. There would have been no shelf on the western side of the Gulf and the 500-m contour shows the steepness of the bathymetry (Fig. 2.2). Runoff from the adjacent Gulf coast of Baja California would have carried sediment directly into the deep water over Site MD02-2517/2515.

## 2.7 Modern hydrography of the Gulf of California

The barrier islands along the mainland coast south of ~24°N (Figs. 1.1, 2.2 & 2.11) result from the abundant sediment brought into the Gulf by the copious rainfall of this region and the southward longshore drift, caused by the prevailing wind pattern and hydrological circulation of the Gulf.

Figure 2.8 illustrates the modern hydrography of the Gulf. The deepest, widest part of the Gulf (~23°N) has an open connection to the Pacific Ocean (Fig. 2.1), allowing the inflow of Pacific Deep Water (PDW) and North Pacific Intermediate Water (NPIW). These waters are of normal salinity (Bray & Robles, 1991) and occupy depths between 3000-900 m and 900-450 m respectively (Bray, 1988). PDW is cold, dense and relatively well oxygenated. Because of its density and the Salsipuedes Sill, PDW does not penetrate into the shallow northern Gulf (Bray, 1988). NPIW is warmer and less dense than PDW (Bray, 1988). When it enters the Gulf, it has a relatively low oxygen content due to bioproductivity in the Pacific Ocean. High rates of primary productivity in the Gulf drive further oxygen depletion and an OMZ, bathing the flanks of Guaymas Basin, is formed (Fig. 2.9; Bray & Robles, 1991; Keigwin & Jones, 1990; Barron *et al.*, 2005). The boundary of NPIW is just below the Salsipuedes Sill and so it does not occupy the northern Gulf (Bray & Robles, 1991).

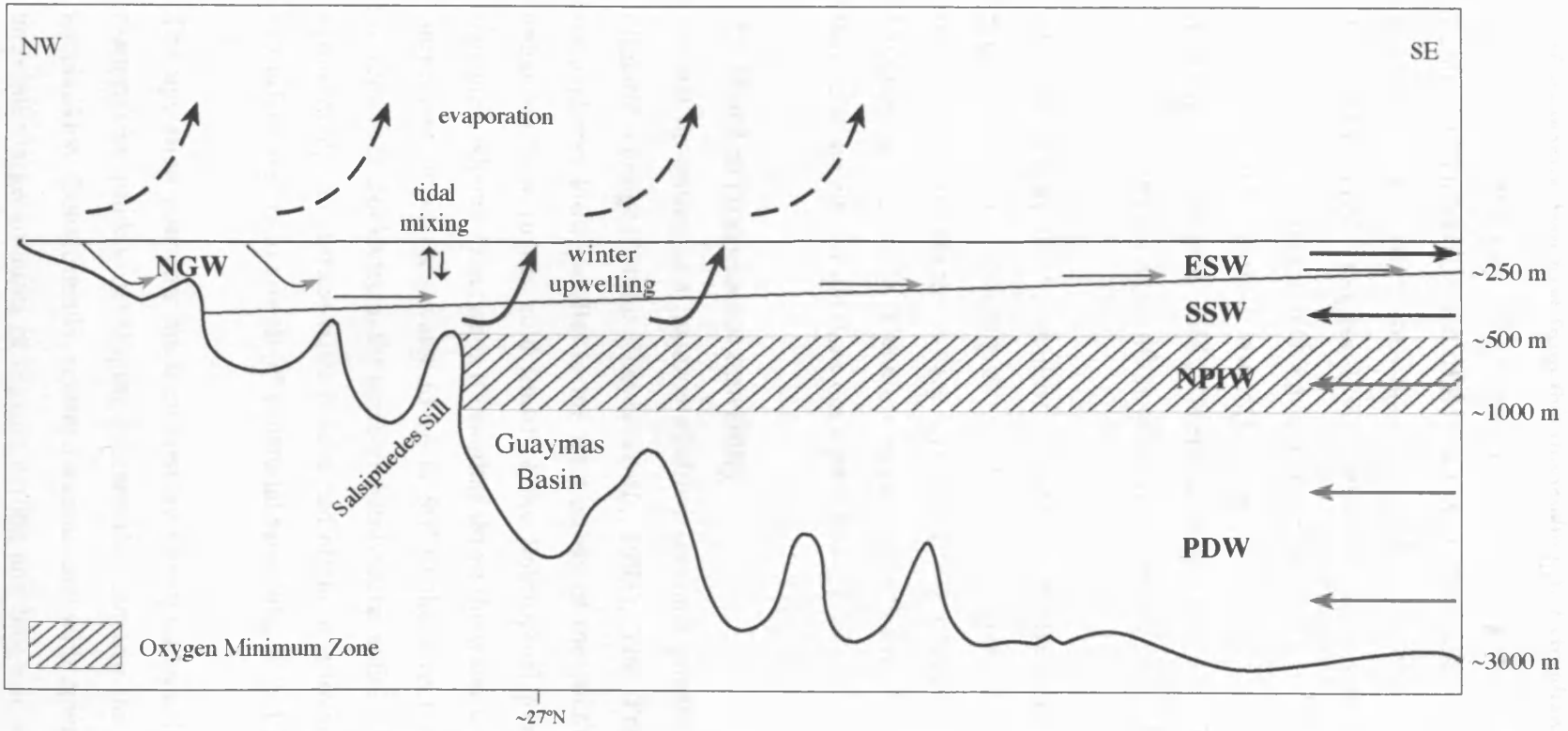


**Figure 2.8:** Schematic of modern hydrography (modified after Bray (1988) and Bray & Robles (1991)).
[Vertical scale exaggerated]
**ESW** - Equatorial Subsurface Water; **SSW** - Subequatorial Subsurface Water; **NPIW** - North Pacific Intermediate Water; **PDW** - Pacific Deep Water; **NGW** - Northern Gulf Water.

The climate of the modern Gulf creates an evaporative regime, under which the surface waters gain heat from the atmosphere, but simultaneously lose moisture. This results in an estuarine (thermohaline) circulation (Bray, 1988; Bray & Robles, 1991). Evaporation in the shallow northern Gulf causes hypersalinity and the formation of Northern Gulf Water (NGW; Bray & Robles, 1991; Lopez, 1997; de Diego & Douglas, 1999). This is advected southwards along with the other surface waters, which are a mixture of Equatorial Subsurface Water and Subequatorial Subsurface Water (ESW and SSW; Fig. 2.8; Bray & Robles, 1991; de Diego & Douglas, 1999). There is an outflow at ~250 m depth which is compensated by the deep inflow of PDW and NPIW (Bray & Robles, 1991).

The topography of the shallow northern Gulf results in strong tidal energy. Significant vertical mixing around the islands just north of Guaymas Basin brings nutrients into the surface layers (Fig. 2.8; Lluch-Cota, 2000; Delgadillo-Hinojosa *et al.*, 2001). These are advected southwards by wind stress and the thermohaline circulation (Gaxiola-Castro *et al.*, 1995).

## 2.8 Wind-driven coastal upwelling

Coastal upwelling is a major wind-driven oceanic process, highly sensitive to climatic change (Summerhayes *et al.*, 1995). The Trade Winds of both hemispheres blow parallel to the west coasts of the continents. Offshore, this enhances flow in the cold limbs of the Subtropical gyres. Inshore, Ekman transport, whereby friction is transmitted down the water column, causes the net movement of surface water to be at 90° to the direction of the wind. The movement is clockwise in the northern hemisphere, anticlockwise in the southern hemisphere, and surface water is advected offshore, allowing cold, nutrient-rich subsurface waters to upwell (cf equatorial upwelling, Fig. 1.3).

The upwelled nutrients are exploited by phytoplankton (principally siliceous diatoms) in quickly developing blooms that outstrip the grazing capacity of zooplankton. Consequently, sediments associated with upwelling areas sequester unusually large amounts of organic carbon and biogenic silica (Calvert, 1966; Thunell *et al.*, 1994; Summerhayes *et al.*, 1995; Pike & Kemp, 1997; 1999). The

intense productivity creates a high bacterial demand for oxygen in the water column. In a restricted setting, this results in an OMZ, which inhibits bioturbation and preserves seasonal sedimentation as annual varves that faithfully record climate change over a wide range of frequencies (Kemp, 1996). High rates of primary productivity are the key factor in making a restricted setting into an anoxic environment (Brumsack, 2006).

If productivity declines, anoxia will decrease and bioturbation will increase, however, if there is a decrease in the contrast between the seasons, bioturbation will not necessarily be the cause of homogeneous sediment. High productivity, a restricted setting and pre-formed low-oxygen bottom waters enhance *preservation*, they do not cause the deposition of varve sediment. *Seasonality* is the key factor in varved sedimentation. For bioclastic varves, this means that there has to be distinct upwelling and non-upwelling seasons. Compare, for instance, the case of clastic varve deposition in a proglacial lake (de Geer (1912), quoted in Anderson, 1996). Clastic varves reflect the different types of sediment carried by glacial outflow in the meltwater and the frozen seasons. If climate around the lake becomes colder (or warmer), the meltwater (or frozen) season will not occur and the sediment will be homogeneous. This is also true for bioclastic varves: if there is no seasonal contrast, there will be no varves. Van Geen *et al.* (2003) discuss this point, despite finding very low bottom water oxygen concentrations (~5 $\mu$mo/kg) on the southern Pacific coast of Baja California millimetre-scale laminations are not found in core tops and they conclude that lack of seasonality is the cause.

The process of coastal upwelling takes place at the shelf edge (Summerhayes *et al.*, 1995; Smith, 1995). Dependent on wind strength, the depth of the overturning cell is ~100-200 m (Smith, 1995) and Ekman transport continues below this depth. The net movement of this deeper water is at 180° to the direction of the wind (the poleward undercurrent; Figure 2.9; see also Fig. 1.3, equatorial upwelling). Locally, the strength of the undercurrent is proportional to the vigour of the upwelling cell (Smith, 1995). Open-ocean upwelling occurs year-round in the cold limbs of the Subtropical gyres, such as the California and

Humboldt Currents, generating a poleward undercurrent, which is seasonally enhanced and pushed inshore by the migration of the Subtropical High.

A schematic representation of nutrient recycling and deposition during west-coast upwelling in the northern hemisphere is presented in Figure 2.9. In spring, when the upwelling cell and the local undercurrent are moving in the same direction, the rain of organic matter from the bloom is recycled not only in the upwelling cell, but also by entrainment in the poleward undercurrent. The process of deposition begins when the ongoing poleward migration of the Subtropical High removes the influence of its alongshore winds and the undercurrent ceases to flow (Fig. 2.9 A). Pike & Kemp (1996) find near-monospecific layers of *Chaetoceros* spp. in early Holocene laminae from Core JPC-56, which, in conjunction with evidence from sediment traps (eg Thunell, 1998), they associate with sedimentation after the spring bloom.

In autumn, when the upwelling cell is weaker and moves equatorwards with the migration of the Subtropical High, the undercurrent does not enhance surface water nutrients (Fig. 2.9B). The result in Guaymas Basin is an overturn of the summer stratified water column rather than a strong upwelling bloom (Pike & Kemp, 1996). Using the early Holocene section of core JPC-56, Kemp *et al.*, (2000) show that this overturn, which they call the 'Fall Dump', results in the sedimentation of the frustules of slow-growing summer diatom species, typically *Rhizosolenia* spp., *Stephanopyxis palmeriana* and *Coscinodiscus* spp..

The Davidson Countercurrent along the North American western seaboard is subsurface during summer when the North Pacific Subtropical High is driving coastal upwelling (Reid *et al.*, 1958; Hendy *et al.*, 2002; McShane *et al.*, 2004; Robert, 2004). In winter, the countercurrent flows on the surface along the southern Californian Margin (that is, surface currents are driven by the southwesterly winds of the southern edge of the Aleutian Subpolar Low; Fig. 1.4). At ~40°N, where the winter Aleutian Subpolar Low winds are shore-parallel, the Davidson Countercurrent downwells (Reid *et al.*, 1958; McShane *et al.*, 2004), and takes oxygen-rich surface waters down to intermediate depths.

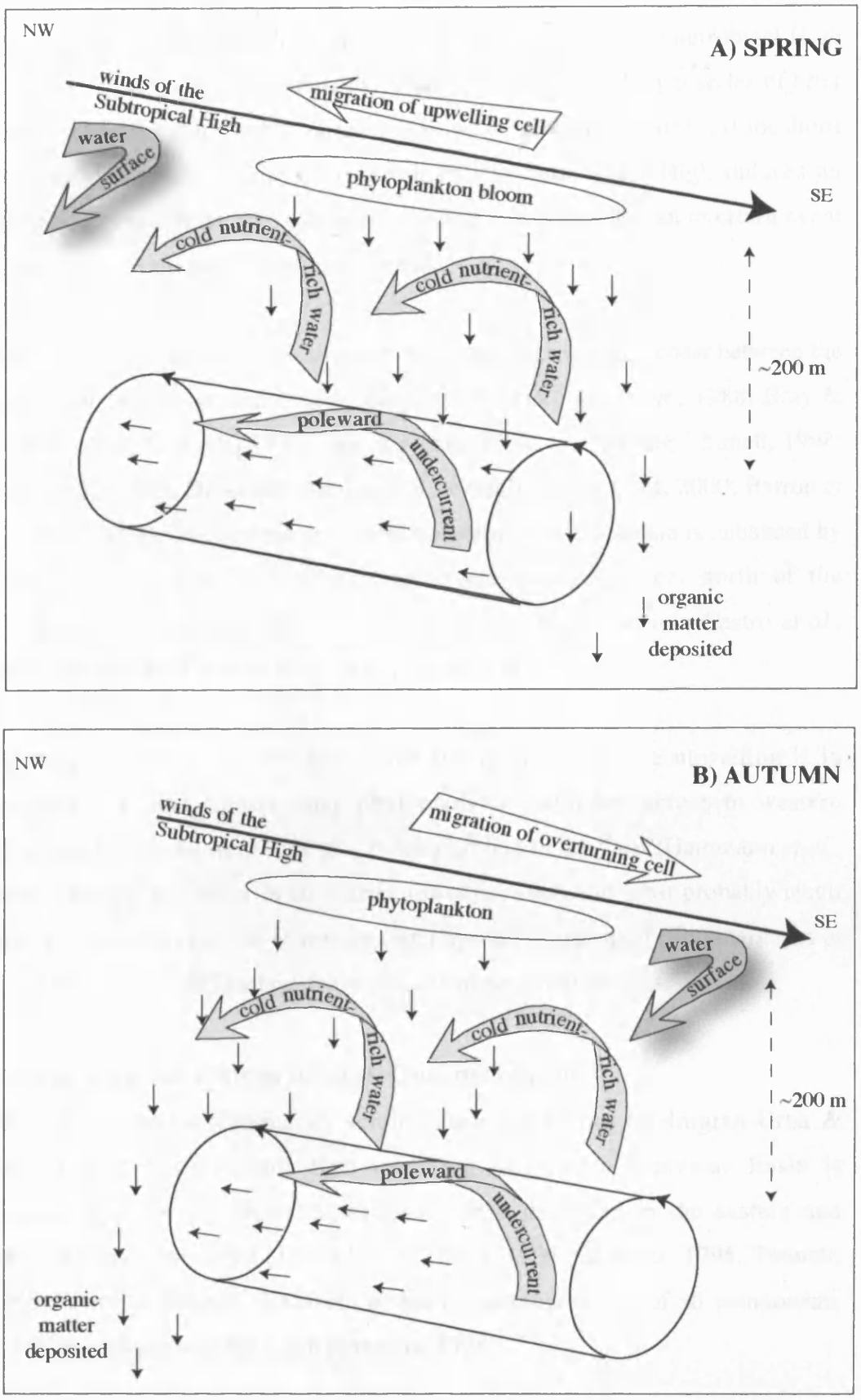


**Figure 2.9**: Nutrient recycling during modern coastal upwelling in the northern hemisphere.

At either end of its migration, the winds of the North Pacific Subtropical High induce a single coastal upwelling event per year, or, most likely a series of brief events reflecting fluctuating energy levels in the Subtropical High. At locations between these two extremes, the North Pacific Subtropical High induces an upwelling event on its poleward passage when it is strong and an overturn event on its equatorward passage when it is weak.

In the Gulf of California, upwelling occurs along the mainland coast between the months of November and March (Bray, 1988; Hammann *et al.*, 1988; Bray & Robles, 1991; Sancetta, 1995; Pike & Kemp, 1996; 1997; 1999; Thunell, 1998; Pride *et al.*, 1999; Delgadillo-Hinojosa *et al.*, 2001; Lluch-Cota, 2000; Barron *et al.*, 2004; 2005). The upwelling bloom in eastern Guaymas Basin is enhanced by nutrients brought in by tidal mixing in the shallow waters north of the Salsipuedes Sill and primary productivity is very high (Gaxiola-Castro *et al.*, 1995; Delgadillo-Hinojosa *et al.*, 2001; Lluch-Cota, 2000).

Figure 2.10 shows the vast basin-wide spring bloom. While upwelling is in progress, jets and squirts carry phytoplankton ~100 km across to western Guaymas Basin, the richest sardine fishing ground in the Gulf (Hammann *et al.*, 1988). Similar jets occur in all coastal upwelling areas and most probably result from the ongoing removal of surface water by Ekman transport (Summerhayes *et al.*, 1995; Smith, 1995) where the winds encounter promontories.

## 2.9 The seasonal cycle in modern Guaymas Basin

The warmer SSTs required by sardine during breeding (Holmgren-Urba & Baumgartner, 1993) imply that upwelling in western Guaymas Basin is comparatively weak. However, sediment traps deployed in the eastern and western Gulf since 1990 (Thunell *et al.*, 1993; 1994; Sancetta, 1995; Thunell, 1998; Ziveri & Thunell, 2000) show that comparable fluxes of all components occur on both sides of the basin (Sancetta, 1995).

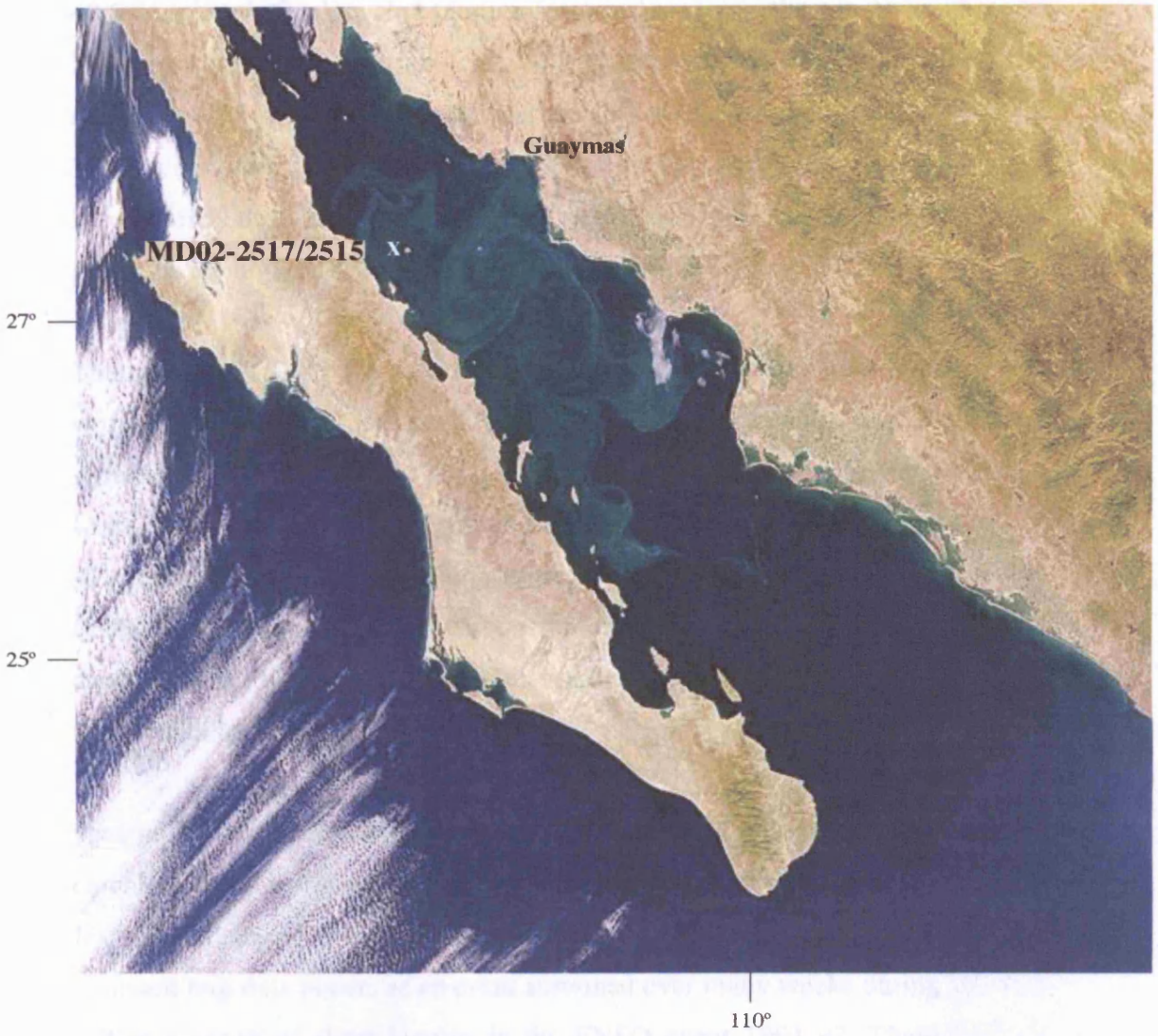


**Figure 2.10:** A phytoplankton bloom in the central Gulf, February, 1999.

Photo credit: SeaWIFS Project, NASA/Goddard Space Flight Center, and ORBIMAGE
http://visibleearth.nasa.gov/

Figure 2.11 shows the dataset from 1990-1996 (Thunell, 1998; 1991-92 was an ENSO event with anomalously high terrigenous flux), together with a composite 'year'. Total flux is usually highest during November and December averaging ~0.5 $g/cm^3/cm^2$. Opaline flux (diatom frustules) is also highest in November and December, averaging ~3 $g/cm^3/cm^2$, closely followed by January and February, averaging ~2.3 $g/cm^3/cm^2$. Organic carbon flux is highest in February, averaging ~0.05 $g/cm^3/cm^2$. Lithogenic flux is highest in July and September. Carbonate flux is steady throughout the year with a slight peak in September when SSTs are generally the highest of the year (Thunell, 1998).

Thunell *et al.* (1993) report occasional midwinter fluxes of mud that coincide with brief periods of low productivity. Thunell (1998) links organic carbon sedimentation to lithogenic flux. Fine particles of organic matter remain in suspension until flocculation occurs through incorporation into fecal pellets or adherence to clay particles, which aggregate by electrostatic attraction. Thunell (1998) finds that the organic carbon produced during spring upwelling is not deposited until the rainy season. This implies that unusually dry years result in varves with low organic carbon.

Seasonal diatom assemblage is investigated by Sancetta (1995), using a combination of sediment trap data (July, 1990-August, 1992) and data from core JPC-56 covering the last 15,000 years. The maximum flux of diatoms in the sediment trap data occurs as an event sustained over many weeks during 1990-91 and as a series of short blooms in the ENSO event 1991-92. There are two distinct phases of diatom deposition: a mixed flora event in November and a near-monospecific event in February-March. The ecological groupings from the sediment trap data are used to put the palaeo-assemblage from core JPC-56 into a seasonal context (Sancetta, 1995).

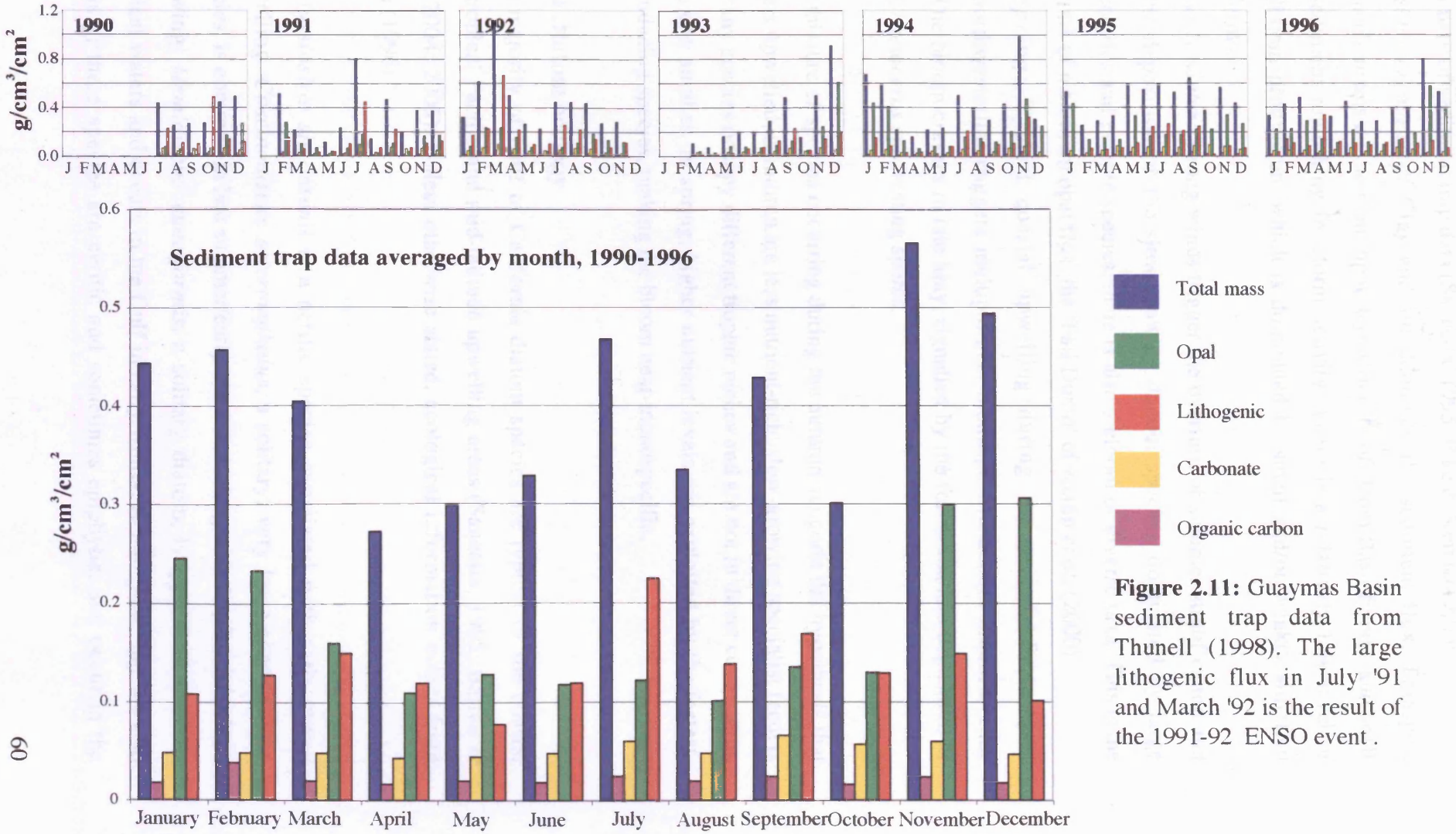


**Figure 2.11:** Guaymas Basin sediment trap data from Thunell (1998). The large lithogenic flux in July '91 and March '92 is the result of the 1991-92 ENSO event .

Summary of sediment trap data (Sancetta, 1995; Pike & Kemp, 1997):

*Summer/autumn:* Clay and silt dominate the sediment flux. Transport mechanisms are aeolian input, terrestrial runoff from flash floods, and shelf sediment reworking by storm activity. There is a relatively low level of diatom production, which is dominated by small and/or weakly silicified forms.

*Early winter:* Strong winds trigger the overturn of summer stratification and the deposition of the slow-growing diatom species, dominated by large centrics and pelagic species, there is also a bloom of diverse taxa. This is the time of maximum opal flux: the 'Fall Dump' of Kemp *et al.* (2000).

*Spring:* Typical coastal upwelling during the period of strongest northwesterlies triggers multiple near-monospecific diatom bloom events. The bloom crashes in late May, signalled by the formation and deposition of *Chaetoceros* spp. resting spores.

The mixture of species occurring during the autumn supports the hypothesis that waters upwelled in autumn are less nutrient-rich: slow-growing specialist feeders of many species occupy different trophic niches and are not in direct competition with one another. In spring, higher nutrient levels are exploited by the fastest-reproducing species, making the bloom near-monospecific.

## 2.10 Diatom ecology

The majority of Gulf of California diatom species are typical of the coastal subtropical Pacific and mid-latitude upwelling areas (Sancetta, 1995; Barron *et al.*, 2004; 2005). Unless otherwise stated, ecological information comes from Pike (1996).

*Thalassiosira simonsenii* is a neritic species associated with early spring upwelling. *Coscinodiscus asteromphalus*, a solitary, very large cosmopolitan species, is common in late summer/early autumn; its largeness implies it is slow-growing. *Hemidiscus cuneiformis*, a solitary diatom, is typical of warm or tropical waters and occurs in the Gulf in early winter. *Actinocyclus* spp. are also solitary; these species are neritic and sometimes epiphytic, and occur in the

autumn bloom. Neither of these are upwelling species, but most probably exploit the nutrients brought up to the surface during autumn overturn. *Roperia tesselata* is a non-colonial species that occurs during the spring bloom (Barron *et al.*, 2004). *Chaetoceros* spp. and *Bacterastrium* spp. are very widespread typical coastal upwelling species; *Chaetoceros* spp., a neritic species, occurs in spring, *Bacterastrium* spp., an oceanic species, occurs in autumn (Sancetta (1995). *Actinoptychus senarius* is a solitary neritic/epiphytic species, common during the upwelling season in the Gulf; its heavy silicification is typical of diatoms living in turbulent waters; it is most probably re-suspended from the eastern shelf and carried across the Gulf during upwelling (Sancetta, 1995).

*Stephanopyxis palmeriana* is a heavily silicified (and hence preferentially preserved), warm water, colonial, non-upwelling species; it occurs in sediment traps in summer; (Sancetta, 1995). *Rhizosolenia* spp., also non-upwelling and colonial, are very widespread, and occur as large tangled mats in late summer; this species is typical of summer stratification (Sancetta, 1995; Kemp *et al.*, 2000). *Thalassionema nitzschioides* is a cosmopolitan warm water species. It is very abundant in the Gulf throughout the year, constituting 30% of the flora in sediment traps and is therefore not associated with upwelling; together, *T. nitzschioides* and *Chaetoceros* resting spores form ~70% of the living assemblage (Sancetta, 1995). *Fragilariopsis doliolus* is a very common oceanic warm water species; in sediment traps, it is associated with the low-productivity stratified water column of summer, with maximum productivity occurring during the autumn overturn. The cosmopolitan oceanic species *Thalassiothrix longissima* forms <2% of sediment trap samples; living colonies are restricted to the southernmost Gulf and dead diatom mats are probably carried into Guaymas Basin during storms.*Azpeitia nodulifera* is a tropical oceanic species (Sancetta, 1995; Barron *et al.*, 2004; 2005; Jiang *et al.* 2004) which in sediment trap data is associated with ENSO conditions, but is common ~15-9 kyr BP in core JPC-56 (Sancetta, 1995; Barron *et al.*, 2005). Jiang *et al.* (2004) make the point that the robustness of *Azpeitia* spp. may contribute to preferential preservation. It is more common in modern sediments than it is in living plankton communities and its ecological preferences are unclear.

## 2.11 Guaymas Basin varves

The ultra-high resolution BSEI study of mid-Holocene laminated sediments from core JPC-56 (Pike, 1996; Pike & Kemp, 1996; 1997; 1999) reveals that the varves consist of a lamina sequence comparable to the three-part modern seasonal sequence identified in sediment trap and diatom assemblage studies (Thunell *et al.*, 1993; Thunell, 1994; 1998; Sancetta, 1995). The BSEI study confirms the exceptional sensitivity of the Guaymas Basin depositional system to climatic events at all timescales.

Pike (1996) divides the varves into two categories: those consisting of two laminae and those consisting of three. The two-component varves have a lithogenic lamina and either a mixed-flora diatomaceous lamina or a near-monospecific diatomaceous lamina. The most numerous of the latter type is composed of *Chaetoceros* spp. frustules and resting spores. The three-component varves have all three lamina types and, additionally, may have sub-laminae of silt within either of the diatomaceous laminae, or diatom-rich sub-laminae within the lithogenic lamina. The former correspond to high fluxes of mud in sediment traps during winter (Thunell *et al.*, 1993; Pike & Kemp, 1996). Additionally, thin near-monospecific laminae (*Coscinodiscus* spp. or *Rhizosolenia* spp. or *Stephanopyxis palmeriana*) may occur between the lithogenic lamina and the mixed-flora lamina.

By comparing the BSEI and sediment trap data (Thunell *et al.*, 1993; Sancetta, 1995), Pike & Kemp (1996; 1997) link the lamina types to the modern seasonal succession. The lithogenic laminae are the result of sedimentation in the wet season; the mixed-flora laminae are linked to deposition during the overturn of wet-season stratification; and the near-monospecific *Chaetoceros* spp. laminae occur at the end of dry-season upwelling. The two-component varve, according to Pike & Kemp (1996), is a 'damped' version of the three-component varve. The missing element is attributed to either unusually low winter productivity combined with over-grazing by zooplankton or an anomalously dry rainy season. The thin near-monospecific laminae between the lithogenic lamina and the

mixed-flora lamina are linked to blooms exploiting increased nutrient-availability during autumn overturn.

On average, the lithogenic laminae are composed of ~60-85% clays and silts with ~15-40% diatom frustules and are ~0.63 mm thick. On average, the mixed-flora laminae are composed of ~75-85% diatom frustules and ~15-25% clays. The near-monospecific laminae are almost totally composed of diatom frustules with a minor clay component. On average, the diatomaceous component of the varves has a thickness of ~1.03 mm (Pike, 1996).

Figure 2.12 is a schematic diagram constructed from the description of the principal varve types discussed by Pike & Kemp (1996). Type A, the three-component varve, is consistent with an annual climate cycle driven by the modern migration pattern of the North Pacific Subtropical High. The occasional occurrence of a silt sub-lamina within the dry-season diatomaceous lamina (Thunell *et al.*, 1993; Pike & Kemp, 1996) indicates that the Subtropical High can be located south of ~23°N at midwinter, which allows the incursion of the Aleutian Subpolar Low rain fronts. The occurrence of a diatomaceous sub-lamina within the lithogenic lamina indicates that the North Pacific Subtropical High can retreat from its summer location (somewhere further north along the Californian margin) and trigger a brief upwelling event in Guaymas Basin. Both of these events imply that either the Subtropical High is weaker, or the Subpolar Low is stronger, than normal.

Figure 2.5 (see also discussion in Section 2.5) shows that the Aleutian Subpolar Low and the Subpolar gyre were expanded during the glacial and dominated climate far to the south of the present limit of their range of influence (~27°N). The result of this would be an equatorward shift of the wet/dry Subtropical divide, which would alter the annual cycle at Guaymas Basin. A moderate shift would give it seasons similar to those occurring north of ~27°N along the modern Californian margin (wet winters/dry summers). In the extremes of glacial

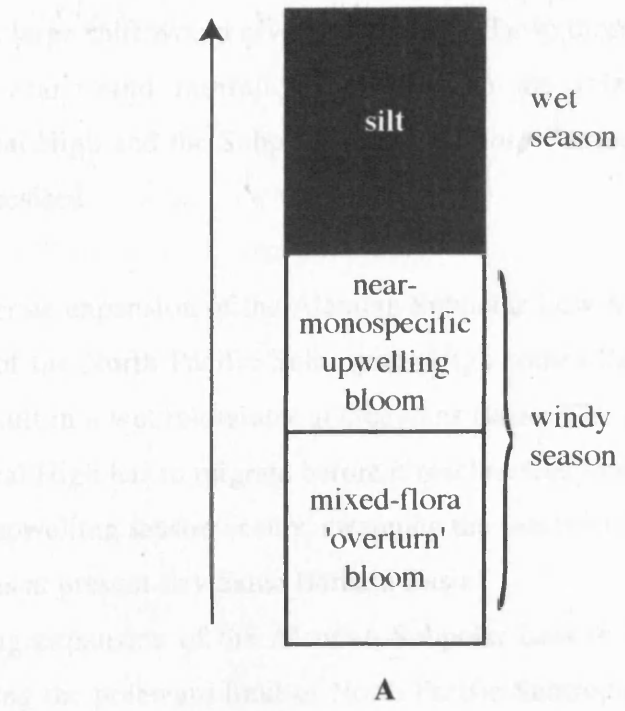


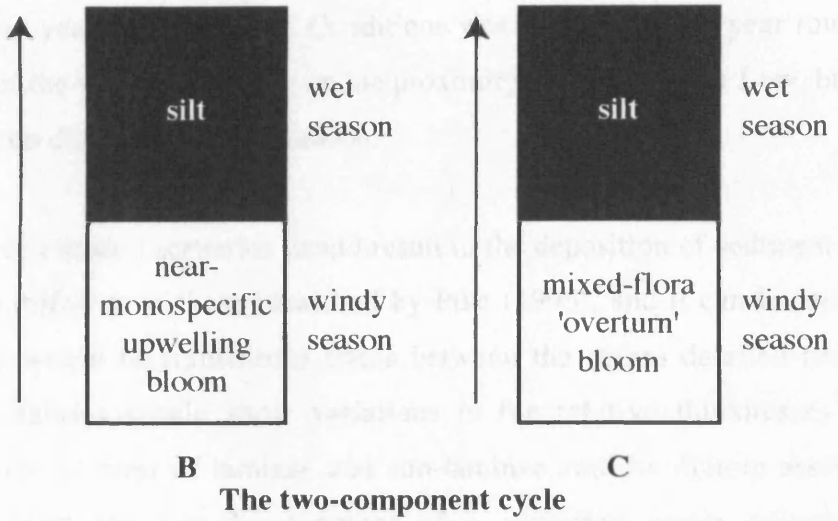


**Figure 2.12:** Schematic diagram of the principal varve types revealed by the BSEI sediment fabric study of core JPC-56 (Pike & Kemp, 1996; 1997; 1999).

Type A is consistent with an annual climate cycle driven by the observed migration of the North Pacific Subtropical High: autumn overturn followed by spring upwelling and summer stratification .

climate, a large shift would give it seasons similar to those north of ~48°N where there is year-round rainfall. Dependent on the relative strengths of the Subtropical High and the Subpolar Low, a series of seasonal configurations can be hypothesised:

1 A moderate expansion of the Aleutian Subpolar Low would force a midwinter location of the North Pacific Subtropical High somewhat south of ~23°N. This would result in a wet midwinter at Guaymas Basin. The greater the distance the Subtropical High has to migrate before it reaches Guaymas Basin, the later in the year the upwelling season occurs, swapping the seasons to a wet winter and a dry summer as at present-day Santa Barbara Basin.

2 A strong expansion of the Aleutian Subpolar Low would result in Guaymas Basin being the poleward limit of North Pacific Subtropical High migration and semi-continuous upwelling during summer. Windy conditions in summer would make SSTs cooler and preclude the formation of a stratified water column.

3 A very energetic, greatly expanded Aleutian Subpolar Low would prevent a weak North Pacific Subtropical High from migrating as far as Guaymas Basin, resulting in year-round rainfall. Conditions would be windy all year round, the strength of the winds depending on the proximity of the Subpolar Low, but there would be no distinct upwelling season.

These three climatic scenarios would result in the deposition of sediment fabrics distinctly different to those identified by Pike (1996), and it can be envisaged that there would be transitional states between the stages detailed here. The sediment fabrics would show variations in the relative thicknesses of the laminae, the number of laminae and sub-laminae and the diatom assemblage would reflect the non-development of a stratified water column. The geochemical composition of the sediment would vary according to variations in biogenic and terrigenous flux, and authigenic flux would vary in response to the varying influence of the Subtropical High and the Subpolar Low on ventilation of intermediate waters and the depth of the coastal thermocline/nutricline.

# Chapter 3 Methods

## 3.1. Introduction

After the acquisition of a physical record, decoding its climate record requires the employment of climate proxies specific to the phenomena encountered in the area of study. Ideal climate proxies are those that can be firmly linked to an established relationship between a primary process and the formation of a structure or the flux of a component to the sediment. A proxy should have a predominant controlling factor, preferably identified by modern observations, and be sensitive to alterations in the primary process (Sageman & Lyons, 2003).

The phenomena specific to modern Guaymas Basin are related to the two contrasting seasons. The strong winds and high biological production that characterise the upwelling season are due to the close proximity of the North Pacific Subtropical High during winter. When the progressing poleward migration removes the influence of the Subtropical High winds, the result is the stratification and storm-deposited aeolian dust influx that typify the summer season (Bray & Robles 1991; Baba *et al.*, 1991a). The products of this seasonal contrast are alternating laminations of distinct sediment types – diatom-rich in the upwelling season and silt-rich in the non-upwelling season (Pike & Kemp, 1997). The low oxygen-content of intermediate waters entering the Gulf, which is caused by upwelling along the eastern North Pacific margin induced by the proximity of the North Pacific Subtropical High on the path of its annual migration, is enhanced by locally high bacterial demand for oxygen due to high productivity within Guaymas Basin. The resultant dysaerobia at Site MD02-2517/2515 restricts the benthos, which preserves the laminations as annual varves (eg de Diego & Douglas, 1999).

Since the effects of climate are the result of the interactions of many variables, the multiproxy approach to sediment analysis gives a more balanced view than that of a single proxy. The modern and early Holocene sediment fabric, sedimentation rate and geochemistry of the varves vary because of subtle variations in seasonal vigour and duration (eg Holmgren-Urba & Baumgartner,

1993; Thunell, 1998; Pike & Kemp, 1996, 1997, 1999; Dean *et al.*, 2004). Late Glacial sediment fabric and composition reveal a climate regime dramatically different to that of the present (Keigwin & Jones, 1990; Sancetta, 1995; Keigwin, 2002; Barron *et al.*, 2004, 2005).

### 3.2. Coring operations and core handling

Core MD02-2515 (Table 1.1 and Fig. 1.1) is a *Calypso* continuous giant piston core. The *Calypso* corer was developed by Yvon Balut of the French Polar Institute (IFP) for use on the RV *Marion Dufresne*. It is an adaptation of the Kullenberg corer (Kullenberg, 1947) and is illustrated in Figure 3.1. The counterweight strikes the seafloor ahead of the nose, activating the trigger that releases the lead weight (in this case, 10 tonnes) and drives the corer into the sediment. Very long continuous cores can be retrieved by the *Calypso* method because the aramide cable, on which the corer is lowered and raised over the side of the ship, is virtually weightless in water. This significantly enhances traction security and the lifting capacity of the winch (Beaufort *et al.*, 2002). Core MD02-2515 is ~63 m long and presently holds the world record for a continuous marine core acquired by this method. The advantages of the *Calypso* coring system are that sediment recovery is very rapid compared to other methods (such as rotary coring or conventional advanced piston coring), and the whole length of sediment is retrieved simultaneously. Conventionally drilled and advanced piston cores are brought up in 9-m sections and parallel holes are drilled to compensate for the loss of sediment at the top and bottom of each section.

Core MD02-2515 is affected by expansion caused by high gas pressure in the organic-rich sediments. Pressure is released as soon as the core is moved from its original position and sediment moves upwards within the core liner, creating artificial gaps in the stratigraphy or even mixing up and homogenising the sediment. Excessive vibration during retrieval has led to some disintegration of the sediment fabric of core MD02-2515. This mainly occurs adjacent to joins in the length of the plastic core liner, which are 12 m apart. On board ship, numerous hand-drilled holes were punched into the core liner to release gas pressure, but, despite this, expansion continued and ~2 m of sediment was

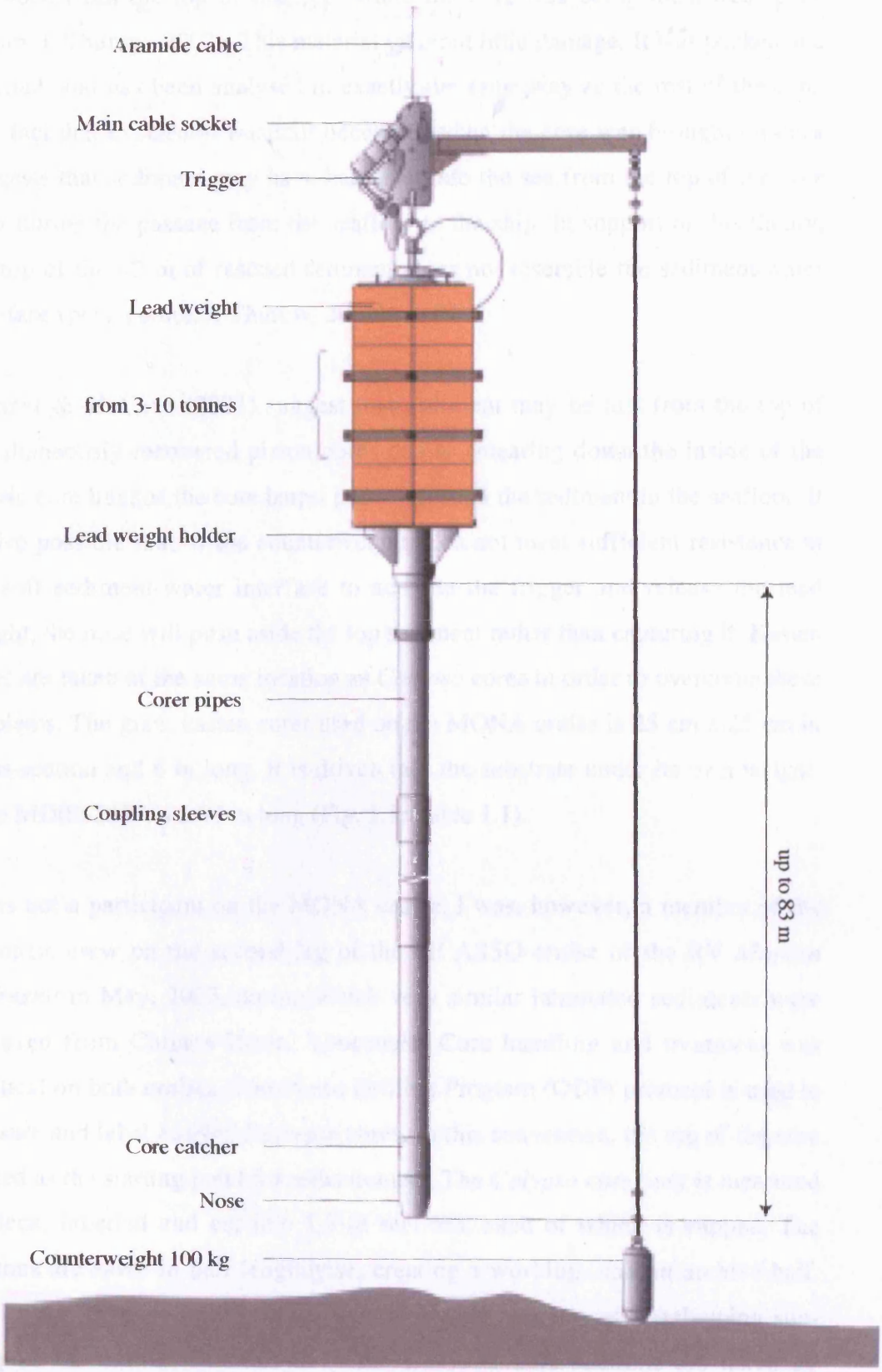


**Figure 3.1:** The *Calypso* giant piston corer. [Adapted from Beaufort *et al.*, 2002]

extruded from the top of the liner while the core was being measured (pers. comm. J. Thurow, 2002). This material suffered little damage. It was packed and labelled, and has been analysed in exactly the same way as the rest of the core. The fact that expansion was still occurring when the core was brought on deck suggests that sediment may have been lost into the sea from the top of the core liner during the passage from the seafloor to the ship. In support of this theory, the top of the ~2 m of rescued sediment does not resemble the sediment-water interface (pers. comm. J. Thurow, 2002).

Skinner & McCave (2003) suggest that sediment may be lost from the top of simultaneously-recovered piston cores due to smearing down the inside of the plastic core liner as the core barrel passes through the sediment in the seafloor. It is also possible that, if the counterweight does not meet sufficient resistance at the soft sediment-water interface to activate the trigger and release the lead weight, the nose will push aside the top sediment rather than capturing it. Kasten cores are taken at the same location as *Calypso* cores in order to overcome these problems. The giant kasten corer used on the MONA cruise is 25 cm x 25 cm in cross-section and 6 m long. It is driven into the substrate under its own weight. Core MD02-2517 is 5.97 m long (Fig. 1.1, Table 1.1).

I was not a participant on the MONA cruise, I was, however, a member of the scientific crew on the second leg of the PICASSO cruise of the RV *Marion Dufresne* in May, 2003, during which very similar laminated sediments were retrieved from Cariaco Basin, Venezuela. Core handling and treatment was identical on both cruises. The Ocean Drilling Program (ODP) protocol is used to measure and label *Marion Dufresne* cores. In this convention, the top of the core is used as the starting point for measurement. The *Calypso* core liner is measured on deck, labelled and cut into 1.5-m sections, each of which is capped. The sections are sawn in half lengthwise, creating a working- and an archive-half. The kasten corer is opened along one side, and two sets of overlapping sub-samples of similar dimensions to the *Calypso* core sections are taken by hammering open core-liner sections into the sediment and cutting them out with a wire.

Each working-half core section is smoothed and the sediment composition, structures and fossils are described and logged. Each core section is photographed (Beaufort *et al.*, 2002). These images are useful for the later assessment of how much sediment may have been lost through shrinkage and mishandling (section 3.4.3).

## 3.3 Shipboard techniques

Non-invasive techniques are employed on board ship for the rapid assessment of the physical properties of the core while preserving its structural integrity (Beaufort *et al.*, 2002). These data are collected for use in constructing sampling strategies for subsequent studies of the cores.

### 3.3.1 Colour analysis

The diffuse spectral reflectance of each split core surface is measured at 2-cm resolution with a handheld Minolta 2022 spectrophotometer. The method provides a rapid, high-resolution estimate of sediment components such as carbonate, organic carbon and biogenic silica (Ortiz & Mix, 1997; Beaufort *et al.*, 2002).

After calibration against open space and a white standard, light from the internal xenon arc lamp is flashed onto the sediment surface, which is covered by thin plastic film to protect the sensor from contamination. The light reflected from the sediment is recorded at wavelengths within the visible range of the electromagnetic spectrum (400-700 nm). The spectrophotometer automatically calculates semi-quantitative L*, a* and b* values. L* is lightness (pure black = 0, pure white = 100); a* are red/green attributes (negative values = green, positive values = red); b* are yellow/blue attributes (positive values = blue, negative values = yellow). Reflectance data for cores MD02-2515 and MD02-2517 have been calibrated against the geochemical analyses of discrete samples (sections 3.5.2 & 3.5.4).

$CaCO_3$ and $SiO_2$ have almost identical L* values (Balsam *et al.* 1999). However, L* values can be affected by increasing ratios of lithogenic to biogenic components and authigenic to biogenic components. Fine-grained particles of dark organic carbon interspersed with skeletal material absorb light and 'dilute' the L* signal. Nederbragt *et al.* (2000) find that diatom rich-sediments from the California margin have a negative correlation with L* because of high TOC content. a* values can be used to estimate redox conditions (Mix *et al.*, 1995). Reddish-brown sediments contain oxides, while sulphide-rich sediments are greenish. For sediments with a high TOC content, a* has higher values and has a positive correlation with TOC (Nederbragt *et al.*, 2000). For b* values, clay-rich sediments tend to be bluish, while carbonate- or silica-rich sediments tend towards yellow (Nederbragt *et al.*, 2000). High organic content can obscure the reflectance values of these minerals (Mix *et al.*, 1995).

### 3.3.2 Magnetic susceptibility and sediment density

The split-core sections are logged at 2-cm resolution with the GEOTEK Ltd Multi Sensor Core Logger (MSCL) magnetic susceptibility sensor. Changes in the operation of mechanisms that bring ferromagnetic minerals into the ocean (fluvial and aeolian processes; section 2.6) alter the magnetic signal at a site (eg Oldfield, 1999; Ellwood *et al.*, 2000). A common ferromagnetic weathering product from igneous rocks is iron. Variations in iron content are a reflection of precipitation and runoff and can be detected by variations in magnetic susceptibility.

At the same time and at the same 2-cm resolution, the MSCL gamma-ray source/detector logs sediment wet bulk density and porosity (Beaufort *et al.*, 2002). Wet bulk density is used in calculating accumulation rates of the sediment components. Accumulation rates are less ambiguous indicators of change within a system than percentage concentration data (wt %; Gardner *et al.*, 1997; Peterson *et al.*, 2000a) because there are closed-sum problems inherent in percentage data. An increase (or decrease) in the volume of one component will force a change in the percentages of the other components even if their volumes have not changed (Sageman & Lyons, 2003).

Mass accumulation rate (MAR; g/cm$^2$/yr) is the product of dry bulk density (DBD; g/cm$^3$), linear sedimentation rate (LSR, section 3.3.6; cm/yr) and component abundance (wt %) (Gardner *et al.*, 1997; Calvert & Carlin, 1998; Peterson *et al.*, 2000a):

$$MAR = DBD \times LSR \times \text{wt \% component} \quad \text{[eq. 3.1]}$$

Gardner *et al.* (1997) calculate DBD as:

$$DBD = \text{Grain density} \times \frac{(WBD - \text{density seawater})}{(\text{grain density} - \text{seawater density})} \quad \text{[eq. 3.2]}$$

Where WBD is wet bulk density; the density of seawater is 1.025 g/cm$^3$; and grain density is calculated as:

$$\text{grain density} = \frac{\%CaCO_3 \times 2.7}{100} + \frac{\%TOC \times 1.0}{100} + \frac{\%\text{biogenic silica} \times 2.05}{100} + \left(1 - \frac{(\%CaCO_3 + \%\,TOC + \%\text{biogenic silica})}{100}\right) \times 2.65 \quad \text{[eq. 3.3]}$$

Where 2.7, 1.0, 2.05 and 2.65 are the respective densities of the components.

## 3.4 Sediment fabric analysis

### 3.4.1 Sediment description

Basic sediment description was determined through analysis by light microscopy of smear slides taken at 50 cm-intervals along the length of the core. Fossil assemblage was analysed with a view to ascertaining the presence or absence of ecologically significant diatom species rather than producing a statistically significant relative abundance count. For each slide, ten fields of view were examined at magnification 100. Standard textbooks were used to identify the microfossils. Estimates were made of the percentage relationship between the most commonly occurring diatoms and ecologically significant diatoms. The

time constraints of this study precluded the undertaking of statistically significant counts of individual diatoms (400-500 per sample). Consequently, this survey represents a first approximation of fossil assemblage and relative abundance.

### 3.4.2 Digital images of the cores

The core sections were carefully cleaned, by scraping parallel to the varves, and digitally photographed. The linescan camera attached to the MSCL at the Core Repository, University of Bremen, Germany, was used in the initial attempt to obtain digital images of the split core sections. The camera is mounted above the track, the core sections are propelled underneath the lens by a stepper motor and a single image is taken. Unfortunately, the motor produces vibration and the images obtained were not suitable for the accurate determination of objects less than ~2 mm in diameter. A second set of images was taken at the University of Southampton, again using an overhead fixed camera, but the cores were positioned by hand and overlapping images 20 cm in length were taken. A measuring tape was included in each image for accurate determination of depth within the core. Further details of the method are described by Nederbragt *et al.* (2000).

The photographs were manipulated using ImageJ software. ImageJ and its Java source code are freely available and in the public domain (http://rsb.info.nih.gov/ij/). The programme can measure area, mean, standard deviation and the maximum and minimum of a selection or the entire image. Angles and lengths can also be measured. Repetitive tasks can be automated using macros.

The images were magnified and the colour levels were adjusted in order to get the clearest possible view of the sediment fabric. The colour of the laminae alternates between light olive-green and dark olive-green. To the unaided eye, these colours appear quite similar, especially where the sediment is darkened by high water-content, and adjustment of the colour levels makes it easier to discern the difference between the two. Additionally, the scraping process temporarily compresses the diatom-rich laminae in the youngest water-filled sediment. These

rebound and cast shadows that can be confused for laminae. Manipulation of the colour levels helps to overcome this problem. The enhanced images were used to log the sediment at 1-cm resolution for, 1) sediment fabric type, and 2) varve thickness. Sedimentary logs were constructed.

### 3.4.3 Void-corrected depth-scale

Before the sediment fabric analyses were carried out, the artificial stratigraphic gaps in core MD02-2515, created by gas expansion during coring operations, were 'closed up' and a void-corrected depth-scale was established. This was done using the digital images and the software ImageJ. The number of pixels which represent a centimetre of sediment is 130 which easily allows the measurement of features which are ~1 mm thick (13 pixels). ImageJ measures and records the number of pixels within a selected area.

Because of uncertainties about continuity (the cores were not taken at exactly the same location; see Table 1.1), cores MD02-2517 and MD02-2515 were treated separately until the age model had been established, after which a composite depth-scale was constructed ('MD02-2517/2515'). By comparing the digital images with the shipboard photographs, which were taken soon after the cores had been split, it is obvious where sediment has been lost at the top and bottom of core liner sections during subsequent handling. Some of the gaps in core MD02-2515 were packed with polystyrene foam on board ship to prevent more sediment loss or to protect the sediment fabric from further damage during transport. The foam draws water out of the sediment and causes some minor compaction, so small adjustments were made for this.

There are no artificial gas-pressure gaps in core MD02-2517. For MD02-2515, the top of the first section of extruded sediment forms the beginning of the void-corrected depth-scale for that core. The *Marion Dufresne* (MD) depth-scale begins at the base of the second extruded section and the top of MD Section I. The two scales run in parallel to the top of the first artificial gap. The gap is measured on the computer screen using the ImageJ software. The measurement is subtracted from the MD depth-scale and then the top of the sediment below the

gap is assigned to the appropriate depth on the void-corrected scale. For convenience, both scales are used during data-handling.

### 3.4.4 Sediment fabric index

Varve structure and composition have previously been used to assess seasonal climatic variations (eg Bull & Kemp, 1995; Pike & Kemp; 1996; 1997; 1999). Both in the wider region and in Guaymas Basin, this has proved to be a highly effective strategy. The variations in Guaymas Basin varve types from core JPC-56 (section 2.11; Pike & Kemp, 1996; 1997; 1999) show the sensitivity of the depositional system through a ~300-year period of the mid-Holocene, which is a good indication that a longer core will give comparable results and extend the palaeorecord. From the wider region, the 1-cm scale bioturbation index curve of Behl & Kennett (1996; section 1.1.6) shows that the occurrence of varved intervals at ODP Site 893 has a strong resemblance to the global climate change record of the GISP2 ice core. In Guaymas Basin, since both the laminated (varved) and non-laminated sediment types are intimately linked with seasonality and climate, it is proposed that a high-resolution index of sediment fabric types, comprising both laminated and non-laminated sediment, will best express the variations which result from alterations in the operation of the overarching mechanism that controls deposition at Site MD02-2517/2515.

The technique used by Pike & Kemp (eg 1996) was to cut overlapping sub-samples, which were set by fluid-displacement and resin-embedding, then cut into thin sections and polished. This is ideal for ultra-high resolution BSEI imagery, but it is costly, time consuming and, given the additional time needed to analyse the images, limited to short sediment sequences. The opportunity to obtain a long, continuous climate record, afforded by core MD02-2517/2515, dictates that a less destructive, less time-consuming method is used even though some complexity and fine details will be lost.

Using the digital images, eight sediment fabric types have been identified, ranging from fully laminated (ie varves with variations in relative lamina thickness and internal continuity), through to homogeneous sediment. Every

centimetre of core MD02-2517/2515 was assessed and assigned to one of the eight categories. This is straightforward where a centimetre contains a single sediment fabric type. Where there is a mixture of sediment fabric types within one centimetre, the dominant type has been chosen. The sediment fabric types have been assigned numbers (1-8); the reasoning behind the order in which the categories appear in the index is discussed in Chapter 6.

This type of analysis, which relies on the judgement of the investigator, always contains an element of subjectivity (Lotte & Lemcke, 1999). Partly because of this and partly because the data come from observations averaged across 1 cm, the results are semi-quantitative. To ensure a reasonable degree of consistency, the survey was repeated three times. The first and second surveys showed the greatest differences; the second and third were almost identical. Experience is the critical factor in obtaining consistent results, but there still remain some centimetre-sections in core MD02-2517/2515 where it was difficult to decide which was the most numerous sediment fabric type: either the numbers were evenly balanced or the sediment fabric was transitional between two types. Logging at such high-resolution over this length of sediment makes it almost impossible to deliberately skew the results in any particular direction.

### 3.4.5 Annual sedimentation rate

Annual sedimentation rate is a variable linked to climate change, reflecting changes in primary productivity and terrigenous flux. Falling sea level increases sedimentation rate; higher precipitation rates increase terrestrial runoff (section 2.6); increased productivity results from a longer or a more vigorous upwelling season (section 2.11).

Deciding where the varve boundaries are in order to measure thicknesses is not always straightforward. In the simplest cases, a varve is a dark and a light lamina-couplet (eg Lotte & Lemcke, 1999), but can also include sub-laminae of either colour (Pike & Kemp, 1996; 1997) or multiple laminae (Anderson, 1993; Dean *et al.*, 1999; Lotte & Lemcke, 1999). Judgements about varve boundaries become more straightforward as the analysis progresses and experience of the

possible variations within the sediment fabric is acquired (Anderson, 1993; Lotte & Lemcke, 1999). For obvious reasons, the assessment of varve type is done before the measurement of varve thickness.

Varve thicknesses were measured using the digital images of the sediment in the software package ImageJ. Every centimetre of core MD02-2517/2515 was assessed. The varve boundaries were judged by eye. An average thickness for the varves occurring in each centimetre was established from the measurement of three varves. In some instances, this was not possible and two varves were used. Laminations affected by microbioturbation have degraded boundaries. There are many instances where the sediment is obviously laminated and probably varved, but the degree of microbioturbation has made accurate measurement impossible.

The use of averages is reliable where sedimentation rate is steady and the standard deviation from the mean is small. Where there is a wide range of thicknesses, the standard deviation is large and the average for that centimetre is less reliable. Abrupt and brief fluctuations in sedimentation rate most probably reflect events such as redeposition during storms or slumping as the result of tectonic activity. No obvious 'event-laminae' were used in measuring varve thicknesses, but some may have been included because they were not recognised. To ensure a reasonable degree of consistency, the survey was repeated three times.

Linear sedimentation rates, generated by measuring varve thicknesses and interpolation across non-laminated intervals (see section 3.6), are used in the calculation of accumulation rates (eg Gardner *et al.*, 1997; Peterson *et al.*, 2000a; section 3.3.2).

## 3.5 Sediment geochemistry

### 3.5.1 Continuous X-ray fluorescence scanning

The potential for obtaining a high-resolution time series over such a long length of sediment dictates the use of the most continuous, least destructive method for geochemical analysis. The CORTEX (Corescanner Texel) X-ray fluorescence

logger (Jansen *et al.*, 1998) was developed for, and has been successfully applied, in rapid, high-resolution determination of sediment geochemistry (eg Röhl & Abrams, 2000; Haug *et al.*, 2003).

The principle of X-ray fluoresence (XRF) is that X-ray bombardment excites secondary X-ray fluorescence with wavelengths characteristic of the elements present under the X-ray beam (Jansen *et al.*, 1998). Samples that produce the best results for conventional XRF analysis are dried, powdered, homogenised and compressed into smooth pellets. In the CORTEX system, analysis is carried out on samples that are less than ideal - smoothed split-core sections covered with cadmium-free film – but which have proved to give reliable results (Jansen *et al.*, 1998; Röhl & Abrams, 2000). The wet, organic-rich sediment of core MD02-2517/2515 presents problems of accuracy through less efficient excitation of elements due to scattering (Croudace *et al.*, 2006), though the effect is lessened partly because the sediment is fine-grained and partly because deeper in the core compaction has expelled the water. Scans of non-homogeneous sediment run the risk of measuring randomly dispersed concentrations of elements contained in macrofossils or thick laminae. Split cores dry out during storage, which presents the problem of calcite recrystallising on the surface. The effect of this is minimised by scraping the surface prior to the scan

However, the CORTEX system is non-invasive, quick and cheap and, as such, is the method of choice for assessing the geochemistry of long laminated cores such as MD02-2517/2515. It measures elemental K, Ca, Ti, Mn, Fe, Cu, and Sr intensities in counts per second (cps) of concentrations from 100% down to parts per mille (ppm). Concentrations below this are detectable, but very low cps (50 or less) are unreliable and such results should be discarded (pers. comm., U. Röhl, 2002). In order to be continuous, the CORTEX system integrates the results obtained under the incident beam, the size of which depends on the step size chosen for the study. Because of the integration and the less than ideal state of the samples, the resultant data are semi-quantitative.

The analysis of core MD02-2517/2515 (at 1-cm resolution) was carried out at the Bremen Core Repository, University of Bremen, Germany. At the time (Dec. 2002 & Feb. 2003), calibration of their newer XRF machine, capable of measuring Al, Si and heavier elements, was still in progress. This is a drawback for Guaymas Basin sediment, where siliceous diatom frustules are a major component (eg Barron *et al.*, 2004; 2005).

A European Union Paleostudies grant (HPRI-CT-2001-0124) was obtained for the continuous XRF analysis of another *Calypso* core (core MD02-2512) from eastern Guaymas Basin (Fig. 1.1; Table 1.1; Cheshire *et al.*, 2005; Appendix I). This work was done at the University of Bremen in November 2003. It was hoped that a transect across Guaymas Basin could be produced, however, subsequent analysis of core MD02-2512 revealed that its stratigraphy is artificially expanded by repetitions caused by numerous small slope failures and the results have not been included in this study.

The method and calibration procedures for the CORTEX XRF system are discussed in Jansen *et al.* (1998). After measurement of a core section is complete, the KEVEX™ software processes the acquired spectra (Röhl & Abrams, 2000). The intensity values can be converted to elemental abundance values using formulas based on the calibration of standards, measured at the time of analysis, and replicate sediment analyses (Jansen *et al.*, 1998; Peterson *et al.*, 2000a). Since actual cps values depend not only on the element being measured, but also on the porosity and texture of the sediment (Jansen *et al.*, 1998), the calibration has to be done independently for each core site. The conventional XRF analysis of discrete samples from core MD02-2517/2515 (section 3.5.2) provides the calibration set for this study. The conventional XRF data was plotted against continuous XRF data (taken at the same sample depths), and a best-fit straight line was fitted through the data by the least squares method (linear regression), yielding the equation:

$$y = mx + c \qquad \text{[eq.3.4]}$$

where m is the slope of the line and c is the point where the line intersects the y-axis.

Röhl & Abrams (2000) take Ca intensities to be representative of $CaCO_3$ flux from calcareous organisms and hence as a biogenic proxy. In Guaymas Basin calcareous phytoplankton are at present minor primary producers compared to siliceous diatoms (Ziveri & Thunell, 2000). Ca in the sediment, however, can be traced to dissolved skeletal material from coccolithophores and foraminifera (Dean *et al.*, 2004). Calcareous planktonic foraminifera are active grazers of the phytoplankton (Pike & Kemp, 1996; 1997; 1999), but the low-oxygen bottom waters militate against large numbers of benthic foraminifera. Ca is also brought into the basin as a minor component of terrigenous flux. Of the non-biological element intensities, Fe is redox sensitive, while Ti is not (Peterson *et al.*, 2000a; Yarincik *et al.*, 2000). Within the suite of elements measured by the continuous scan Ti is, therefore, representative of terrigenous flux.

### 3.5.2 Conventional X-ray fluorescence analysis

In order to obtain a more comprehensive picture of the geochemistry of the sediment and to provide a calibration set for the continuous semi-quantitative XRF data, discrete samples for conventional XRF analysis were taken at ~50 cm-intervals along the full length of core MD02-2515. Invasive techniques are labour-intensive and costly, and for these reasons tend to be of lower resolution than non-invasive techniques.

The samples were dried overnight in an oven at 100° C and powdered ready to be made into pellets. Non-metallic utensils were used to avoid contamination before analysis. The basic preparation was done by me at the Wolfson Laboratory, University College London; the pelletisation and XRF analysis were carried out at the University of Oldenburg (Professor H.-J. Brumsack).

In principle, the method is the same as that for continuous XRF scanning. The sample (~3 g) is made into a pressed powder pellet and irradiated with X-rays, which stimulate secondary X-ray fluorescence. The separation of individual wavelengths is done by Bragg diffraction from crystals of particular lattice spacings. The intensity of the fluorescent radiation allows the determination of

element concentrations in the sample. The intensities are compared with standards of known composition for a quantitative result (Tertian & Claisse, 1982).

The environmental significance of major and trace elements, and their potential as palaeoclimatic proxies, are discussed in Sageman & Lyons (2003) and Brumsack (2006). Al and Ti are the products of crustal weathering least susceptible to redox changes (Taylor & MacLennan, 1985; Peterson, *et al.*, 2000a; Yarincik *et al.*, 2000; Brumsack, 2006) and are, therefore, the most useful terrigenous proxies. Variations in the volume of the terrigenous components can concentrate or dilute the climate signal of biogenic or authigenic proxies. Detrital $SiO_2$ forms part of the terrigenous flux, but conventional XRF cannot distinguish between detrital and biogenic silica, and so a separate analysis for the latter was undertaken (section 3.5.4).

The flux of redox-sensitive metals to the sediment is a reflection of bottom water oxygenation. Fe oxides are precipitated with slight increases in oxygen, while Mn ions remain in the water column until oxygen levels are significantly elevated (Broecker & Peng, 1982). Variations in productivity-driven anoxia can be tracked by the trace metal Molybdenum, which readily reacts with organic matter (Sageman & Lyons, 2003). Vanadium hydroxides precipitate at Eh conditions corresponding to the range at which denitrification occurs (Piper, 1994). Denitrification is usually taken to indicate intervals of high productivity and anoxia. In the absence of oxygen, bacteria utilise nitrates to break down organic matter. This causes the loss of the lighter nitrogen isotope to the atmosphere, leaving the sediment enriched in the heavier isotope ($\delta^{15}N$; Broecker & Peng, 1982).

### 3.5.3 Carbon analysis

Carbonate carbon and total organic carbon are biogenic proxies (eg Sageman & Lyons, 2003). The sediments associated with coastal upwelling areas are typically organic-rich due to excess rates of productivity by siliceous diatoms. At sites where preservation factors are high, variations in climate-driven

productivity through time can be traced via organic carbon flux in conjunction with the other biogenic proxies, biogenic silica, $CaCO_3$, Mo and V.

An aliquot of each of the discrete samples (50-cm resolution) from the full length of core MD02-2517/2515 was dried overnight in an oven at 100° C. The dried samples (~4 g) were then homogenised and prepared for the analysis of total carbon (TC) and total organic carbon (TOC) by the LECO carbon analyser in the Wolfson Laboratory, University College London. Analysis of TC and TOC were also carried out in tandem with the conventional XRF analysis (Professor H.-J. Brumsack).

For TC analysis, the prepared sample is weighed in a crucible (the measurements are used after analysis to calculate the wt % carbon) and covered by a small amount of accelerator (a 2:1 ratio of Fe and Sn chippings). The sample is combusted in the LECO induction furnace. This releases $CO_2$, which is passed through a train of purifying reagents before being measured by the carbon detector. The precision of the machine is ±3.1%. TOC is determined in the same way except that, before combustion, the sample is treated with a 10% solution of hydrochloric acid to remove carbonate minerals.

$$TC - TOC = \text{Total Inorganic Carbon (TIC)} \qquad \text{[eq. 3.5]}$$

$$TIC \times (\text{molecular wt } CaCO_3/\text{molecular wt } CO_2) = CaCO_3 \qquad \text{[eq. 3.6]}$$

Equation 3.6 assumes that all of the carbonate present in the sample is calcium carbonate.

The results of a high-resolution analysis for TOC from the archive-half of core MD02-2515 were kindly made available for use in this study by R. Ganeshram (University of Edinburgh). Samples were taken at 5-cm intervals along the core and processed as part of a $\delta^{15}N$ study. All of the carbonate in the samples was dissolved and they were measured by accelerator mass spectrometry (AMS).

This method returns a slightly higher percentage of TOC than the LECO analysis because the LECO combustion process removes a proportion of organic carbon.

### 3.5.4 Biogenic silica analysis

At present in Guaymas Basin, siliceous diatoms and silicoflagellates flourish in the upwelling season. Biogenic silica represents the flux to the seafloor of the skeletal remains of these organisms. Variations in the flux reflect climate-driven changes in the high-productivity season.

An aliquot of each of the discrete samples (50-cm resolution) was dried overnight in an oven at 100° C in the Wolfson Laboratory, University College London. The dried samples (~12 $\mu$g) were homogenised and then mixed with 2M $Na_2CO_3$, and heated in a water bath at 85°C for two hours. They were then centrifuged, and the supernatant was diluted and acidified to remove the carbonate. After this was complete, the $SiO_2$ concentrations were measured by molybdate-blue spectrophotometry (absorption peak at 812 nm; Shapiro & Brannock, 1962). The precision of the method is 0.1%.

The assumption behind this method is that only biogenic silica is released during the two hours the samples are heated with $Na_2CO_3$,. USGS Open-File Report 02-371 details a method of silica analysis that is almost identical to the one used in this study (http://pubs.usgs.gov/of/2002/of02-371/bsimeth.htm). In their method, preparation and procedure is the same as that used in the Wolfson Laboratory, except that the samples are heated for five hours. This extracts both the biogenic silica fraction and the non-biogenic silt grains. The silica-content of the samples is assessed every hour. A graph of the results shows that after two hours silica release abruptly slows to a very low rate. Repeated experimentation shows that diatom frustules dissolve within the first two hours of extraction. The loss of water during the process is ~1%, which is very close to the 1.1% $H_2O$ content of diatom frustules (pers. comm. A. Nederbragt, 2005).

The conventional XRF analysis and the biogenic silica analysis were carried out on aliquots of the same samples. Therefore, it was possible to subtract the results

of the biogenic silica analysis from the total silica results of the XRF analysis, giving detrital silica, which is a component of terrigenous flux

### 3.5.5 Oxygen and carbon stable isotope analysis

A low-resolution stable isotope analysis ($\delta^{18}O$ and $\delta^{13}C$) was carried out on core MD02-2515 as part of a separate pilot-study (A.J. Nederbragt, University College London) and the results have kindly been made available for use in this study. Samples (~20 g) were taken every metre and were washed and dry-sieved over 250 $\mu$m. The residues were hand-picked for individual species of benthic foraminifera (*Bolivina* spp.). The samples were measured on a Kiel III/Mat 253 mass spectrometer at the Bloomsbury Environmental Isotope Facility, University College London. The results are expressed in ‰ of the Vienna Pee Dee Belemnite standard; internal precision for $\delta^{18}O$ is 0.1‰ (Cheshire *et al.*, 2005; Appendix I).

Stable isotope analysis uses the fact that naturally occurring heavy and light isotopes of oxygen and carbon exist in known ratios, both elements are commonly taken up from ocean water by test-secreting organisms such as foraminifera and, therefore, isotopic variations in foraminiferal calcite reflect isotopic variations in seawater.

Ratios of $^{18}O$ and $^{16}O$ ($\delta^{18}O$) were first used to estimate SSTs (Emiliani, 1955), but were later shown to be a reflection of global ice volume (Shackleton & Opdyke, 1973): ocean water is enriched in $^{18}O$ when $H_2{}^{16}O$ is stored in ice. Ocean mixing takes ~1000 years and therefore $\delta^{18}O$ profiles, allowing for differences caused by sedimentation rate and bioturbation, are similar for all deep ocean cores. The cyclicity in these profiles during the last two million years has been linked to Milankovitch orbital forcing (Hays *et al.*, 1976) and a Quaternary timescale has been constructed from stacked records (SPECMAP; eg Martinson *et al.*, 1987). $\delta^{18}O$ is affected by the recrystallisation of calcite during diagenesis and by variation in temperature and salinity. The deep ocean is less susceptible to local variations in temperature and salinity and benthic foraminifera tests therefore provide a more reliable reflection of global ocean $\delta^{18}O$.

When plants photosynthesise, $^{12}C$ is preferentially taken up and ocean water becomes enriched in $^{13}C$. $\delta^{13}C$ can therefore be used as a measure of changes in the rate of local productivity. Ocean mixing time allows gross changes in global productivity to be recorded in foraminifera tests. Attempts have been made to link global changes in the rate of photosynthesis to atmospheric $CO_2$ volume (Shackleton *et al.*, 1983; 1992) via the analysis of paired benthic and planktonic foraminifera. $\delta^{13}C$ excursions have been associated with $CH_4$-release from methane hydrates, which could be a reflection of slope instability due to sea level rise (Kennett *et al.*, 2000). On the other hand, such excursions could be caused by the sudden introduction of stored organic carbon by flooding of previously exposed and vegetated shelves during rising sea level.

### 3.6 Age model

In order to compare the information contained in the sediment of core MD02-2517/2515 to other palaeoclimate records, an age model for the core has to be established and the data firmly set within the framework of the standard timescale used for the Late Neogene (Quaternary).

The 1-cm scale average varve thicknesses (section 3.4.5) were used to calculate the number of years per centimetre in the laminated intervals. In order to establish a linear sedimentation rate (cm/yr) for the whole core, interpolations were made across the non-laminated intervals by using an average between the rates immediately below and above. This assumes that sedimentation rate is steady across the interval. The small errors, which undoubtedly occur because of this assumption, may become problematic in intervals that contain many brief episodes of non-laminated sediment, reflecting rapid climate instability. Without a second method of calibrating the age model, the time span estimated for non-laminated intervals can only be a first approximation. The calculation of sedimentation rate from variations in varve thickness and interpolation across non-laminated intervals establishes a chronology in 'varve years'.

Some of the previously published palaeorecords from Guaymas Basin have radiocarbon dates and correlation between the dated cores and core MD02-2517/2515 can be used to establish calendar ages for the 'varve year' chronology. Keigwin & Jones (1990) produced radiocarbon dates for the last 20,000 years of DSDP Site 480 (Fig. 1.1; Table 1.1) and these, revised with the $^{14}C$ reservoir age of Gulf of California waters (Goodfriend & Flessa, 1997), were used by Barron *et al.* (2004) in their investigation of the palaeoceanographic record of eastern Guaymas Basin over the last ~15,000 years. For core JPC-56, Sancetta (1995), Pike & Kemp (1996; 1997; 1999) and Pride *et al.* (1999) used (at the time) unpublished AMS radiocarbon dates from benthic foraminifera (LD Keigwin, WHOI). Pride *et al.* (1999), acknowledging that the top of core JPC-56 is missing due to overpenetration by the corer, correlated laminated intervals with those in gravity core GGC55 and used 14 unpublished radiocarbon dates (LD Keigwin, WHOI) to construct an age model for the spliced record. These radiocarbon dates were re-calibrated by Keigwin (2002), using the revised reservoir correction of 725 years ($\partial R$ = 395 years; Goodfriend & Flessa, 1997). Barron *et al.* (2005) also use Keigwin (2002)'s re-calibrated radiocarbon dates. However, their age model differs from his in that their correlation between the two cores puts the top of core JPC-56 at 220 cm depth in core GGC55 instead of 150 cm. They estimate that the last ~2100 years are missing from the top of the GGC55 record.

Core GGC55/JPC-56 was taken ~5 km to the southwest of Site MD02-2515, from a similar water depth and it is probable that both reflect the same local environment of deposition. Pike (1996)'s high-resolution sedimentary log of JPC-56 presented the opportunity for comparison between the two cores. In order to establish a tie-point that could be dated via interpolation of the AMS radiocarbon data, Keigwin (2002)'s $\delta^{13}C$ analysis of benthic foraminifera in core GGC55/JPC-56 (*B. seminuda*) was compared with that of the section of MD02-2515 identified by the sedimentary correlation with core JPC-56. Radiocarbon dates are subject to margins of error. In the age-range relevant to this site, these are in the order of tens of years. This means that instead of a single date for the tie-point, there is a range of possible dates. Establishing a tie-point means that

the floating 'varve year' chronology becomes fixed to within, at least, a century and gives a small range of possible dates for both the top and the bottom of core MD02-2515. The top of core MD02-2517 represents the sediment-water interface (pers. comm., J. Thurow, 2002) and its 'varve year' chronology will reveal whether there is an overlap or a gap between the two cores.

The age model gives a time-range for core MD02-2517/2515 and allows the further analysis of the sediment fabric index. In order to obtain a measure of which sediment fabric was dominant at any given time, the core has been divided into 'time-slices'. The establishment of a linear sedimentation rate in cm/yr means that each centimetre represents a known number of years (yr/cm). A time-slice of, say, 250 years will vary in length depending on the sedimentation rate. Each of the centimetres within the time-slice has been assigned to one of the sediment fabric types (section 3.4.4). Therefore, the number of 'occurrences' of a sediment fabric type in a time-slice can be summed and the dominant type for that time-slice can be determined.

The method for this procedure is the same as for a frequency distribution histogram, where the number of occurrences (the frequency) of a component within a particular range (ie length, weight, etc) is summed in order to get a graphic representation of the distribution of size within a sample population. For the sediment fabric types, the 'range' is the 250-yr time-slice (0-249; 250-499; 500-749 ... etc) and the 'frequency' is the number of times a sediment fabric type occurs within that time-slice.

## 3.7 Summary of techniques

Table 3.1 is a summary of the techniques used in this study.

| Method | Resolution | Analysis | Climate proxies | References |
|---|---|---|---|---|
| Coring (*Calypso* & kasten) | | | | Kullenberg (1947); Balut (IFP); Beaufort *et al.* (2002); Skinner & McCave (2003) |
| Colour reflectance (Minolta 2022) | 2 cm | Lightness; red/green & blue/yellow attributes | Productivity/preservation; redox conditions | Ortiz & Mix (1997); Beaufort *et al.* (2002); Balsam *et al.* 1999; Nederbragt *et al.* (2000) |
| Magnetic susceptibility (GEOTEK Ltd MSCL) | 2 cm | | Runoff/sea level | Oldfield (1999); Ellwood *et al.* (2000) |
| Sediment density (GEOTEK Ltd MSCL) | 2 cm | Wet bulk density | Accumulation rates | Beaufort *et al.* (2002); Gardner *et al.* (1997); Peterson *et al.* (2000); Calvert & Carlin (1998) |
| Sediment description/microfossil identification | Continuous/50 cm | Minerals, grainsize/diatoms and other microfossil species | Environmental variation | Sancetta (1995); Pike (1996); Barron *et al.* (2004; 2005) |
| Digital photography | 130 pixels/cm | | | Nederbragt *et al.* (2000) |
| Sediment fabric index | 1 cm | Degree of lamination; variations of relative lamina thickness and internal continuity | Upwelling season vigour/duration and wetness/dryness; migration of North Pacific Subtropical High | Bull & Kemp (1995); Behl & Kennett (1996); Pike & Kemp (1996; 1997; 1999) Dean *et al.* (1999) |
| Continuous XRF scan | 1 cm | K, Ti, Mn, Fe, Cu, Sr | Productivity/preservation; terrigenous and authigenic flux | Jansen *et al.* (1998) Röhl & Abrams (2000); Haug *et al.* (2003); Peterson *et al.* (2000); Yarincik *et al.* (2000); Sageman & Lyons (2003) |

**Table 3.1:** Summary of techniques used in this study.

| Method | Resolution | Analysis | Climate proxies | References |
|---|---|---|---|---|
| Conventional XRF | 50 cm | Major and trace elements | Productivity/preservation; terrigenous and authigenic flux | Tertian & Claisse (1982); Sageman & Lyons (2003); Brumsack (2006); Taylor & MacLennan (1985); Piper (1994); Peterson *et al.* (2000); Yarincik *et al.* (2000) |
| LECO carbon analyser | 50 cm | TC, TOC | Carbonate productivity & general productivity | Sageman & Lyons (2003) |
| AMS spectrometry | 5 cm | TOC | Productivity/preservation | Sageman & Lyons (2003) |
| Biogenic silica extraction | 50 cm | Biogenic silica | Siliceous (diatom) productivity | Shapiro & Brannock (1962); USGS Open File Report 02-371; Sageman & Lyons (2003); Barron *et al.* (2004; 2005) |
| Stable isotope mass spectrometry | 1 m | $\delta^{18}O$ & $\delta^{13}C$ | Global ice volume; productivity | Schrader *et al.* (1982); Keigwin & Jones (1990); Sancetta (1995); Pike & Kemp (1996; 1997;1999); Goodfriend & Flessa (1997); Pride *et al.* (1999); Keigwin (2002); Barron *et al.* (2004; 2005); Cheshire *et al.* (2005) |

**Table 3.1 (continued):** Summary of techniques used in this study

# Chapter 4 Sediment Fabric Results

## 4.1 Introduction

The BSEI study of Pike & Kemp (1996; 1997; 1999) on early and mid-Holocene sediment from western Guaymas Basin shows that the year-on-year structure, appearance and dimensions of the laminated sediment fabric is of prime importance in recording seasonality and climatic events.

Accordingly, the results of the sediment fabric analyses from core MD02-2517/2515 are presented in this chapter and are used to construct a framework within which the geochemical analyses will be reported (Chapter 5). The age model is established first, allowing the other results to be presented with reference to the standard Quaternary timescale. All the data presented in this chapter are in Appendix II (on CD).

## 4.2 Age of core MD02-2517/2515

The full length of Kasten core MD02-2517 is ~5.97 m (Beaufort *et al.*, 2002). The top ~0.9 m are very dark and waterlogged. Fine laminae occur immediately below this zone, suggesting that the uppermost sediment is not homogeneous, but, rather, that high water-content obscures the appearance of the laminae. Colour-banding (an alternation of light olive-green and dark olive-green) is also visible below ~0.9 m bsf (m below seafloor). This banding occurs throughout both cores and is, most frequently, ~2-3 cm thick. In the waterlogged section, the bands are ~4 cm thick and thin to ~3 cm below ~2.3 m bsf. This suggests that, at this depth, the overburden is sufficient to compress the sediment and expel water. Sedimentation rate has been adjusted accordingly. Sedimentation rate, calculated from the varve thickness measurements and linear interpolation (sections 3.4.6 & 3.6), gives a cumulative total of 3028 'varve years'.

The void-corrected length (section 3.4.3) of continuous piston core MD02-2515 is ~62.60 m. Sedimentation rates calculated from varve thickness measurements and linear interpolation yield 29,846 'varve years'. Intervals between ~26-37 m bsf and ~59-63 m bsf contain many brief episodes of non-laminated sediment

and accumulated small errors in the linear interpolations may have under- or over-estimated the time represented.

This guide to the number of years represented in core MD02-2517/2515 suggests that the age range covers Marine Isotope Stages (MIS) 1, 2 and part of 3. Although the resolution of the $\delta^{18}O$ stratigraphy is too low for conclusive correlation, comparison to SPECMAP (Mapping SPEctral variability in global CliMAte Project; Martinson *et al.*, 1987) supports this idea (see figure in Appendix II, 'Age Model').

Figure 4.1 compares the sedimentary logs of core JPC-56 (Pike, 1996) and the top ~19 m of core MD02-2515. The overall similarities in the appearance of the sediments are quite striking, while the minor differences, such as the more frequent occurrence of coarse laminae and non-laminated sediment in JPC-56, probably reflect its location closer inshore. Two non-laminated intervals occur in both cores: at ~8.5 and ~14 m in MD02-2515, and ~11.2 m and ~16.5 m in JPC-56.

Figure 4.2 shows the $\delta^{13}C$ stratigraphy of core GGC-55/JPC-56 (Keigwin, 2002) and the top ~21 m of the low-resolution $\delta^{13}C$ profile of core MD02-2515. Most of the dissimilarities are due to the difference in resolution, though some may be due to differences in sedimentation rate. The striking features of both records are the negative excursions at ~3.20 m and ~10.30 m in MD02-2515, and ~5.40 m and ~11.90 m in GGC55/JPC-56. The $\delta^{13}C$ values of the lower excursion are almost identical in both cores. Accordingly, this was chosen as the tie-point and the records were aligned. In GGC/JPC-56, this point occurs just above the calibrated AMS radiocarbon date 13146 ±45 Calendar yr BP at ~12.20 m (Keigwin, 2002). The next reliable date above is 11114 ±60 Calendar yr BP at ~8.70 m. After calculating all the possible permutations (error bars moving in the same direction, in opposite directions, etc), the mean age of the tie-point is 130001 ±36 Calendar yr BP. The floating chronology of core MD02-2515 puts the tie-point at 6916 'varve years'; with the application of the interpolated

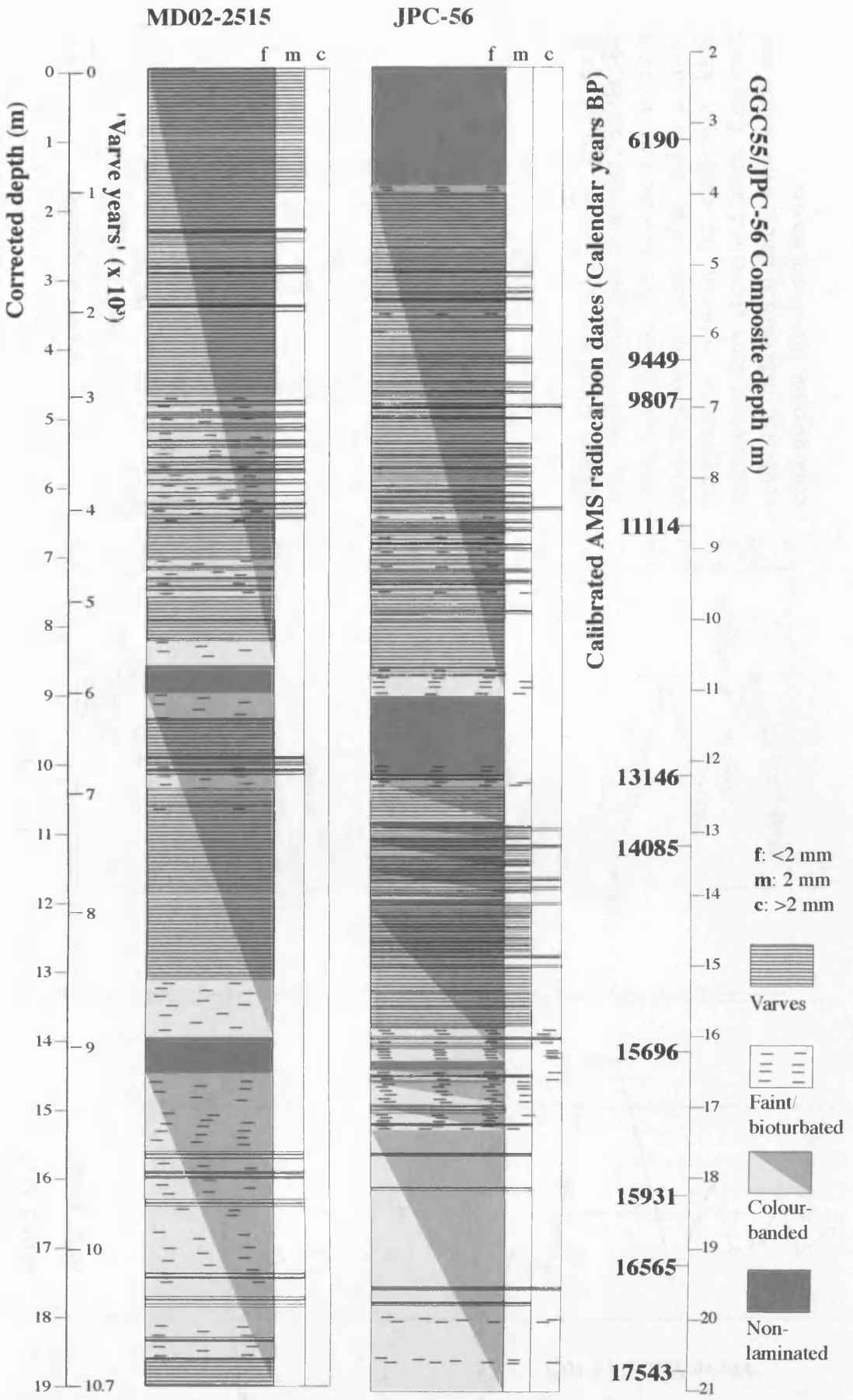


**Figure 4.1:** Comparison between the top ~19 m of core MD02-2515 - 'varve years' calculated from varve thicknesses - and JPC-56 (Pike, 1996); AMS dates from Keigwin (2002).

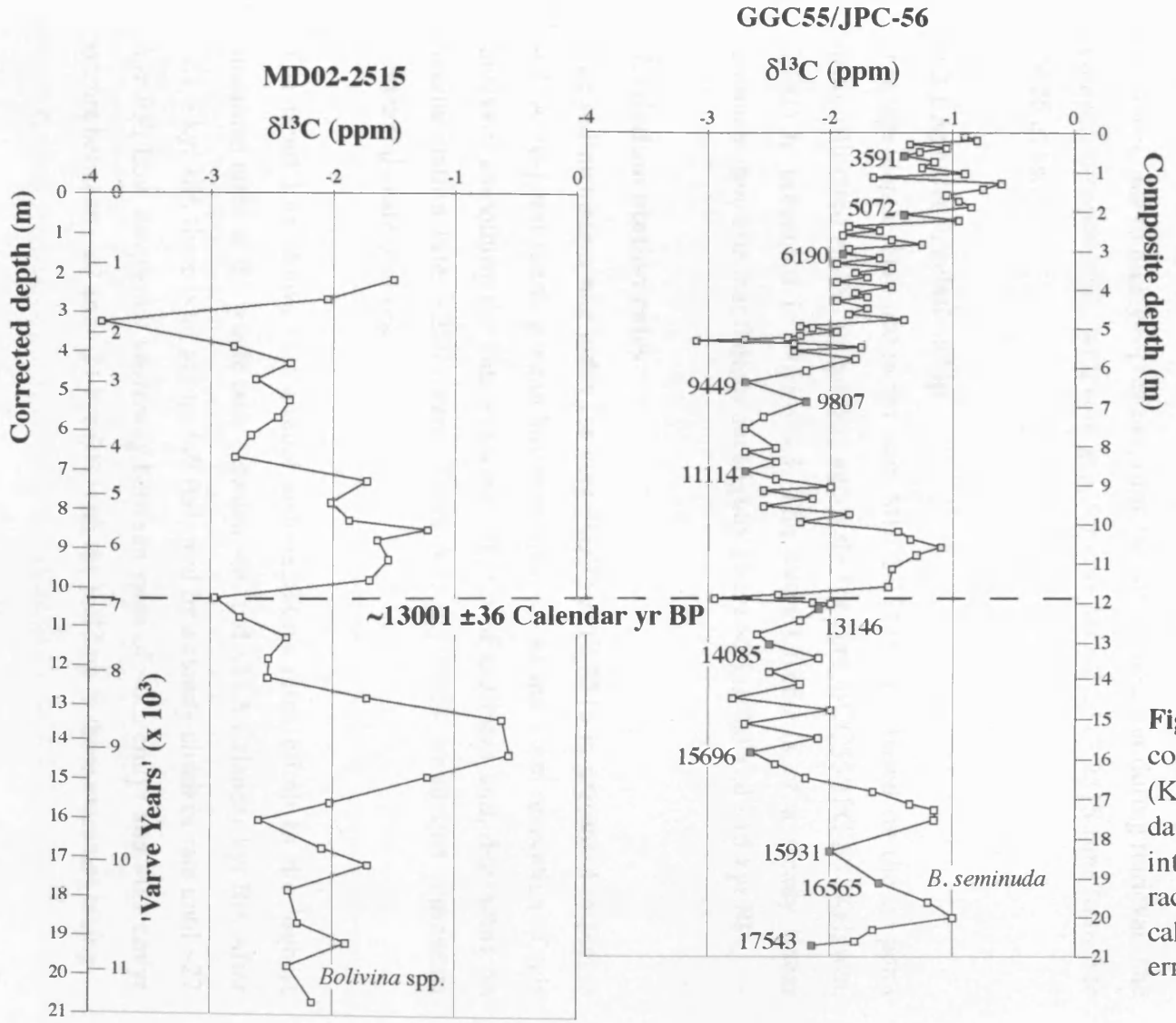


| GGC55/JPC-56 | | |
|---|---|---|
| Depth (m) | Calibrated age (yr BP) | Error (±) |
| 0.60 | 3591 | 30 |
| 2.10 | 5072 | 25 |
| 3.20 | 6190 | 35 |
| 6.40 | 9449 | 55 |
| 6.90 | 9807 | 45 |
| 8.70 | 11114 | 60 |
| 12.20 | 13146 | 45 |
| 13.20 | 14085 | 60 |
| 16.20 | 15696 | 55 |
| 18.20 | 15931 | 55 |
| 19.20 | 16565 | 65 |
| 20.70 | 17543 | 60 |

**Figure 4.2:** $\delta^{13}C$ data from the top 21 m of core MD02-2515 and core GGC55/JPC-56 (Keigwin, 2002). The tiepoint runs through datapoints of the same value and is a linear interpolation between the calibrated AMS radiocarbon dates above and below. Keigwin's calibrated radiocarbon dates, with depths and error margins, are shown above.

radiocarbon date, this results in an upper age of the core at 6085 ±36 Calendar yr BP and a lower age at 35931 ±36 Calendar yr BP.

The chronology now set for core MD02-2515 reveals a stratigraphic gap between the top of this core and the bottom of core MD02-2517. If the top of the Kasten core represents the sediment-water interface (pers. comm. J. Thurow, 2002), then ~3057 years or (using the average of sedimentation rates above and below the gap – 0.19 cm/yr) ~5.70 m of sediment are missing between the two cores and ~6100 years or ~12 m from the top of MD02-2515. The simplest, and therefore most likely, explanation is that this loss is due to a combination of overpenetration by the nose of the corer into very soft sediment and extrusion of sediment, due to high gas pressure, from the top of the corer during retrieval. The composite depth-scale, with core gap, for core MD02-2517/2515 runs from 0 to 74.25 m bsf.

### 4.2.1 Age-depth relationship

The age-depth relationship for core MD02-2517/2515, based on the tie-point with calibrated AMS radiocarbon age-scale for core GGC55/JPC-56 (Keigwin, 2002) is presented in Figure 4.3. The overall trend is of a steady linear sedimentation rate that flattens out slightly above ~25 m bsf and ~15 kyr BP.

## 4.3 Sedimentation rates

The sedimentation rate index for core MD02-2517/2515 is presented in Figure 4.4. A 50-point running mean has been applied. At the 1-cm resolution of this analysis, smoothing the data averages ~50 cm of sediment and, depending on sedimentation rate, ~250 years. Therefore, the black trend line represents centennial-scale changes.

The trend line shows that annual sedimentation rates climb to the highest sustained rates of the whole core between ~36 and ~31.5 Calendar kyr BP. After ~31.5 kyr BP, there is an abrupt fall followed by a steady climb in rate until ~27 kyr BP. Low frequency switching between rates of ~0.5 cm/yr and ~0.1 cm/yr occurs between ~27 and ~21 kyr BP, with the build up to these extremes taking

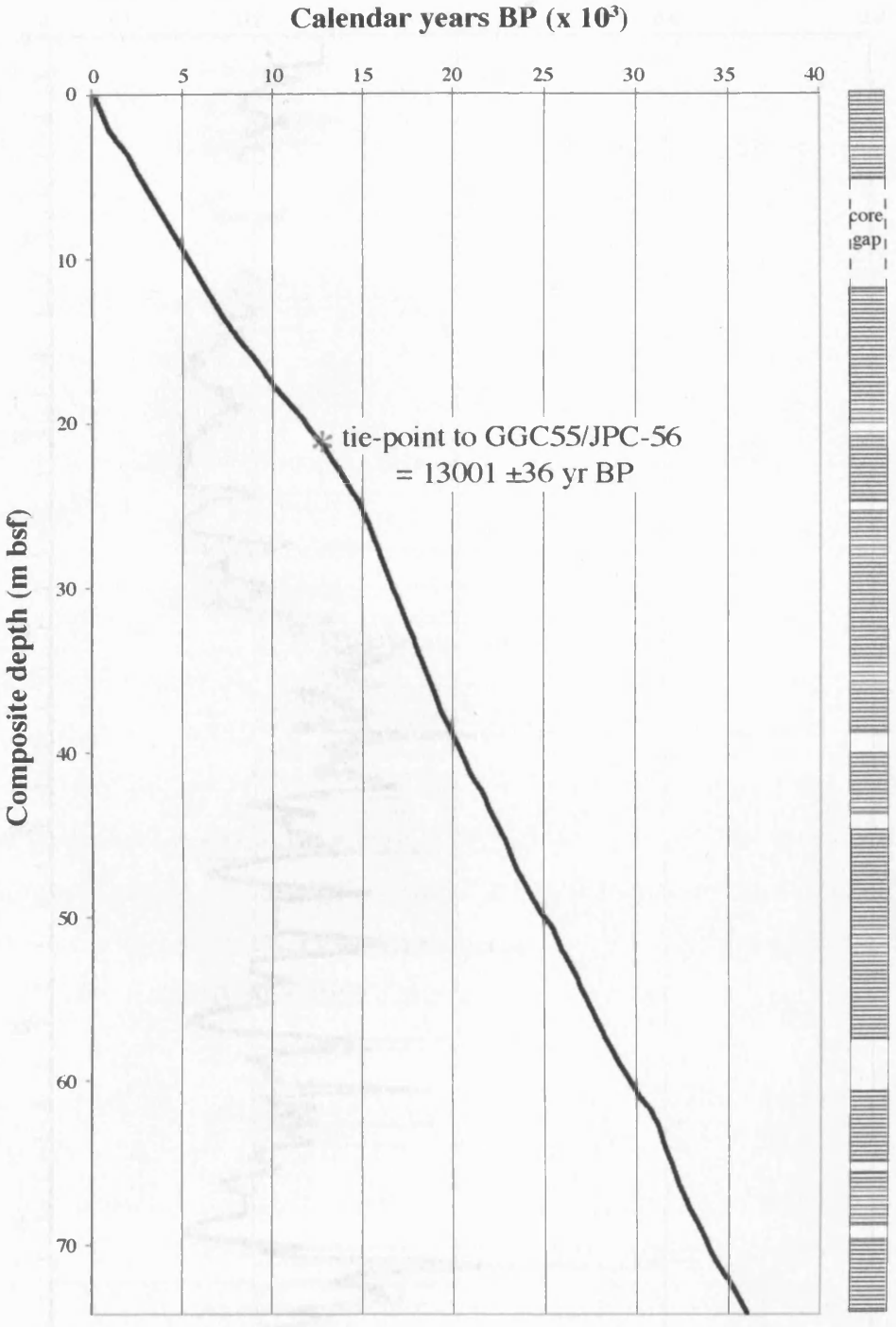


**Figure 4.3:** The age-depth relationship for core MD02-2517/2515 with the major laminated intervals.

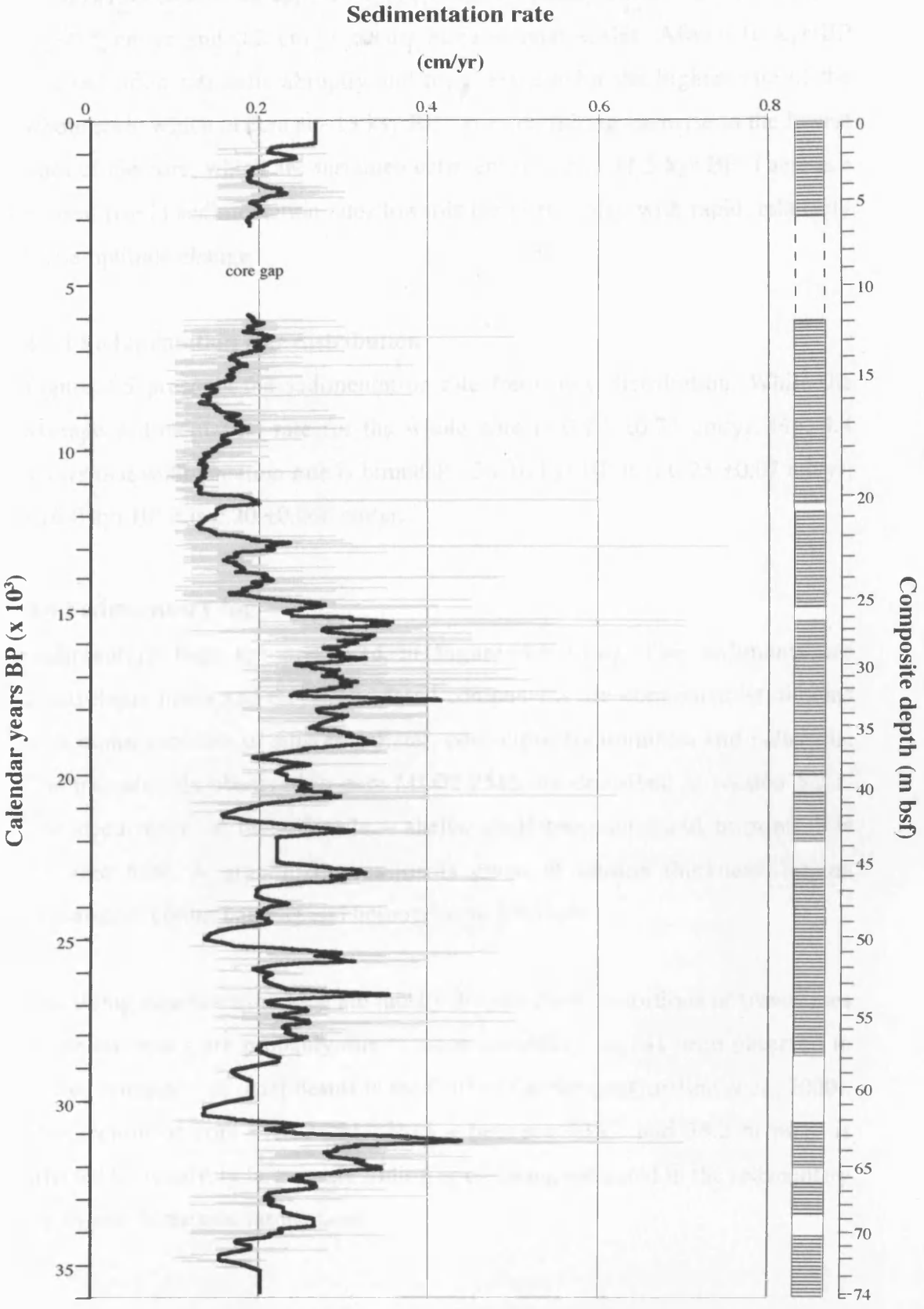


**Figure 4.4**: The sedimentation rate index, calculated from measured varve thicknesses and linear interpolation across non-laminated intervals. 1-cm resolution with a 50-point running mean.

~1000 yr. Between ~21 and ~16 kyr BP, high frequency switching between rates of ~0.5 cm/yr and 0.2 cm/yr occurs at centennial scales. After ~16 kyr BP sedimentation rate falls abruptly and then - except for the highest rate of the whole core, which occurs at ~13 kyr BP - goes on falling stepwise to the lowest rates of the core, which are sustained between ~12 and ~11.5 kyr BP. There is a modest rise in sedimentation rates towards the present day with rapid, relatively low-amplitude change.

### 4.3.1 Sedimentation rate distribution

Figure 4.5 presents the sedimentation rate frequency distribution. While the average sedimentation rate for the whole core is 0.23 ±0.73 cm/yr, Fig. 4.4 shows that sedimentation rate is bimodal: ~36-16 kyr BP it is 0.25 ±0.07 cm/yr; ~16-0 kyr BP it is 0.20 ±0.068 cm/yr.

## 4.4 Sedimentary log

Sedimentary logs are presented in Figure 4.6 (a-e). The sediments are hemipelagic muds and clays. The fossil components are dominated by diatoms with minor amounts of silicoflagellates, coccoliths, foraminifera and radiolaria. The microfossils observed in core MD02-2515 are described in section 5.3.1. The occurrence of macrofossils – shells, shell fragments and burrows – is reported here. A graphic impression is given of lamina thickness, lamina appearance, colour banding and homogeneous intervals.

The slump structures – which are mostly 2-3 cm-thick distortions or truncations of the laminae - are probably due to slope instability, as has been observed in varved sediments of other basins in the Gulf of California (Gorsline *et al.*, 2000). One section of core MD02-2517/2515 – between ~35.1 and 38.2 m bsf – is affected by relatively large-scale sliding or creeping, indicated in the sedimentary log by sub-horizontal laminations.

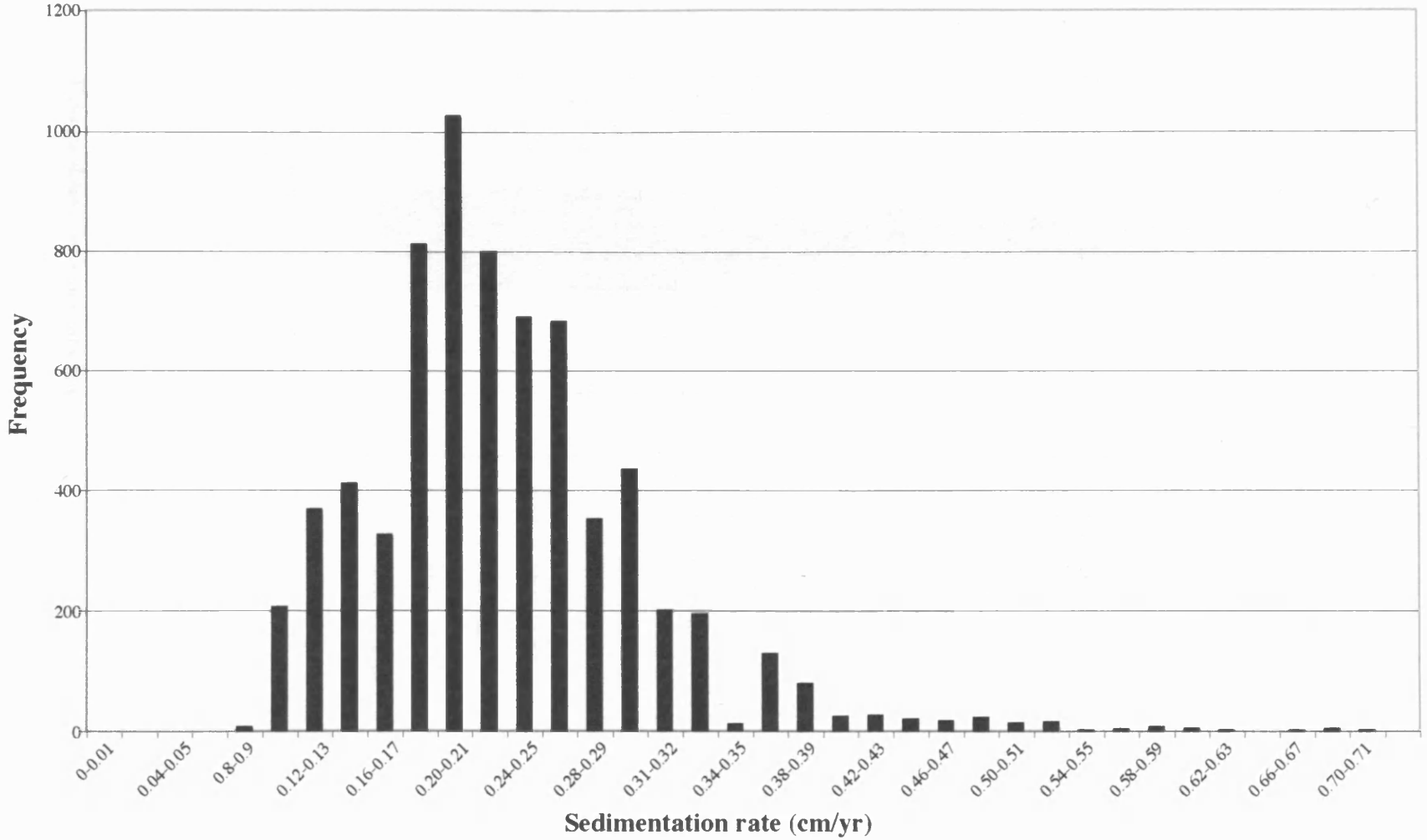


**Figure 4.5:** Sedimentation rate distribution. Average sedimentation rate for the whole core is 0.23 ±0.08 cm/yr

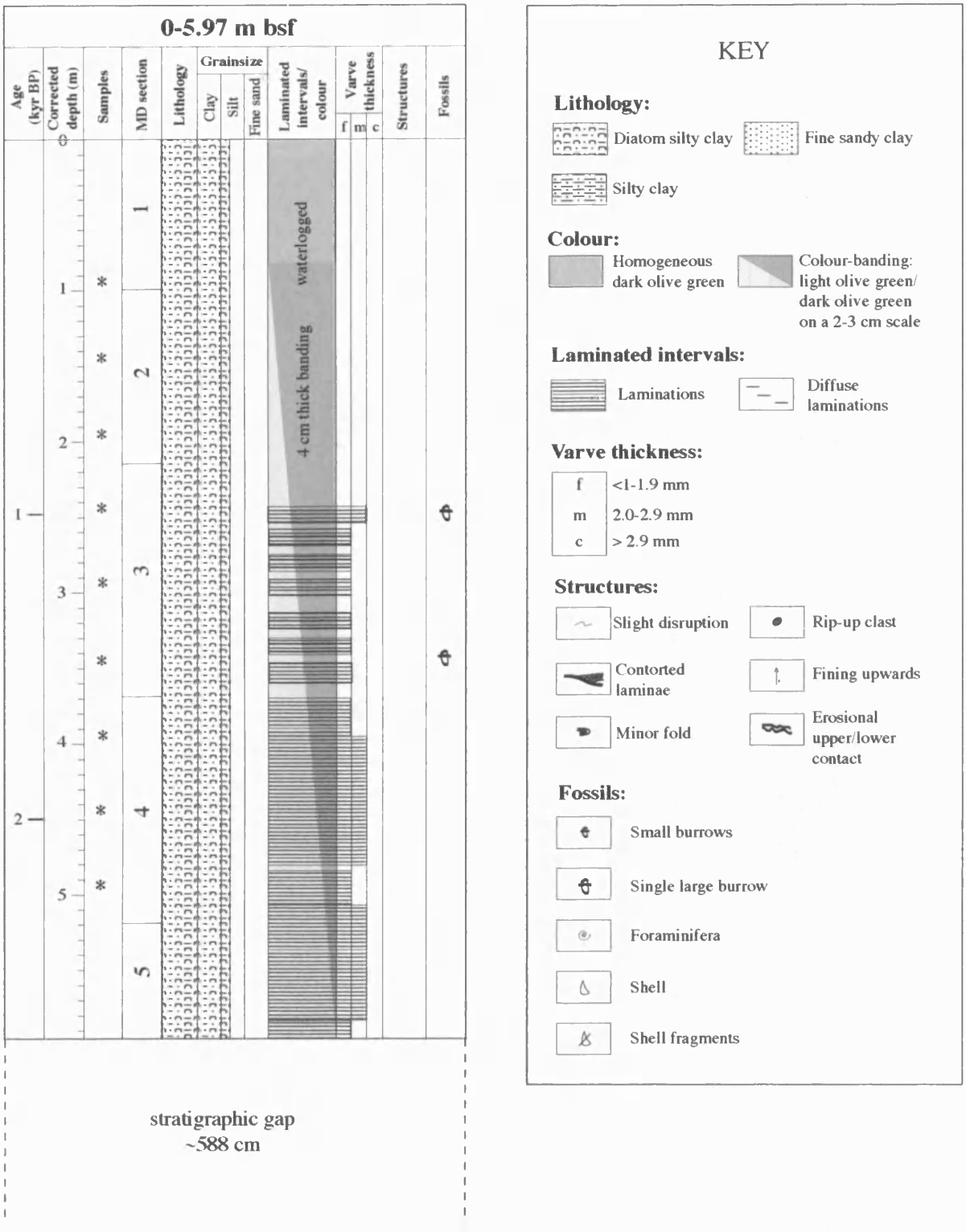


**Figure 4.6a:** Sedimentary log

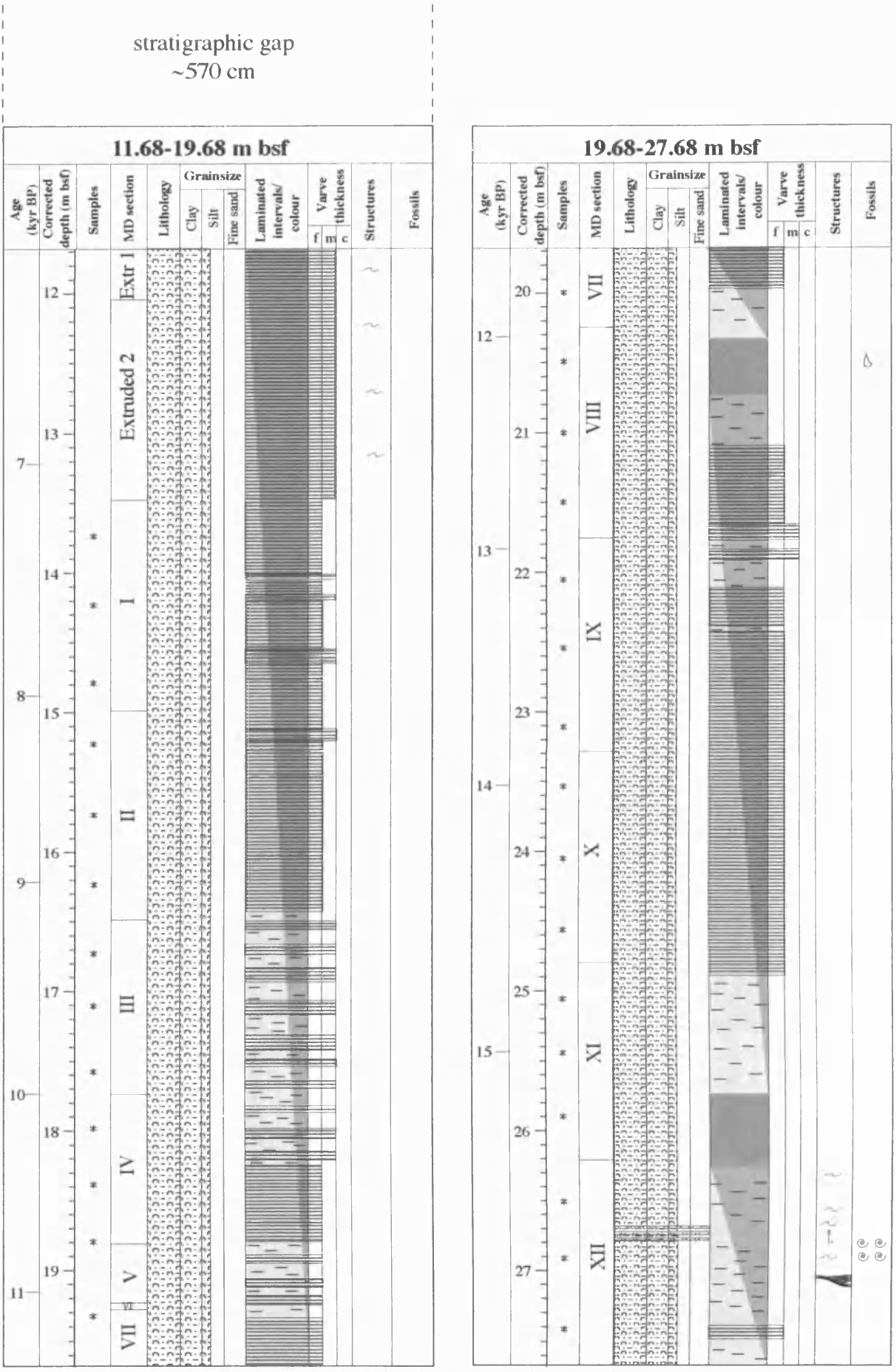


**Figure 4.6b:** Sedimentary log [For key, see Fig. 4.6a]

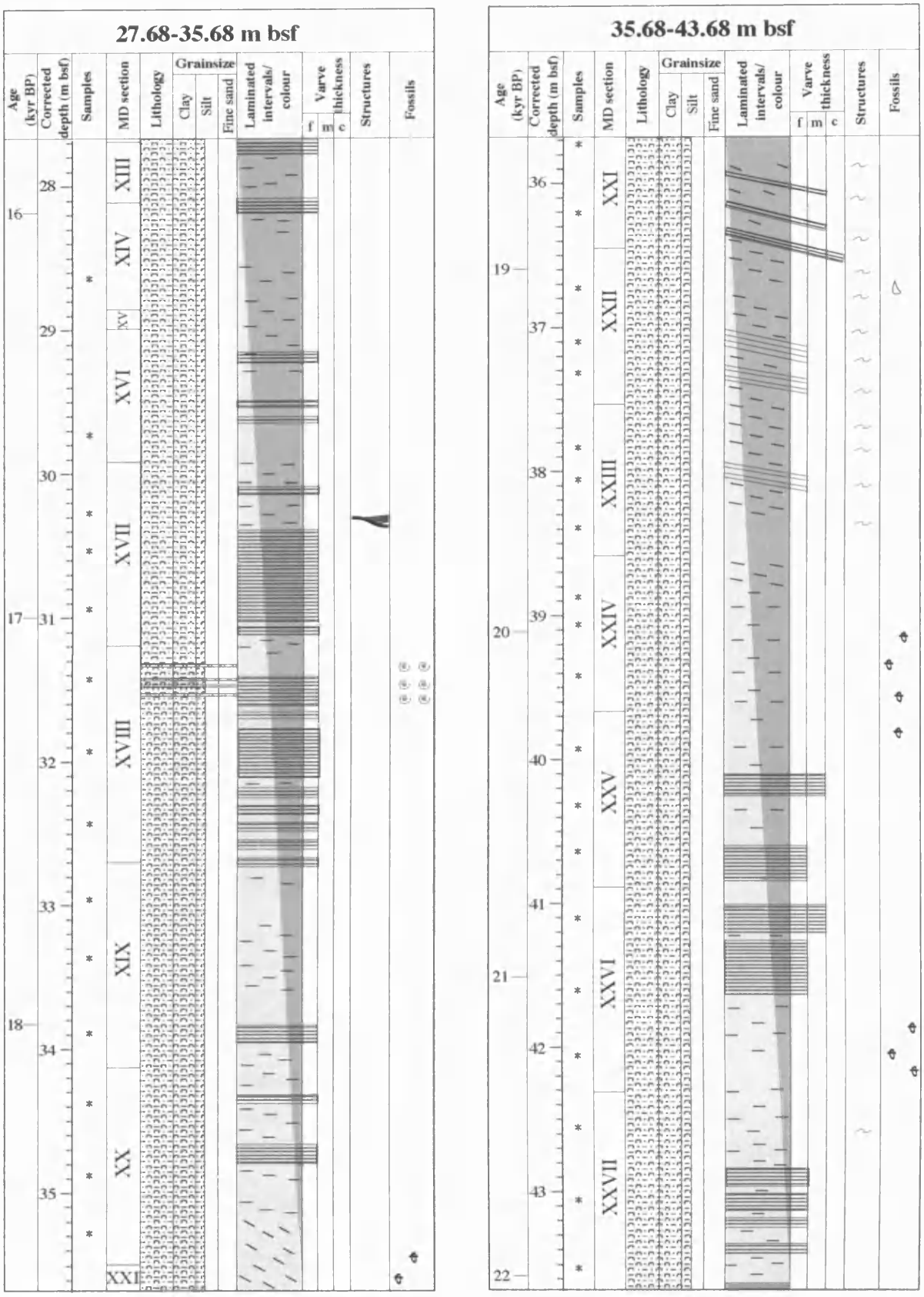


**Figure 4.6c:** Sedimentary log [For key, see Fig. 4.6a]

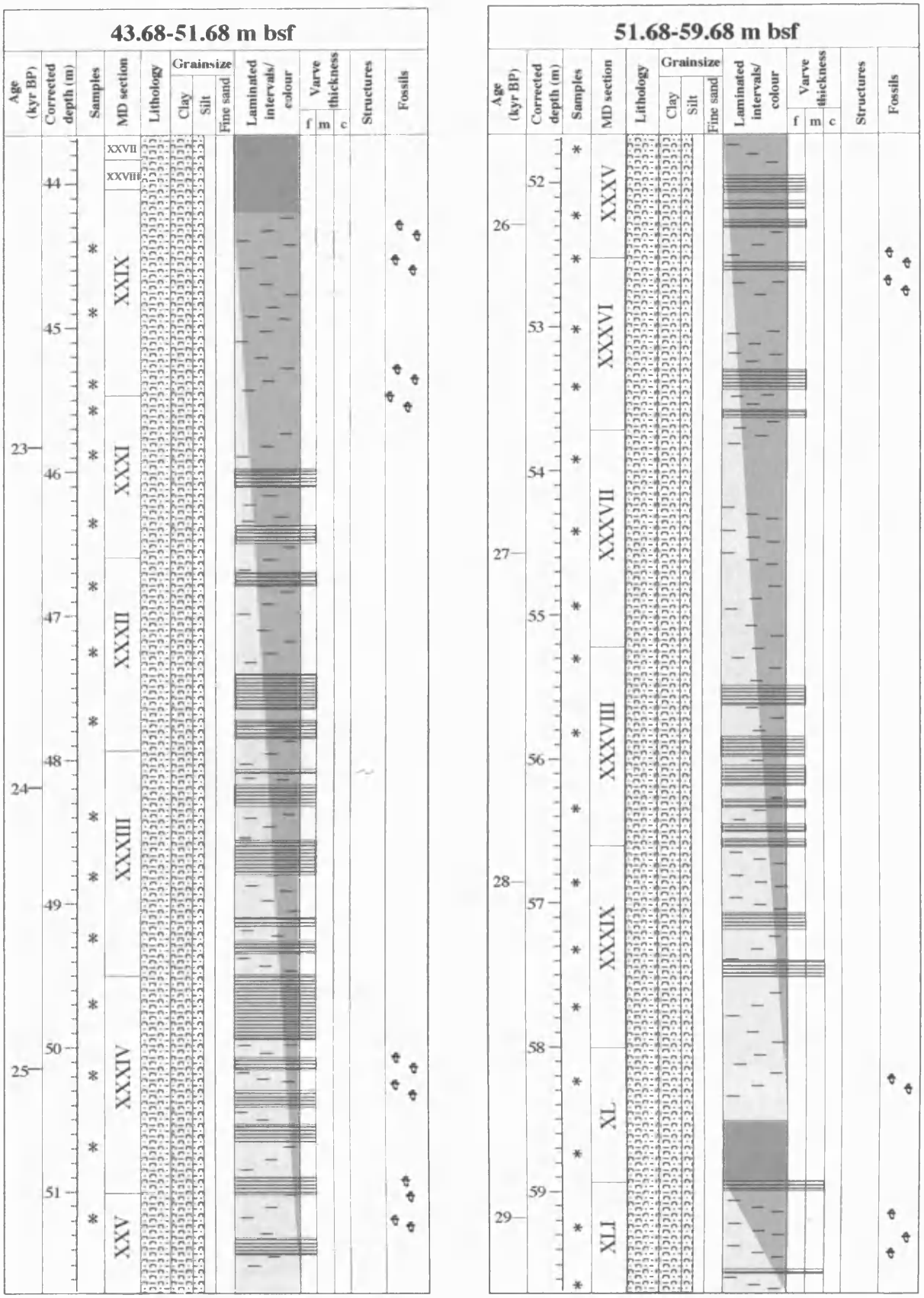


**Figure 4.6d:** Sedimentary log [For key, see Fig. 4.6a]

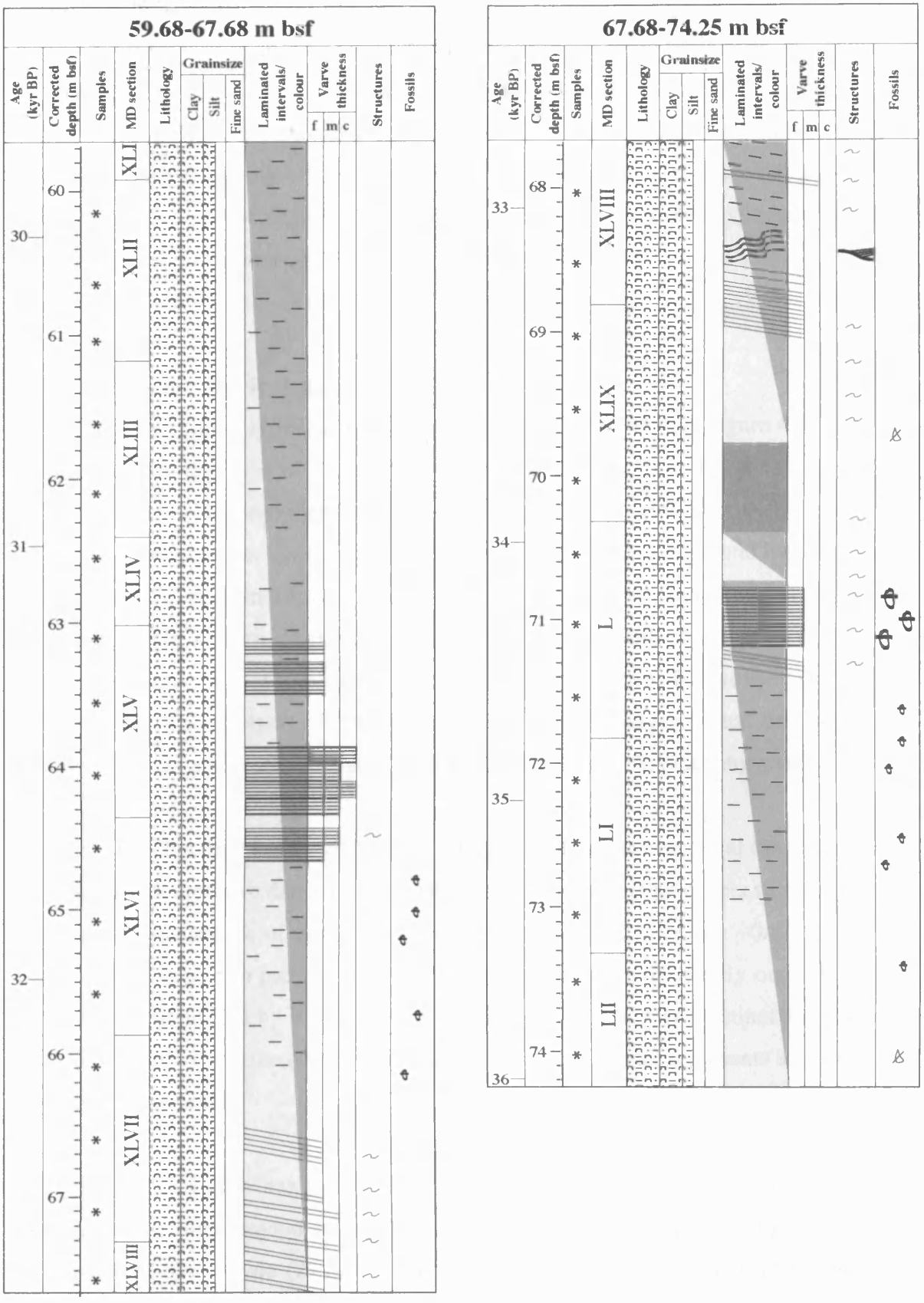


**Figure 4.6e:** Sedimentary log [For key, see Fig. 4.6a]

## 4.5 Sediment fabric

The sedimentary log shows that the sediment fabric has three basic states: it can be laminated and colour-banded; it can be colour-banded without being laminated; and it can be homogeneous. The sections of completely homogeneous sediment are relatively small. There is a large amount of variation within the laminated sections, with abrupt switching between varved sediment types and the sharpness of the laminae. Every centimetre has been assigned to one of the eight categories in the sediment fabric index (section 3.4.4).

### 4.5.1 Sediment fabric types

The sediment fabric types identified in this study are presented in Figure 4.7 (for data, and photographs of types (1) to (7), see Appendix II). Varved sediment fabric type (1) has been identified by Pike & Kemp (1996; 1997) in 50-cm early and mid-Holocene sections of core JPC-56 (section 2.11, Fig. 2.12) and has been linked to the modern annual climate cycle. Their detailed study reveals that, although this pattern of lamination is the most frequently occurring, other configurations are not uncommon (eg Pike & Kemp, 1997). The advantage of identifying the sediment fabric types using the digital images is that the areal coverage (~15 x 150 cm) is large enough to discern long-term recurring patterns.

**Type (1).** This type has light and dark laminae of more or less equal thickness. Although quantitative diatom identification is beyond the scope of this study, the dominant occurrence of type (1) in core MD02-2517, representing ~0-3000 yr BP, gives support to making it the equivalent of the most frequently occurring varve type identified by Pike & Kemp (1996; 1997) that has two distinct diatom blooms within the same continuous light-coloured lamina and represents a three-season annual cycle.

**Type (2).** This type has two distinct diatom blooms separated by a thin silt lamina. The three-season cycle of type (1) cannot be distinguished by visual inspection, but in type (2) they are distinctly shown, with a very brief fourth season in between.


**Type (1)**
Light and dark lamina of equal thickness; no obvious sub-laminae; one annual cycle of two seasons; up to ~0.19 cm


**Type (2)**
Light and dark lamina of equal thickness; dark sub-lamina; one annual cycle of three seasons up to ~0.19 cm thick.


**Type (3)**
Repeating 4-lamina pattern; alternate thinner dark laminae; one annual cycle of four seasons; 0.2- 0.5 cm thick.


**Type (4)**
Light and dark lamina of unequal thickness; no obvious sub-laminae; one annual cycle of two seasons; ~0.2-0.7 cm thick.

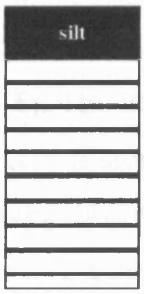


**Type (5)**
Light and dark lamina of unequal thickness; multiple dark sub-laminae; one annual cycle of two seasons with low contrast; ~0.3-0.4 cm thick

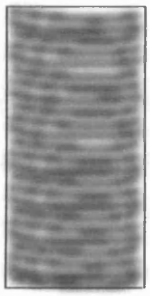

**Type (6)**
Diffuse alternating dark and light laminae; can be wavy or discontinuous; many annual cycles.

**Type (7)**
Colour-banded; no laminations; average band-thickness ~3 cm.

**Type (8)**
Homogeneous

**Figure 4.7:** The sediment fabric types. Types (1)-(6) occur with colour-banding.

**Type (3).** This type is similar to type (2) with roughly double the sedimentation rate. There is a degree of ambiguity in type (3) because the laminae are relatively thick: does it represent one or two annual cycles? However, the advantage of seeing and comparing long sections of core means that repetitive patterns of variation are relatively easy to recognise. The two light laminae and one dark one are the same thickness, the second dark lamina is thinner. Thin dark laminae could be attributed to drought in the non-upwelling season, but here, putting together four laminae as one annual cycle and the associated high sedimentation rates makes high precipitation and runoff the dominant climatic feature. This type represents an annual cycle with four seasons: two dry upwelling/high productivity seasons and two wet seasons, one long, one short.

**Type (4).** This type is distinguished from type (1) partly by its thickness (the thickest varves in core MD02-2517/2515 are type (4)), but mostly because the light lamina is much thicker than the dark lamina. There are no obvious sub-laminae. This type represents a two-season year dominated by the upwelling/high productivity season.

**Type (5).** The dominant feature of this type is the thick light lamina, which has many thin diatomaceous sub-laminae separated by very thin silt sub-laminae. Like type (4), the dark lamina is much thinner than the light lamina. This represents a quasi two-season year where the winds periodically die down during the upwelling/high productivity season.

During the development of the sediment fabric index, seven varved sediment fabric types were identified: another similar to type (3) and another like type (5). The complexity of this scheme did not add anything to the overall result, but it would undoubtedly enhance the study of a much shorter time-period within this core.

**Type (6).** This type comprises alternating light and dark laminae with such a diffuse appearance that it impossible to assign any given lamina-couplet to one of the varved sediment fabric categories. Wavy or discontinuous laminations also

occur, but very infrequently. Alternating laminae imply a contrast between seasons, but preservation factors were diminished due, perhaps, to lower productivity or higher ventilation of bottom waters, or both, and microbioturbation has destroyed the integrity of the lamina boundaries.

**Type (7).** This type represents colour-banded sediment with no laminations. Colour-banding has been observed in other cores from the Gulf of California region (Pike, 1996; Ganeshram & Pedersen, 1998; van Geen *et al.*, 2003). The geochemical properties of the colour-banding have not been specifically investigated in this study and its origin remains speculative. It is a prominent feature of the shipboard photographs, which were taken immediately after the core sections were split open. For the purposes of this study, it has been taken as an indication that the cause of the non-appearance of laminations is not bioturbation and, hence, sediment fabric type (7) is not necessarily the result of either lower productivity or higher bottom-water ventilation.

**Type (8).** This is completely homogeneous sediment with no laminations and no colour-banding.

### 4.5.2 Sediment fabric index

The sediment fabric index is presented in Figure 4.8. The data are noisy because of the high resolution and frequent switching between sediment fabric types. Accordingly, a 50-point running average has been applied. Smoothing the data averages ~50 cm of sediment and, depending on the sedimentation rate, ~250 years. The black trend line therefore represents centennial-scale change.

**~36 to ~15 kyr BP:** The sediment fabric index is relatively high, mostly oscillating between types representing a weak seasonal contrast. This period is notably interrupted between ~25 and ~20 kyr BP by a series of four millennial-scale excursions into lower values representing types with a strong seasonal contrast at ~24.5 ~23.5, ~22, and ~21 kyr BP; a series of four millennial-scale excursions into homogeneous and non-laminated sediment at ~34, ~28, ~22 and

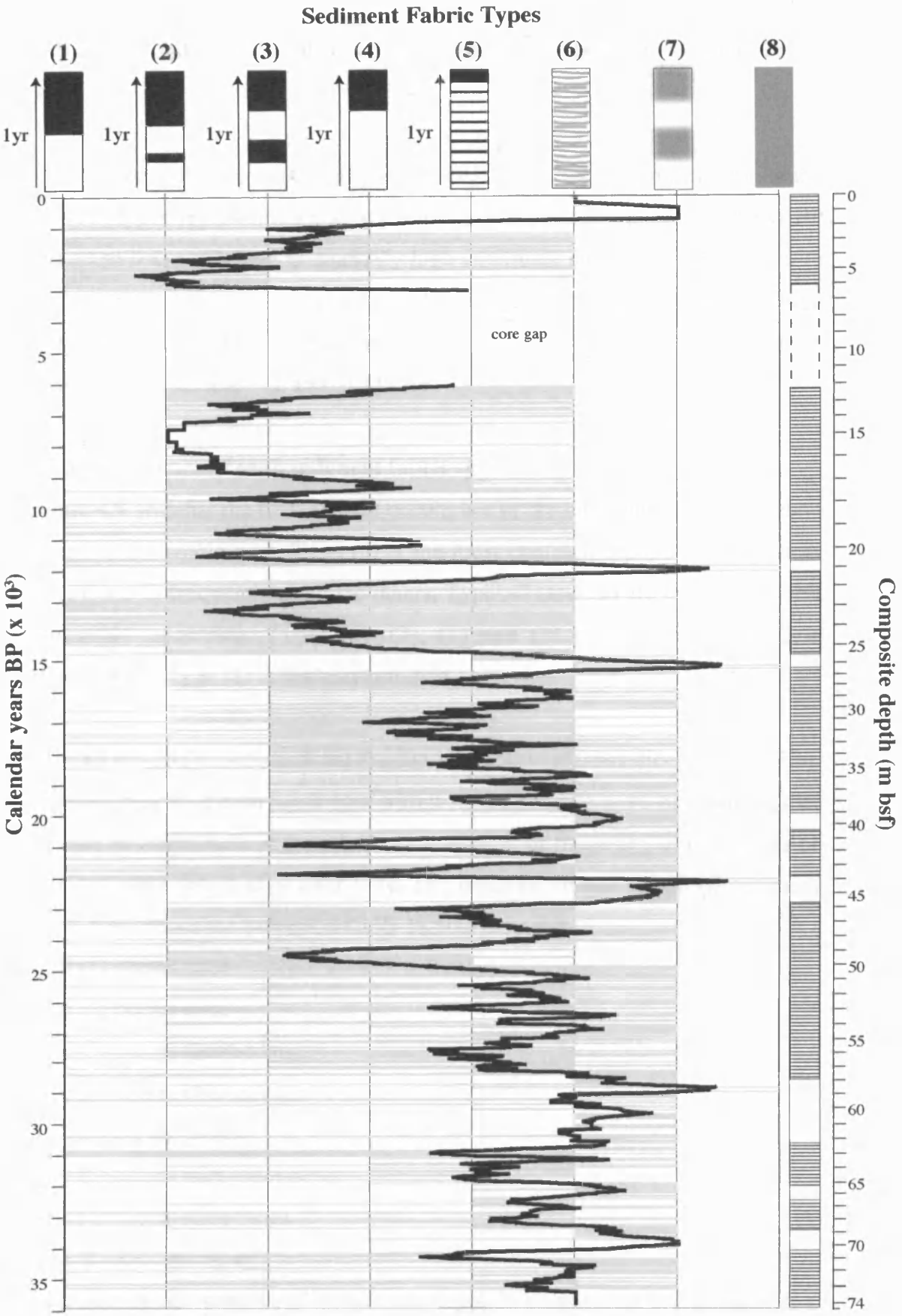


**Figure 4.8:** The sediment fabric index; 1-cm resolution with a 50-point running mean. See Fig. 4.7 for details of sediment fabric types.

~15 kyr BP; and a prolonged period of low seasonality between ~30 and ~28 kyr BP.

**~15 to 0 kyr BP:** The sediment fabric index is relatively low, mostly oscillating between types representing a strong seasonal contrast. From ~15 to ~9 kyr BP and ~3 to 0 kyr BP there is relatively high amplitude change, while from ~9 to ~7 kyr BP there is very low amplitude change and types representing high seasonality. There are two millennial-scale intervals of homogeneous or non-laminated sediment at ~12 and ~1 kyr BP.

### 4.5.3 Occurrence of each sediment fabric type

Figure 4.9 presents the frequency of occurrence of the individual sediment fabric types for the whole core. Type (6) is the most common type, occurring about three times as frequently as all the others. Types (7) and (2) are the second most commonly occurring. Types (5), (3), (1) and (4) occur increasingly less frequently and type (8) is the least common.

Core MD02-2517/2515 has been divided into 250-year time-slices (section 3.6). The occurrences of each fabric type within each time-slice were summed in order to make an assessment of the relative 'abundance' or frequency of occurrence of each sediment fabric type over time. For instance, in the 72 cm of sediment which were deposited between 18,250-18,500 years BP:

Type (1) occurs once
Type (2) occurs once
Type (3) occurs nineteen times
Type (4) occurs twelve times
Type (5) occurs twice
Type (6) occurs thirty-four times
Type (7) occurs three times
Type (8) does not occur.

If the sum of occurrences of an individual type in a time-slice is expressed as a percentage of the total occurrences of all of the types in that time-slice, this represents the relative abundance or frequency of occurrence of that type. In the

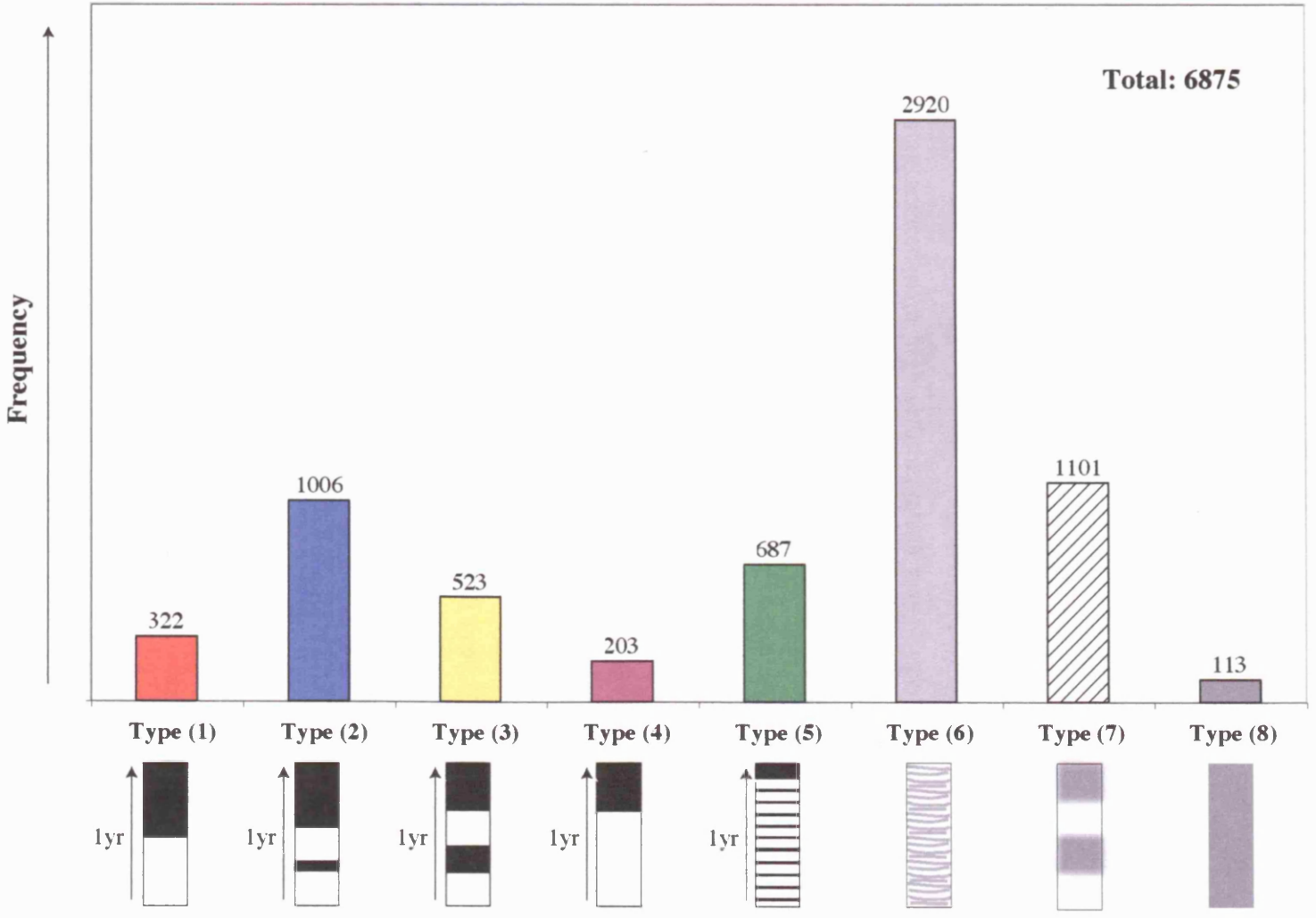


**Figure 4.9:** Frequency of sediment fabric types. See Fig. 4.7 for full details of sediment fabric types.

case outlined above, the sum of occurrences of type (1) equals ~1.5% of the total, type (2) equals ~1.5%, type (3) equals ~25.7%, and so on. This enables a graphic representation to be made of where in the timeline of the core a particular type is most common. Figure 4.10 presents the percentage abundance of each sediment fabric type (in 250-year time-slices) over time.

**Type (1)** occurs throughout the core, but is the typical sediment fabric type of the mid to late Holocene. It occurs in times of low sedimentation rate. **Type (2)** occurs throughout the core and is typical of the Bølling-Alleröd (~15 to 12.5 kyr BP) and the early to mid Holocene. It occurs in times of low sedimentation rate. **Type (3)** features in the mid to late Holocene along with types (1) and (2), but is the typical sediment fabric type between ~22 and 15 kyr BP; otherwise, it rarely occurs. It is associated with high sedimentation rate. **Type (4)** occurs in small numbers throughout the glacial. The peak in the late Holocene may be an artefact of the increased sedimentation rate in the waterlogged top of the core (see also section 6.2.3). Elsewhere, it occurs in times of high sedimentation rate. **Type (5)** is the typical sediment fabric type between ~36 and 22 kyr BP. It features in the Bølling-Alleröd (~15 to 12 kyr BP) and at ~8 kyr BP, but, apart from this, it is without analogue in the mid to late Holocene. It occurs in times of high sedimentation rate. **Type (6)** is the most common type during the glacial. Its relative abundance falls at ~15 kyr BP, but it remains quite common up to ~10 kyr BP. After this, it occurs sporadically. Although type (6) is most common during times of high sedimentation rate, it also occurs with less frequency during times of lower sedimentation rate. **Type (7)** occurs commonly during the glacial, but rarely after ~15 kyr BP. Its relative abundance falls after ~14 kyr BP and it occurs sporadically up to ~11 kyr BP. This type does not occur during the Holocene. It is associated exclusively with times of high sedimentation rate. **Type (8)** occurs only four times throughout the length of core MD02-2517/2515: at ~29 kyr BP, at ~22.5 kyr BP, at ~15.5 kyr BP and ~12.5 kyr BP. It is associated exclusively with times of high sedimentation rate.

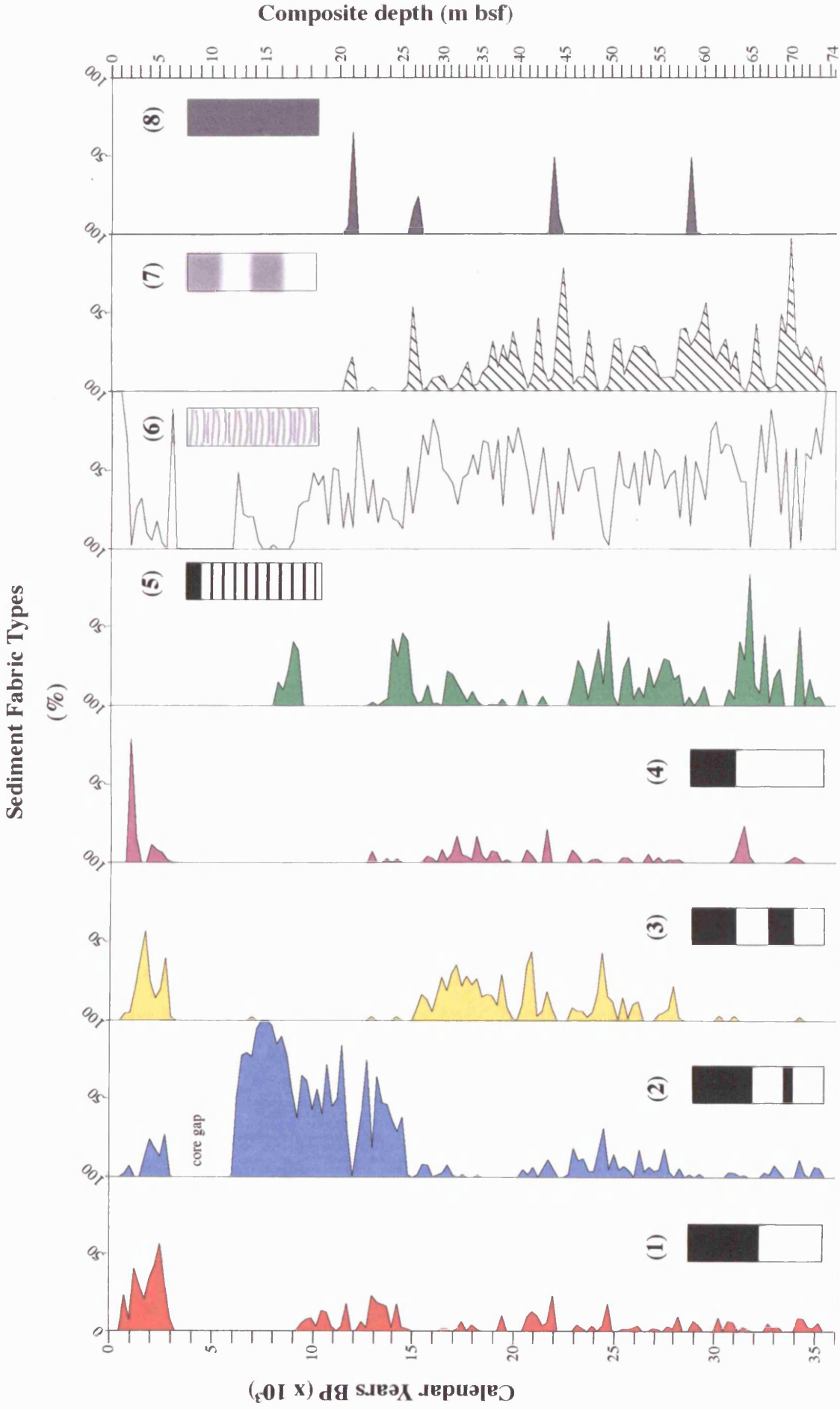


**Figure 4.10:** The relative abundance of sediment fabric types through time.

### 4.5.4 Sedimentation zones

The sediment fabric index, the relative abundance of sediment fabric types and sedimentation rate are compared in Figure 4.11. The core has been divided into sedimentation zones based on long-term cyclical alternations in the rate of change.

In the sediment fabric index there are alternating ~5000-year periods of long-term stability (relatively low-amplitude, high-frequency change) and long-term instability (relatively high-amplitude, low-frequency change) with boundaries at ~30.8, 25.1, 19.7, 14.8 and 9.2 kyr BP. The occurrence of the varved sediment fabric types suggests that divisions of ~2500 and ~1000 years could also be made. The occurrence of non-laminated sediment fabric types indicates that the sequence can be divided into ~5000-year segments with boundaries at ~34, ~28, ~22.5, ~15.5 and 11.5 kyr BP.

The colours used in the graphic presentation of the sediment fabric types show that the predominance of either one or a combination of two types changes over time. Types (5) and (1) dominate between ~36-28 kyr BP; types (5) and (2) between ~28-22.5 kyr BP; all types occur between ~22.5-15 kyr BP, but type (3) is predominant; type (2) features between ~15-6 kyr BP; and types (1) and (3) between ~3-0 kyr BP.

***~36-30.8 kyr BP***

This zone is characterised by low-frequency change in the sediment fabric index, and medium to very high sedimentation rates. For the majority of the zone, the sediment fabric types are diffusely laminated or non-laminated. The varved sediment fabric types are predominantly type (5). The subordinate types are (1) and (2) before the non-laminated interval which occurs between ~34.3 and 33.6 kyr BP and (1) and (4) afterwards.

***~30.8-25.1 kyr BP***

This zone is characterised by high-frequency change in the sediment fabric index, and very variable sedimentation rates.

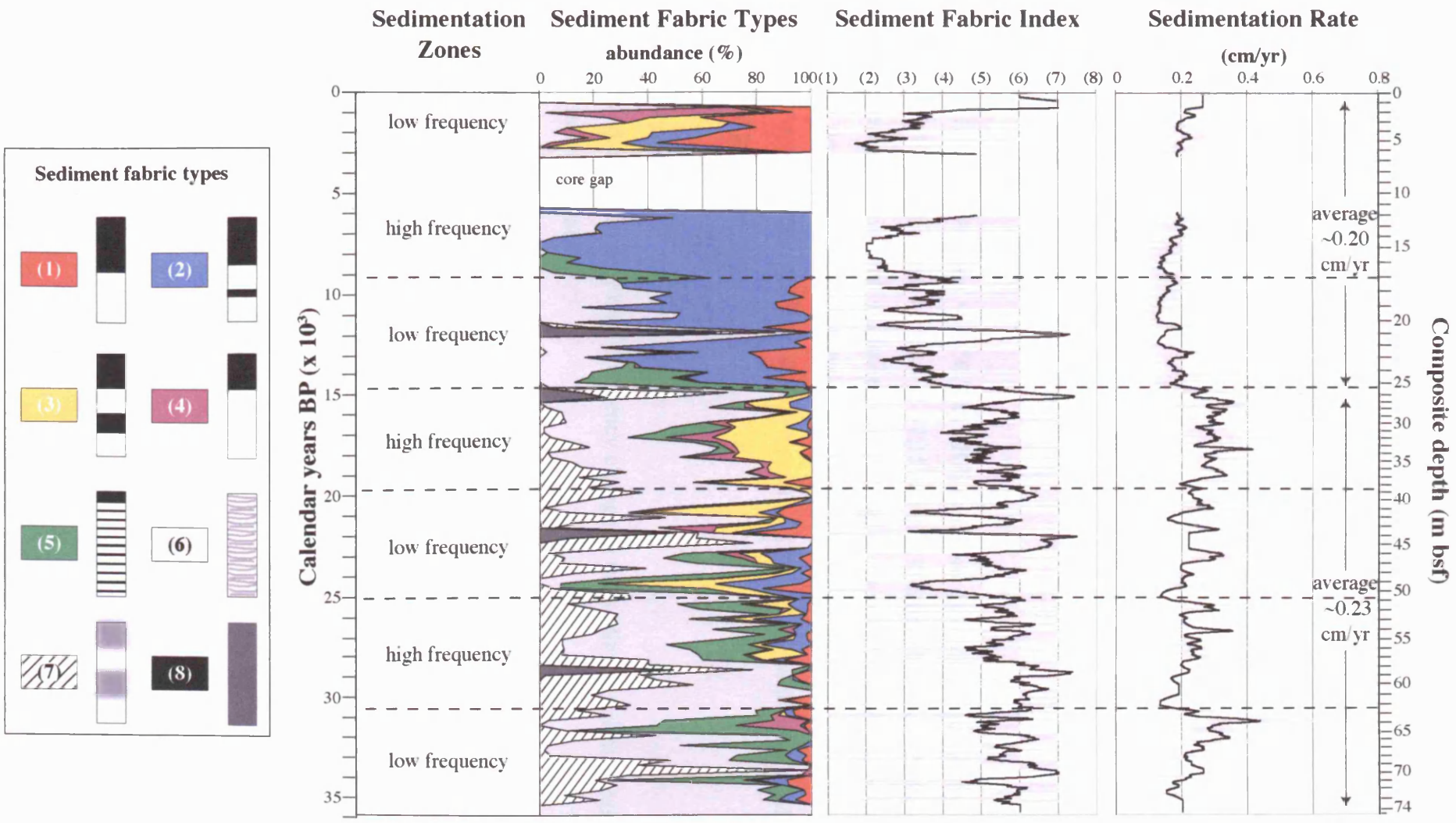


**Figure 4.11:** Sedimentation zones. The comparison of sedimentation rate, the sediment fabric index and the relative abundance of sediment fabric types reveals a ~5000-year alternation in the rate of change.

The predominantly non-laminated interval between ~31 and 28 kyr BP features brief episodes of varved sediment types (5) and (1), and ends with a homogeneous interval. After this, switching between varved sediment types is very rapid; the two most frequent types are (5) and (2), with subordinate amounts of (3) and (1).

***~25.1-19.8 kyr BP***

This zone is characterised by low-frequency change in the sediment fabric index and in sedimentation rates.

Like the sedimentation zone ~36-30.8 kyr BP, this zone is divided in two by a non-laminated/homogeneous interval at ~22.5 kyr BP. Before the interval, there are two 'peaks' of varved sediment consisting of types (5) and (2) with subordinate amounts of type (3) and (1). After ~22.5 kyr BP, there are two 'peaks' of varved sediment consisting of types (1), (3) and (4) with very small amounts of types (2) and (5).

***~19.8-14.9 kyr BP***

This zone is characterised by high-frequency change in the sediment fabric index and in sedimentation rates.

This rapidity of change is also seen in the varved sediment types. The majority of the interval between ~20 and 18 kyr BP is diffusely laminated or non-laminated and the relatively rare varved sediment types are a combination of types (3) and (4). Between ~18 and 16.5 kyr BP, types (3) and (5) dominate, with subordinate amounts of types (4) and (2). After this, sediment fabric is predominantly diffusely laminated with small amounts of varved types (2), (3) and (5). The zone ends with an interval of homogeneous sediment at ~15.5 kyr BP.

***~14.9-9.2 kyr BP***

This zone is characterised by low-frequency change in the sediment fabric index and low sedimentation rates.

Like the two other high-amplitude, low-frequency zones, this zone is divided into two by a homogeneous interval at ~12 kyr BP. The occurrence of non- or diffusely laminated sediment is much less than in any previous zone. Between ~15 and 12 kyr BP, the varved sediment fabric types are (5) and (2), which switch to (2) and (1) after ~13 kyr BP. After the homogeneous interval, the dominant varved sediment type is (2) with lesser amounts of type (1).

***~9.2-0 kyr BP***

There is no information about the stratigraphic gap between the cores, but the change in cyclicity below and above the gap suggests that another zone boundary could be placed at ~4 kyr BP. The lower part of the present zone (~9.2 to 6 kyr BP) is characterised by high-frequency change in the sediment fabric index and low sedimentation rates. The upper part of the zone (~3 to 0 kyr BP) is characterised by low-frequency change in the sediment fabric index and rising sedimentation rates.

The varved sediment fabric type (2) is predominant from ~9.2 to 6 kyr BP, with a brief interval of type (4) between ~9.1 and 8.6 kyr BP. After ~7 kyr BP there are frequent episodes of sediment fabric type (6) in a time of rising sedimentation rates. After the stratigraphic gap, sediment fabric types (1) and (3) dominate with subordinate amounts of (4) and (2). At ~3 kyr BP there is an interval of predominantly type (3). After this, types (1) and (4) dominate.

# Chapter 5 Geochemistry Results and Climate Proxies

## 5.1 Introduction

The age-depth relationship and the high-resolution sediment fabric analyses have provided a framework for core MD02-2517/2515. The geochemical analyses presented in this chapter identify and quantify sediment component flux. From this, climate proxies can be established which constrain and clarify the conditions prevailing during deposition of each sediment fabric type and, hence variations in the processes that bring them into Guaymas Basin. The semi-quantitative high-resolution continuous scan data are calibrated against the low-resolution data, which allows the calculation of accumulation rates for all of the sediment component fluxes. The geochemical data are in Appendix III (on CD).

## 5.2 Calibration of semi-quantitative data

### 5.2.1 Low-resolution XRF data

The results of the conventional XRF analysis of discrete samples from core MD02-2515 are shown in Figure 5.1a and b, with the sedimentation zones (Section 4.5.4; Fig. 4.11) and major laminated intervals. The data are at ~50 cm spacing.

The majority of the geochemical species display the ~5000-year alternations in the frequency of the rate of change seen in the sediment fabric results (section 4.5.4; Fig. 4.11). The exceptions are CaO, MgO, Sr, $SO_3$, Co and Mo, all of which exhibit relatively high-amplitude, low-frequency change throughout the core.

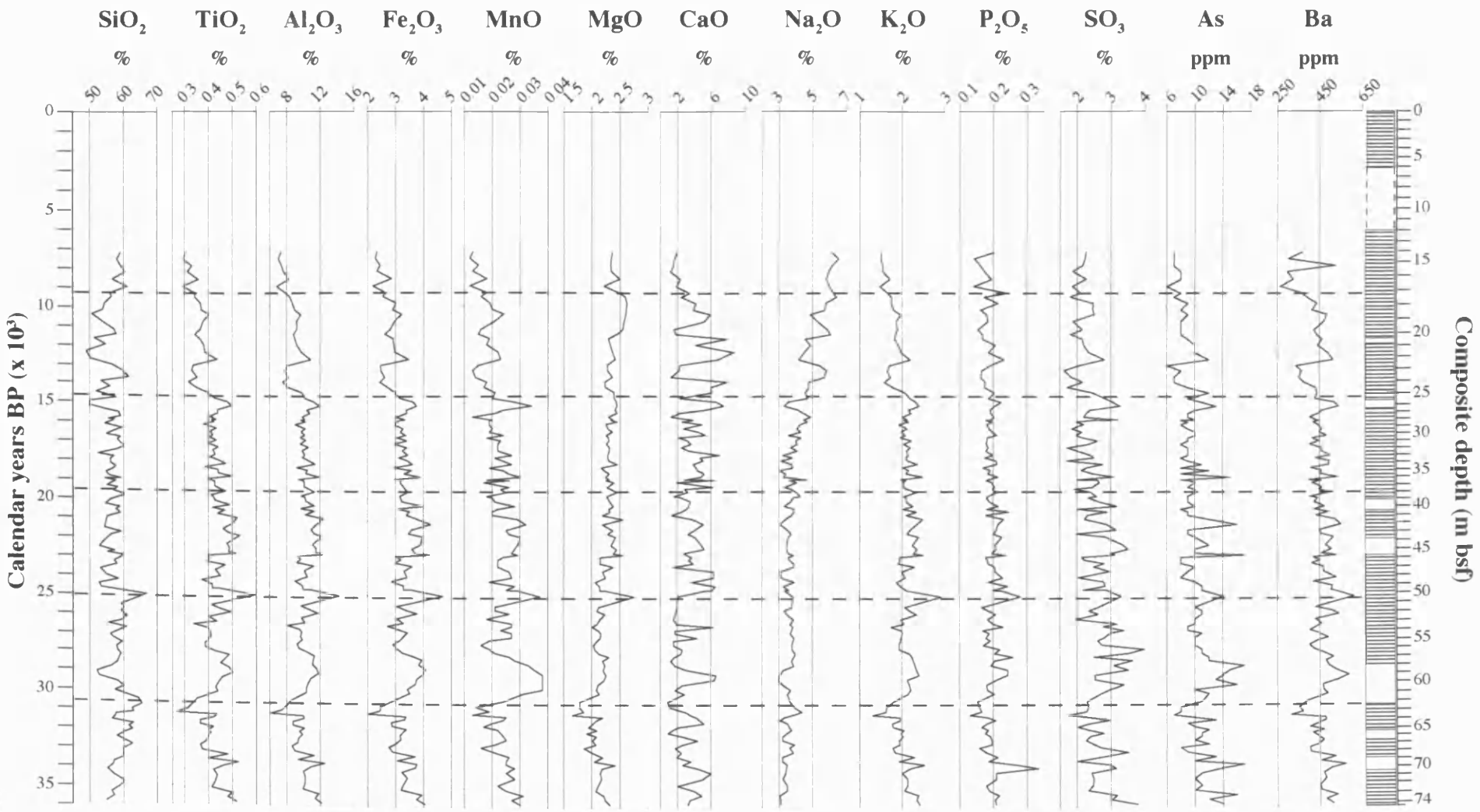


**Figure 5.1a:** Concentration data from the conventional XRF analysis of discrete samples. Resolution is ~50-cm; sedimentation zones as in Fig. 4.11; major laminated intervals are shown on the right.

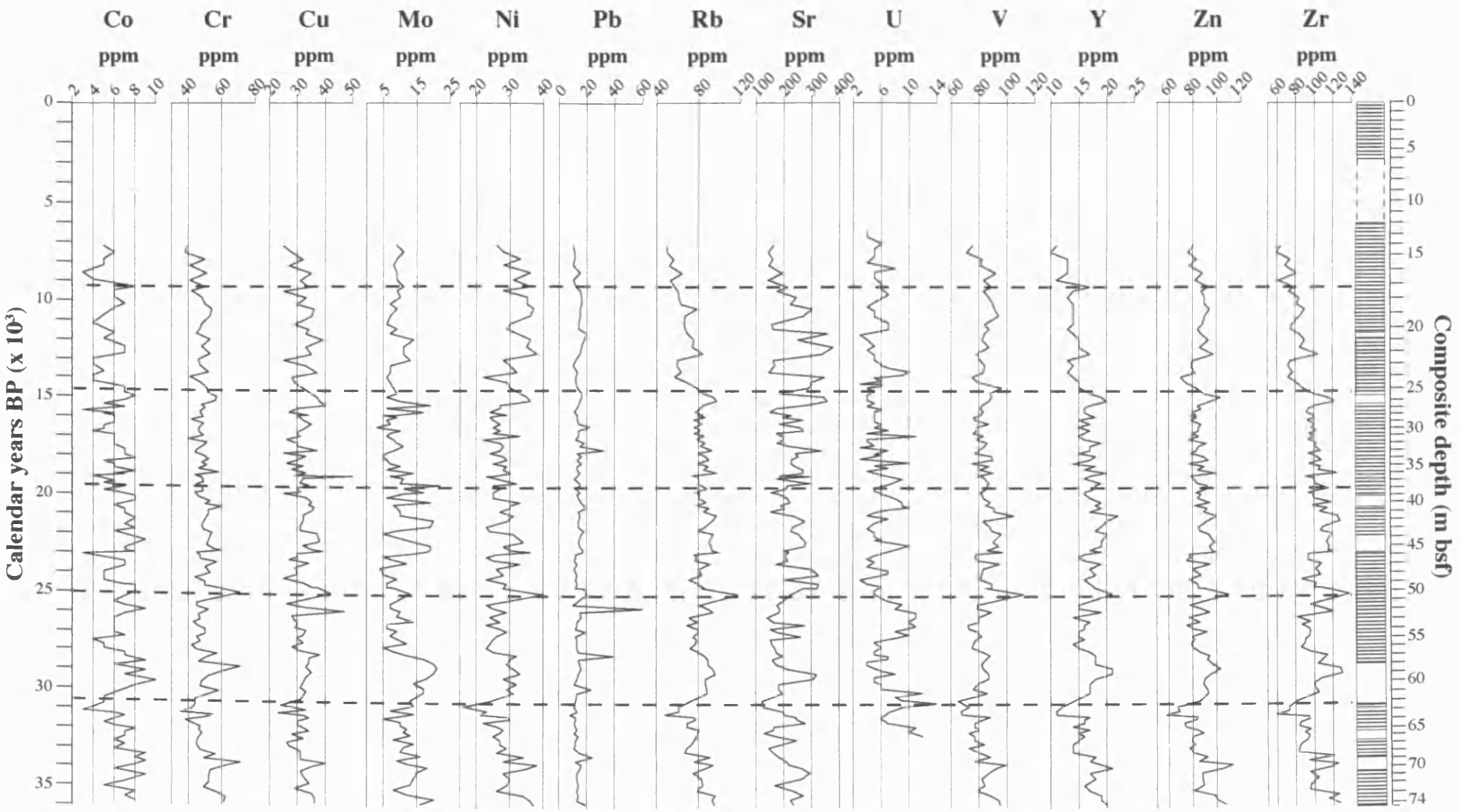


**Figure 5.1b:** Concentration data from the conventional XRF analysis of discrete samples. Resolution is ~50-cm; sedimentation zones from Fig. 4.11; major laminated intervals are shown on the right.

### 5.2.2 Colour data

The semi-quantitative colour data are presented in Figure 5.2. The sedimentation zones (section 4.5.4) and major laminated intervals are also shown. These data are at 2-cm resolution and a 25-point running mean has been applied. At this resolution, the smoothing averages ~50 cm of sediment and, depending on sedimentation rate, ~250 years.

Except for the interval between ~30.8 and 25.1 kyr BP, L*, a* and b* follow the high-amplitude/low-frequency, low-amplitude/high frequency alternation between sedimentation zones seen in the sediment fabric results (section 4.7). From ~30.8 to 25.1 kyr BP, L* and b* display high-amplitude, low frequency change. All three parameters show long-term trends through the core. L* jumps towards darker sediment at ~12 kyr BP; a* becomes abruptly redder at ~15 kyr BP; b* becomes less blue at ~20 kyr BP.

The correlation with the low-resolution XRF data is shown in Figure 5.3 (for method see section 3.5.1). The Pearson product-moment correlation coefficient ('r') has been calculated in order to measure of the tendency of the two variables to increase or decrease together (the covariance of the two variables is divided by the product of their standard deviations). The coefficient ranges from –1 to 1, where 1 is a perfect positive relationship and –1 is a perfect negative relationship; a value of 0 shows that there is no linear relationship between the variables. In the measurement of natural systems, results of 0.5 and above are considered good (Dean & Anderson, 1974).

The Pearson correlation coefficients for L* and $SiO_2$ + $CaCO_3$, and b* and $SiO_2$ + $CaCO_3$ are very low and therefore it is assumed that the TOC-rich sediment has diluted the L* and b* values. There is a strong positive correlation between a* and TOC, and between a* and $Fe_2O_3$, but these parameters have been measured directly and conversion of the a* values is not necessary. b* data were also plotted against the low-resolution $Al_2O_3$ data, which produced a low negative Pearson coefficient of -0.2.

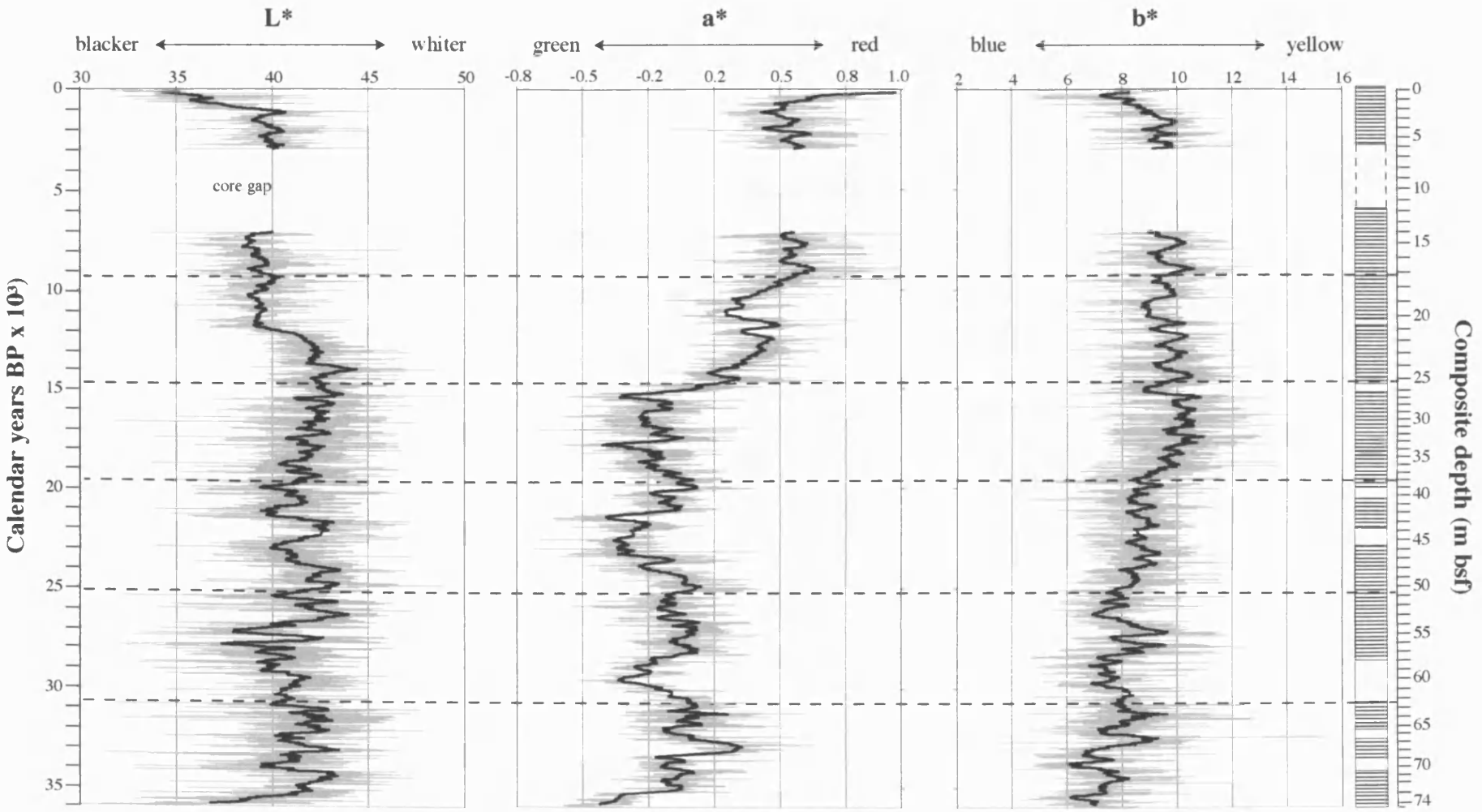


**Figure 5.2:** Semi-quantitative colour results. 2-cm resolution with 25-point running average. Sedimentation zones and major laminated intervals are also shown.

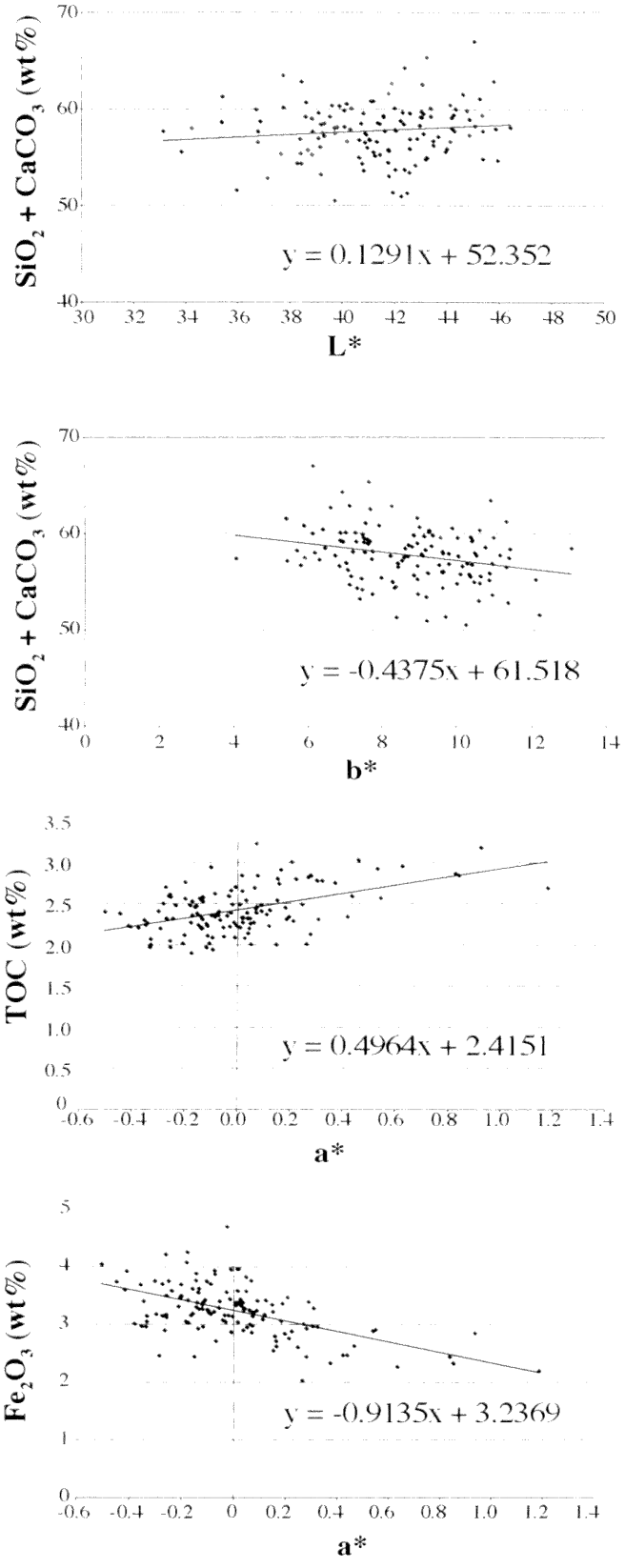


**Figure 5.3:** Discrete XRF mineral data plotted against continuous 2-cm resolution colour data at the same sample depths.

| Parameter | Correlation | Calibration equation | N | r |
|---|---|---|---|---|
| **L*** | $SiO_2 + CaCO_3$ | y = 0.291x + 52.352 | 131 | 0.12 |
| **b*** | $SiO_2 + CaCO_3$ | y = -0.4375x + 61.518 | 131 | 0.27 |
| **a*** | $Fe_2O_3$ | y = -0.9153x + 3.2369 | 131 | 0.55 |
| **a*** | TOC | y = 0.4964x + 2.4151 | 131 | 0.50 |

**Table 5.1:** The linear regression equations resulting from plotting the semi-quantitative colour data against the quantitative geochemical data.

### 5.2.3 Continuous XRF data

The semi-quantitative continuous XRF data are presented in Figure 5.4, with the sedimentation zones (section 4.5.4) and major laminated intervals. The data are at 1-cm resolution and a 50-point running mean has been applied. In addition to the elemental data presented here, the analysis measured copper and strontium, but the results for these were below the reliability limits of the scanner and have not been included. The manganese curve is often close to and sometimes below the limits of the scanner, which makes the results noisy, but the majority of the data are within reliable limits.

Except for Ca, the concentration data exhibit the ~5000-year alternations in rate of change seen in the sediment fabric results (section 4.5.4). Ca displays large amplitude of change from ~36 kyr BP until ~12 kyr BP, after which the curve is similar to those of the other elements.

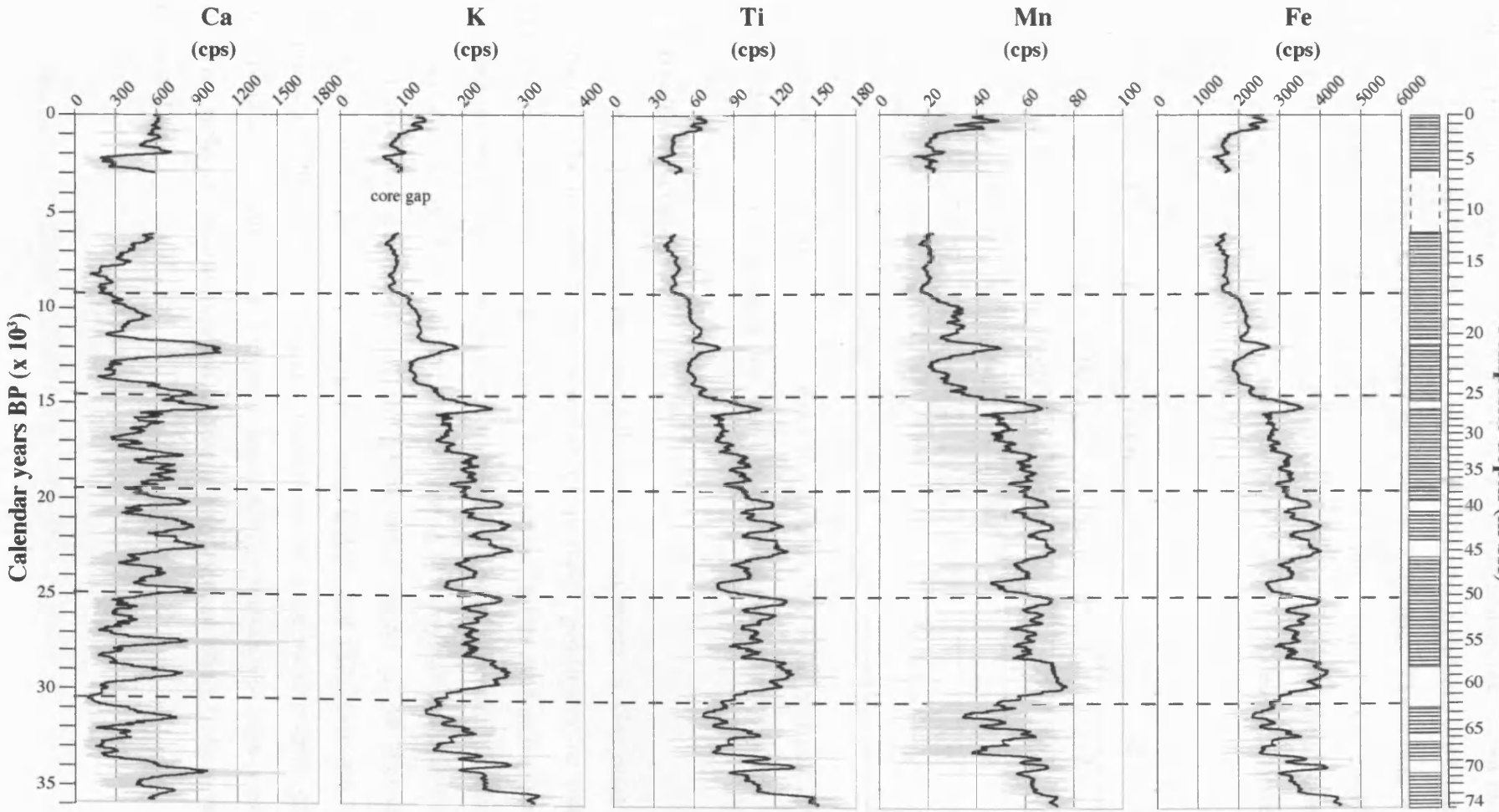


**Figure 5.4:** Concentration data from the continuous XRF scan. 1-cm resolution with a 50-point running mean; sedimentation zones from Fig. 4.11; major laminated intervals are shown on the right.

The semi-quantitative XRF data have been assessed against the quantitative XRF data to produce a calibration set (section 3.5.1). The results are shown in Figure 5.5. Using the same sample depths, the element intensities from the continuous XRF scan have been plotted against the discrete XRF data. The spread is small between K and $K_2O$, Ti and $TiO_2$, Mn and MnO, and Fe and $Fe_2O_3$, but is wider between Ca and $CaCO_3$. A linear regression through each of the datasets has been used to calculate the calibration equations. The Pearson correlation coefficient ('r') is 0.5 or higher in all cases.

| **Mineral** | **Calibration equation** | **N** | **r** |
|---|---|---|---|
| $K_2O$ | y = 0.0031x + 1.4382 | 132 | 0.71 |
| $CaCO_3$ | y = 0.0006x + 0.1905 | 129 | 0.50 |
| $TiO_2$ | y = 0.0014x + 0.2869 | 132 | 0.69 |
| MnO | y = 0.0002x + 0.0123 | 132 | 0.66 |
| $Fe_2O_3$ | y = 0.0005x + 1.758 | 132 | 0.78 |

**Table 5.2:** The equations used to calibrate the XRF element intensity data; y is the converted data and x is the elemental intensity in cps.

## 5.3 Biogenic proxies

The biogenic proxies are the autochthonous components in Guaymas Basin sediment, which reflect the response of primary producers to nutrient-availability, modulated by variations in preservation factors such as bottom water ventilation. In this case, the proxies comprise the assemblage and abundance of the ecologically significant diatom species living in Guaymas Basin at the time the sediment was deposited, and the geochemical signal of the skeletal and organic remains of all species (biogenic silica, $CaCO_3$ and TOC). Mo and V have affinities with the amount of organic matter/anoxia in the water column (section 3.5.2) and are included here. Magnetic susceptibility responds to high runoff and therefore reflects conditions when organic matter is most likely to be deposited (section 2.8).

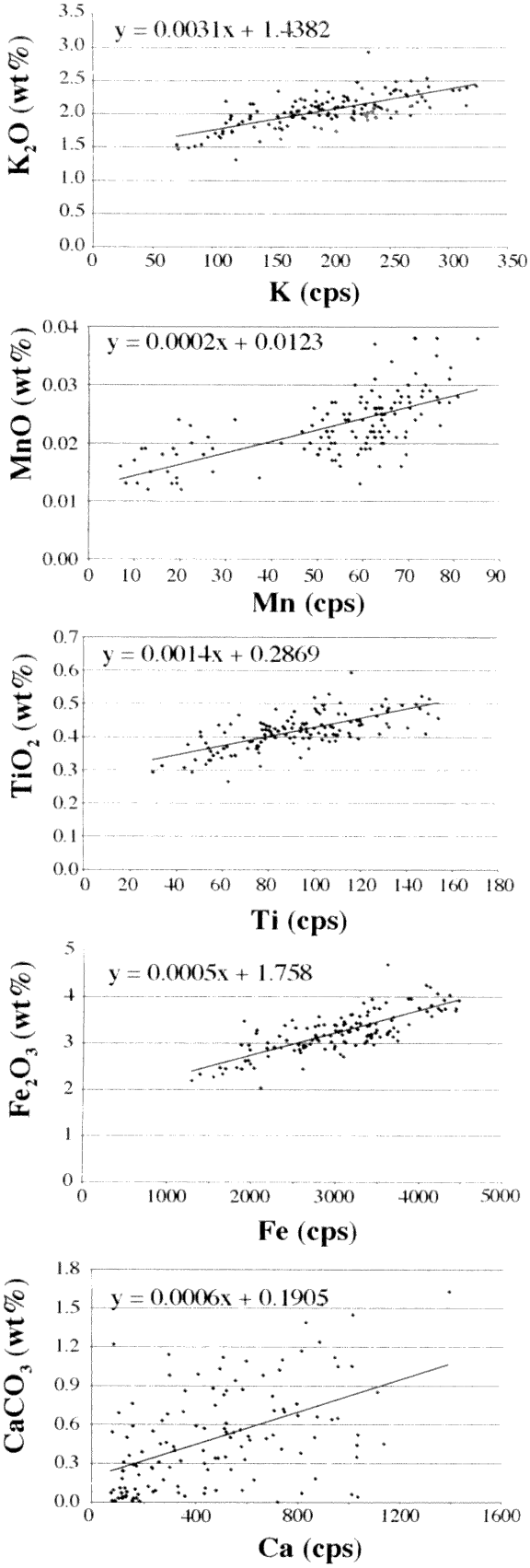


**Figure 5.5:** Discrete XRF wt% mineral data plotted against continuous XRF elemental intensities (cps) at the same sample depths.

Some land-derived organic matter is brought into the Gulf by fluvial transport. However, with the exception of homogeneous intervals, marine organic matter always exceeds terrestrial (Simoneit, 1991). The ratio of autochthonous to allochthonous organic matter varies with the rate of autochthonous productivity, runoff and terrigenous productivity.

### 5.3.1. Microfossils

The ecologically significant diatom species (discussed in section 2.10) were identified from the smear slides using the SEM images of single species in Pike (1996). The some of the less frequently occurring microfossils are presented in Figure 5.6 (a-d). The less common diatom species have been identified using Tomas (1996) as the reference; all are tropical/warm water species. Other microfossils have been identified using Lipps (1993) as the reference. Silicoflagellates, which are relatively abundant in some samples, are a component of upwelling blooms (eg Barron *et al.*, 2004; 2005). Radiolaria and foraminifera are zooplankton; the ones seen in the smear slides are undoubtedly juveniles.

In general, coccoliths comprise <5% of the microfossil assemblage. Dissolution in the water column may be a factor contributing to their sparsity (eg Sancetta, 1995; Thunell, 1998, Ziveri & Thunell, 2000). The species most commonly seen in the smear slides are *Gephyrocapsa oceanica* and *Helicosphaera carteri*; both are low latitude species. *G. oceanica* is tolerant of a wide range of salinities and prefers high nutrient levels; it is the typical species of low latitude upwelling areas (Winter, 1994).

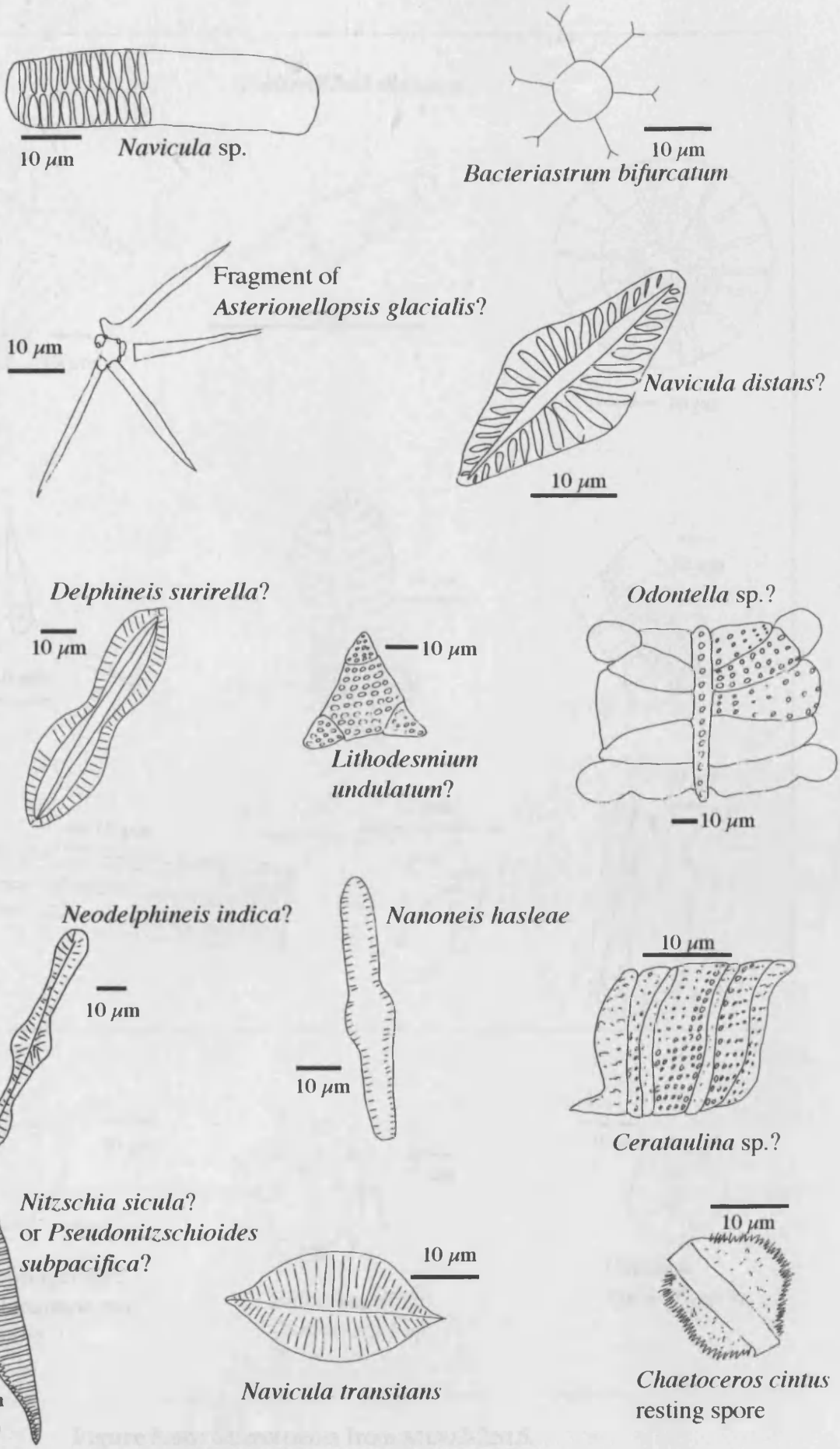


Figure 5.6a: Less common diatoms from MD02-2515.

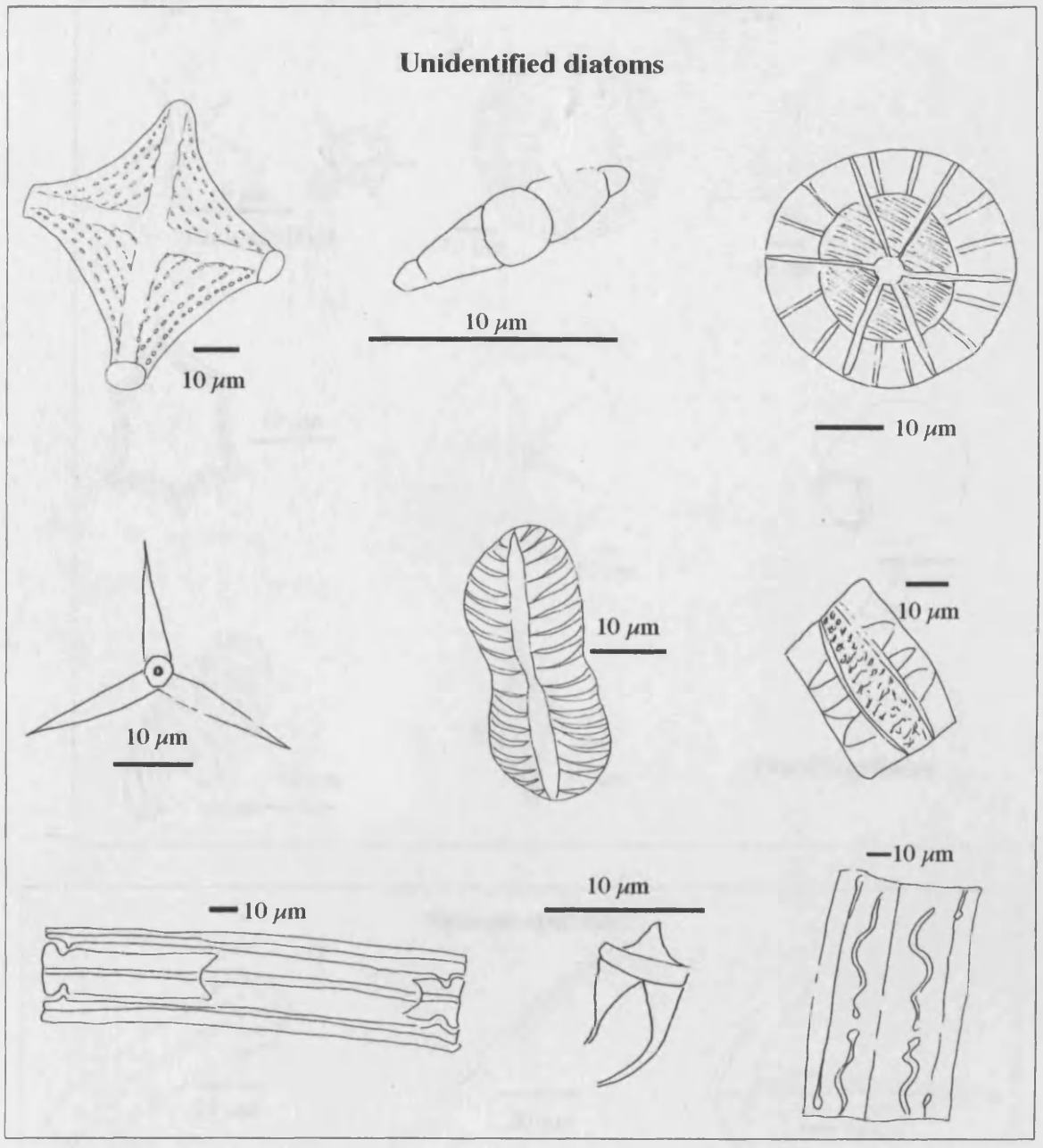


**Figure 5.6b:** Microfossils from MD02-2515.

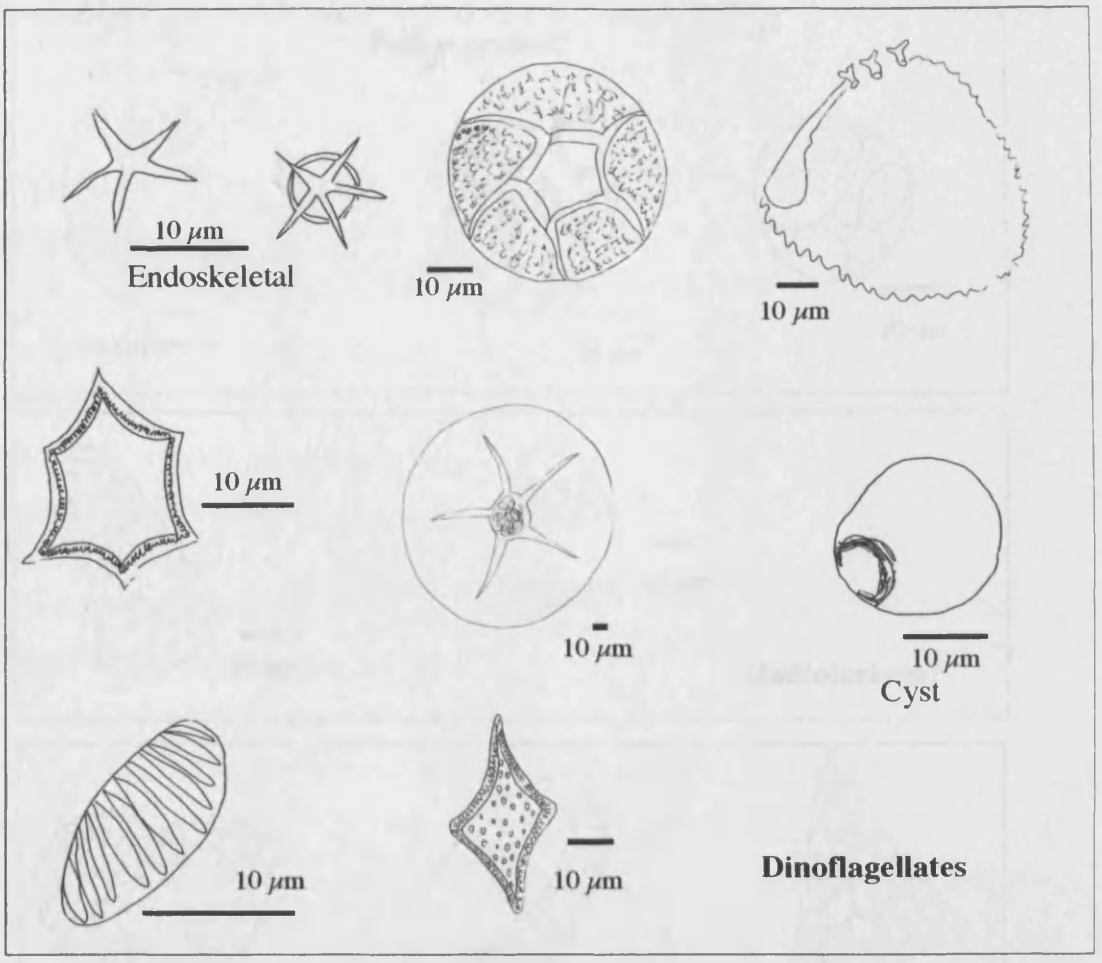


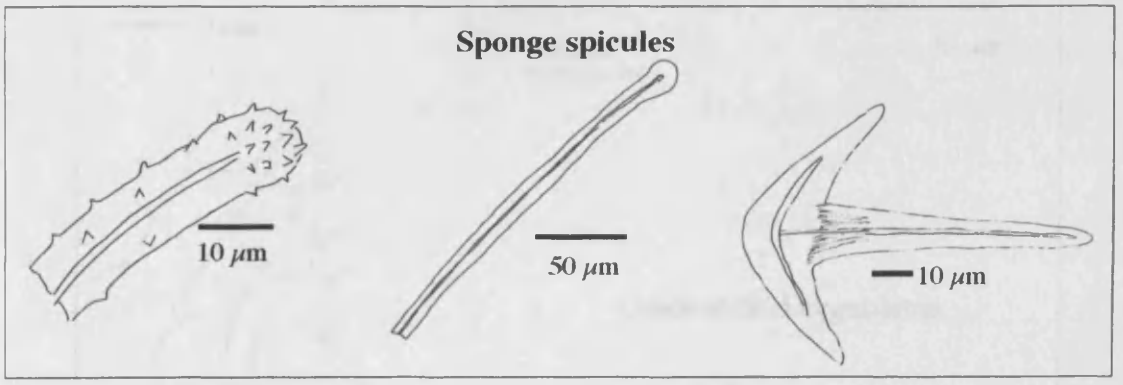


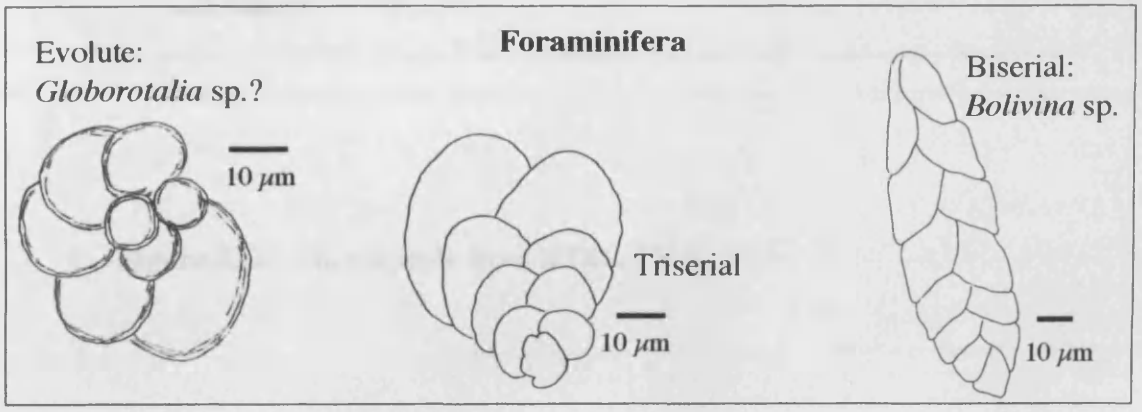


**Figure 5.6c:** Microfossils from MD02-2515

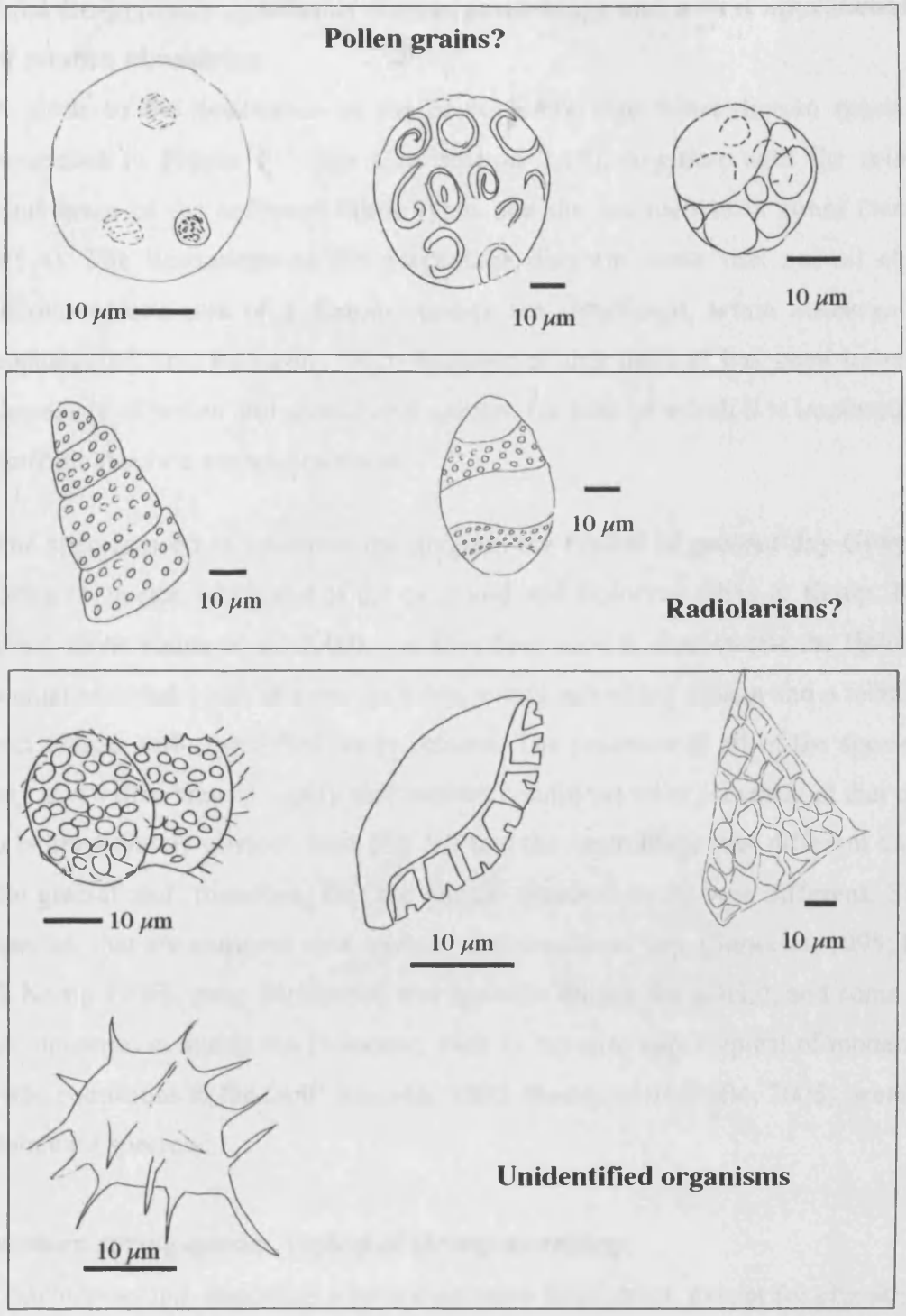


**Figure 5.6d:** Microfossils from MD02-2515.

### 5.3.2 Ecologically significant diatom assemblage and a first approximation of relative abundance

A guide to the occurrence of the ecologically significant diatom species is presented in Figure 5.7 (see also section 2.10), together with the relative abundance of the sediment fabric types and the sedimentation zones (section 4.5.4). The limitations of the percentage diagram mean that not all of the increases/decreases of a diatom species are significant, while absences and appearances are. However, the robustness of this method has been tested on thousands of pollen and nannofossil spectra, for both of which it is impossible to perform absolute abundance counts.

The species used to construct the diagram are typical of present-day Guaymas Basin (Sancetta, 1995) and of the early and mid Holocene (Pike & Kemp, 1996, 1997, 1999; Kemp *et al.*, 2000), and have been used to characterise the Holocene annual seasonal cycle as a two-part dry, windy upwelling season and a relatively wet season with a stratified water column. The presence of all of the species at any given time should signify that modern conditions were prevalent at that time. It is immediately obvious from Fig. 5.7 that the assemblage was different during the glacial and, therefore, that the annual seasonal cycle was different. Some species, that are common now, such as *Coscinodiscus* spp. (Sancetta, 1995; Pike & Kemp 1996), were uncommon and sporadic during the glacial, and some that are uncommon during the Holocene, such as *Azpeitia* spp. (typical of modern El Niño conditions in the Gulf; Sancetta, 1995; Barron *et al.*, 2004; 2005), were the dominant species.

**Modern spring species, typical of strong upwelling:**

*Chaetoceros* spp. maintains a strong presence throughout, except for absences at ~28 and ~18.5-15.5 kyr BP, implying that, except for these times, high levels of nutrients were available in surface waters at some time during the year. *Actinoptychus* spp., on the other hand, are strongly present when *Chaetoceros* spp. are absent or low. These are known to be shelf species resuspended during the turbulence of upwelling (Pike, 1996). Their occasional inverse relationship with *Chaetoceros* spp. may be indicative of general storminess rather than

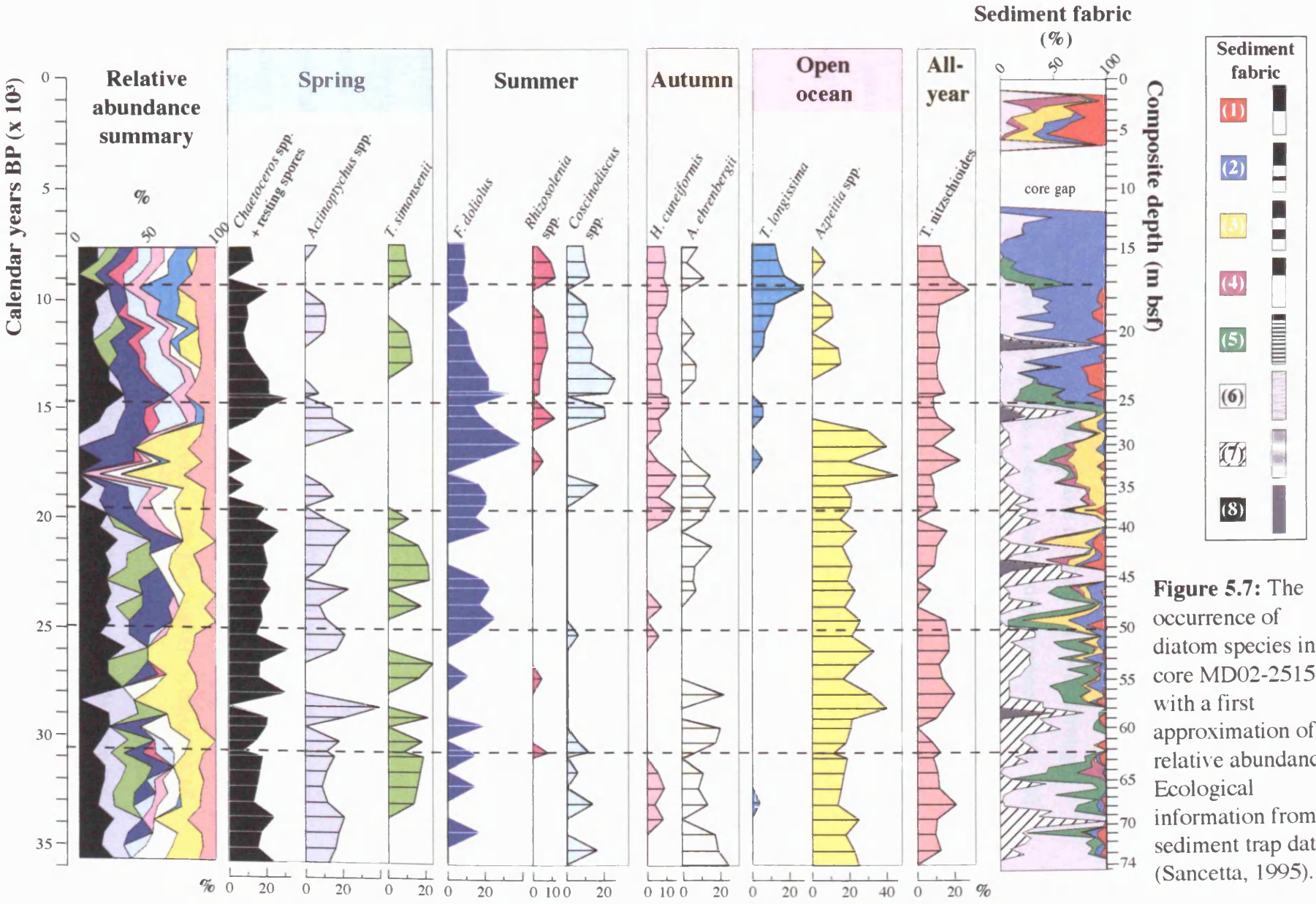


**Figure 5.7:** The occurrence of diatom species in core MD02-2515, with a first approximation of relative abundance. Ecological information from sediment trap data (Sancetta, 1995).

seasonal upwelling. Peaks of *Actinoptychus* spp. coincide with major non-laminated intervals and sediment fabric types (7) and (8). Peaks of *T. simonsenii* typically coincide with occurrences of sediment fabric types (1) and (2). Its abundance is low or it is absent during non-laminated intervals and occurrences of types (3) and (5).

**Modern summer species typical of a stratified water column:**

During the glacial, *F. doliolus* is sporadic and has most affinity with strongly laminated intervals. *Rhizosolenia* spp. has a semi-continuous presence from ~16 kyr BP onwards; before this, it is briefly present at ~30.5, ~17 and ~15 kyr BP. *Coscinodiscus* spp. has sporadic occurrences ~35–30 kyr BP and is then very nearly absent until ~15 kyr BP. This contrast with the present day implies that the summer season stratified water column generally did not develop during the glacial.

**Modern autumn overturn species:**

Until ~20 kyr BP, *H. cuneiformis* is mostly absent, with sporadic occurrences ~33-31 and ~25-23.5 kyr BP, after this it is almost continuously present. *A. ehrenbergii* is present in higher abundances and more continuously than *H. cuneiformis* ~35-27 kyr BP, after this it is at best sporadic. The non-occurrence of stratification during the glacial would disadvantage these species, which reproduce quickly during overturn to avoid over-predation.

**Modern open ocean species:**

*T. longissima* is revealed as an indicator of modern conditions. Though only present in the Gulf interannually during the Holocene (Pike & Kemp, 1997), presumably when summer heat in the tropics is sufficient to generate strong enough tropical storms, these conditions evidently very rarely occurred during the glacial, with the exception of ~33, ~17 and ~15 kyr BP. The occurrence of *Azpeitia* spp. throughout the glacial coincides with the higher occurrence of sediment types (6) - diffuse laminae most probably the result of less anoxic conditions - (7) and (8) – non-laminated sediment. If the Trade Winds were not

continuously operative at ~23°N, then subthermocline waters entering the Gulf would be better ventilated than those entering at present and so productivity levels in Guaymas Basin would have to be much higher in order to maintain the same preservation factors at Site MD02-2517/2515. Additionally (or alternatively), if the North Pacific Subtropical High did not migrate past Guaymas Basin, then seasonality there would be non-existent and the sediment would be homogeneous regardless of productivity rates and preservation factors.

**Modern all-year-round species:**

*T. nitzschioides* is present throughout the glacial. Lows coincide with non-laminated intervals and highs with peaks of sediment type (5).

### 5.3.3 Geochemical biogenic proxies

The accumulation rates of the biogenic proxies are presented in Figure 5.8 and are shown together with the sedimentation zones and the relative abundance of sediment fabric types. The accumulation rates were calculated using equations 3.1, 3.2 and 3.3 (section 3.3.2).

***~36-30.8 kyr BP***

At the base of the zone during the non-varved interval, magnetic susceptibility, V and Mo are high (4 s.u., 0.04 and 0.008 g/cm$^2$/yr respectively) compared to TOC, $CaCO_3$ and biogenic silica. At ~33.5 kyr BP, during the prominent peak of sediment fabric type (7), all biogenic proxies rise. At ~31.5 kyr BP, all the components except magnetic susceptibility are at their highest accumulation rates for the entire core (0.09, 0.03, 0.005 and 0.45 g/cm$^2$/yr respectively) during the prominent peak of sediment type (6) at the top of the zone.

***~30.8-25.1 kyr BP***

All of the biogenic proxies are low (-1 s.u., 0.02, 0.01, 0.004, 0.001 and 0.1 g/cm$^2$/yr respectively) at the base of the zone during the non-laminated/non-varved interval. During the homogeneous episode at ~29 kyr BP, all components except biogenic silica are high or rising (2 s.u., 0.04, 0.015, 0.01, 0.002 and 0.01 g/cm$^2$/yr respectively). V, Mo and biogenic silica are high compared to the other components during varved intervals for the rest of the zone.

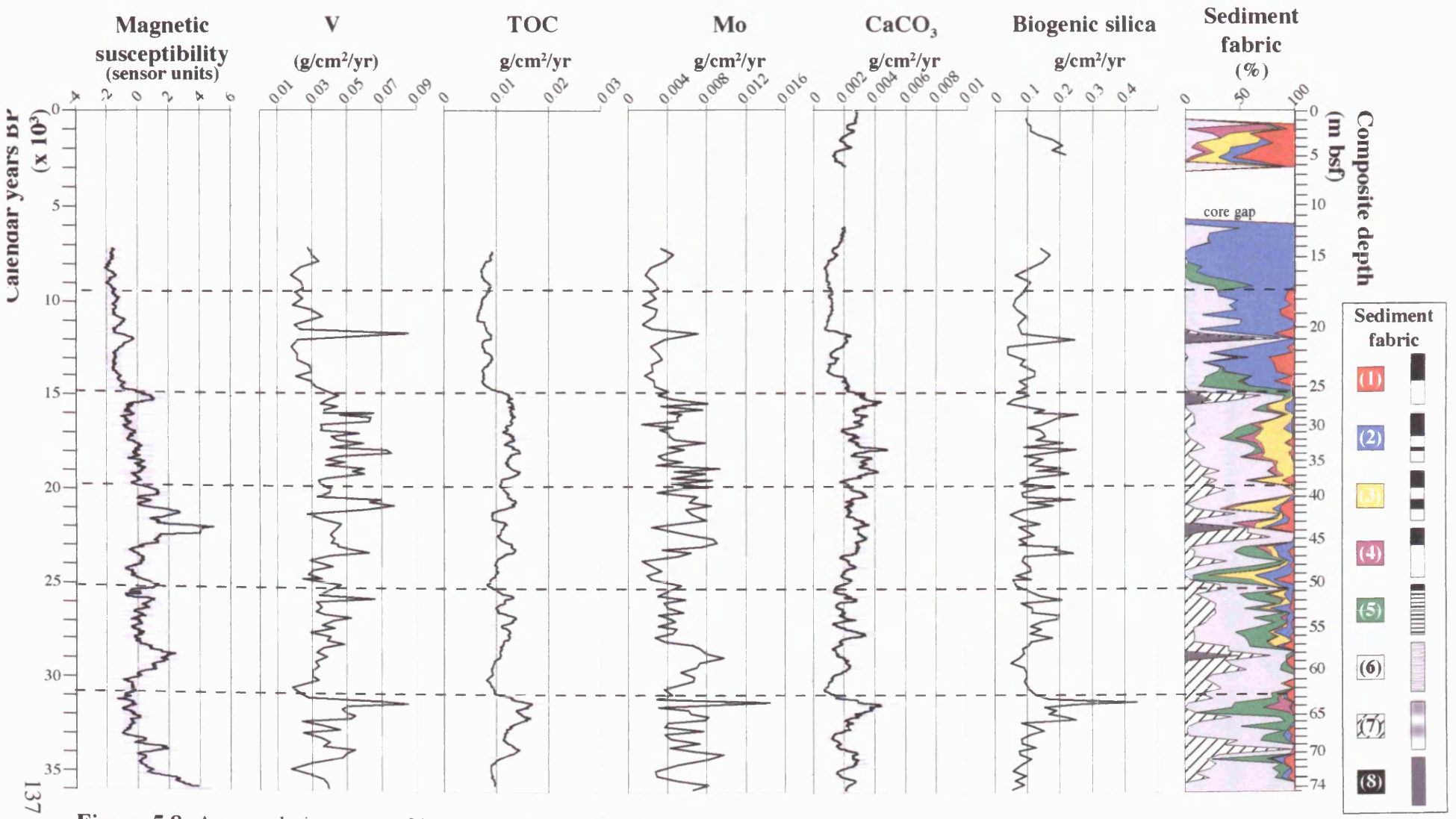


**Figure 5.8:** Accumulation rates of biogenic proxies. TOC is AMS data.

***~25.1-19.8 kyr BP***

The strongly varved interval between ~25-23 kyr BP corresponds to a low in all of the biogenic proxies (-2 s.u., 0.03, 0.01, 0.002, 0.002, 0.005 g/cm$^2$/yr, respectively). A rise in all components, except magnetic susceptibility, occurs at ~23 kyr BP (to 0.06, 0.015, 0.005, 0.003 and 0.25 g/cm$^2$/yr respectively), coincident with a varved interval of predominantly type (2). The homogeneous episode at ~22 kyr BP coincides with the highest magnetic susceptibilities of the entire core (5 s.u.), the other components are relatively low, although V and TOC are rising. A peak in magnetic susceptibility occurs at ~21.2 kyr BP coincident with a peak of sediment type (7). At ~20.9 kyr BP during a peak of type (1) all components except magnetic susceptibility and $CaCO_3$ are high (0.08, 0.015, 0.008 and 0.25 g/cm$^2$/yr respectively).

***~19.8-14.9 kyr BP***

With the exception of brief excursions, magnetic susceptibility declines steadily from the beginning of this zone to the top of core MD02-2515. All of the other biogenic proxies display high frequency change throughout the zone. At ~15 kyr BP during the homogeneous interval, magnetic susceptibility and $CaCO_3$ peak briefly while the other components are low (0.03, 0.01, 0.004 and 0.05 g/cm$^2$/yr respectively).

***~14.9-9.2 kyr BP***

The peak in biogenic silica (0.15 g/cm$^2$/yr) at ~14 kyr BP coincides with a peak of sediment type (1). Peaks of magnetic susceptibility, $CaCO_3$ and biogenic silica (0 s.u., 0.003 and 0.25 g/cm$^2$/yr respectively) occur during the homogenous interval at ~12 kyr BP. V, TOC and Mo are high (0.09, 0.01 and 0.008 g/cm$^2$/yr respectively) during the peak of type (1) at ~11.7 kyr BP.

***~9.2-0 kyr BP***

Although all components are low compared to the rest of the core, all except magnetic susceptibility rise slightly from the base of the zone to ~6.1 kyr BP. After ~3 kyr BP, $CaCO_3$ is rising while biogenic silica is falling.

Frequency distribution histograms for the accumulation rates of the biogenic proxies are shown in Figure 5.9. Biogenic silica, Mo, V and TOC have a normal distribution with a slight skew towards the higher range of values. $CaCO_3$ distribution is strongly skewed towards the lower range of values.

Table 5.3 shows the average accumulation rates for ~36-0 kyr BP. Fig. 4.4 shows that sedimentation rates fall after ~16 kyr BP, and so average accumulation rates have been calculated for ~36-16 kyr BP and ~16-0 kyr BP. On average, accumulation rates for biogenic silica, Mo, V and $CaCO_3$ fall after ~16 kyr BP, while accumulation rates for TOC are steady throughout the core.

| **Biogenic proxy** | **~36-0 kyr BP ($g/cm^2/yr$)** | **~36-16 kyr BP ($g/cm^2/yr$)** | **~16-0 kyr BP ($g/cm^2/yr$)** |
|---|---|---|---|
| Biogenic $SiO_2$ | 0.12 ±0.06 | 0.13 ±0.06 | 0.11 ±0.05 |
| Mo | 0.005 ±0.002 | 0.005 ±0.002 | 0.003 ±0.001 |
| V | 0.04 ±0.014 | 0.04 ±0.013 | 0.03 ±0.014 |
| TOC | 0.01 ±0.004 | 0.01 ±0.003 | 0.01 ± 0.005 |
| $CaCO_3$ | 0.0022 ±0.001 | 0.0024 ± 0.001 | 0.0018 ±0.001 |

**Table 5.3:** Average accumulation rates for biogenic proxies

## 5.4 Terrigenous proxies

Terrigenous proxies are the allochthonous components of Guaymas Basin sediment, derived from the surrounding land areas via direct runoff, fluvial transport and airborne dust. Rates of flocculation (section 2.8) vary according to the amount of clay particles in suspension and so TOC is included with the terrigenous proxies. Varying amounts of Fe cause variation in magnetic susceptibility and so this component is included as a terrigenous proxy.

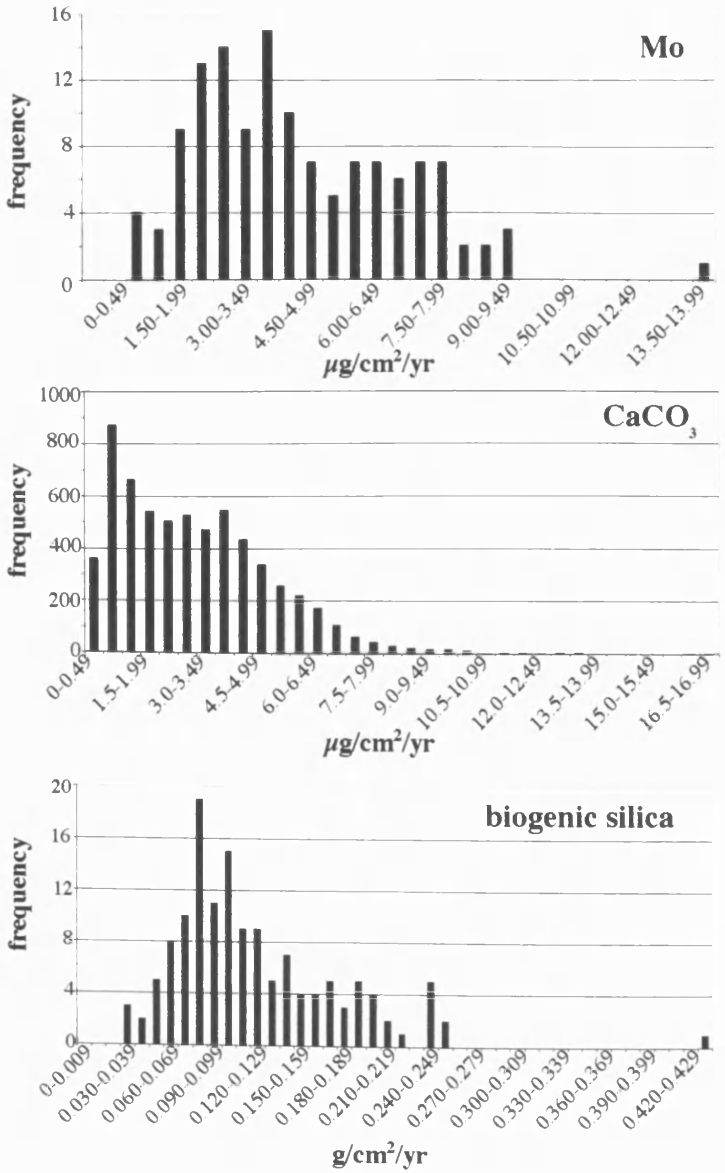


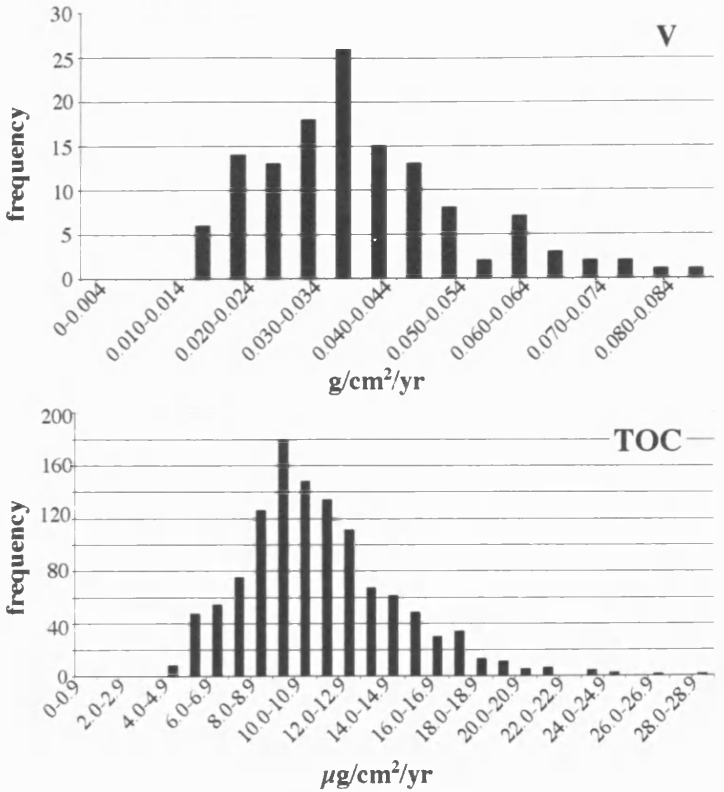


**Figure 5.9:** Distribution histograms for the biogenic proxies.

The accumulation rates for the terrigenous proxies, calculated using equations 3.1, 3.2 and 3.3 (section 3.3.2), are presented in Figure 5.10. Detrital silica was obtained from the total silica data in the discrete XRF analysis by the subtraction of biogenic silica. Comparison with Fig. 4.11 shows that the terrigenous proxies also exhibit the ~5000-year alternations in low and high frequency of change (section 4.5.4).

***~36-30.8 kyr BP***

At the base of the zone during the non-varved interval, all components are falling and a low occurs at ~35 kyr BP (0 s.u., 0.01, 0.08, 0.02 and 0.001 $g/cm^2/yr$ respectively). The magnetic susceptibility peak at ~34 kyr BP, coincident with a peak of sediment fabric type (7), is matched by all the other components. All of the terrigenous proxies except magnetic susceptibility reach their highest values for the entire core at ~31.5 kyr BP (0.015, 0.32, 0.1 and 0.0035 $g/cm^2/yr$ respectively), coincident with a peak of sediment type (4).

***~30.8-25.1 kyr BP***

All components are low at the beginning of the zone. The broad high in magnetic susceptibility (~30-28 kyr BP), coincident with the non-laminated/non-varved interval and homogeneous event at ~29 kyr BP, is matched by a broad high in detrital silica and Al2O3 (2 s.u., 0.2, and 0.6 $g/cm^2/yr$ respectively). After this there is frequent, low-amplitude change with peaks in the terrigenous proxies matching peaks in sediment type (6), most notably at ~26 kyr BP (1 s.u., 0.01, 0.25, 0.09, and 0.0025 $g/cm^2/yr$ respectively).

***~25.1-19.8 kyr BP***

TOC and $TiO_2$ do not match the peaks seen in magnetic susceptibility, detrital silica, $Al_2O_3$ and sediment type (7) at ~25 kyr BP. The strongly varved interval at ~24 kyr BP corresponds to a low in all the terrigenous proxies (-1 s.u., 0.01, 0.1, 0.03, 0.01 $g/cm^2/yr$ respectively). The prominent but less strongly varved interval at ~23.2 kyr BP coincides with highs in all the components except magnetic susceptibility (0.015, 0.25, 0.08, 0.003 $g/cm^2/yr$ respectively). The broad, largely

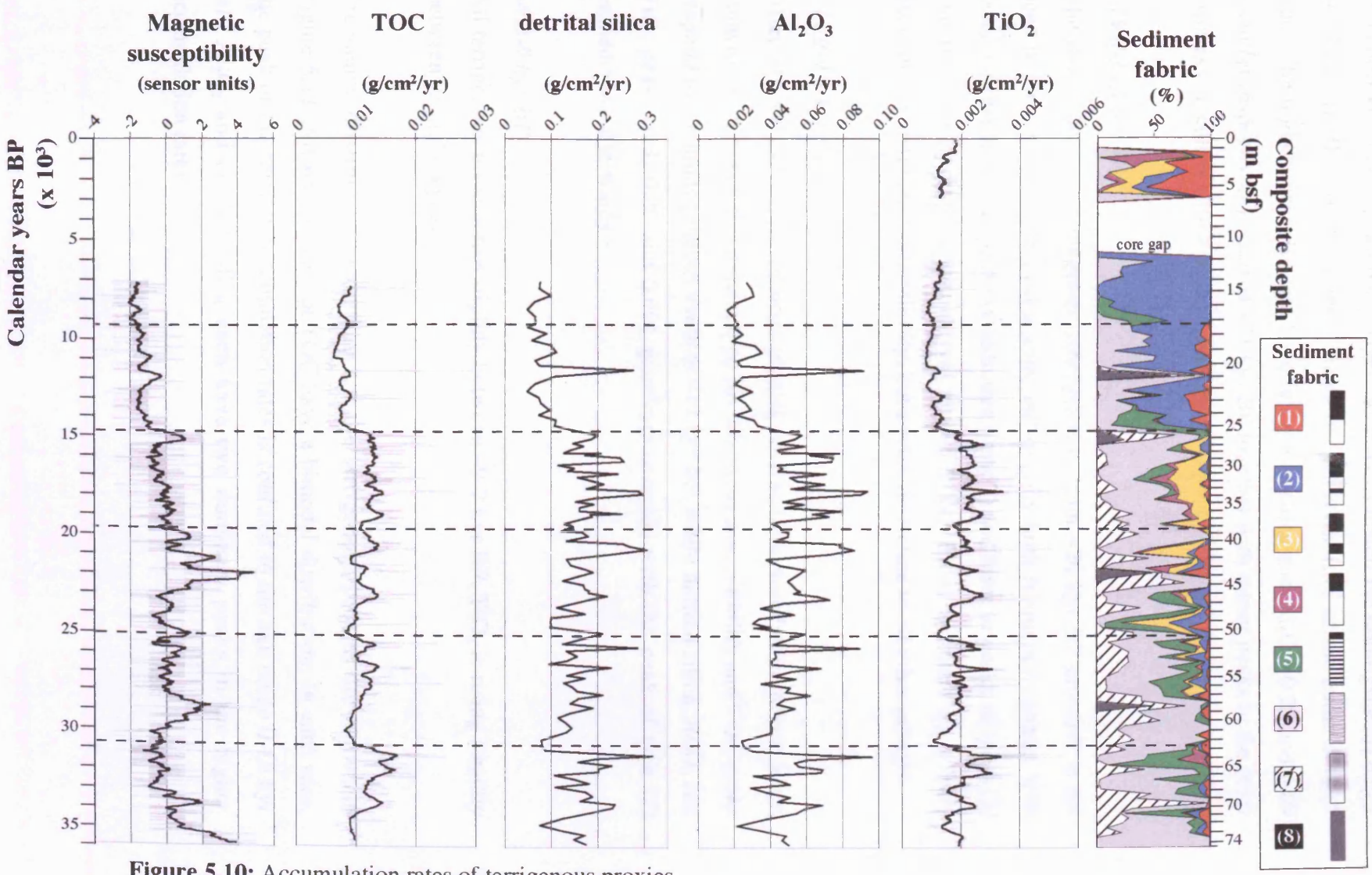


**Figure 5.10:** Accumulation rates of terrigenous proxies.

non-laminated interval ~23-21 kyr BP is matched by high magnetic susceptibility. Peaks in all the terrigenous proxies match the homogeneous event at ~22.5 kyr BP with the highest magnetic susceptibilities of the entire core (5 s.u.). The highest peaks of this zone in detrital silica and $Al_2O_3$ (0.25 and 0.09 g/cm$^2$/yr respectively) occur at ~21 kyr BP together with minor peaks in the other proxies coincident with a peak of type (6).

***~19.8-14.9 kyr BP***

The steady decline in magnetic susceptibility from ~20 kyr BP onwards is not seen in the other proxies in this zone. All display high frequency change, with peaks corresponding to peaks in sediment type (7) and lows to peaks of types (2) and (4). The homogeneous interval at ~15.5 kyr BP is matched by a brief excursion of magnetic susceptibility, but a relative decline in all other proxies.

***~14.9-9.2 kyr BP***

After ~15 kyr BP, all terrigenous proxies decline in accumulation. Minor peaks coincide with peaks of sediment type (6). Magnetic susceptibility and TOC peaks respond to the homogeneous event at ~12 kyr BP, while detrital silica, $Al_2O_3$ and $TiO_2$ peaks (0.3, 0.09 and 0.001 g/cm$^2$/yr) coincide with the peak of type (7) immediately afterwards.

***~9.2-0 kyr BP***

All terrigenous proxies rise slightly between ~9-7 kyr BP. $TiO_2$ is rising steadily between ~3 and 0 kyr BP.

Frequency distribution histograms for the terrigenous proxies are shown in Figure 5.11. All proxies except TOC have a bimodal distribution. In each case, the peak of the smaller accumulation rates is confined to the age range 0-15 kyr BP. $Al_2O_3$ and detrital silica each have two dominant peaks in the higher accumulation rates.

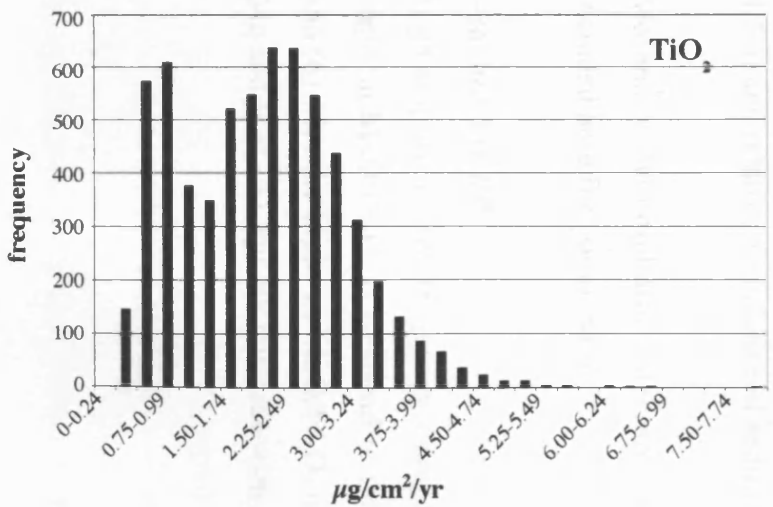


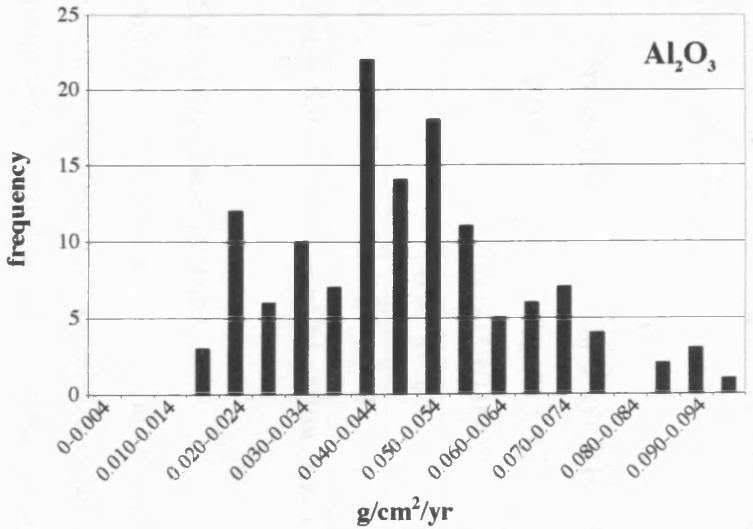


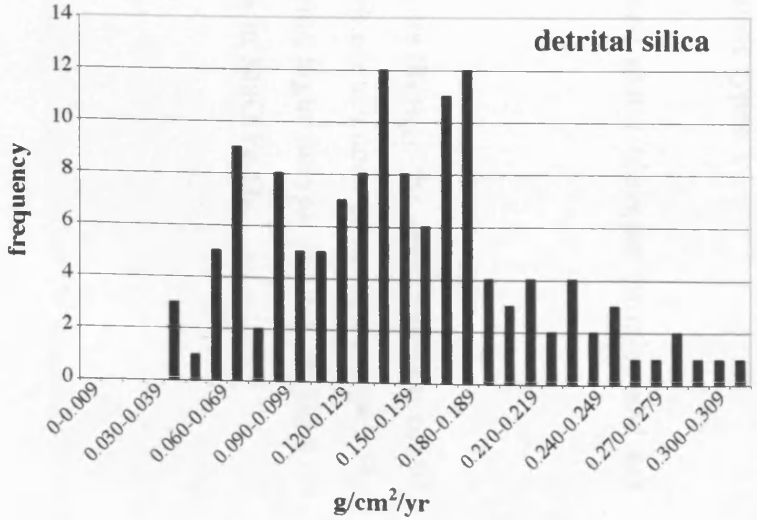


**Figure 5.11:** Distribution histograms for the terrigenous proxies. See Fig. 5.9 for TOC.

Table 5.4 shows the average accumulation rates for the terrigenous proxies (see Table 5.3 for TOC). Apart from TOC, the accumulation rates for the terrigenous proxies fall after ~16 kyr BP.

| **Terrigenous proxy** | **~36-0 kyr BP ($g/cm^2/yr$)** | **~36-16 kyr BP ($g/cm^2/yr$)** | **~16-0 kyr BP ($g/cm^2/yr$)** |
|---|---|---|---|
| $TiO_2$ | 0.002 ±0.0007 | 0.002 ±0.0006 | 0.001 ±0.0005 |
| $Al_2O_3$ | 0.48 ±0.02 | 0.52 ±0.02 | 0.34 ±0.02 |
| Detrital $SiO_2$ | 0.15 ±0.06 | 0.17 ±0.05 | 0.11 ±0.05 |

**Table 5.4:** Average accumulation rates of the terrigenous proxies

## 5.5 Authigenic proxies

Authigenic proxies are chemical species that are sensitive either to water column redox conditions or to variations in the accumulation of organic matter. Mn is a more sensitive redox indicator than Fe and, since both are brought into Guaymas Basin via terrestrial runoff and their accumulation rates are a reflection of variation in this process, the ratio of MnO to $Fe_2O_3$ has been used. When the ratio is high, oxygen levels at the seafloor are significantly high. The accumulation rates of the authigenic proxies, calculated using equations 3.1, 3.2 and 3.3 (section 3.3.2), are shown in Figure 5.12, with the sedimentation zones (section 4.5.4) and relative abundance of sediment fabric types.

Mo and V accumulation rates are described under biogenic proxies and are included here for comparison.

*~36-30.8 kyr BP*

High amplitude, low-frequency change occurs through the zone. The two broad highs in $MnO:Fe_2O_3$ correspond to the peak occurrences of sediment types (7) and (6) with the highs in $MnO:Fe_2O_3$ matching highs in type (6). The maxima in Mo and V at ~31 kyr BP coincide with a low in $MnO:Fe_2O_3$.

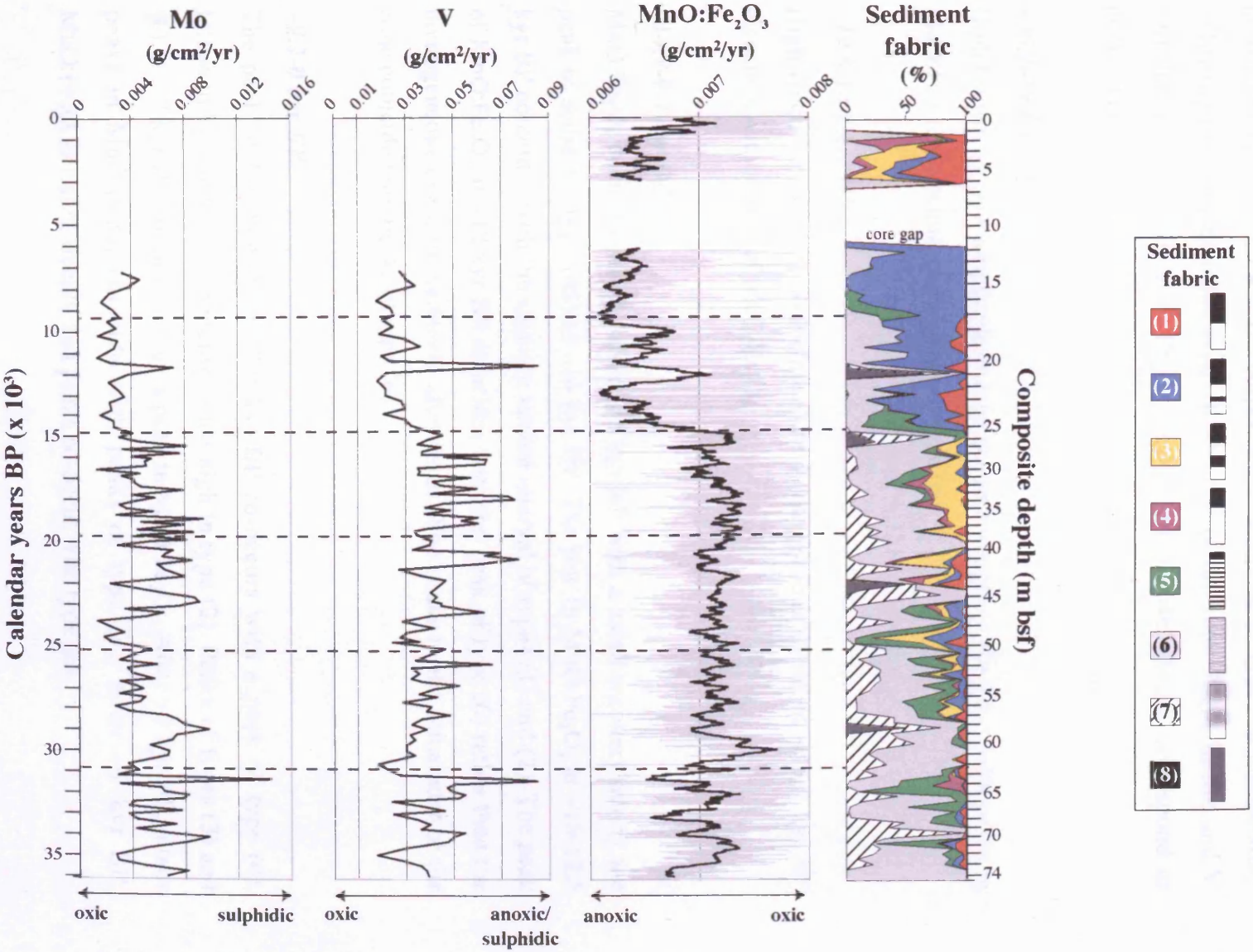


**Figure 5.12:** Accumulation rates of the authigenic proxies.

***~30.8-25.1 kyr BP***

The broad high in $MnO:Fe_2O_3$ between ~30-28 kyr BP (the highest of the entire core at 0.0072 $g/cm^2/yr$) coincides with highs in types (6) and (7). A small peak in $MnO:Fe_2O_3$ at ~28.5 kyr BP corresponds to a peak of type (6) immediately following the homogeneous event. In the rest of the zone, highs in Mo and V coincide with lows in $MnO:Fe_2O_3$, while highs in $MnO:Fe_2O_3$ correspond to peaks in sediment type (6).

***~25.1-19.8 kyr BP***

High frequency, low amplitude change occurs throughout the zone, with peaks in $MnO:Fe_2O_3$ coinciding with peaks of type (6).

***~19.8-14.9 kyr BP***

High frequency change as before. The homogeneous event at ~15.5 kyr BP coincides with a peak of $MnO:Fe_2O_3$.

***~14.9-9.2 kyr BP***

$MnO:Fe_2O_3$ declines sharply after ~15 kyr BP with a small recovery during the peak of sediment type (45) at ~14 kyr BP. The low in $MnO:Fe_2O_3$ at ~13-12.5 kyr BP coincides with the strongly varved interval of types (1) and (2). The peak of $MnO:Fe_2O_3$ at ~12 kyr BP coincides with the peak of type (6) rather than the homogeneous event immediately afterwards. The peaks in the remainder of the zone coincide with peaks of type (6).

***~9.2-0 kyr BP***

The peak of $MnO:Fe_2O_3$ at ~7.9 kyr BP co-occurs with a peak of type (4), followed by a low corresponding to the high in type (2). Peaks of types (3) and (6) at ~ 7 kyr BP are matched by a peak in $MnO:Fe_2O_3$. After ~3 kyr BP, minor peaks in $MnO:Fe_2O_3$ coincide with peaks of type (3). After ~1 kyr BP, $MnO:Fe_2O_3$ is rising steeply and peaks co-occur with type (6).

The frequency distribution histogram of $MnO:Fe_2O_3$ is presented in Figure 5.13. It has normal distribution, skewed towards the larger range of sizes.

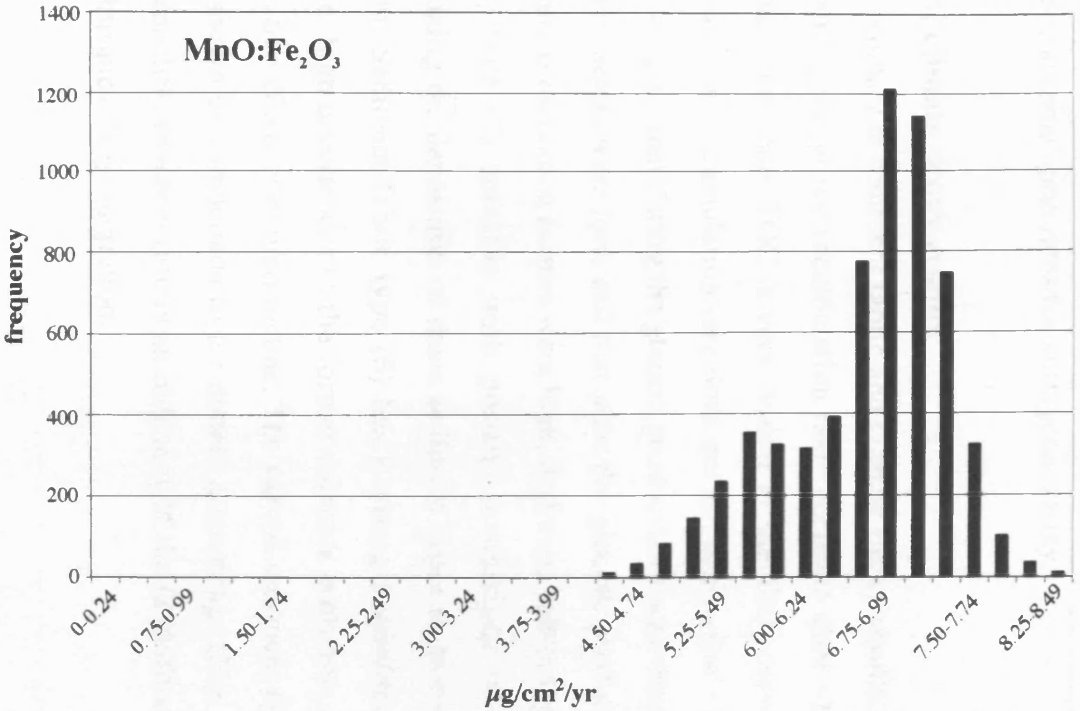


**Figure 5.13:** Frequency distribution histogram for the authigenic proxy MnO:Fe2O3. For Mo, V and magnetic susceptibility see Fig. 5.9.

Table 5.5 shows the average accumulation rates for MnO:Fe2O3 (for Mo and V see Table 5.3). Compared to average accumulation rates from ~36 to 16 kyr BP, those from ~16 to 0 kyr BP are lower and more variable.

| **Authigenic proxy** | **~36-0 kyr BP ($g/cm^2/yr$)** | **~36-16 kyr BP ($g/cm^2/yr$)** | **~16-0 kyr BP ($g/cm^2/yr$)** |
|---|---|---|---|
| $MnO:Fe_2O_3$ | 0.007±0.0007 | 0.007 ±0.0005 | 0.006 ±0.0008 |

**Table 5.5:** Average accumulation rates for authigenic proxy.

## 5.6 Summary of climate proxy results

Figure 5.14 is a summary of sediment fabric and climate proxy results. Biogenic, terrigenous and authigenic proxy accumulation rates decrease after ~16 kyr BP, along with sedimentation rate. TOC is very similar to the $TiO_2$ curve (see Fig 5.10) and yet its average accumulation rate does not decrease after ~16 kyr BP (Table 5.3). This suggests that during the glacial, productivity was relatively high while preservation factors were low, and that after the glacial, productivity was relatively low while preservation factors were high. Sediment fabric type (8) and, to some extent, type (7) coincide with positive excursions of magnetic susceptibility, linking the deposition of these sediment types to storminess and high precipitation. Sediment fabric type (6) has a strong resemblance to the $MnO:Fe_2O_3$ curve: high occurrences of the former coincide with times of higher ventilation, indicative of a deeper thermocline. The varved sediment fabric types (1-5) have been shown by comparison to the diatom assemblage (Fig. 5.7) to be indicators of seasonality, which in turn is an indicator of the latitudinal extent of North Pacific Subtropical High migration.

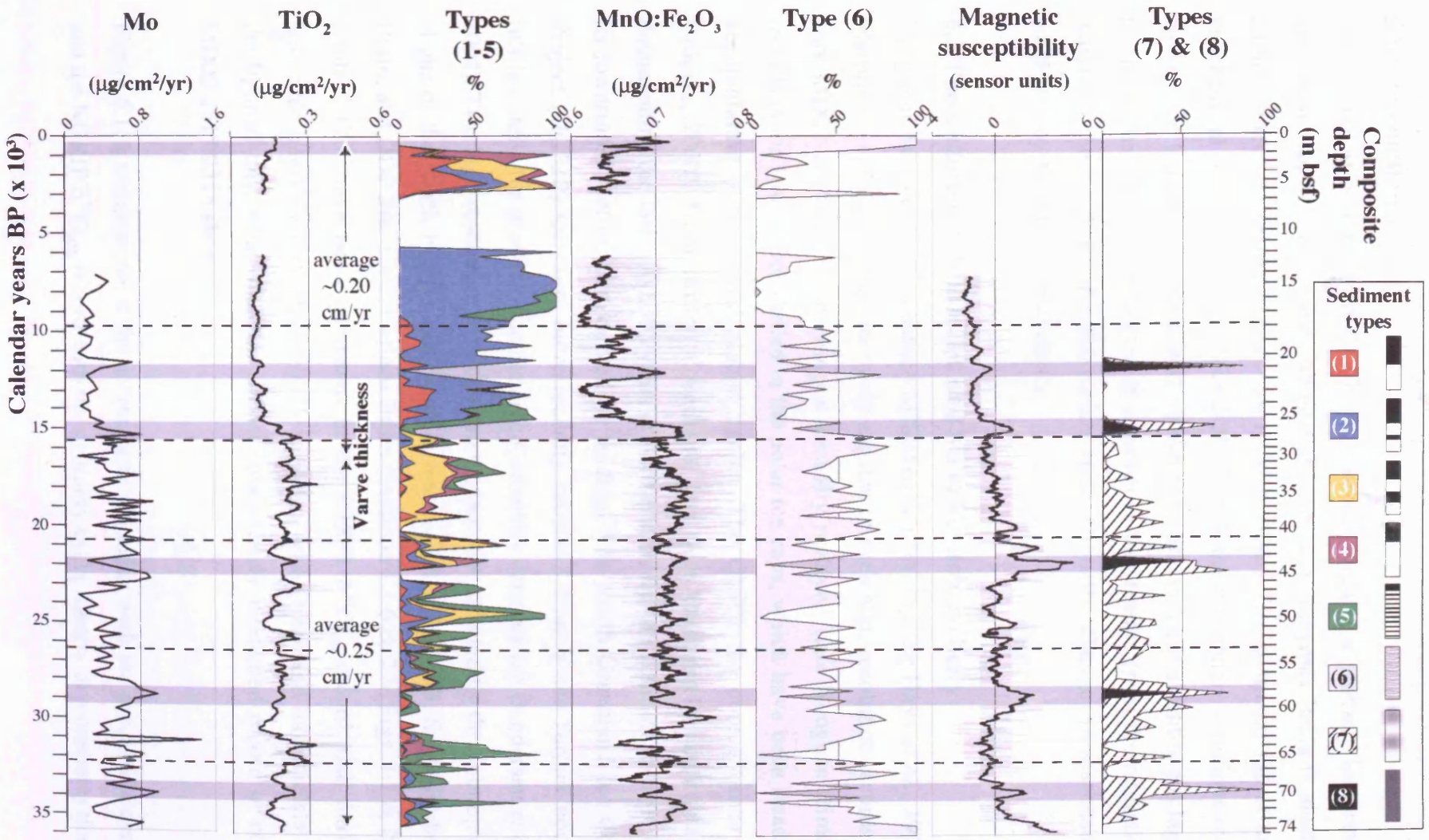


**Figure 5.14:** Summary of sediment fabric and climate proxy results.

# Chapter 6 Discussion

## 6.1 Introduction

The migration of the North Pacific Subtropical High is a globally important mechanism for heat and water vapour transport, and Guaymas Basin is ideally circumstanced to record changes in its behaviour. The sediment fabric and geochemical results from core MD02-2517/2515 show in detail variations over the last ~36 kyr BP. In particular, the sediment fabric index is a continuous high-resolution monitor of the degree of seasonality that results from the migration pattern of the North Pacific Subtropical High. Globally, changes in seasonality are driven by Milankovitch cyclicity.

## 6.2 The sediment fabric index and Milankovitch cyclicity

Long marine records demonstrate Milankovitch forcing (eg Hays *et al.*, 1976; Martinson *et al.*, 1987), but are rarely capable of such high-resolution records as core MD02-2517/2515. The longest annually resolved Late Neogene climate records come from cores drilled in the polar ice caps, which have been steadily accumulating over several glacial cycles. The GISP2 ice core (Stuiver & Grootes, 2000), from central Greenland, has been extensively employed in documenting the last ~100,000 years of northern hemisphere climate change, but its lowermost section is disturbed by folding. The North Greenland Ice Core Project (NGRIP) ice core, more recently retrieved from a site further north, fulfils criteria for producing undisturbed, annually dateable ice (Andersen *et al.*, 2004). Two high-resolution records from the latitudes affected by the Subtropical Highs of the North Pacific and North Atlantic – ODP Site 893, Santa Barbara Basin, and ODP Site 1002, Cariaco Basin (Sections 1.1.6 & 2.5; Figs. 1.1 & 2.5; Table 1.1) – have been compared to the GISP2 $\delta^{18}O_{ICE}$ record and, during laminated intervals, both show good correlation with Greenland interstadials. In the light of this, what does the almost continuously laminated record of core MD02-2517/2515 show?

Figure 6.1, a comparison of the sediment fabric index with the precession cycle and the NGRIP $\delta^{18}O_{ICE}$ record with the obliquity cycle, clearly demonstrates that

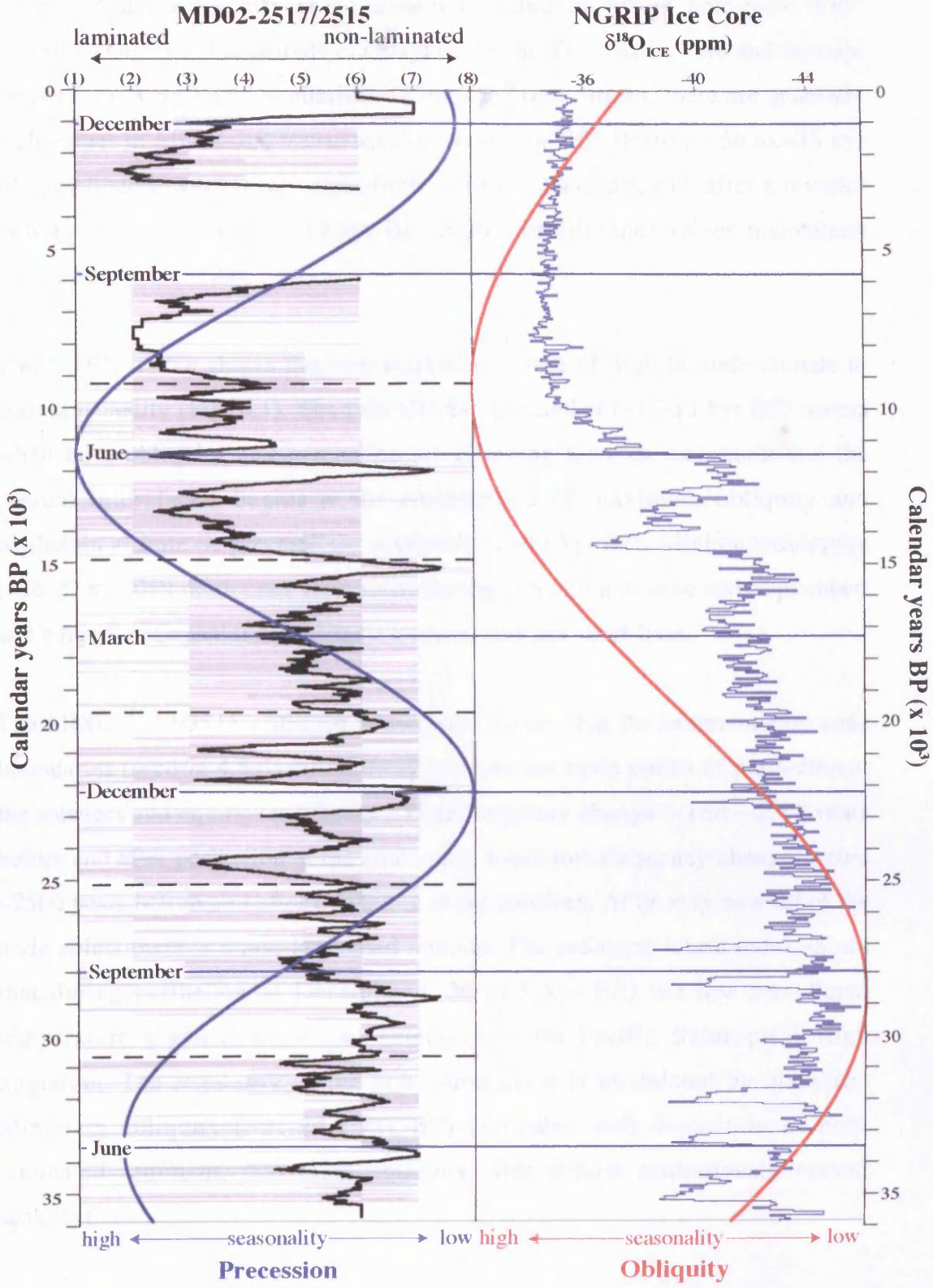


**Figure 6.1:** The Sediment Fabric Index compared to the Precession curve and the NGRIP oxygen isotope record compared to the Obliquity curve. [Laskar *et al.*, 2004; NGRIP members, 2004]

while obliquity is dominant at the latitude of central Greenland, precession is the prevailing factor at the latitude of Guaymas Basin. The marine core and ice core curves show very broad similarities. With some fluctuations, there are generally high values in MD02-2517/2515 and low values in NGRIP from ~36 to ~15 kyr BP, sustained lower/higher values from ~15 to ~13 kyr BP, and, after a reversal to lower/higher values at ~12 kyr BP, steady lower/higher values maintained towards the present day.

The NGRIP curve shows the very marked response of high latitude climate to high seasonality (Fig. 6.1). The Late Glacial interstadial (~15-13 kyr BP) occurs when both obliquity and precession are climbing towards maximum and the present Interglacial begins at the combination of maximum obliquity and perihelion at June (ie precessional maximum at ~11 kyr BP). Minimum obliquity (~36-27 kyr BP) moderates seasonality during perihelion at June and September, and while five Greenland interstadials occur, they are short-lived.

The MD02-2517/2515 sediment fabric index shows that the sedimentation zone boundaries (section 4.5.4) fall halfway between the node points of perihelion at the solstices and equinoxes (Fig 6.1). High frequency change occurs ~2500 years before and after perihelion at the equinoxes, while low frequency change occurs ~2500 years before and after perihelion at the solstices. At or very near all of the node points there is a non-laminated interval. The sediment fabric index shows that during perihelion at December (~26-21.5 kyr BP) the low meridional temperature gradient allows an extensive North Pacific Subtropical High migration. The regularity of the precession cycle is modulated by obliquity. Minimum obliquity (~31-28.5 kyr BP) coincides with deposition of non-laminated sediment, maximum obliquity with almost continuously varved sediment.

## 6.3 Interpretation of sediment fabric and climate proxy data

Figure 6.1 gives strong indications that seasonality is the key to northern hemisphere climate change. Low to mid-latitude climate responds to precessional forcing modulated by the obliquity cycle, while high latitude climate responds to

obliquity forcing modulated by the precession cycle. During a glacial cycle, these responses are modified by feedbacks from the growth of continental ice sheets and consequent higher albedo and lower greenhouse gases, and re-organisation of atmospheric and oceanic circulation.

The geographical extent of North Pacific Subtropical High migration can be forced from low latitudes by changes in the amount of available sensible and latent heat, or from high latitudes by a steep/shallow meridional temperature gradient. Change in the dominant forcing mechanism is brought about by natural Milankovitch cyclicity with which the sediment fabric index shows a strong correlation. Low latitude forcing is strongest when perihelion is at the equinox (the time of year when the Sun is overhead at the equator). High latitude forcing is greatest when there are large continental ice sheets and/or when perihelion is at the solstice (either hot summers/cold winters or mild winters/cool summers).

At present, the midwinter location of the North Pacific Subtropical High is close to Guaymas Basin, resulting in a long wind-driven high-productivity season during winter. If the midwinter location were closer to the equator, Guaymas Basin would be somewhere in the middle of the migration, which would split the upwelling season and affect its timing. A large midwinter displacement towards the equator would put Guaymas Basin at or close to the midsummer location of the North Pacific Subtropical High, resulting in a long wind-driven high-productivity season during summer. An extreme midwinter displacement would place Guaymas Basin beyond the migration range and there would be no upwelling season. Productivity at Guaymas Basin will always be relatively high because of high nutrient-availability due to tidal mixing, but preservation is controlled by the geographical extent of North Pacific Subtropical High migration. Removal of Trade Wind influence causes a deeper coastal thermocline and better ventilation of intermediate depth waters entering the Gulf of California. Milankovitch forcing and the presence/absence of large continental ice sheets affects the strength and location of the Aleutian Subpolar Low (through expansion/contraction of the Polar High). With the midwinter location of the North Pacific Subtropical High displaced towards the equator, the Aleutian

Subpolar Low would dominate climate along the eastern North Pacific margin, bringing higher rainfall to the region and more extensive coastal downwelling.

In sequence, the sediment fabric types from core MD02-2517/2515 show first an increasing number of seasons and then a diminishing seasonal contrast:
Type (1) Two/three seasons – third season not visible in the digital images
Type (2) Three/four seasons – fourth season very brief
Type (3) Four seasons
Type (4) Two seasons – diatomaceous lamina much thicker than the silt lamina
Type (5) Two weakly contrasting seasons – diatomaceous lamina much thicker than the silt lamina
Type (6) Alternating sediment types poorly preserved
Type (7) No annual seasonality
Type (8) No seasonality

Observed natural variability in subtropical climate (McGregor & Nieuwolt, 1998; Barry & Chorley, 2003), sediment trap data (Thunell *et al.*, 1993; 1994; Sancetta, 1995; Thunell, 1998; Ziveri & Thunell, 2000) and the BSEI study of Holocene sediment fabric in core JPC-56 (Pike & Kemp, 1996, 1997, 1999) serve as the model for interpretation of the sediment fabric index. This is supported by the variations in biogenic, terrigenous and authigenic flux provided by the XRF data, geochemical analyses and diatom ecology.

### 6.3.1 Sediment fabric type (1)

Sediment fabric type (1) is a varve consisting of a light and a dark lamina of equal thickness. It is the typical varved sediment of the mid to late Holocene. Quantitative diatom identification within the light-coloured laminae (which is beyond the scope of this study) would confirm that type (1) is identical to the most numerous type identified in the study of Holocene varves from core JPC-56 (Pike & Kemp, 1996; 1997; 1999).

Figure 6.2 illustrates the contrast between the seasons during the deposition of sediment fabric type (1). The wet summer season with rainfall from the south is

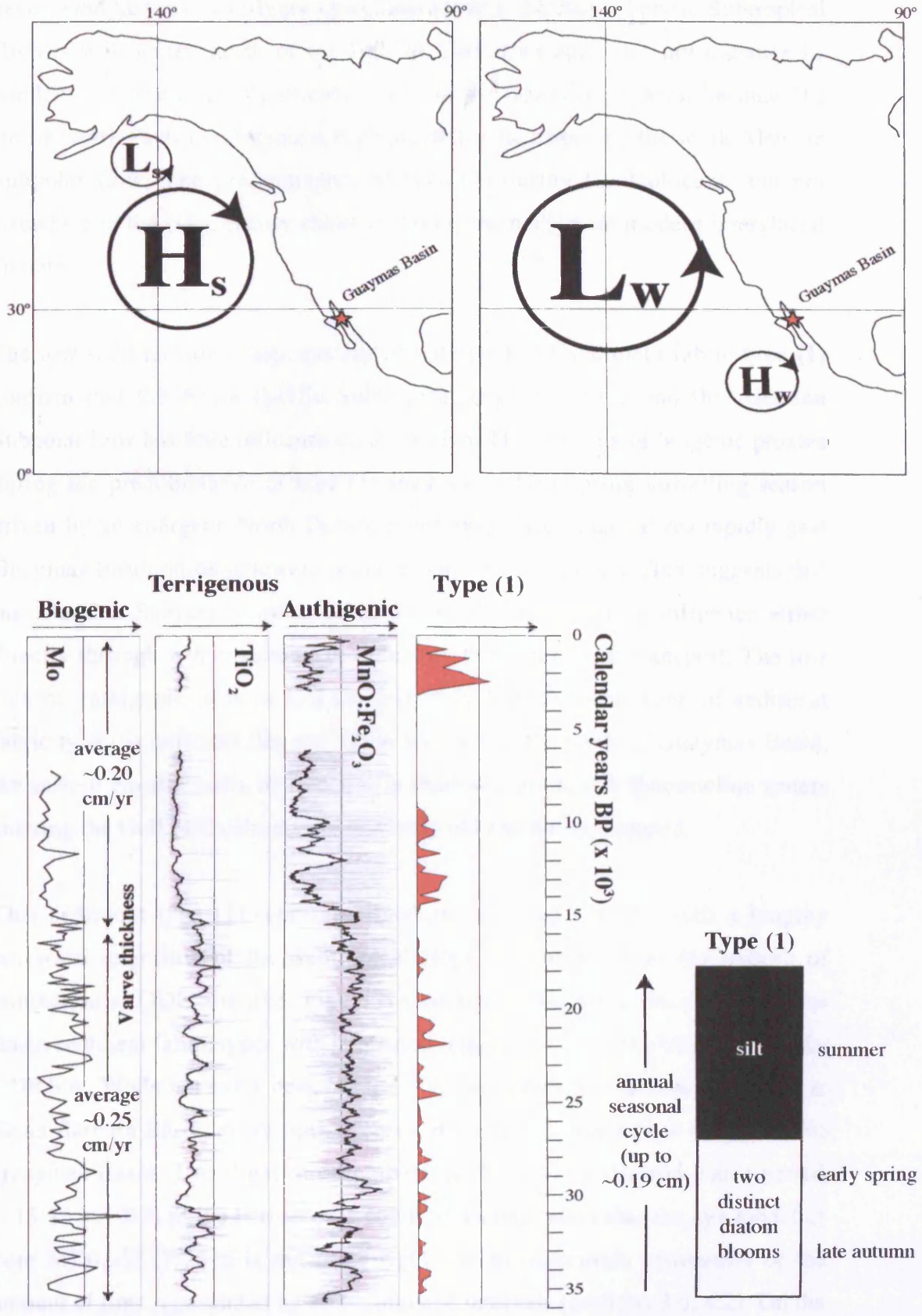


**Figure 6.2:** Interpretation of sediment fabric type (1).
Subscript 's' denotes midsummer location; subscript 'w' denotes midwinter location.

never windy enough to trigger upwelling because the North Pacific Subtropical High is well to the north of the Gulf of California and does not enhance its windfield. There is no significant runoff in the upwelling season because the strong North Pacific Subtropical High precludes incursions by the weak Aleutian Subpolar Low. The predominance of type (1) during the Holocene, but not elsewhere in the core, clearly shows that it represents typical modern interglacial climate.

The low sedimentation rates associated with peaks of sediment fabric type (1) confirm that the North Pacific Subtropical High is strong and the Aleutian Subpolar Low has little influence on deposition. The low flux of biogenic proxies during the predominance of type (1) suggests a short spring upwelling season driven by an energetic North Pacific Subtropical High that moves rapidly past Guaymas Basin on its poleward passage. The low terrigenous flux suggests that the Aleutian Subpolar Low is relatively weak and has little influence either directly through winter rainfall or indirectly through fluvial transport. The low flux of authigenic proxies and the relatively low co-occurrence of sediment fabric type (6) indicates that the Trade Winds operate north of Guaymas Basin, the eastern North Pacific thermocline is shallow and the sub-thermocline waters entering the Gulf of California are relatively old and de-oxygenated.

That sediment type (1) represents modern observed climate with a lengthy poleward migration of the Subtropical High is confirmed by the pattern of lamination at ODP Site 893. Figure 6.3 compares the occurrence of Guaymas Basin sediment fabric types with laminated intervals of the last ~36 kyr BP at the ODP Site. While not every peak of type (1) corresponds to a laminated interval at Santa Barbara Basin, every peak at Santa Barbara matches a peak of type (1) at Guaymas Basin. The slight misalignment of the Bølling-Alleröd warm period (~15-13 kyr BP) in the two records could be an indication that the age model of core MD02-2517/2515 is not quite right due to inaccurate estimation of the amount of time represented by non-laminated intervals (sections 3.6; 4.2). On the other hand, at ODP Site 893, Nederbragt & Thurow (2005) find a discrepancy between accumulation rates calculated from varve thicknesses and those

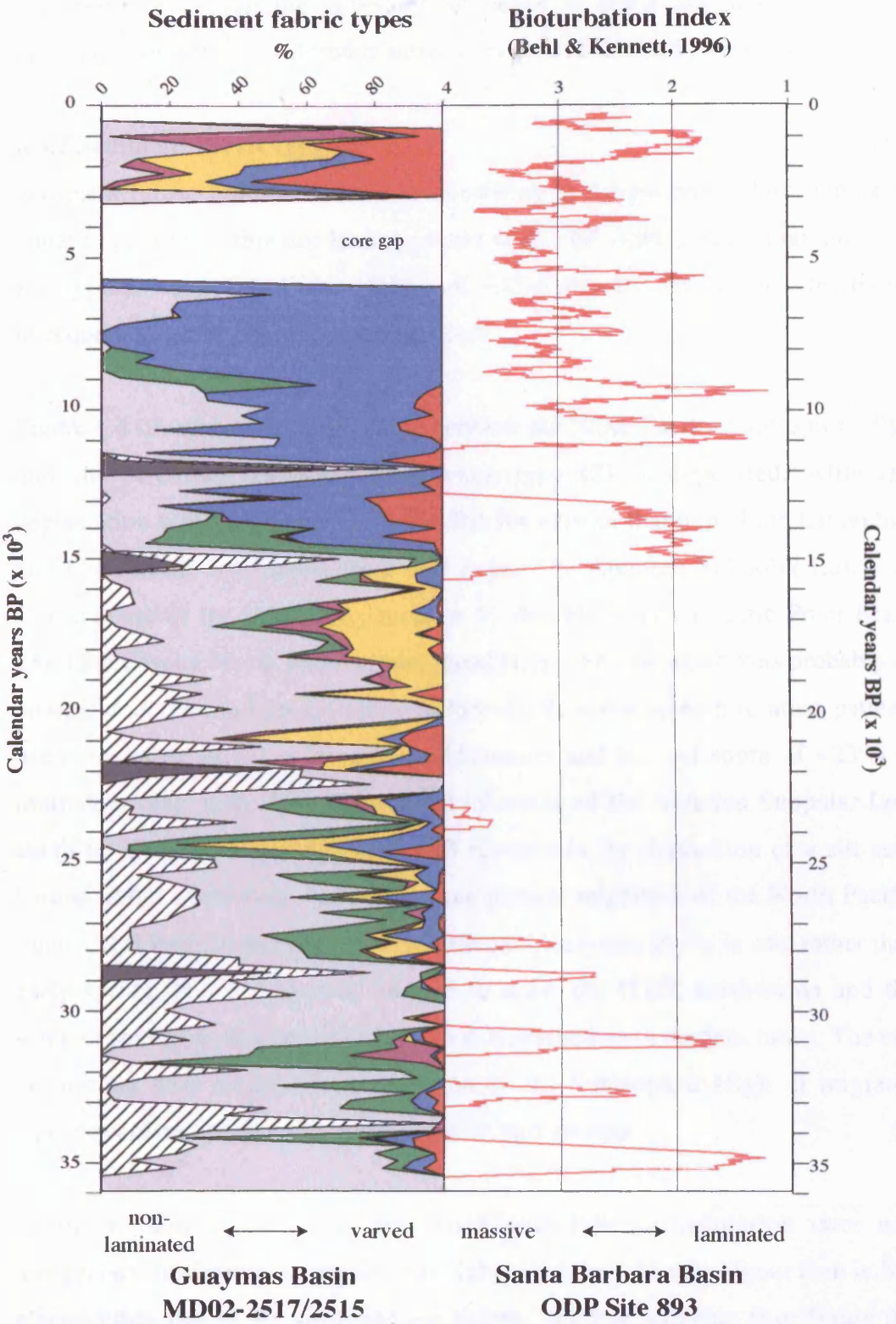


**Figure 6.3:** Occurrence of sediment fabric type (1) compared to the bioturbation index from ODP Site 893.

calculated from radiocarbon dates and infer a slump at ~8.6-8.1 kyr BP. This may have thickened the Holocene sequence at Santa Barbara Basin, thus displacing the Bølling-Alleröd relative to the MD02-2517/2515 record.

### 6.3.2 Sediment fabric type (2)

Sediment fabric type (2) is a varve consisting of a light and a dark lamina of equal thickness. A thin silt lamina occurs within the light-coloured lamina. It is the typical varved sediment fabric of ~15-6 kyr BP and occurs relatively infrequently throughout the rest of the core.

Figure 6.4 illustrates the relationship between the North Pacific Subtropical High and the Aleutian Subpolar Low when type (2) is deposited. Although deglaciation was under way ~15-6 kyr BP, for most of that period the Laurentide and Cordilleran Ice Sheets were still large. The Aleutian Subpolar Low was forced south of its present-day location by the relatively energetic Polar High. The Late Glacial North Pacific Subtropical High, even though it was probably as energetic as the modern system, was forced into a restricted migration pattern, not penetrating as far poleward at midsummer and located south of ~23°N at midwinter (Fig. 6.4). This allowed the incursion of the Aleutian Subpolar Low south of 27°N (cf Fig. 2.6) and runoff resulted in the deposition of a silt sub-lamina. After midwinter, the longer-than-present migration of the North Pacific Subtropical High meant that its winds affected Guaymas Basin in mid rather than early spring. It was vigorous enough to draw the ITCZ northwards and the summer season dark-coloured lamina was deposited as in modern times. The end of summer heat forced the contraction of the Subtropical High. It migrated equatorward and passed Guaymas Basin in mid autumn.

Sediment fabric type (2) is associated with low sedimentation rates and terrigenous flux, implying an Aleutian Subpolar Low with less vigour than in full glacial times due to the shrinking ice sheets. The low biogenic flux during the predominance of type (2) implies a short spring upwelling season driven by an energetic North Pacific Subtropical High that moves rapidly past Guaymas Basin. The low authigenic flux and relatively low co-occurrence of sediment

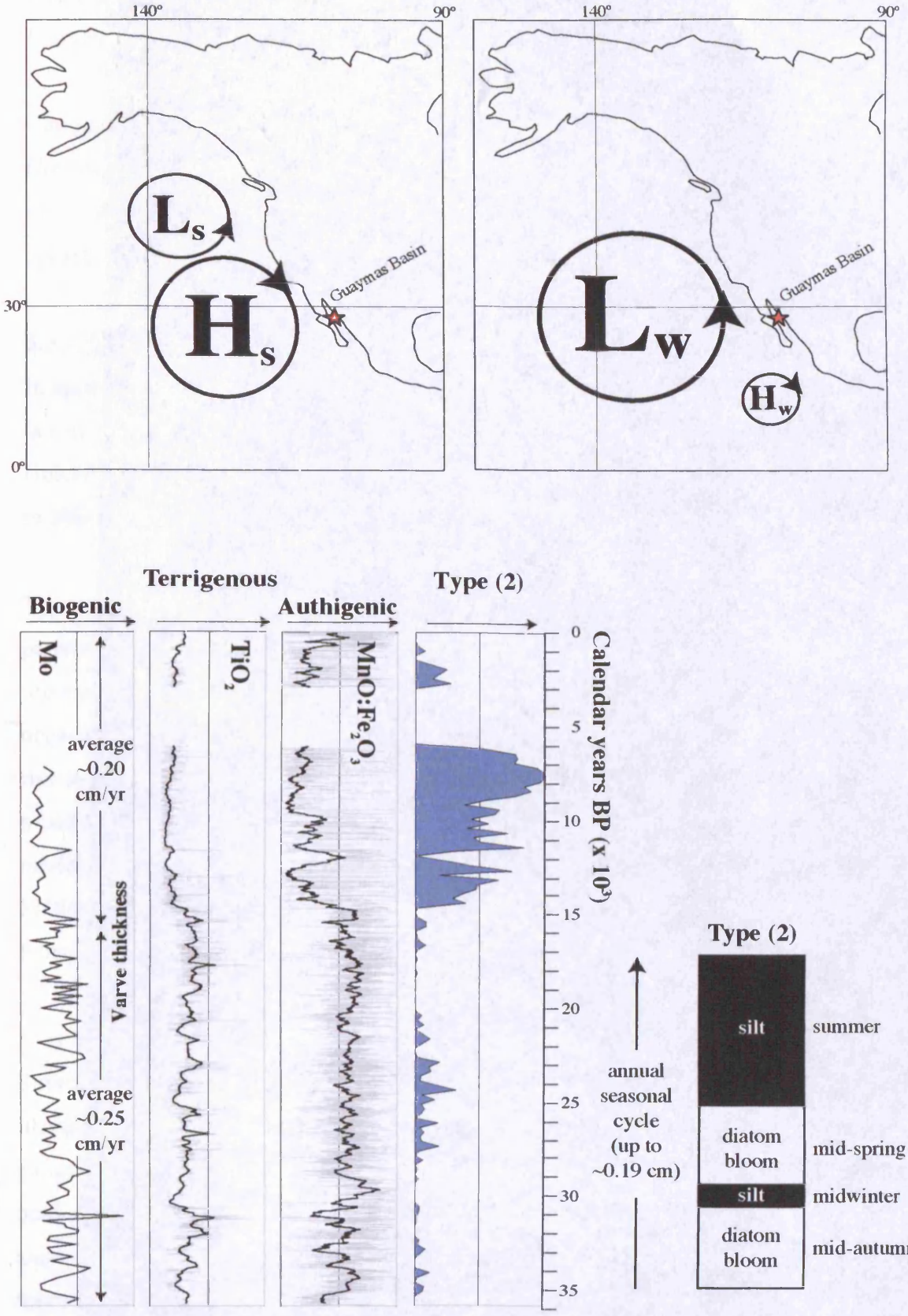


**Figure 6.4:** Interpretation of sediment fabric type (2).

fabric type (6) implies that the Trade Winds were blowing at latitudes north of Guaymas Basin.

The diatom species indicate that upwelling (*Chaetoceros* spp.), stratification (*Rhizosolenia* spp.) and overturn (*Coscinodiscus* spp.) occurred. The appearance of *T. longissima* after ~12 kyr BP supports the idea that the Trade Winds were operative well to the north of ~23°N in summer.

### 6.3.3 Sediment fabric type (3)

In appearance, sediment fabric type (3) is like type (2), but with greatly expanded lamina thicknesses. It occurs in considerable numbers in the early to mid Holocene and is the typical sediment fabric of ~20-16 kyr BP, during perihelion in March.

Type (3) is identified in this study by its subtle but distinctive four-laminae pattern that repeats for decades at a time. Despite the thickness of the laminae, it represents a single annual cycle. Pike & Kemp (1996; 1997; section 2.10) note occasions when either the 'Fall dump' or the spring bloom are missing, giving rise to a two-component varve. These 'missing' diatom laminae may be due to misidentification of sediment fabric type (3) as two annual cycles; the same misidentification could also be made for type (2). The longer time span of MD02-2517/2515 and the lower-resolution method of examining the sediment fabric in this study contribute to the recognition of varves with four components.

It is proposed that type (3) occurs when the winds of the North Pacific Subtropical High affect Guaymas Basin only at the equinoxes. Figure 6.5 illustrates the relationship of the pressure systems. The Sun is overhead at the equator in March and September. At the present day, this provides the heat to push the North Pacific Subtropical High rapidly past Guaymas Basin in March and to delay its equatorward passage beside Santa Barbara Basin in October. At times when the midwinter location of the North Pacific Subtropical High was far to the south of the Gulf of California, the boost of energy at the equinoxes was sufficient to take the high-pressure system to the latitude of Guaymas Basin (cf

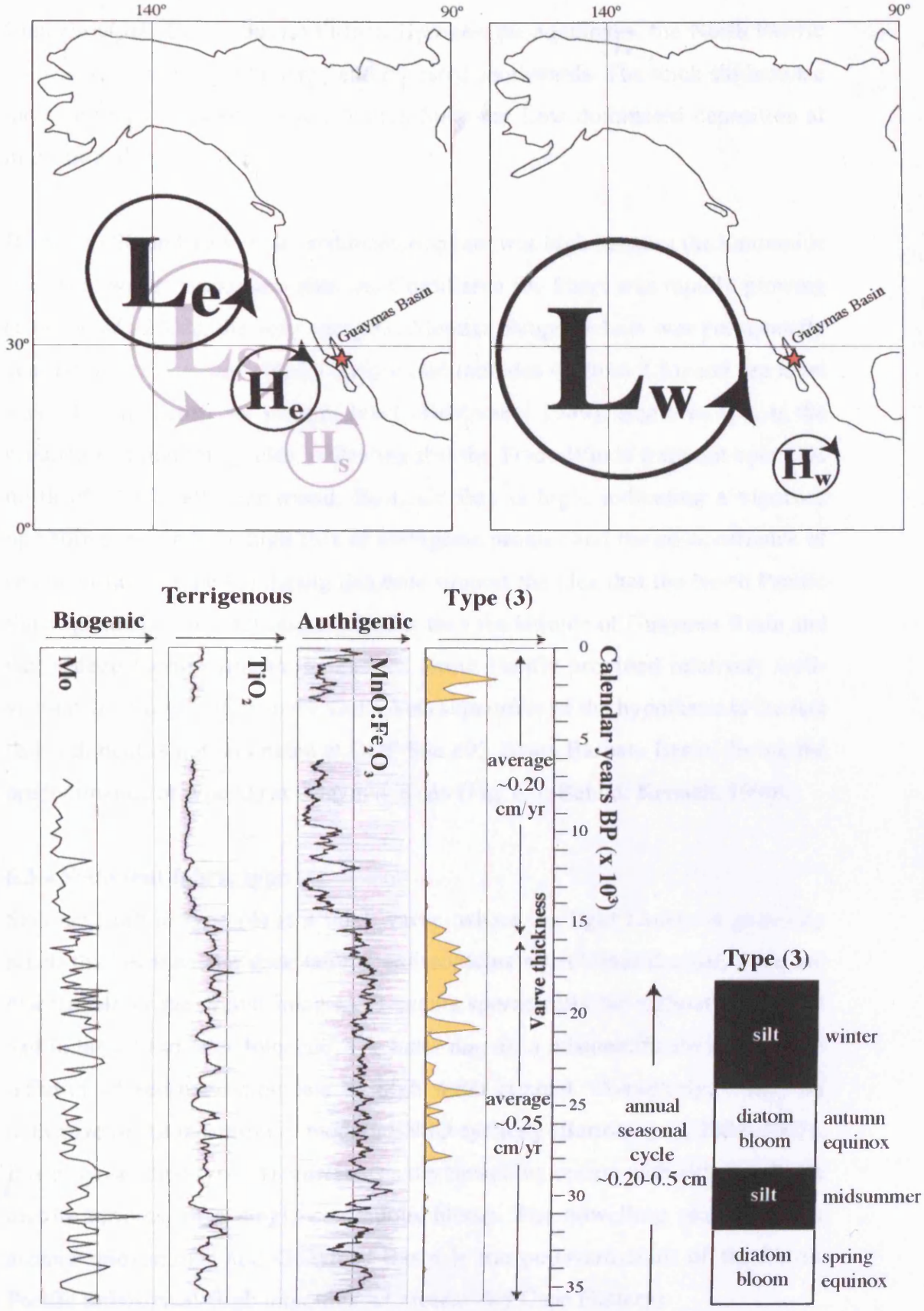


**Figure 6.5:** Interpretation of sediment fabric type (3).
Subscript '**e**' denotes location at the spring and autumn equinox;
subscript '**s**' denotes location at midsummer.

Clement *et al.*, 1999), but no further. Between the equinoxes, the North Pacific Subtropical High lacked energy and retreated southwards. The thick silt laminae indicate that a very energetic Aleutian Subpolar Low dominated deposition at midsummer and midwinter.

Between ~20 and 16 kyr BP, sedimentation rate was high because the Laurentide Ice Sheet was at maximum size, the Cordilleran Ice Sheet was rapidly growing (Dyke *et al.*, 2002), the very energetic Aleutian Subpolar Low was permanently centred over the eastern North Pacific mid-latitudes (section 2.5), and sea level was ~120 m below its present level (Fairbanks, 1989). *Azpeitia* spp. is the predominant diatom species, indicating that the Trade Winds were not operative north of ~23°N all year round. Biogenic flux is high, indicating a vigorous upwelling season. The high flux of authigenic proxies and the co-occurrence of sediment fabric type (6) during this time support the idea that the North Pacific Subtropical High did not migrate further than the latitude of Guaymas Basin and that a deep thermocline in the eastern North Pacific provided relatively well-ventilated bottom waters in the Gulf. Also supportive of the hypothesis is the fact that sediment is not laminated at ODP Site 893, Santa Barbara Basin, during the predominance of type (3) at Guaymas Basin (Fig. 6.3; Behl & Kennett, 1996).

### 6.3.4 Sediment fabric type (4)

Sediment fabric type (4) is a thick varve, where the light lamina is generally much thicker than the dark lamina and contains no sub-laminae (or, none are discernable in the digital images). It occurs sporadically throughout the glacial and in the mid to late Holocene. The latter may be a misidentification due to the inflation of sedimentation rate by high water content. Conversely, it may be indicative of the inception of modern ENSO cyclicity (Barron *et al.*, 2004; 2005). It is proposed that type (4) represents a dry upwelling season with either multiple diatom blooms, or a single continuous bloom. The upwelling season occurs around midsummer and Guaymas Basin is the poleward limit of the North Pacific Subtropical High migration (cf present-day Cape Flattery).

Figure 6.6 illustrates the relationship of the North Pacific Subtropical High and the Aleutian Subpolar Low during times of type (4). The Aleutian Subpolar Low was forced well south of its present-day location by the expanded Polar High (not shown, but see Fig. 1.4). The latter scoured heat and moisture off the North American ice sheets and fed them into the very energetic Aleutian Subpolar Low, the rains of which dominated Gulf climate during winter when the dark coloured lamina was deposited. The absence of silt sub-laminae in the high-productivity season indicates that the North Pacific Subtropical High was energetic enough to maintain its summer position just north of Guaymas Basin. Previous work in the eastern North Pacific indicates southward displacement of the Aleutian Subpolar Low (Sabin & Pisias, 1996; Ortiz *et al.*, 1997), reduced upwelling along the Californian Margin (Sancetta *et al.*, 1992, Gardner *et al.*, 1997, Heusser, 1998; Kienast *et al.*, 2002) and higher ventilation (Stott *et al.*, 2000) consistent with this migration pattern. Flow in the California Current was reduced (Doose *et al.*, 1997; Herbert *et al.*, 2001) which indicates that the ocean gyre was forced south in response to the repositioning of the Aleutian Subpolar Low. Consequently, enhancement of flow in its eastern limb by the winds of the North Pacific Subtropical High occurred much closer to the equator than at present (cf Loubere, 2002).

The open tropical Pacific is the modern distribution of *Azpeitia* spp. (section 2.9; Sancetta, 1995; Barron *et al.*, 2004; 2005; Jiang *et al.* 2004). This species is very abundant throughout the deposition of type (4) (Fig. 5.7), indeed, the evidence from this study, over the ~36 kyr time span of core MD02-2517/2515, is that during the glacial *Azpeitia* spp. is the typical Gulf species. The modern association of *Azpeitia* spp. with incursions of tropical water into the Gulf (Sancetta, 1995; Barron *et al.*, 2004; 2005) indicates that this species prefers a deep thermocline/nutricline. Therefore, its abundance during the deposition of type (4) is consistent with diminishment of the geographic extent of the Trade Winds. The high authigenic flux and strong co-occurrence of type (6) suggest that, due to the reorganisation of the Trade Wind system, intermediate waters entering the Gulf were relatively well ventilated.

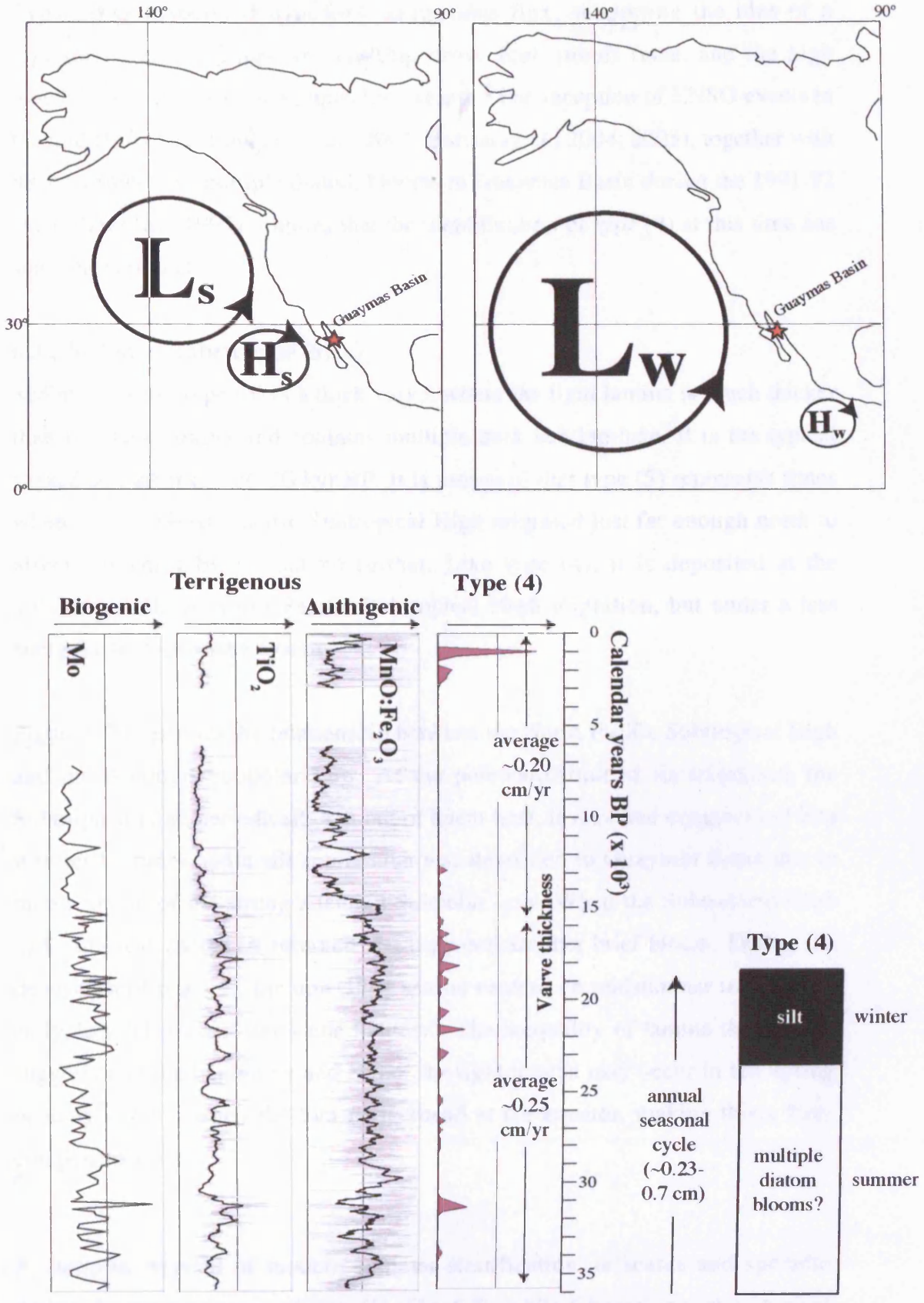


**Figure 6.6:** Interpretation of sediment fabric type (4).

Type (4) is associated with high terrigenous flux, supporting the idea of a vigorous Aleutian Subpolar Low that drove high runoff rates, and the high biogenic flux implies a long upwelling season. The inception of ENSO events in the mid Holocene (Loubere *et al.*, 2003; Barron *et al.*, 2004; 2005), together with the occurrence of multiple diatom blooms in Guaymas Basin during the 1991-92 event (Sancetta, 1995), implies that the identification of type (4) at this time has some basis in fact.

### 6.3.5 Sediment fabric type (5)

Sediment fabric type (5) is a thick varve, where the light lamina is much thicker than the dark lamina and contains multiple dark sub-laminae. It is the typical varved sediment of ~36-20 kyr BP. It is proposed that type (5) represents times when a weak North Pacific Subtropical High migrated just far enough north to affect Guaymas Basin, but no further. Like type (4), it is deposited at the poleward limit of North Pacific Subtropical High migration, but under a less energetic high-pressure system.

Figure 6.7 illustrates the relationship between the North Pacific Subtropical High and the Aleutian Subpolar Low. At the poleward limit of its migration, the Subtropical High periodically ran out of latent heat. It retreated equatorward into warmer latitudes and a silt sub-lamina was deposited in Guaymas Basin due to the incursion of the strong Aleutian Subpolar Low. When the Subtropical High had sufficient energy, it returned and triggered another brief bloom. During the deposition of type (5), the upwelling season centred on midsummer in June and early July (cf present-day Cape Flattery). The inequality of lamina thicknesses suggests that the beginning and end of the light lamina may occur in late spring or early autumn when the Sun is overhead at the equator, making this a five-component varve.

*F. doliolus*, typical of modern summer stratification, is scarce and sporadic during the predominance of type (5) (Fig. 5.7), while *Chaetoceros* spp., typical of the modern upwelling season, are very common. Together, this suggests that stratification did not occur and, perhaps, that summer was the upwelling season.

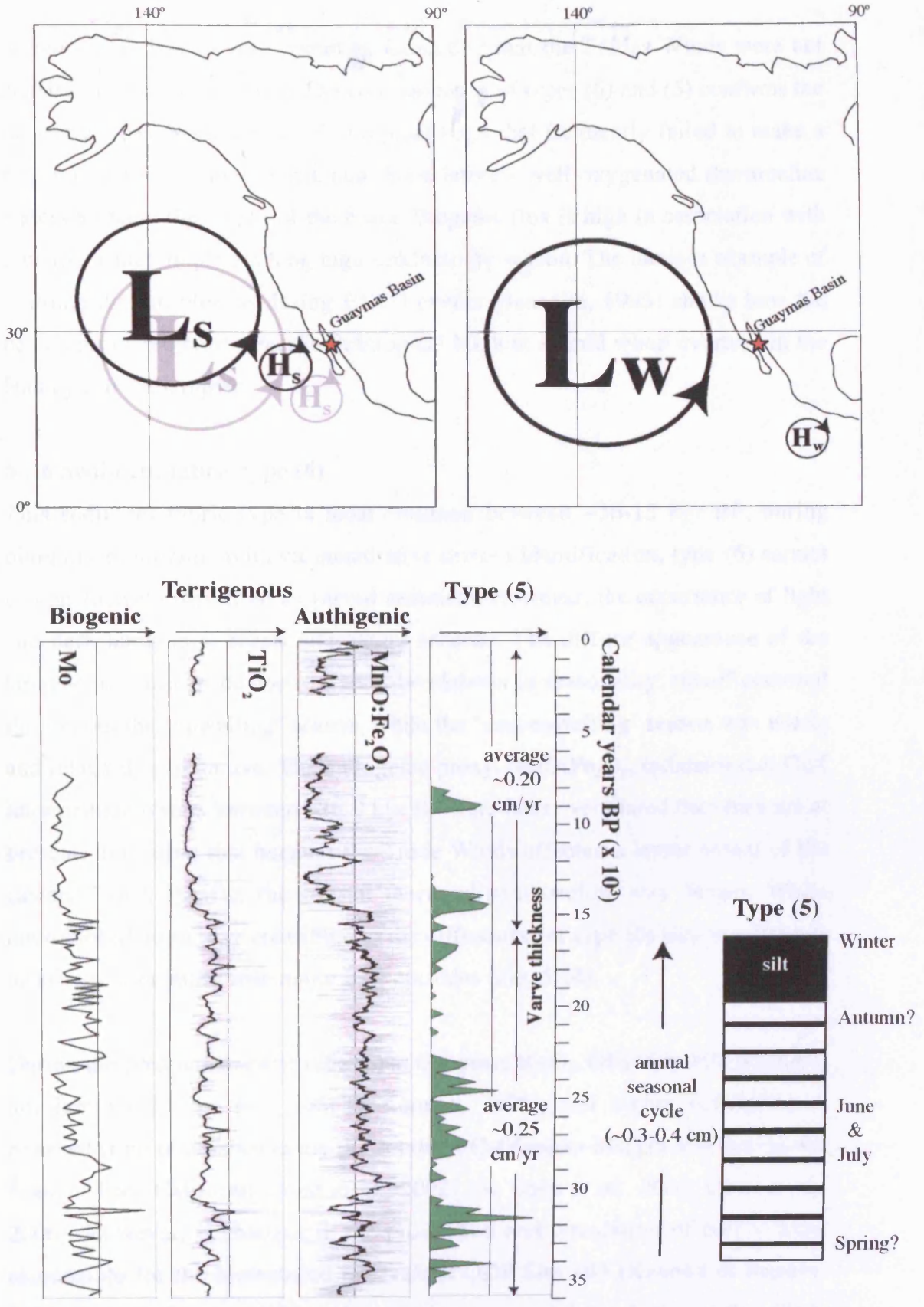


**Figure 6.7:** Interpretation of sediment fabric type (5).

*Azpeitia* spp. is also very common, indicating that the Trades Winds were not consistently active at ~23°N. The co-occurrence of types (6) and (5) confirms the idea of a weak North Pacific Subtropical High that frequently failed to make a full impact in Guaymas Basin, and that relatively well-oxygenated thermocline waters affected the slopes of the basin. Biogenic flux is high in association with type (5), which implies a long high-productivity season. The modern example of multiple diatom blooms during ENSO events (Sancetta, 1995) shows how the behaviour of the North Pacific Subtropical High is altered when overturn in the Hadley cell is disrupted.

### 6.3.6 Sediment fabric type (6)

This sediment fabric type is most common between ~36-15 kyr BP, during obliquity minimum. Without quantitative diatom identification, type (6) cannot be conclusively identified as varved sediment. However, the occurrence of light and dark laminae suggests alternating seasons. The diffuse appearance of the laminae may in part be due to a semi-breakdown in seasonality: runoff occurred throughout the 'upwelling' season, while the 'non-upwelling' season was windy and relatively productive. The authigenic proxy, $MnO:Fe_2O_3$, indicates that Gulf intermediate waters between ~36-9 kyr BP were better ventilated than they are at present, indicating that because the Trade Winds affected a lesser extent of the eastern North Pacific, the coastal thermocline/nutricline was deeper. While microbioturbation may contribute to the diffuseness of type (6) laminae, there is no strong association with major oxic episodes (Fig. 5.14).

During the predominance of type (6) at Guaymas Basin, ODP Site 893 is largely non-laminated (Fig. 6.3; Behl & Kennett, 1996), and higher ventilation is reported from other sites along the southern Californian Margin and the Pacific coast of Baja California (Stott *et al.*, 2002; van Geen *et al.*, 2003; Dean *et al.*, 2006). However, if changes in the production and circulation of NPIW were responsible for the bioturbated intervals at ODP Site 893 (Kennett & Ingram, 1995; Behl & Kennett, 1996), why was there so much bioturbation at the silled, restricted Santa Barbara site, but comparatively little at the Guaymas Basin site, which has an open connection with the Pacific Ocean? A major difference

between the two basins was seasonality. When the North Pacific Subtropical High did not migrate as far as Santa Barbara Basin and the Aleutian Subpolar Low dominated the region all year round, there was little or no contrast between the seasons at ODP Site 893 (cf section 2.5; Heusser, 1998). Inevitably, this resulted in the deposition of homogeneous sediment regardless of the rate of productivity or the preservation factors. Additionally, but incidentally to the deposition of homogeneous sediment, the Trade Winds did not affect the Basin, the bottom waters were better ventilated and bioturbation occurred.

Figure 6.8 illustrates the likely relationship between the high- and low-pressure systems. The North Pacific Subtropical High was relatively weak throughout the year. In summer, it migrated to, or just north of, Guaymas Basin. The Aleutian Subpolar Low dominated the North Pacific and its cyclonic winds ran parallel to those of the North Pacific Subtropical High at their point of interaction. The close proximity of the Aleutian Subpolar Low to Guaymas Basin resulted in runoff during the upwelling season. The situation was similar in winter, except that the Aleutian Subpolar Low was stronger and the North Pacific Subtropical High was weaker.

During the predominance of type (6), the high abundance of *Azpeitia* spp. indicates that the Trade Winds were not continuously active at the mouth of the Gulf. *F. doliolus* and *Rhizosolenia* spp. occur only in strongly varved intervals, particularly when types (1) and (2) occur. Type (6) is associated with high sedimentation rate and, despite likely microbioturbation, TOC flux is also high, indicating high productivity and runoff rates.

### 6.3.7 Sediment fabric type (7)

This type occurs exclusively between ~36 and 11.5 kyr BP during the period of higher-than-present ventilation, but its association with this phenomenon is not clear-cut. Bioturbation is not necessarily the cause of non-laminated sediment in core MD02-2517/2515 (see also Schrader (1982) and Simoneit (1991) for discussion of the homogeneous intervals in DSDP Site 480). Seasonality plays a pivotal role in the occurrence of varved sediment (section 2.8). It is proposed that

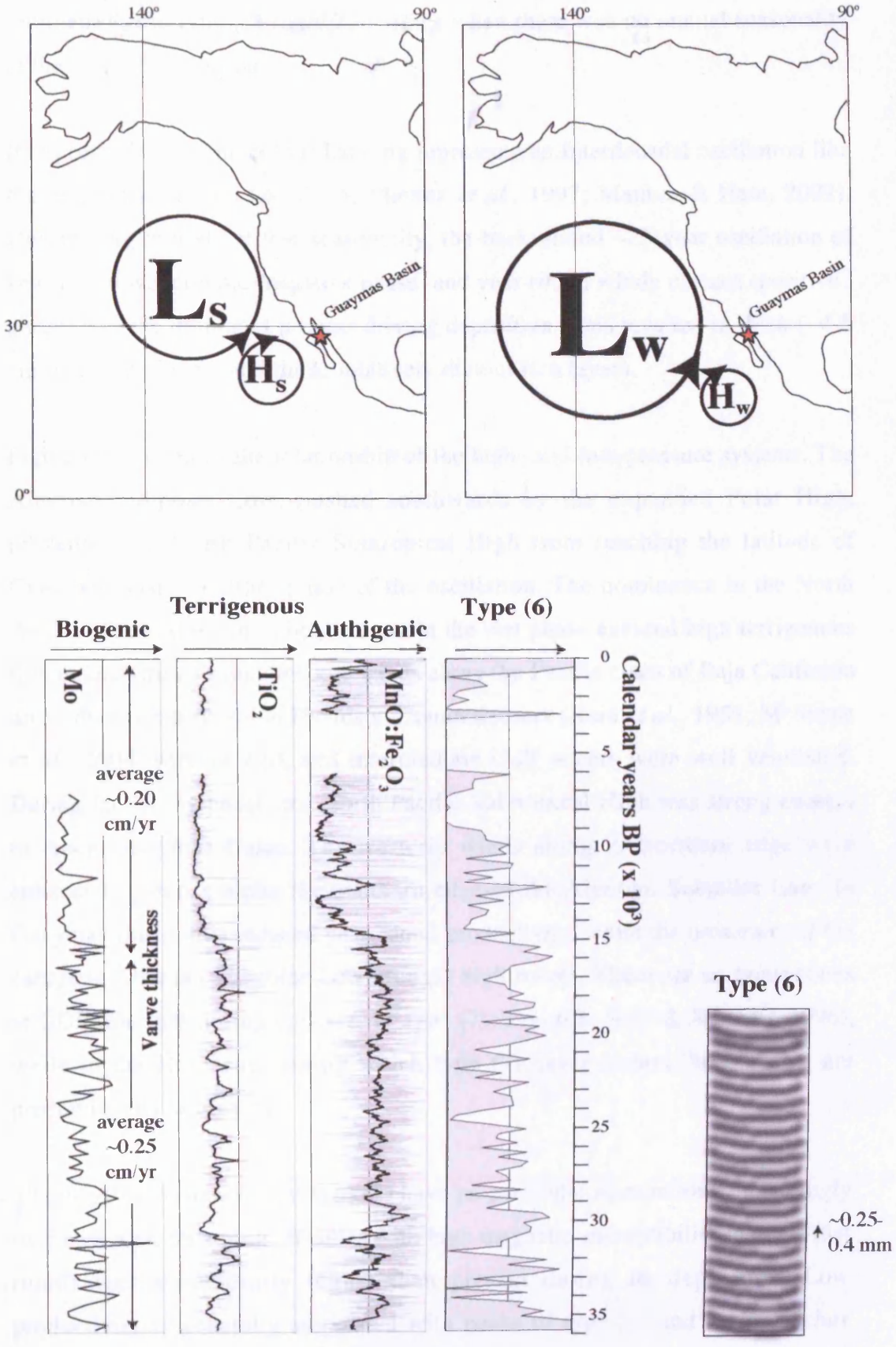


**Figure 6.8:** Interpretation of sediment fabric type (6).

sediment fabric type (7) represents times when there was no annual seasonality in the Gulf of California.

It is proposed that the colour-banding represents an interdecadal oscillation like the modern PDO (section 1.1.5; Mantua *et al.*, 1997; Mantua & Hare, 2002). During long periods of low seasonality, the background ~25-year oscillation of year-round wet climate (negative phase) and year-round windy climate (positive phase) was the dominant process driving deposition. This resulted in thick (~4-5 cm) dark silty layers and thick, relatively diatom-rich layers.

Figure 6.9 illustrates the relationship of the high- and low-pressure systems. The Aleutian Subpolar Low, pushed southwards by the expanded Polar High, prevented the North Pacific Subtropical High from reaching the latitude of Guaymas Basin in either phase of the oscillation. The dominance in the North Pacific of the Aleutian Subpolar Low in the wet phase ensured high terrigenous flux in Guaymas Basin. Onshore winds along the Pacific coast of Baja California drove downwelling of the Davidson Countercurrent (Reid *et al.*, 1958; McShane *et al.*, 2004; section 2.6), and intermediate Gulf waters were well ventilated. During the windy phase, the North Pacific Subtropical High was strong enough to reach Guaymas Basin. The westerly winds along its northern edge were enhanced by those along the southern edge of the Aleutian Subpolar Low. In Guaymas Basin, this induced year-round productivity, while the proximity of the energetic Aleutian Subpolar Low brought high runoff. There are no laminations at ODP Site 893 during episodes of type (7) (Fig. 6.3; Behl & Kennett, 1996), while in the Holocene, during which type (7) never occurs, both basins are predominantly laminated.

The majority of intervals of type (7) have no particular association with strongly oxic episodes. Its strong affinities with high magnetic susceptibility indicate that runoff was significantly higher than present during its deposition. Low productivity is generally associated with peaks of type (7) and *Actinoptychus* spp., a solitary neritic species swept into deeper waters during turbulence (Sancetta, 1995), shows the clearest relationship with it (Fig. 5.7).

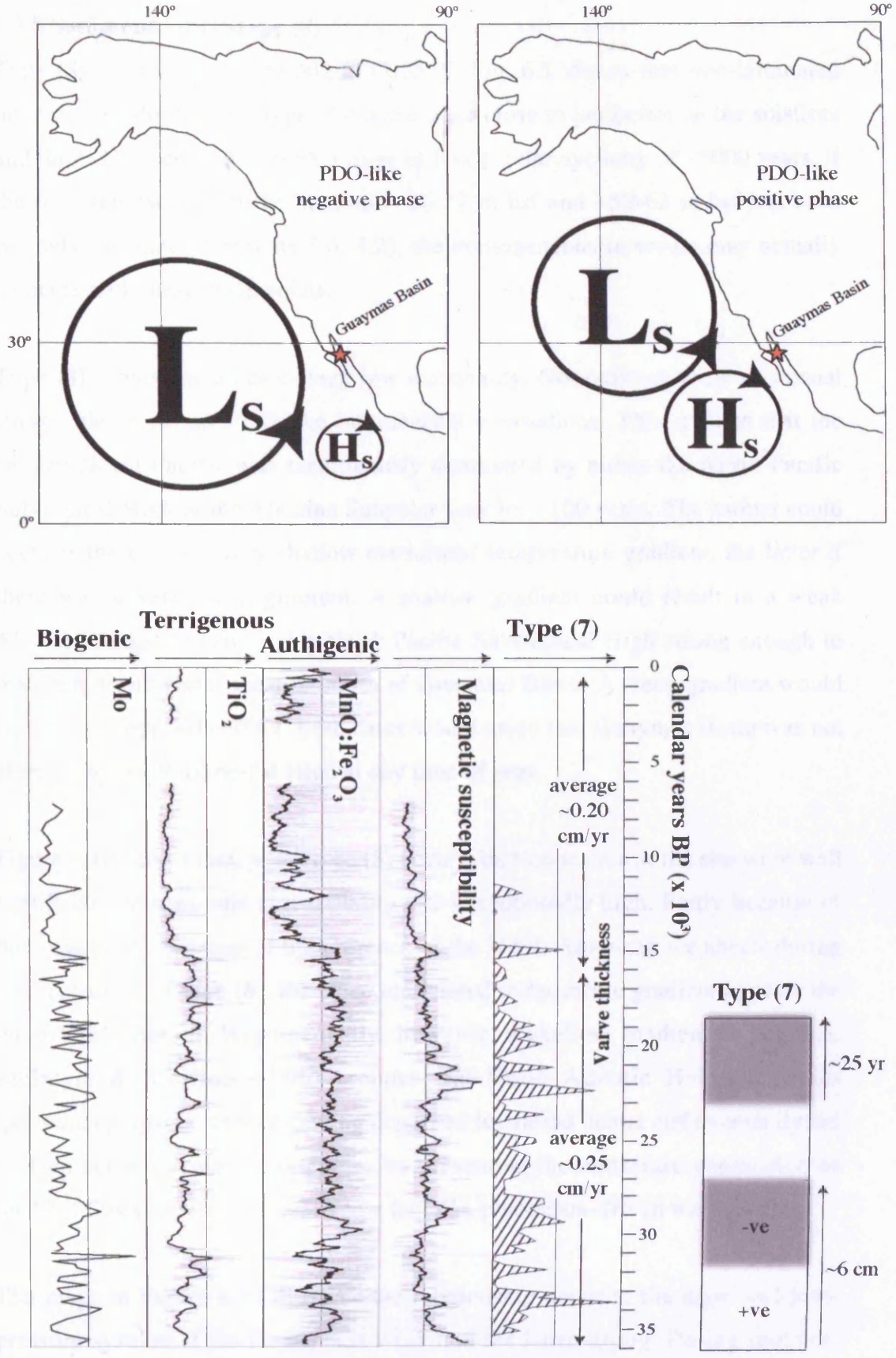


**Figure 6.9:** Interpretation of sediment fabric type (7).

### 6.3.8 Sediment fabric type (8)

Type (8) is rare in core MD02-2517/2515. Fig. 6.1 shows that non-laminated intervals (predominantly type (8)) occur at or close to perihelion at the solstices and the equinoxes, that is, with a more or less regular cyclicity of ~5000 years. If the time represented in the intervals ~26-37 m bsf and ~59-63 m bsf has been wrongly estimated (sections 3.6; 4.2), the homogeneous intervals may actually coincide with these node-points.

Type (8) represents times of very low seasonality. Not only are there no annual varves, there are no PDO-like interdecadal alternations. This implies that the eastern North Pacific was continuously dominated by either the North Pacific Subtropical High or the Aleutian Subpolar Low for ~100 years. The former could occur if there was a very shallow meridional temperature gradient, the latter if there was a very steep gradient. A shallow gradient could result in a weak Aleutian Subpolar Low and a North Pacific Subtropical High strong enough to maintain a midwinter location north of Guaymas Basin. A steep gradient would result in the opposite effect. Both cases would mean that Guaymas Basin was not affected by the Subtropical High at any time of year.

Figure 6.10 shows that, when type (8) occurs, bottom waters at the site were well ventilated and magnetic susceptibility was exceptionally high. Partly because of this, and partly because of the presence of the North American ice sheets during the deposition of type (8), the steep meridional temperature gradient appears the more likely option. Hypothetically, however, a shallow gradient is possible. McIntyre & Molfino (1996) propose that North Atlantic Heinrich events (periodic excessive iceberg calving deposited ice-rafted debris and eventually led to deep-ocean circulation shutdown by preventing the northward penetration of the Gulf Stream) were caused by low-latitude, precession-driven warm events.

The maps in Figure 6.10 illustrate the relationship between the high- and low-pressure systems if the former was weak and the latter strong. During summer, the Aleutian Subpolar Low was pushed south of its present location by feedbacks from the ice sheets. Due to a lack of latent heat (the reduced extent of the Pacific

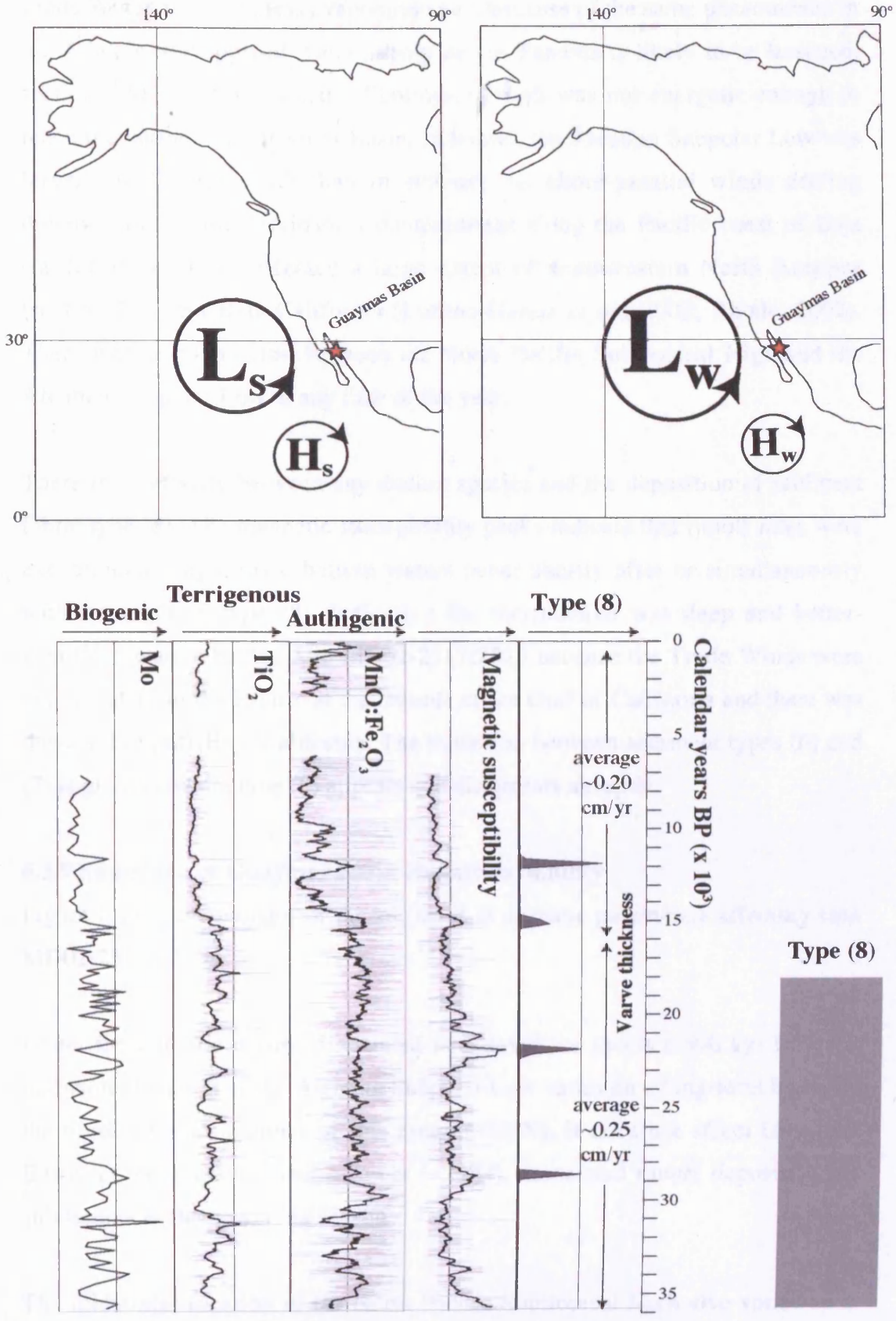


**Figure 6.10:** Interpretation of sediment fabric type (8).

Trade Winds results in less evaporation and, because of the same phenomenon in the Atlantic, transport of water vapour across Panama is likely to be lessened; section 2.5), the North Pacific Subtropical High was not energetic enough to reach the latitude of Guaymas Basin. In winter, the Aleutian Subpolar Low was larger and further south than in summer, its shore-parallel winds driving downwelling of the Davidson Countercurrent along the Pacific coast of Baja California. Its rains affected a large extent of southwestern North America (section 2.5) and Baja California (Lozano-Garcia *et al.*, 2002; Rhode, 2002). There was no interaction between the North Pacific Subtropical High and the Aleutian Subpolar Low at any time of the year.

There is no affinity between any diatom species and the deposition of sediment fabric type (8). The magnetic susceptibility peaks indicate that runoff rates were exceptionally high. Oxic bottom waters occur shortly after or simultaneously with intervals of type (8), indicating the thermocline was deep and better-ventilated waters bathed Site MD02-2517/2515 because the Trade Winds were not operative in the Pacific at the latitude of the Gulf of California and there was downwelling off Baja California. The transition between sediment types (6) and (7) is gradual, while type (8) appears and disappears abruptly.

### 6.3.9 Summary of Guaymas Basin climate variability

Figure 6.11 is a summary of the variation of climatic parameters affecting core MD02-2517/2515.

Under the climatic regime associated with small ice sheets (~9-0 kyr BP), the midwinter location of the Aleutian Subpolar Low varies on a long-term basis. At the northerly end-member of this range (~35°N), it does not affect Guaymas Basin; at the southerly end-member (~30°N), associated runoff deposits a silt sub-lamina in the upwelling season.

The midwinter location of the North Pacific Subtropical High also varies on a long-term basis. The distance the North Pacific Subtropical High migrates from this location controls the timing of the two-part high-productivity season in

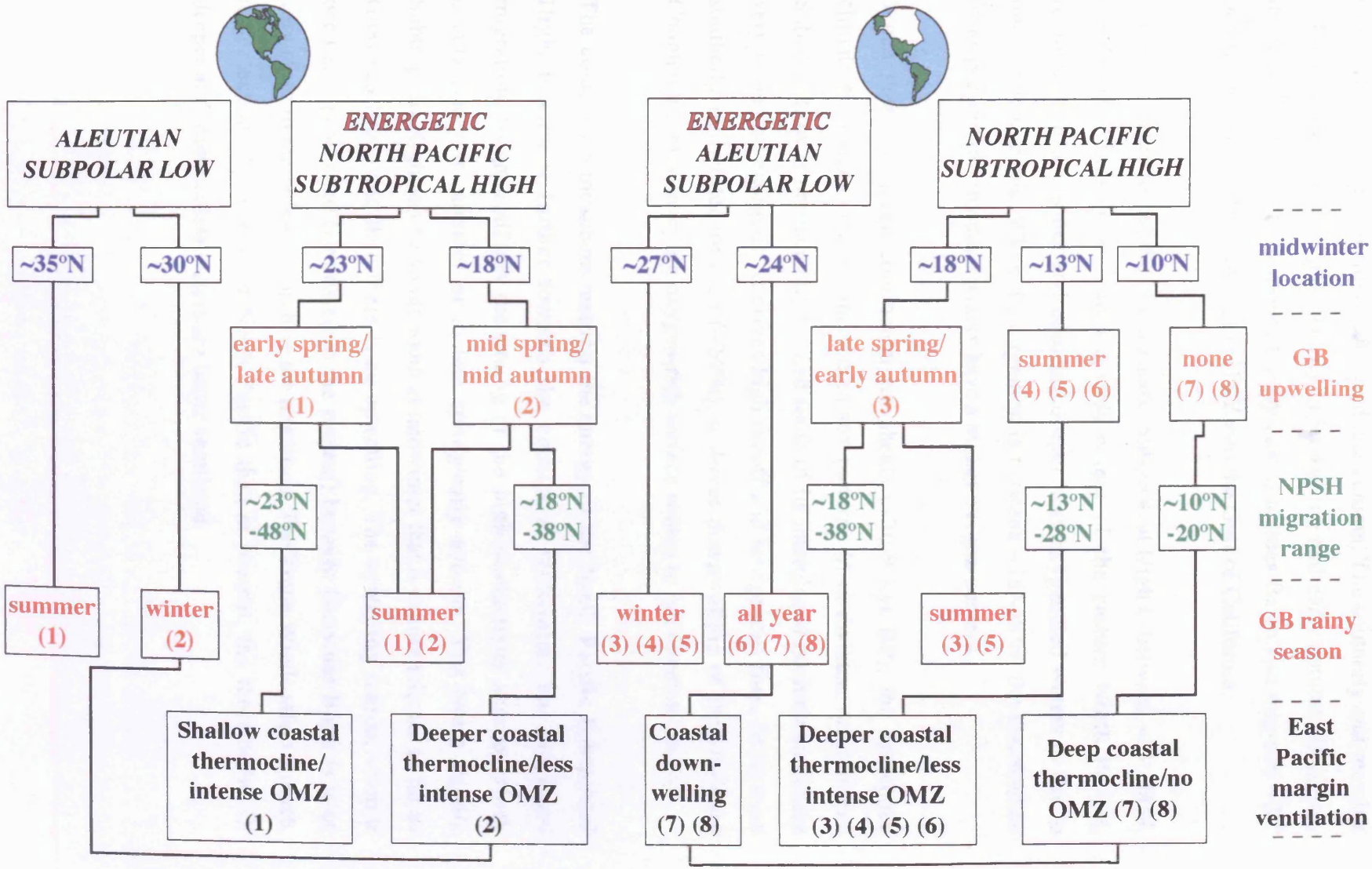


**Figure 6.11:** Summary of the climatic factors affecting Site MD02-2517/2515.

Guaymas Basin. The northerly end-member of the midwinter range (~23°N) causes its occurrence in early spring and late autumn. The southerly end-member (~18°N) occasions high productivity in late spring and early autumn. In spring, the high-pressure system moves briskly past Guaymas Basin and migrates ~25° of latitude polewards, drawing the ITCZ into the Gulf of California.

When the migration of the North Pacific Subtropical High is between ~23°-48°N, the Trade Winds blow across a wide extent of the eastern North Pacific, removing surface water and allowing deeper, less oxygenated waters to rise to intermediate levels. When the migration is between ~18°-38°N, the thermocline is deeper and intermediate waters have a higher oxygen content.

When there are large continental ice sheets (~36-9 kyr BP), the associated climate feedbacks create a more complex pattern. At midwinter, the Aleutian Subpolar Low is permanently located south of its interglacial position and canbe very large and energetic. It drives high runoff and terrigenous flux. At its most southerly midwinter location (~24°N), it drives downwelling of the Davidson Countercurrent, conveying oxygen-rich surface waters to intermediate levels.

The cold, dry atmosphere restricts the energy of the North Pacific Subtropical High, forcing it further towards the equator at midwinter. The increased migration distance affects the timing of the high-productivity season, which occurs either in summer or in late spring/early autumn. The North Pacific Subtropical High can be so far south at midwinter that it cannot migrate as far as Guaymas Basin and then there is no upwelling. The upwelling season, when it occurs, is prolonged (compared to the present) because Guaymas Basin is at or very close to the poleward limit of the migration. The Trade Winds affect a much lesser extent of the eastern North Pacific than at present, the thermocline is deeper and intermediate waters are better ventilated.

## 6.4 The evolution of Guaymas Basin climate over the last ~36,000 years

Figure 6.12 compares the relative abundance of sediment fabric types to the precession and obliquity curves for the last ~36,000 years (Laskar *et al.*, 2004). As a direct reflection of the behaviour of the North Pacific Subtropical High, the dominant varved sediment type (or combination of types) changes on either side of the node points of perihelion at the solstices and equinoxes. The changeover from one type to another builds up and falls away with increasing rapidity immediately before and after the node point.

### 6.4.1 Climate ~36-30.8 kyr BP

The low meridional temperature gradient resulted in a midwinter location of the North Pacific Subtropical High proximal to the Gulf of California. As precession moved towards perihelion at June, the high-productivity season occurred in spring and autumn with increasing frequency. The delivery of heat into the mid-latitudes in autumn led to higher precipitation and ice sheet build-up. The climatic feedback from this eventually resulted in a colder, drier atmosphere, which progressively weakened the North Pacific Subtropical High until less heat was transported to the mid-latitudes and the ice fronts retreated through lack of accumulation. At ~33.5 kyr BP, when the meridional temperature gradient was shallow in both summer and winter, the ice sheets were starved of precipitation because the North Pacific Subtropical High was too weak to migrate as far as Guaymas Basin (cf Ganeshram & Pedersen, 1998; Ortiz *et al.*, 2004). Seasonality broke down and the region was dominated by the onshore winds of the Aleutian Subpolar Low. Variation of the sediment fabric types and the climate proxies demonstrate this millennial-scale pattern of interplay between the North Pacific Subtropical High migration and ice sheet build-up repeating throughout this zone. Dyke *et al.* (2002) refer to the period ~30-27 $^{14}$C kyr BP (~34-31 kyr BP) as the Middle Wisconsinan Interstadial, indicating that in the north of the continent mean annual temperature was relatively warm. At this time in Guaymas Basin, sediment type (5) was predominant, indicating that, although the North Pacific Subtropical High was relatively weak, it was still able to migrate to ~30°N due to the shallow meridional gradient.

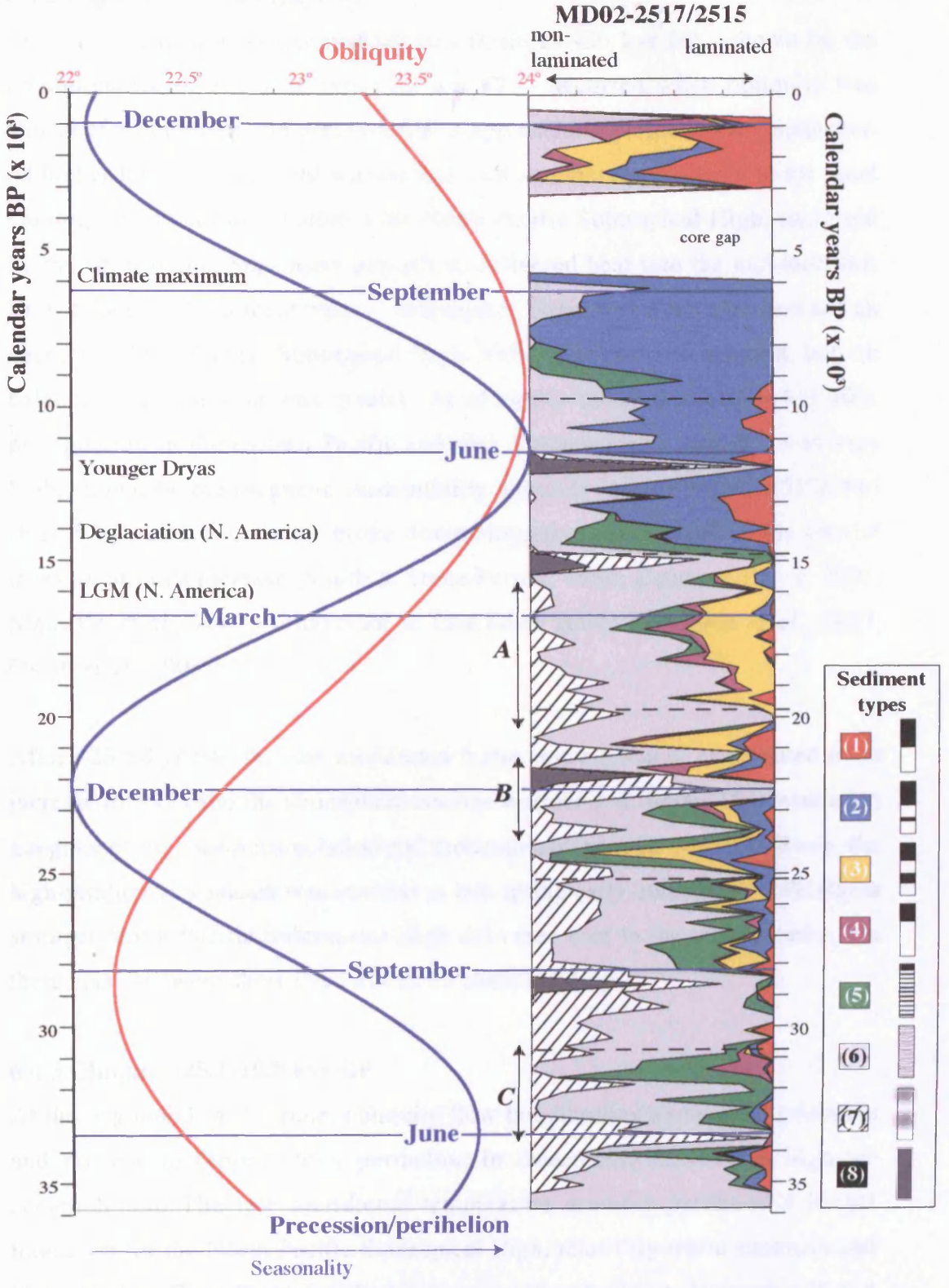


**Figure 6.12:** Relative abundance of sediment types (with sedimentation zones) compared to precession and obliquity for the last ~36 kyr (Laskar, *et al.*, 2004).
***A*** = growth of Cordilleran Ice Sheet;
***B*** = maximum build up of Laurentide Ice Sheet;
***C*** = Middle Wisconsinan Interstadial (Dyke *et al.*, 2002).

### 6.4.2 Climate ~30.8-25.1 kyr BP

The collapse of seasonality in Guaymas Basin at ~30 kyr BP - shown by the predominance of sediment types (6) and (7) - occurred when obliquity was almost at a minimum and precession was approaching perihelion in September. At higher latitudes, the mild winters and cool summers contributed to ice sheet build-up, while at lower latitudes the North Pacific Subtropical High, energised by the approaching September perihelion, delivered heat into the mid-latitudes. Brief episodes of sediment type (1) in Guaymas Basin reveal hot summers and an energetic North Pacific Subtropical High. This contributed to ablation, but, on balance, accumulation was greater. At obliquity minimum (~28.5 kyr BP), precipitation in the eastern Pacific and over western North America was very high, shown by the magnetic susceptibility anomaly in core MD02-2517/2515 (Fig. 5.14), and seasonality broke down altogether. Shorelines of the pluvial lakes record this increase (Smith & Street-Perrott, 1984; Betancourt *et al.* 2001; Metcalfe *et al.*, 2002; Tchakerian & Lancaster, 2002; Holmgren *et al.*, 2003; Oviatt *et al.*, 2003)

After ~28.5 kyr BP, the low meridional temperature gradient contributed to an increase in SSTs and the atmosphere became warmer and wetter. This resulted in a regime of high ice accumulation and moderate ablation. In Guaymas Basin, the high-productivity season was summer or late spring/early autumn. Periodically, a stronger North Pacific Subtropical High delivered heat to the mid-latitudes, but these episodes were short-lived due to ice sheet build-up.

### 6.4.3 Climate ~25.1-19.8 kyr BP

At the beginning of the zone, obliquity (low but climbing away from minimum and precession (approaching perihelion in December) resulted in high ice accumulation. The low meridional temperature gradient permitted a longer migration for the North Pacific Subtropical High, relatively warm summers and high ablation. Overall, this resulted in slow ice sheet build-up. Between ~25 and ~23 kyr BP, climate in Guaymas Basin cycled twice between long episodes of high productivity (~1-1.5 kyr) - occurring in either late spring/early autumn or summer - and complete breakdowns in seasonality.

Dyke *et al.* (2002) state that ~23-20 $^{14}$C kyr BP (~24-21 kyr BP) is the period when the Laurentide Ice Sheet grew to its maximum size. After ~23 kyr BP, climate in Guaymas Basin was either very dry, with a strong North Pacific Subtropical High delivering heat to mid-latitudes, or very wet with a weak Subtropical High unable to pass beyond Guaymas Basin. Rising obliquity and perihelion moving towards March resulted in an energetic North Pacific Subtropical High. The consequent ice build-up and feedback from atmospheric drying was severe, the Subtropical High weakened and was forced towards the equator, allowing the Aleutian Subpolar Low - energised by the Polar High - to dominate regional climate (cf Sabin & Pisias, 1996; Ortiz *et al.*, 1997; Bradbury, 1997). The magnetic susceptibility anomaly between ~22 and ~21 kyr BP (Fig. 5.12) reveals the resultant high precipitation rate in Guaymas Basin.

**6.4.4 Climate ~19.8-14.9 kyr BP**

After ~19.7 kyr BP, Laurentide Ice Sheet-driven feedbacks made a significant contribution to Guaymas Basin climate, primarily energising the Aleutian Subpolar Low, then progressively drying the atmosphere. At the beginning of this zone, obliquity was rising and perihelion was moving towards March, resulting in cool winters at high latitudes and long summers in the Subtropics. Regional seasonality was low and intermittent, relatively ineffective Trade Winds resulted in relatively high ventilation of intermediate waters in Guaymas Basin. As the effects of rising precession and obliquity increased seasonality, high ablation and moderate accumulation of the ice sheets created short-lived wet and dry cycles. The Cordilleran Ice Sheet began to build up (Dyke *et al.*, 2002), fed by precipitation from the very energetic Aleutian Subpolar Low. When perihelion was at March (~17 kyr BP), heat and moisture was delivered to mid-latitudes by the North Pacific Subtropical High in summer and by the Aleutian Subpolar Low in winter (Fig. 6.5). The Subpolar Low - energised by moisture drawn off the Cordilleran Ice Sheet - curtailed the migration north of Guaymas Basin of the relatively energetic Subtropical High, and dominated the eastern North Pacific in both seasons. After ~17 kyr BP, the atmosphere was very dry and, when the Cordilleran Ice Sheet reached its maximum size at ~15 $^{14}$C kyr BP

(~15.5 kyr BP), seasonality completely broke down in Guaymas Basin. This was the North American LGM (Dyke *et al.*, 2002).

### 6.4.5 Climate ~14.9-9.2 kyr BP

The rise towards perihelion at June and obliquity maximum caused increasingly hotter summers and colder winters at higher latitudes. This resulted in very high ablation and a warmer, wetter atmosphere that energised the North Pacific Subtropical High. At the beginning of this zone, the high-productivity season cycled between summer and late spring/early autumn, by ~13 kyr BP, it was alternating between late spring/early autumn and early spring/late autumn. The North Pacific Subtropical High migrated past Guaymas Basin most years, which resulted in fully varved sediment at Santa Barbara Basin (Fig. 6.3; Behl & Kennett, 1996). This was a local effect, however, and sites further north were experiencing glacial conditions (cf Gardner *et al.*, 1997, Heusser, 1998; Stott *et al.*, 2000; Kienast *et al.*, 2002). The delivery of heat and moisture to mid-latitudes by the Subtropical High created feedbacks from the ice sheet and there were long-term cycles of ice build up and atmospheric drying. The most severe of these cycles occurred at ~11.5 kyr BP just before perihelion at June. After this, the predominant upwelling season was late spring/early autumn, denoting an energetic North Pacific Subtropical High with a somewhat restricted migration due to feedbacks from the relatively large ice sheets. The long-term wet and dry cycles continued as obliquity moved towards maximum at ~9.4 kyr BP.

### 6.4.6 Climate ~9.2-0 kyr BP

At the very beginning of the zone, the very cold winters that occurred with obliquity maximum made the meridional temperature gradient steep and the dry atmosphere restricted the migration of the North Pacific Subtropical High. After this, with precession moving perihelion towards September, the long subtropical summers, together with decreasing feedbacks from the shrinking ice sheets, made climate very stable in Guaymas Basin. This was the Holocene climate maximum. At ~3 kyr BP, perihelion as moving towards December and obliquity was declining from maximum. The cool summers and mild winters at high latitudes led to long-term cycles of high accumulation, followed by drying of the

atmosphere and ice front retreat. The Polar Highs expanded during episodes of high accumulation and fed energy into the Subpolar Lows; they contracted during episodes of ablation, which resulted in less active Subpolar Lows. The net result, in the absence of large ice sheets, was wet and dry cycles at mid- to low-latitudes (eg Haug *et al.*, 2003). During the wet cycles, which continue into the present day, the North Pacific Subtropical High was weak and the Aleutian Subpolar Low dominated the eastern North Pacific. In the dry cycles, the energetic Subtropical High dominated the ocean and climate was warm and stable.

## 6.5 Wider implications of the palaeoclimate record from core MD02-2517/2515

The hypothesis formed from the review of glacial climate in the eastern Pacific and across the Americas (section 2.5; Fig. 2.5) is borne out by the highly detailed record of North Pacific Subtropical High behaviour from core MD02-2517/2515. The indications are that, due to changes in the hydrological cycle and reinforced by ice sheet feedbacks, the Subtropical Highs and Trade Winds of both oceans were more closely confined around the equator during the glacial. Consequently, west coast upwelling systems were reduced in poleward extent, coastal thermoclines were deeper and intermediate waters were better ventilated, and water vapour transport by the Trade Winds was reduced, which further weakened the Subtropical Highs. The western halves of North and South America were wetter than present due to the influence of the energetic Subpolar Lows. The eastern halves of the continents were drier than present due to the globally colder atmosphere and the reduction of water vapour transport across the subtropical ocean.

These reorganisations are strongly indicated by the types of sediment fabric laid down at site MD02-2517/2515. The strength of the North Pacific Subtropical High and its interplay with the Aleutian Subpolar Low dictates the number of seasonal laminae deposited each year. Biogenic, terrigenous and authigenic flux also indicate the complex interplay between the atmospheric pressure systems.

During the glacial, the intimate link between the hydrological systems of the Atlantic and the Pacific periodically broke down. At present, the water vapour transported across Panama is lofted from the Doldrums and transported polewards by the Pacific Subtropical Highs. When the Atlantic Trade Winds were confined around the equator, this water vapour was advected into the Amazon Basin where it was recycled by the forest and the River Amazon (cf Colinvaux & de Olivera, 2000)

A consequence of the relocation of water vapour transport from the equatorial Atlantic is that the glacial Pacific Subtropical Highs are less energetic and less capable of transporting atmospheric heat into the mid latitudes. The weak North Pacific Subtropical High cannot modify the behaviour of the dominant Aleutian Subpolar Low, which, as a result, continually feeds moisture into northern North America and contributes to the growth of the ice sheets.

Within the steady rhythm of precession-driven Pacific climate, the sediment fabric and geochemistry of core MD02-2517/2515 reveal a downward trend from ~36-15 kyr BP. The frequent rapid shifts in the extensiveness of the North Pacific Subtropical High migration demonstrate how delicate the balance is between interglacial- and glacial-type hydrological circulation and how sensitive and responsive the equatorial mechanisms are to alterations of heat and moisture input. After ~15 kyr BP, the orbital cycles of precession, obliquity and eccentricity combined to ameliorate climate in equatorial regions, which, over the following ~5 kyr minimised the feedbacks from the continental ice sheets and eventually brought about their destruction. Without the amplification of the ice sheet feedbacks, interglacial climate progresses through the wet and dry cycles, which are driven by precession and modulated by obliquity. Since the hydrological system of the Pacific is so sensitive, it seems that it only requires the extra nudge from high eccentricity combined with low obliquity and perihelion at December, for climate conditions to fix into the spiral of ice sheet build up.

Although the climate record of core MD02-2517/2515 only covers ~36-0 kyr BP - long after the initiation of the last glacial cycle - it can be surmised that at the beginning of the cycle all of the world's Subtropical Highs shift equatorward simultaneously. For the Pacific, this means that the source of water vapour from the Atlantic is cut off. This further weakens the Pacific Subtropical Highs and allows the Subpolar Lows to dominate the mid latitudes, which provides a moisture source for the North American ice sheets. In the Atlantic, the equatorward shift of the Azores Subtropical High and the recycling of the warm pool by the River Amazon results in a less saline Gulf Stream, lower production of NADW and less benign climate over northwest Europe. The Icelandic Subpolar Low dominates the mid latitudes and provides a moisture source for the northern European ice sheets.

# Chapter 7 Conclusions and Future Work

## 7.1 Conclusions

This high-resolution study of laminated sediments of ~36-0 kyr BP from site MD02-2517/2515, Guaymas Basin, reveals a number of important conclusions.

1) Sediment fabric type in this core is a direct reflection of climatic processes in the eastern North Pacific.

2) Sediment fabric in this core can be categorised as eight types, five of which are varved, one is laminated/probably varved, and two are non-laminated.

3) Based on the model of observed climate processes and supported by geochemistry and diatom assemblage, the eight sediment types define the atmospheric/oceanic interactions which produce them.

4) The predominant sediment type/set of climatic interactions changes over time:

a) Between ~36-23 kyr BP, the predominant deposition of type (4) reveals that a weak North Pacific Subtropical High migrates only as far as Guaymas Basin and eastern North Pacific climate is dominated by a strong Aleutian Subpolar Low. High precipitation rate and build up of the Laurentide Ice Sheet.

b) Between ~23-15 kyr BP, the predominant deposition of type (5) reveals that a very weak North Pacific Subtropical High reaches Guaymas Basin only at the equinoxes and eastern North Pacific climate is dominated by a very energetic Aleutian Subpolar Low. High precipitation rate and build up of the Cordilleran Ice Sheet.

c) Between ~15-6 kyr BP, the predominant deposition of type (2) reveals that a strong North Pacific Subtropical High migrates past Guaymas Basin, but while the ice sheets are large the Aleutian Subpolar Low is dominant in winter.

d) Between ~6-0 kyr BP, the predominance of type (1) reveals that a strong North Pacific Subtropical High dominates the low- and mid-latitudes of the eastern North Pacific all year round.

e) Between ~36-15 kyr BP, the high abundance of type (6) reveals that the Trade Winds are not constantly operating at latitudes north of ~23°N.

**5)** North Pacific Subtropical High migration drives changes in the oceanic processes of coastal upwelling and intermediate water ventilation, and changes in atmospheric heat transport which affect ice accumulation and ablation. This model of climate behaviour provides an over-arching mechanism that ties together existing palaeoclimate records from the eastern Pacific.

**6)** The sediment fabric study reveals ~5000-year sedimentation zones of millennial-scale, low frequency change alternating with centennial-scale, high frequency change. These zones are bisected by the occurrence of perihelion at the equinoxes and the solstices. Millennial-scale change occurs in association with perihelion at June or December and centennial-scale change is associated with perihelion at March or September. While both types of change indicate low-latitude forcing with heat and moisture introduced into the mid-latitudes by the North Pacific Subtropical High, the millennial-scale cycles reveal the long-term stability created by milder conditions at high-latitudes.

**7)** Climate ~36-0 kyr BP in Guaymas Basin, controlled by the precession cycle modified by the obliquity cycle, is manifested by wet/dry cycles amplified or dampened by feedbacks from large or small ice sheets.

**8)** North Pacific Subtropical High migration over the last ~36,000 years shows that the Trade Winds are confined around the equator during the glacial. Regionally, this results in better-than-present ventilation of intermediate depth coastal waters. The wider implication is that, if the Atlantic Trade Winds are similarly forced equatorwards, water vapour will be advected into the Amazon Basin rather than across the Panama Isthmus. This diminishes the energy available for Pacific Subtropical High migration, which reduces their capability

of transporting heat to the mid-latitudes. It also results in lower salinity Gulf Stream waters.

## 7.2 Future work

Quantitative diatom identification will closely define and further constrain the sediment fabric types. The additional sediment fabric types identified but not used during this study should be analysed in order to investigate whether more modes of climate behaviour can be defined. Time series analysis of the geochemical data will quantitatively identify the long- and short-term cyclicity within core MD02-2517/2515.

The tentative correlation with ODP Site 893, Santa Barbara Basin, and the $\delta^{18}O$ record of GISP2 ice core, Greenland, reveals possible discrepancies in the age model of this study. These can be corrected by obtaining radiometric dates for the Guaymas Basin core. While the discrepancies do not affect the overall age model in this study, better age-constraint will provide a definitive model of eastern North Pacific climate behaviour over time.

This study reveals the excellence of the laminated record from Guaymas Basin. The site is ideally located at the wet/dry subtropical divide and is capable of tracking high-resolution climate change through time. DSDP Site 480 shows that a much longer record (~250,000 years) is obtainable from Guaymas Basin. A core of this length would provide high-resolution data through two glacial cycles and would be an invaluable, unique palaeoclimate record. Given the hydrological link to the Atlantic Ocean through water vapour transport across Panama, Guaymas Basin sediment would provide a means of tracking global climate change other than records from the Atlantic Ocean, which is overly sensitive to its own feedback mechanisms.

## **Appendix II** [on CD]

Age model:
- MD02-2515 stable isotopes
- Varve thickness
- Comparison with SPECMAP

Core images:
- MD02-2517
- MD02-2515

Sediment fabric analyses:
- Sediment fabric types

## **Appendix III** [on CD]

Shipboard results
- Colour analysis
- Magnetic susceptibility
- Sediment density

Geochemistry
- Discrete XRF analysis
- Continuous XRF analysis
- Carbon and biogenic silica analyses
- Total organic carbon analysis (AMS)

Diatoms
- Semi-quantitative abundance
- Assemblage

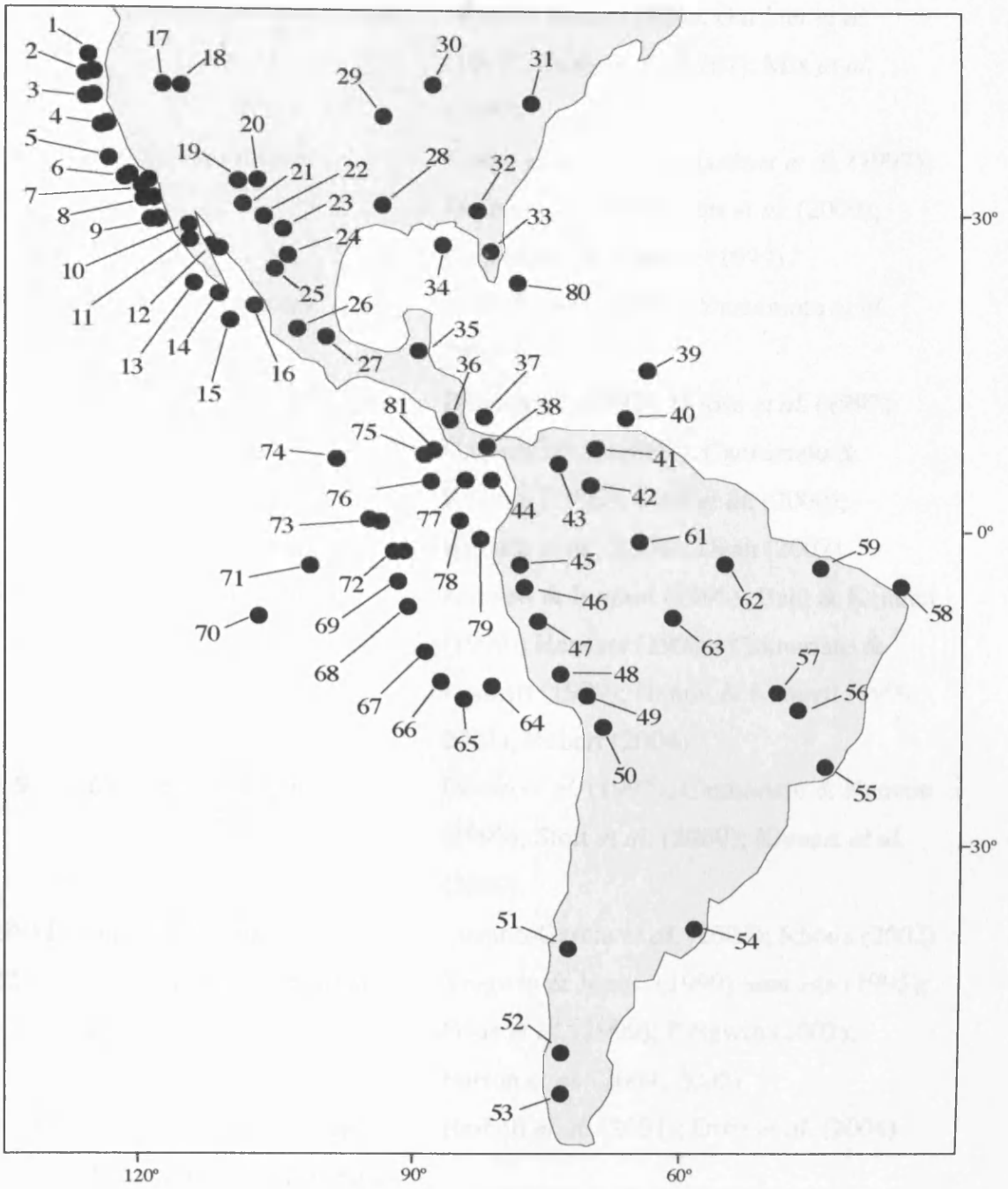


**Appendix IV:** Key to locations used in the construction of Figure 2.5.

**Appendix IV:** Locations and references to construct Fig. 2.5:

| | Location | References |
|---|---|---|
| **1** | *California-Oregon border* | Sabin & Pisias (1996); Gardner *et al.* (1997); Dean *et al.* (1997); Mix *et al.* (1999) |
| **2-4** | *California margin* | Doose *et al.* (1997); Gardner *et al.* (1997); Dean *et al.* (1997); Stott *et al.* (2000); Cannariato & Kennett (1999) |
| **5** | *California Current* | Herbert *et al.* (2001); Yamamoto *et al.* (2007) |
| **6** | *California margin* | Dean *et al.* (1997); Doose *et al.* (1997); Gardner *et al.* (1997); Cannariato & Kennett (1999); Stott *et al.* (2000); Kienast *et al.* (2002); Dean (2007) |
| **7** | *Santa Barbara Basin* | Kennett & Ingram (1995); Behl & Kennett (1996); Heusser (1998); Cannariato & Kennett (1999); Hendy & Kennett (1999, 2003); Robert (2004) |
| **8-9** | *California margin* | Doose *et al.* (1997); Cannariato & Kennett (1999); Stott *et al.* (2000); Kienast *et al.* (2002) |
| **10-11** | *Baja California* | Lozano-Garcia *et al.* (2002); Rhode (2002) |
| **12** | *Guaymas Basin, Gulf of California* | Keigwin & Jones, (1990) Sancetta (1995); Pride *et al.* (1999); Keigwin (2002); Barron *et al.* (2004; 2005) |
| **13-15** | *California Current and Magdalena Margin, Baja California* | Herbert *et al.* (2001); Ortiz *et al.* (2004) |
| **16** | *Matzatlán, Mexico* | Ganeshram & Pedersen (1998) |
| **17-18** | *Lakes Bonneville & Lahontan, southwest USA* | Hostetler *et al.* (1994); Reheis (1999); Oviatt *et al.* (2003); Tchakerian & Lancaster (2000) |
| **19-20** | *New Mexico* | Betancourt *et al.* (2001); Holmgren *et al.* |

| | | |
|---|---|---|
| | | (2003); Menking *et al.* (2004) |
| **21-25** | *Sonora & Chihuahua Deserts, northwest Mexico* | van Devender (1990a & b); Metcalfe *et al.* (2002) |
| **26** | *Patzcuaro, Michoan, Mexico* | Watts & Bradbury (1982) |
| **27** | *Cuenco de Mexico* | Bradbury (1989) |
| **28** | *Pinckneyville Creek, Missouri* | Jackson *et al.* (2000 and refs) |
| **29** | *Graham County, Kansas* | Jackson *et al.* (2000 and refs) |
| **30** | *Anderson Run, Ohio* | Jackson *et al.* (2000 and refs) |
| **31** | *Browns Pond, Virginia* | Jackson *et al.* (2000 and refs) |
| **32** | *Sheelar Lake, Florida* | Jackson *et al.* (2000 and refs) |
| **33** | *Lake Tulane, Florida* | Watts & Hansen (1988) |
| **34** | *Northeast Gulf of Mexico* | Emiliani *et al.* (1975) |
| **35** | *Laguna de Quexil, Guatemala* | Leyden *et al.* (1993) |
| **36** | *Parque Vicente Lachner, Costa Rica* | Martin (1964); Leyden, *et al.* (1993) |
| **37** | *Western Caribbean* | Kameo *et al.* (2004) |
| **38** | *El Valle, Panama* | Bush & Colinvaux (1990) |
| **39** | *Barbados* | Guilderson *et al.* (1994) |
| **40** | *Cariaco Basin, Venezuela* | Overpeck *et al.* (1989); Lea *et al.* (2003); Peterson *et al.* (2000a; 2000b); Yarincik *et al.* (2000); Haug *et al.* (2001); Peterson & Haug, (2006) |
| **41** | *Lake Valencia, Venezuela* | Bradbury *et al.* (1981); Leyden (1985) |
| **42** | *Laguna de Fuquene, Colombia* | van Geel & van der Hammen (1973) |
| **43** | *Llanos Orientales, Colombia* | Behling & Hooghiemstra (1998) |
| **44** | *Cuenca de Panama* | Pedersen *et al.* (1991) |
| **45-46** | *Lake San Juan Bosco; Laguna Pallcacocha,* | Colinvaux *et al.* (1997); Rodbell *et al.* (1999) |

| | | |
|---|---|---|
| | *Ecuador* | |
| **47-48** | *Laguna Baja; Lakes Junin & Titicaca, Peru* | Hansen & Rodbell (1995); Seltzer *et al.* (2002) |
| **49** | *Subtropical Andes* | van der Hammen & Absy (1994) |
| **50** | *Peruvian-Bolivian Andes* | Klein *et al.* (1999) |
| **51** | *Huelmo, Chile* | Moreno & Leon (2003); Hajdas *et al.* (2003) |
| **52-53** | *Southern Andes, Chile* | Hulton *et al.* (2002) |
| **54** | *Eastern Argentina* | Prieto (2000) |
| **55** | *Southeast Brazil* | Behling & Lichte (1997) |
| **56-57** | *Subtropical Brazil* | Salgado-Labouriau *et al.* (1998) |
| **58** | *Northeast Brazil* | Arz *et al.* (1998); Wang *et al.* (2004) |
| **59** | *Lagoa de Caco, Brazil* | Jacob *et al.* (2004) |
| **61-62** | *Amazon Basin* | Colinvaux & de Olivera (2000); McCulloch *et al.* (2000) |
| **63** | *Western Brazil* | de Freitas *et al.* (2001) |
| **64-71** | *Eastern Equatorial Pacific* | Loubere (2002); Andreason & Ravelo (1997) |
| **72-73** | *Galapagos* | Koutavas *et al.* (2002); Lea *et al.* (2000); Lea *et al.* (2006) |
| **74-79** | *Eastern Equatorial Pacific* | Loubere (2002) |
| **80** | *Florida Straits* | Lynch-Stieglitz *et al.* (1999) |
| **81** | *Eastern Pacific Warm Pool* | Benway *et al.* (2006); Leduc *et al.* (2007) |

## References


Alvarez-Borrego, S., 1983, *The Gulf of California*; in, Ketchum, B.H. (ed), *Estuaries and enclosed seas*, Elsevier Science, New York: 427-449.

Andersen, K.K., Azuma, N., Barnola, J.M., Bigler, M., Biscaye, P., Caillon, N., Chapellaz, J., Clausen, H.B., Dahl-Jensen, D., Fischer, H., Flückiger, J., Fritzsche, D., Fujii, Y., Goto-Azuma, K., Grønvold, K., Gundestrup, N.S., Hansson, M., Huber, C., Hvidberg, C.S., Johnsen, S.J., Jonsell, U., Jouzel, J., Kipfstuhl, S., Landais, A., Leuenberger, M., Lorrain, R., Masson-Delmotte, V., Miller, H., Motoyama, H., Narita, H., Popp, T., Rasmussen, S.O., Raynaud, D., Rothlisberger, R., Ruth, U., Samyn, D., Schwander, J., Shoji, H., Siggard-Andersen, M.-L., Steffensen, J.P., Stocker, T., Sveinbjörnsdottir, A.E., Svensson, A., Takata, M., Tison, J.-L., Thorsteinsson, Th., Watanabe, O., Wilhelms, F., White, J.W.C., 2004, *High-resolution record of Northern Hemisphere climate extending into the last interglacial period*; Nature **431**: 147-151.

Anderson, R.Y., 1993, *The varve chronometer in Elk Lake: record of climatic variability and evidence for solar-geomagnetic-$^{14}C$-climate connection*; in Bradbury, J.P., Dead, W.E. (eds), *Elk Lake, Minnesota: evidence for rapid climate change in the North-Central United States*; Geological Society of America Special Paper **276**: 45-67.

Anderson, R.Y., 1996, *Seasonal sedimentation: a framework for reconstructing climatic and environmental change*; in Kemp, A.E.S. (ed), *Palaeoclimatology and palaeoceanography from laminated sediments*; Geological Society Special Publication **116**: 1-15.

Andreason, D.J., Ravelo, A.C., 1997, *Tropical Pacific Ocean thermocline depth reconstructions for the Last Glacial Maximum*; Paleoceanography **12**: 395-413.

Arz, H.W., Pätzold, J., Wefer, G., 1998, *Correlated millennial-scale changes in surface hydrography and terrigenous sediment yield from Last-glacial marine deposits off northeastern Brazil*; Quaternary Research **50**: 157-166.

Baba, J., Petersen, C.D., Schrader, H.J., 1991a, *Fine-grained terrigenous sediment supply and dispersal in the Gulf of California during the last century*; in *The Gulf and Peninsular Province of the Californias*, Dauphin, J.P., Simoneit, B.R.T. (eds) American Association of Petroleum Geologists Memoir **47**: 569-599.

Baba, J., Peterson, C.D., Schrader, H.J., 1991b, *Modern fine-grained sediments in the Gulf of California*, in *The Gulf and Peninsular Province of the Californias*, Dauphin, J.P., Simoneit, B.R.T. (eds) American Association of Petroleum Geologists Memoir **47**: 569-599.

Badon-Dangon, A., Dorman, C.E., Merrifield, M.A., Winant, C.D., 1991, *The lower atmosphere over the Gulf of California*; Journal of Geophysical Research **96**: 16,877-16896.

Balsam, W.L., Deaton, B.C., Damuth, J.E., 1999, *Evaluating optical lightness as a proxy for carbonate content in marine sediment cores*, Marine Geology **161**: 141-153.

Barron, J.A., Bukry, D., Bischoff, J.L., 2004, *High resolution paleoceanography of the Guaymas Basin, Gulf of California, during the past 15,000 years*; Marine Micropaleontology **50**: 185-207.

Barron, J.A., Bukry, D., Dean, W.E., 2005, *Paleoceanographic history of the Guaymas Basin, Gulf of California, during the past 15,000 years based on diatoms, silicoflagellates, and biogenic sediments*; Marine Micropaleonotology **56**: 81-102.

Barry, R.G., Chorley, R.J., 2003, *Atmosphere, weather and climate*, 8th Edition, Routledge, London, pp421.

Baumgartner, T.R., Christiansen, N., 1985, *Coupling of the Gulf of California to large-scale interannual variability*; Journal of Marine Research **43**: 825-848.

Baumgartner, T.R., Ferreira-Bartrina, V., Cowen, J., Soutar, A., 1991a, *Reconstruction of a 20th Century varve chronology from the central Gulf of California*, in Dauphin, J.P., Simoneit, B.R. (eds), *The Gulf and Peninsular Province of the Californias*, American Association of Petroleum Geologists Memoir **47**: 603-616.

Baumgartner, T.R., Ferreira-Bartrina, V., Hentz-Moreno, P., 1991b, *Varve formation in the central Gulf of California: a reconsideration of the origin of the dark laminae from the 20th century record*; in Dauphin, J.P., Simoneit, B.R. (eds), *The Gulf and Peninsular province of the Californias*; American Association of Petroleum Geologists Memoir **47**: 617-636.

Baumgartner, T.R., Soutar, A., Ferreira-Bartrina, V., 1992, *Reconstruction of the history of Pacific sardine and Northern anchovy populations over the past two millennia from sediments of the Santa Barbara Basin, California*; Californian Co-operative Oceanic Fisheries Investigations Report **33**: 24-40.

Beaufort, L., and the members of the scientific party, 2002, Cruise Report: MD 126, MONA IMAGES VIII. Institut Polaire Français Paul-Emile Victor (IPEV), Plouzané, France, pp 453.

Behl, R.J., Kennett, J.P., 1996, *Brief interstadial events in the Santa Barbara basin, NE Pacific, during the past 60 kyr*; Nature **379**: 243-246.

Behling, H., Hooghiemstra, H., 1998, *Late Quaternary palaeoecology and palaeoclimatology from pollen records of the savannas of the Llanos Orientales in Colombia*; Palaeogeography, Palaeoclimatology, Palaeoecology **139**: 251-267.

Behling, H., Lichte, 1997, *Evidence of dry and cold climatic conditions at glacial times in tropical southeastern Brazil*; Quaternary Research **48**: 348-358.

Benway, H.M., Mix, A.C., Haley, B.A., Klinkhammer, G.P., 2006, *Eastern Pacific Warm Pool paleosalinity and climate variability: 0-30 kyr*; Paleoceanography **21**: doi:1029/2005PA001208.

Betancourt, J.L., Rylander, K.A., Peñalba, M.C., McVickar, J.L., 2001, *Late Quaternary vegetation history of Rough Canyon, central New Mexico, USA*, Palaeogeography, Palaeoclimatology, Palaeoecology **165**: 71-95.

Bigg, G.R., 2003, *The oceans and climate*; 2nd Edition, Cambridge University Press, Cambridge: pp 273.

Bond, G., Heinrich, H., Broecker, W., Labeyrie, L., McManus, L., Andrews, J., Huon, S., Jantschik, R., Clasen, S., Simet, C., Tedesco, K., Klas, M., Bonani, G. and Ivy, S., 1992, *Evidence for massive discharges into the North-Atlantic Ocean during the last glacial period*; Nature **360**: 245-249.

Bradbury, J.P., 1989, *Late Quaternary lacustrine paleoenvironments in the Cuenca de Mexico*; Quaternary Science Reviews **8**: 75-100.

Bradbury, J.P., 1997, *Sources of glacial moisture in Mesoamerica*; Quaternary International **43/44**: 97-110.

Bradbury, J.P., Leyden, B.W., Salgado-Labouriau, M., Lewis, W.M., Jr., Binford, M.W., Frey, D.G., Whitehead, D.N.K., Weibezahn, F.H., 1981, *Late Quaternary environmental history of Lake Valencia, Venezuela*; Science **214**: 1299-1305.

Bradley, R.S., 1999, *Paleoclimatology: reconstructing climates of the Quaternary*; in Dmowska, R., Holton, J.R. (eds), *International Geophysics Series* Vol. **64**, pp613, 2nd Edition, Academic Press, San Diego.

Bray, N., 1988, *Thermohaline circulation in the Gulf of California*; Journal of Geophysical Research **93**: 4993-5020.

Bray, N., Robles, J.M., 1991, *Physical oceanography of the Gulf of California*; in Dauphin, J.P., Simoneit, B.R. (eds) *The Gulf and Peninsular province of the Californias*; American Association of Petroleum Geologists Memoir **47**: 511-553.

Broecker, W.S., 1990, *Salinity history of the Northern Atlantic during the last deglaciation*; Palaeoceanography **5**: 459-467.

Broecker, W.S., Peng, T-H., 1982, *Tracers in the sea*, Lamont-Doherty Geological Observatory Publication, Columbia University, Palisades, New York.

Broecker, W.S., Bond, G., Klas, M., Bonani, G., Wolfi, W., 1990, *A salt oscillator in the glacial Atlantis? The concept*; Paleoceanography **5**: 469-477.

Brumsack. H.-J., 2006, *The trace metal content of recent organic carbon-rich sediments: implications for Cretaceous black shale formation*, Palaeogeography, Palaeoclimatology, Palaeoecology **232**: 344-361.

Bull, D., Kemp, A.E.S., 1995, *Composition and origins of laminae in late Quaternary and Holocene varved sediments from Santa Barbara Basin*; in Kennett, J.P., Baldauf, J.G., Lyle, M. (eds) *Proceedings of the Ocean Drilling Program, Scientific Results* **146** (pt 2), College Station Texas, 77-87.

Bush, M.B., Colinvaux, P.A., 1990, *A pollen record of a complete glacial cycle from lowland Panama*; Journal of Vegetation Science **1**: 105-118.

Calvert, S.E., 1966, *Accumulation of diatomaceous silica in the sediments of the Gulf of California*; Geological Society of America Bulletin **85**: 1893-1904.

Calvert, S.E., Karlin, R.E., 1998, *Organic carbon accumulation in the Holocene sapropel of the Black Sea*, Geology **26**: 107-110.

Cannariato, K., Kennett, J.P., 1999, *Climatically related millennial-scale fluctuations in strength of California margin oxygen-minimum zone during the past 60 ky*; Geology **27**: 975-978.

Chavez, F.P., Pennington, J.T., Castro, C.G., Ryan, J.P., Michisaki, R.P., Schlining, B., Walz, P., Buck, K.R., McFadyen, A., Collins, C.A., 2002, *Biological and chemical consequences of the 1997-1998 El Niño in central California waters*; Progress in Oceanography **54**: 205-232.

Chavez, F.P., Ryan, J., Lluch-Cota, S.E., Ñiquen, M.C., 2003, *From anchovies to sardines and back: multidecadal change in the Pacific Ocean*; Science **299**: 217-221.

Cheshire, H., Thurow, J., Nederbragt, A.J., 2005, *Late Quaternary climate change record from two long sediment cores from Guaymas Basin, Gulf of California*; Journal of Quaternary Science **20**: 457-469.

Clement, A.C, Seager, R., Cane, M.A., 1999, *Orbital controls on the El Niño/Southern Oscillation and the tropical climate*; Paleoceanography **14**: 441-456.

Colinvaux, P.A., Bush, M.B., Steinitz-Kannan, M., Miller, M.C., 1997, *Glacial and postglacial pollen records from the Ecuadorian Andes and Amazon*; Quaternary Research **48**: 69-78.

Colinvaux, P.A., de Olivera, P.E., 2000, *Palaeoecology and climate of the Amazon Basin during the last glacial cycle*; Journal of Quaternary Science **15**: 347-356.

Comité de la Carta Geologíca de México, 1960, *Carta Geologíca de la Répúblíca Méxicana*; Perry-Casteñada Library Map Collection, University of Texas.

Croudace, I.W., Rindby, A., Rothwell, R.G., 2006, *ITRAX: description and evaluation of a new multi-function X-ray core scanner*; in Rothwell, R.G. (ed), 2006, *New techniques in sediment core analysis*; Geological Society of London Special Publication **267**: 51-63.

Curray, J.R.; Blakeslee, J., Platt, L.W., Stout, L.N., Moore, D.G. Aguayo, J.E. Aubry, M.-P., Einsele, G. Fornari, D.J. Gieskes, J.M., Guerrero, G.J., Kastner, M., Kelts, K.R. Lyle, M. Matoba, Y., Molina-Cruz, A. Niemitz, J., Rueda-Gaxiola, J., Saunders, A.D., Schrader, H., Simoneit, B.R.T., Vacquier, V. (eds) 1982, *Initial Reports of the Deep Sea Drilling Project, Leg 64*: Washington DC, U.S. Government Printing Office, pp1313.

Dansgaard, W., Johnsen, S.J., Clausen, H.B., Dahl, J.D., Gundestrup, N.S., Hammer, C.U., Hvidberg, C.S., Steffensen, J.P., Sveinbjornsdottir, A.E., Jouzel, J., Bond, G., 1993, *Evidence for general instability of past climate from a 250-kyr ice-core record*; Nature **364**: 218 – 220.

Dean, J.M., Kemp, A.E.S., Bull, D., Pike, J., Patterson, G., Zolitscha, B., 1999, *Taking varves to bits: scanning electron microscopy in the study of laminated sediments and varves*; Journal of Palaeolimnology **22**: 121-136.

Dean, W.E., Anderson, R.Y., 1974, *Application of some correlation coefficient techniques to time-series analysis*; Mathematical Geology **6**: 363-372.

Dean, W.E., Gardner, J.V., Piper, D.Z., 1997, *Inorganic geochemical indicators of glacial-interglacial changes in productivity and anoxia in the California continental margin*; Geochimica et Cosmochimica Acta **61**: 4507-4518.

Dean, W., Pride, C., Thunell, R., 2004, *Geochemical cycles in sediments deposited on the slopes of the Guaymas and Carmen Basins of the Gulf of California over the last 180 years*; Quaternary Science Reviews **23**: 1817-1833.

Dean, W.E., Zheng, Y., Ortiz, J.D., van Geen, A., 2006, *Sediment Cd and Mo accumulation in the oxygen-minimum zone off western Baja California linked to global climate over the past 52 kyr*; Paleaoceanography **21**: doi: 10.1029/2005PA001239

de Diego, T., Douglas, R.G., 1999, *Oxygen-related sediment microfabrics in modern 'black shales', Gulf of California, Mexico*; Journal of Foraminiferal Research **29**: 453-464.

de Freitas, H.A., Pessenda, L.C.R., Aravena, R., Marques, Gouveia, S.E., de Souza Ribeiro, A., Boulet, R., 2001, *Late Quaternary vegetation dynamics in the Southern Amazon inferred from carbon isotopes in soil organic matter*; Quaternary Research **55**: 39-46.

de la Lanza-Espino, G., Soto, L.A., 1999, *Sedimentary geochemistry of hydrothermal vents in Guaymas Basin, Gulf of California,* Applied Geochemistry, **14**: 499-510.

Delgadillo-Hinojosa, F., Marcias-Zamora, J.V., Segovia-Zavala, J.A., Tores-Valdes, S., 2001, *Cadmium enrichment in the Gulf of California*; Marine Chemistry **75**: 109-122.

Doose, H., Prahl, F.G., Lyle, M.W., 1997, *Biomarker temperature estimates for modern and last glacial surface waters of the California Current system between 33° and 42° N*; Paleoceanography, **12**, 615-622.

Douglas, M.W., Maddox, R., Howard, K., Reyes, S., 1993, *The Mexican monsoon*; Journal of Climatology **6**:1665-1667.

Dyke, A.S., Andrews, J.T., Clark, P.U., England, J.H., Miller, G.H., Shaw, J., Veillette, J.J., 2002, *The Laurentide and Innuitian ice sheets during the Last Glacial Maximum*; Quaternary Science Reviews **21**: 9-31.

Einsele, G., 1992, *Sedimentary Basins: evolution, facies and sedimentary budget*; Springer-Verlag, Berlin, pp628.

Einsele, G., Gieskes, J.M., Curray, J., Moore, D.M., Aguayo, E., Aubry, M.-P., Fornari, D., Guerrero, J., Kastner, M., Kelts, K., Lyle, M., Matoba, Y., Molina-Cruz, A., Niemitz, J., Rueda, J., Saunders, A., Schrader, H., Simoneit, B., Vacquier, V., 1980, *Intrusions of basalt into highly porous sediments and resulting hydrothermal activity*; Nature **283**: 441-445.

Ellwood, B.B., Crick, R.E., El Hassani, A., Benoist, S., Young, R.H., 2000, *Magnetosusceptibility event and cyclostratigraphy method applied to marine rocks: detrital versus carbonate productivity*, Geology **28**: 1135-1138.

Emiliani, C., 1955, *Pleistocene temperatures*; Journal of Geology **63**: 538-578.

Emiliani, C., Gartner, S., Lidz, B., Eldridge, K., Elvey, D.K., Ting, C.H., Stipp, J.J., Swanson, M.F., 1975, *Paleoclimatological analysis of late Quaternary cores from the northeastern Gulf of Mexico*; Science **189**: 1083-1088.

Ganeshram, R.S., Pedersen, T.F., 1998, *Glacial-interglacial variability in upwelling and bioproductivity off New Mexico: implications for Quaternary palaeoclimate*; Paleoceanography **13**: 634-645.

Gardner, J.V., Dean, W.E., Dartnell, P., 1997, *Biogenic sedimentation beneath the California Current system for the past 30 kyr and its paleoceanographic significance*, Paleoceanography **12**: 207-225.

Gaxiola-Castro, G., Garcia-Cordova, J., Valdez-Holguin, J.E., Botello-Ruvalcaba, M., 1995, *Spatial distribution of chlorophyll a and primary productivity in relation to winter physical structure in the Gulf of California*; Continental Shelf Research **15**: 1043-1059.

Gibbard, P.L., Lewin, J., 2002, *Climate and related controls on interglacial fluvial sedimentation in lowland Britain*; Sedimentary Geology **151**: 187-210.

Goni, M.A, Woodwort, M.P., Müller-Karga, F.E., 2006, *Changes in wind-driven upwelling during the last three centuries: interocean teleconnections*; Geophysical Research Letters **33**: L15604, doi: 10.1029/2006GL026415

Goodfriend, G.A., Flessa, K.W., 1997, *Radiocarbon reservoir ages in the Gulf of California: roles of upwelling and flow from the Colorado River;* Radiocarbon **39**: 139-148.

Gorsline, D., de Diego, T., Nava-Sanchez, E.H., 2000, *Seismically triggered turbidites in the small margin basins: Alfonso Basin, western Gulf of California, and Santa Monica Basin, California Borderland*; Sedimentary Geology **135**: 21-35.

Grootes, P.M., Stuiver, M., White, J.W.C., Johnsen, S., Jouzel. J., 1993, *Comparison of oxygen isotope records from the GISP2 and GRIP Greenland ice cores*; Nature **366**: 552-554.

Grotjahn, R., 2004, *Remote weather associated with South Pacific Subtropical sea-level properties*; International Journal of Climatology **24**: 823-839.

Guilderson, T.P., Fairbanks, R.G., Rubenstone, J.L., 1994, *Tropical temperature variations since 20,000 years ago: modulating interhemispheric climate change*; Science **263**: 663-665.

Hajdas, I., Bonani, G., Moreno, P.I., Ariztegui, D., 2003, *Precise radiocarbon dating of Late-glacial cooling in mid-latitude South America*; Quaternary Research **59**: 70-78.

Hales, E.H., 1972, *Surges of maritime tropical air northward over the Gulf of California*; Monthly Weather Review **100**: 298-306.

Hammann, M.G., Baumgartner, T.R., Badon-Dangon, A., 1988, *Coupling of the Pacific sardine (Sardinops sagax caerulus) life cycle with the Gulf of California pelagic environment*; Californian Co-operative Oceanic Fisheries Investigations Report **29**: 102-109.

Hansen, B.C., Rodbell, D.T., 1995, *A Late-glacial/Holocene pollen record from the eastern Andes of northern Peru*; Quaternary Research **44**: 216-227.

Harrison, S,P., Kohfeld, K.E., Roelandt, C., Claquin, T., 2001, *The role of dust in climate changes today, at the last glacial maximum and in the future*, Earth-Science Reviews **54**: 43-80.

Hastenrath, S., 2002, *The Intertropical Convergence Zone of the eastern Pacific revisited*; International Journal of Climatology **22**: 347-356.

Haug, G.H., Günther, D., Peterson, L.C., Sigman, D.M., Hughen, K.A., Aeschlimann, B., 2003, *Climate and collapse of the Maya civilization*; Science **299**: 1731-1735.

Haug, G.H., Hughen, K.A., Sigman, D.M., Peterson, L.C., Röhl, U., 2001, *Southward migration of the Intertropical Convergence Zone through the Holocene*; Science **293**: 1304-1308.

Hays, J.D., Imbrie, J., Shackleton, N.J., 1976, *Variations in the Earth's orbit: pacemaker of the Ice Ages*; Science **194**: 1121-1132.

Hendy, I.L., Kennett, J.P., 1999, *Latest Quaternary North Pacific surface-water responses imply atmosphere-driven climate instability*; Geology, **27**: 291-294.

Hendy, I.L., Kennett, J.P., Roark, E.B., Ingram, B.L., 2002, *Apparent synchroneity of submillennial climate events between Greenland and Santa Barbara Basin, California from 30-10 ka*; Quaternary Science Reviews **21**: 1167-1184.

Hendy, I.L., Kennett, J.P., 2003, *Tropical forcing of North Pacific intermediate water distribution during Late Quaternary rapid climate change?* Quaternary Science Reviews **22**: 673-689.

Herbert, T.D., Schuffert, J.D., Andreasen, D., Heusser, L., Lyle, M., Mix, A.C., Ravelo, A.C., Stott, L.D., Herguera, J.C., 2001, *Collapse of the California Current during glacial maxima linked to climate change on land*; Science, **293**, 71-75.

Heusser, L., 1998, *Direct correlation of millennial-scale changes in western North American vegetation and climate with changes in the California Current system over the past ~60 kyr*; Paleoceanography **13**: 252-262.

Holmgren, C.A., Peñalba, M.C., Rylander, K.A., Betancourt, J.L., MacKay, A., 2003, *A 16,000 $^{14}C$ yr BP packrat midden series from the USA-Mexico Borderlands*; Quaternary Research **60**: 319-329.

Holmgren-Urba, D., Baumgartner, T.R., 1993, *A 250-year history of pelagic fish abundances from the anaerobic sediments of the central Gulf of California*; Californian Co-operative Oceanic Fisheries Investigations Report **34**: 60-68.

Hostetler, S.W., Giorgi, F., Bates, G.T., Bartlein, P.J., 1994, *Lake-atmosphere feedbacks associated with paleolakes Bonneville and Lahontan*; Science **263**: 665-668.

Hulton, N.R., Purves, R.S., McCulloch, R.D., Sugden, D.E., Bentley, M.J., 2002, *The Last Glacial Maximum and deglaciation in southern South America*; Quaternary Sciences Reviews **21**: 233-241.

Humphreys, E.D., Weldon, R.J., 1991, *Kinematic constraints on the rifting of Baja California*; in Dauphin, J.P., Simoneit, B.R. (eds), *The Gulf and Peninsular province of the Californias*; American Association of Petroleum Geologists Memoir **47**: 217-227.

Jackson, S.T., Webb, R.S., Anderson, K.D., Overpeck, J.T., Webb, T., III, Williams, J.W., Hansen, B.C., 2000, *Vegetation and environment in eastern North America during the Last Glacial Maximum*; Quaternary Science Reviews **19**: 489-508.

Jacob, J., Disnar, J-R., Boussafir, M., Sifeddine, A., Turcq, B., Spadino Albuquerque, A.L., 2004, *Major environmental changes recorded by lacustrine sedimentary organic matter since the Last Glacial Maximum near the equator (Lago do Caço, NE Brazil)*; Palaeogeography, Palaeoclimatology, Palaeoecology **205**: 183-197.

Jansen, J.H.F., Van der Gaast, S.J., Kotser, B., Vaars, A.J., 1998, *CORTEX, a shipboard XRF scanner for element analyses in split sediment cores*, Marine Geology **151**: 143-153.

Jiang, H., Zheng, Y., Ran, L., Seidenkrantz, M-S., 2004, *Diatoms from the surface sediments of the South China Sea and their relationships to modern hydrography*, Marine Micropaleontology **53**: 279-292.

Kameo, K., Shearer, M.C., Droxler, A. W., Mita, I., Watanabe, R., Sato, T., 2004, *Glacial-interglacial surface water variations in the Caribbean during the last 300 ky based on calcareous nannofossil analysis*; Palaeogeography, Palaeoclimatology, Palaeoecology **212**: 65-76.

Keigwin, L.D., 1987, *North Pacific deep water formation during the last glaciation*; Nature **330**: 362-364.

Keigwin, L.D., 2002, *Late Pleistocene-Holocene paleoceanography and ventilation in the Gulf of California*; Journal of Oceanography **58**: 421-432.

Keigwin, L.D., Jones, G.A., 1990, *Deglacial climatic oscillations in the Gulf of California*; Paleoceanography **5**: 1009-1023.

Keigwin, L.D., Jones, G.A., Froelich, P.N., 1992, *A 15,000-year palaeoenvironmental record from Meiji Seamount, far northwestern Pacific*; Earth & Planetary Science Letters **111**: 425-440.

Kelts, K., Niemitz, J., 1982, *Preliminary sedimentology of late Quaternary diatomaceous muds from Deep Sea Drilling Project Site 480, Guaymas Basin slope, Gulf of California*; in Curray, J.R.; Blakeslee, J., Platt, L.W., Stout, L.N., Moore, D.G. Aguayo, J.E. Aubry, M.-P., Einsele, G. Fornari, D.J. Gieskes, J.M., Guerrero, G.J., Kastner, M., Kelts, K.R. Lyle, M. Matoba, Y., Molina-Cruz, A. Niemitz, J., Rueda-Gaxiola, J., Saunders, A.D., Schrader, H., Simoneit, B.R.T., Vacquier, V. (eds), *Initial Reports Deep Sea Drilling Project* **64**: 1191-1210.

Kemp, A.E.S., 1996, *Laminated sediments as palaeo-indicators*; in Kemp, A.E.S. (ed), *Palaeoclimatology and palaeoceanography from laminated sediments*, Geological Society Special Publication **116**: vii-xii.

Kemp, A.E.S., Pike, J., Pearce, R.B., Lange, C.B., 2000, *The 'Fall Dump' – a new perspective on the role of a 'shade flora' in the annual cycle of diatom production and export flux*; Deep-Sea Research II **47**: 2129-2154.

Kennett, J.P., Baldauf, J.G., Behl, R., Bryant, W.R., Fuller, M., Grimm, K., Heusser, L., Kemp, A., Lange, C., Lund, S.P., Merrill, R., Olivier, F., Polgreen, E., Pratt, L., Rack, F., Schimmelmann, A., Schwartz, M., Stein, R., Thurow, J., Musgrave, R.J., 1994, *Proceedings of the Ocean Drilling Program, Part A: Initial Reports* **146**, Part 2: 15-50.

Kennett, J.P., Ingram, B.L., 1995, *A 20,000-year record of ocean circulation and climate change from the Santa Barbara Basin*; Nature **377**: 510-514.

Kennett, J.P., Cannariato, K.G., Hendy, I.L., Behl, R.J., 2000, *Carbon isotopic evidence for methane instability during Quaternary interstadials*; Science **288**: 128-133.

Kienast, S., Calvert, S.E., Pedersen, T.F., 2002, Nitrogen isotope and productivity variations along the northeast Pacific margin over the last 120 kyr: surface and subsurface paleoceanography; Paleoceanography **17**: 1005-1022.

Klein, A.G., Seltzer, G.O., Isacks, B.L., 1999, *Modern and last local glacial maximum snowlines in the Central Andes of Peru, Bolivia and northern Chile*; Quaternary Science Reviews **18**: 63-84.

Koutavas, A., Lynch-Steiglitz, J., Marchitto, T.M., Sachs, J.P., 2002, *El Niño-like pattern in ice age tropical Pacific sea surface temperature*; Science **297**: 226-230.

Kowalewski, M., Avila Serrano, G. E., Flessa, K.W., Goodfriend, G.A., 2000, *Dead delta's former productivity: two trillion shells at the mouth of the Colorado River*; Geology **28**: 1059-1062.

Kullenberg B., 1947. *The piston core sampler*; Svenaka Hydro-Biol. Komm. Skr. **3**: 1-46.

Laskar, J., Robutel, P., Joutel, F., Gastineau, M., Correia, A.C., Levrard, B., 2004, *A long-term numerical solution for the insolation quantities of the Earth*; Astronomy & Astrophysics **428**: 261-285.

Lea, D.W., Hak, D.K., Spero, H.J., 2000, *Climate impact of late Quaternary equatorial sea surface temperature variations*; Science **289**: 1719-1724.

Lea, D.W., Pak, D.K., Peterson, L.C., Hughen, K.A., 2003, *Synchroneity of tropical and high-latitude Atlantic temperatures over the last glacial termination*; Science **301**:1361-1364.

Lea, D.W., Pak, D.K., Belanger, C.L., Spero, H.J., Hall, M.A., Shackleton, N.J., 2006, *Palaeoclimate history of the Galapagos surface waters over the last 135,000 years*; Quaternary Science Reviews **25**: 1152-1167.

Ledesma-Vazquez, J., Johnson, M.E., 2001, *Miocene-Pleistocene tectono-sedimentary evolution of Bahia Concepcion region, Baja California Sur (Mexico)*; Sedimentary Geology **144**: 83-96.

Leduc, G., Vidal, L., Tachikawa, K., Rostek, F., Sonzogni, C., Beaufort, L., Bard, E., 2007, *Moisture transport across Central America as a positive feedback on abrupt climate changes*; Nature **445**: 908-911.

Leyden, B.W., 1985, *Late Quaternary aridity and Holocene moisture fluctuations in the Lake Valencia basin, Venezuela*; Ecology **66**: 1279-1295.

Leyden, B.W., Brenner, M., Hodell, D.A., Curtis, J.H., 1993, *Orbital and internal forcing of climate on the Yucatan Peninsula for the past ~36 kyr*; Palaeogeography, Palaeoclimatology, Palaeoecology **109**: 193-210.

Lipps, J.H. (ed), *Fossil Prokaryotes and Protists*, Blackwell Scientific Publications, Boston, pp 342.

Lluch-Cota, S.-E., 2000, *Coastal upwelling in the eastern Gulf of California*; Oceanologica Acta **23**: 731-740.

Lonsdale, P.F., 1989, *Geology and tectonic history of the Gulf of California*; in Winterer, E.L., Hussong, D.M., Decker, R.W. (eds), *The geology of North America*, vol. **N**: *The eastern Pacific and Hawaii*; Geological Society of America, Denver, 499-521.

Lopez, M., 1997, *A numerical simulation of water mass formation in the northern Gulf of California during winter*; Continental Shelf Research **17**: 1581-1607.

Lotte, A.F., Lemcke, G, 1999, *Methods for preparing and counting biochemical varves*; Boreas **28**: 243-252.

Loubere, P., 2002, *Remote vs local control of changes in the eastern equatorial Pacific bioproductivity from the Last Glacial Maximum to the present*; Global and Planetary Change **35**: 113-126.

Loubere, P., Richaud, M., Liu, Z., Mekik, F., 2003, *Oceanic conditions in the eastern equatorial Pacific during the onset of ENSO in the Holocene*; Quaternary Research **60**: 142-148.

Lowe, J.J., Walker, M.R., 1997, *Reconstructing Quaternary environments*, 2nd Edition, Longman, Harlow, pp 446.

Lozano-Garcia, M.S., Ortega-Guerrero, B., Sosa-Najera, S., 2002, *Mid-to Late-Wisconsin pollen record of San Felipe Basin, Baja California*; Quaternary Research **58**: 84-92.

Lutgens, F.K., Tarbuck, E.J., 2004, *The atmosphere, an introduction to meteorology*, 9th Edition, Prentice Hall, New Jersey, pp 508.

Lynch-Stieglitz, J., Curry, W.B., Slowey, N., 1999, *Weaker Gulf Stream in the Florida Straits during the Last Glacial Maximum*; Nature **402**: 644-648.

McCulloch, R.D., Bentley, M.J., Purves, R.S., Hulton, N.R., Sugden, D.E., Clapperton, C.M., 2000, *Climatic inferences from glacial and palaeoecological evidence at the last glacial termination, southern South America*; Journal of Quaternary Science **15**: 409-417.

McGregor, G.R., Nieuwolt, S., 1998, *Tropical climatology: an introduction to climates of the low latitudes*, 2nd Edition, Wiley, Chichester, pp 339.

McShane, C., Hamer, T., Carter, H., Swartzman, G., Friesen, V., Ainley, D., Tressler, R., Nelson, K., Burger, A., Spear, L., Mohagen, T., Martin, R., Henkel, L., Prindle, K., Strong, C., Keany, J., 2004, *Evaluation report for the 5-year status review of the marbled murrelet in Washington, Oregon, and California*; U.S. Fish and Wildlife Service, Portland, Oregon.

Manar, T.A. (ed) and many others, 1950, *California Co-operative Fisheries Investigations annual progress report*, Vol. 1.

Mangerud, J., Anderson, S.T., Berglund, B.E., Donner, J.J., 1974, *Quaternary stratigraphy of Norden: a proposal for terminology and classification*; Boreas **3**: 109-127.

Mantua, N.J., Hare, S.R., Zhang, Y., Wallace, J.M., Francis, R.C., 1997, *A Pacific interdecadal climate oscillation with impacts on salmon production*; Bulletin of the American Meteorological Society **78**: 1069-1079.

Mantua, N.J., Hare, S.R., 2002, *The Pacific Decadal Oscillation*; Journal of Oceanography, **58**: 35-44.

Martin, P.S., 1964, *Paleoclimatology and a tropical pollen profile*; Report of the VI International Congress of the Quaternary, Warsaw (1961) Vol. **2**: 319-323.

Martinson, D.G., Pisias, N.G., Hays, J.D., Imbrie, J., Moore, T.C. (Jr), Shackleton, N.J., 1987, *Age dating and the orbital theory of ice ages: development of a high-resolution 0 to 300,000-year chronostratigraphy*; Quaternary Research **27**: 1-29.

Menking, K.M., Anderson, R.Y., Shafike, N.G., Syed, K.H., Allen, B.D., 2004, *Wetter or colder during the Last Glacial Maximum? Revisiting the pluvial lake question in Southwest America*; Quaternary Research **62**: 280-288.

Merrifield, M.A., Winant, C.D., 1989, *Shelf circulation in the Gulf of California: a description of the variability*; Journal of Geophysical Research **94**: 18133-18160.

Metcalfe, S.E., Say, A., Black, S., McCulloch, R., O'Hara, S.L., 2002, *Wet conditions during the last glaciation in the Chihuanhuan Desert, Alta Babicora Basin, Mexico*, Quaternary Research, **57**, 91-101.

Mix, A.C., Harris, S.E., Janacek, T.R., 1995, *Estimating lithology from non-intrusive reflectance spectra: Leg 138*, Proceedings of the Ocean Drilling Program, Scientific Results **138**: 413-427.

Mix, A.C., Lund, D.C., Pisias, N.G., Boden, P., Bornmalm, L., Lyle, M., Pike, J., 1999, *Rapid climate oscillations in the northeast Pacific during the last deglaciation reflect northern and southern hemisphere sources*. In Clarke, P.K. *et al.* (eds), *Mechanisms of global climate change at millennial time scales*; Geophysical Monograph **112**: 127-148.

Moreno, P.I., Leon, A.L., 2003, *Abrupt vegetation changes during the last glacial to Holocene transition in the mid-latitude South America*; Journal of Quaternary Science **18**: 787-800.

Nederbragt, A.J., Thurow, J., Merrill, R.B., 2000, *Color records from the California margin; proxy indicators for sediment composition and climatic change*; Lyle, M., Koizumi, I., Richter, C., Moore, T.C. (eds), Proceedings of the Ocean Drilling Program, Scientific Results **167**: 319-329.

Nederbragt, A.J., Thurow, J., 2005, *Geographic coherence of millennial scale cycles during the Holocene*; Palaeogeography, Palaeoclimatology, Palaeoecology **221**: 313-324.

Oldfield, F., 1999, *Environmental magnetism: the range of applications*, in *Environmental magnetism: a practical guide*, Walden, J., Oldfield, F., Smith, J.P. (eds), Technical Guide No. **6**, Quaternary Research Association, London.

Ortiz, J. D., Mix, A., 1997, *The California Current of the Last Glacial Maximum: reconstruction at 42°N based on multiple proxies*; Paleoceanography **12**: 191-205.

Ortiz, J.D., O'Connell, S.B., DelViscio, J., Dean, W.E., Carriquiry, J.D., Marchitto, T.M., Zheng, Y., van Geen, A., 2004, *Enhanced marine productivity off western North America during warm intervals of the past 52 k.y.*; Geology **32**: 521-524.

Overpeck, J.T., Peterson, L.C., Kipp, N., Imbrie, J., Rind, D., 1989, *Climate change in the circum-North Atlantic during the last deglaciation*; Nature **338**: 553-557.

Oviatt, C.G., Madsen, D.B., Schmitt, D.N., 2003, *Late Pleistocene and early Holocene rivers and wetlands in the Bonneville Basin of western North America*, Quaternary Research **60**: 200-210.

Pares-Sierra, A., Mascarenhas, A., Marinone, S.G., Castro, R., 2003, *Temporal and spatial variation of the surface winds in the Gulf of California*; Geophysical Research Letters **30**: 1312-1315.

Pedersen, T.F., Nielsen, B., Pickering, M., 1991, *Timing of Late Quaternary productivity pulses in the Panama Basin and implications for atmospheric $CO_2$*; Paleoceanography **6**: 657-677.

Peter, J.M., Scott, S.D., *Hydrothermal mineralization in the Guaymas Basin, Gulf of California*; in Dauphin, J.P., Simoneit, B.R. (eds), *The Gulf and Peninsular province of the Californias*; American Association of Petroleum Geologists Memoir **47**: 721-741.

Peterson, L.C., Haug, G.H., Hughen, K.A., Röhl, U., 2000a, *Rapid changes in the hydrological cycle of the tropical Atlantic during the last glacial*, Science **290**: 1947-1951.

Peterson, L.C., Haug, G. H., Murray, R.W., Yarincik, K.M., King, J.W., Bralower, T.J., Kameo, K., Rutherford, S.D., Pearce, R.B., 2000b, *Late Quaternary stratigraphy and sedimentation at Site 1002, Cariaco Basin (Venezuela);* in Leckie, R.M., Sigurdsson, H., Acton, G.D., Drapers, G. (eds), Proceedings of the Ocean Drilling Program, Scientific Results Vol. **165**: 85-99.

Peterson, L.C., Haug, G.H., 2006, *Variability in the mean latitude of the Atlantic Intertropical Convergence Zone as recorded by riverine input of sediments to the Cariaco basin (Venezuela)*; Palaeogeography, Palaeoclimatology, Palaeoecology **234**: 97-113.

Pierrehumbert, R.T., 1999, *Subtropical water vapor as a mediator of rapid global climate change*; in Clark, P.U., Webb, R.S., Keigwin, L.D. (eds), *Mechanisms of global climate change at millennial time scales*, Geophysical Monograph 112: 339-361.

Pike, J., 1996, *High resolution palaeoceanography and palaeoclimatology from late Pleistocene and Holocene sediments, Gulf of California*, unpublished PhD Thesis, University of Southampton.

Pike, J., Kemp, A.E.S., 1996, *Records of seasonal flux in Holocene laminated sediments, Gulf of California*; in Kemp, A.E.S. (ed), *Palaeoclimatology and palaeoceanography from laminated sediments*, Geological Society Special Publication **116**: 157-170.

Pike, J., Kemp, A.E.S., 1997, *Early Holocene decadal-scale ocean variability recorded in Gulf of California laminated sediments*; Paleoceanography **12**: 227-238.

Pike, J., Kemp, A.E.S., 1999, *Diatom mats in Gulf of California sediments: implications for the palaeoenvironmental interpretation of laminated sediments and silica burial*; Geology **27**: 311-314.

Piper, D.Z., 1994, *Seawater as a source of minor elements in black shales, phosphorites and other sedimentary rocks*; Chemical Geology **114**: 95-114.

Pride, C., Thunell, R., Sigman, D., Keigwin, L., Altabet, M., Tappa, E., 1999, *Nitrogen isotopic variations in the Gulf of California since the last deglaciation: response to global climate change*; Paleoceanography **14**: 397-409.

Prieto, A.R., 2000, *Vegetational history of the Late-glacial-Holocene transition in the grasslands of eastern Argentina*; Palaeogeography, Palaeoclimatology, Palaeoecology **157**: 167-188.

Reheis, M., 1999, *Highest pluvial-lake shorelines and Pleistocene climate of the Western Great Basin*; Quaternary Research **52**: 196-205.

Reid, J.L., Roden, G.I., Wyllie, J.G., 1958, *Studies of the California Current system*; Californian Co-operative Oceanic Fisheries Investigations Report **6**: 28-56.

Reid, J.L., 1960, *Oceanography of the northeastern Pacific Ocean during the last ten years*, Californian Co-operative Oceanic Fisheries Investigations Report **7**: 77-90.

Reverdin, G., 1995, *The physical processes of open ocean upwelling systems*; in Summerhayes, C.P., Emeis, K.-C., Angel, M.V., Smith, R.L., Zeitschel, B. (eds), *Upwelling in the Ocean: modern processes and ancient records*; Report of the Dahlem Workshop, 1994; John Wiley & Sons, Chichester: 125-148.

Rhode, D., 2002, *Early Holocene juniper woodland and chaparral taxa in the central Baja California Peninsula*: Mexico, Quaternary Research **57**: 102-108.

Ripa, P., 1997, *Towards a physical explanation of the seasonal thermodynamics of the Gulf of California*; Journal of Physical Oceanography **26**: 597-614.

Robert, C., 2004, *Late Quaternary variability of precipitation in Southern California and climatic implications: clay mineral evidence from the Santa Barbara Basin, ODP Site 893*; Quaternary Science Reviews **23**: 1029-1040.

Rodbell, D.T., 2000, *The Younger Dryas: cold, cold everywhere?* Science **290**: 285-286.

Rodbell, D.T., Seltzer, G.O., Anderson, D.M., Enfield, D.B., Newman, J.H., 1999, *An ~15,000 year record of El Niño-driven alluviation in southwestern Ecuador*; Science **283**: 516-520.

Roden, G.I., 1958, *Oceanographic and meteorological aspects of the Gulf of California*; Pacific Science **12**: 21-45.

Röhl, U., Abrams, L.J., 2000, *High resolution down hole and non-destructive core measurements from sites 999 and 1001 in the Caribbean Sea: application to the Late Paleocene Thermal Maximum*, Proceedings of the Ocean Drilling Program, Scientific Results **165**: 191-203.

Sabin, A.L., Pisias, N.G., 1996, *Sea surface temperature changes in the northeastern Pacific ocean during the past 20,000 years and their relationship to climate change in northwestern North America*; Quaternary Research **46**: 48-61.

Sageman, B.B., Lyons, T.W., 2003, *Geochemistry of fine-grained sediments and sedimentary rocks*. In: Mackenzie, F.T. (ed), *Treatise on Geochemistry*, Vol. 7 *Sediments, Diagenesis and Sedimentary Rocks*, Elsevier, Pergamon, 115-158.

Salgado-Labouriau, M.L., Barberi, M., Feraz-Vicentini, K.R., Parizzi, M.G., 1998, *A dry climatic event during the late Quaternary of tropical Brazil*; Review of Palaeobotany and Palynology **99**: 115-129.

Sancetta, C., 1995, *Diatoms in the Gulf of California: seasonal flux patterns and the sediment record for the last 15,000 years*, Paleoceanography **10**: 67-84.

Sancetta, C., Lyle, M., Heusser, L., Zahn, R., Bradbury, J.P., 1992, *Late-glacial to Holocene changes in winds, upwelling and seasonal production of the Northern California current system*; Quaternary Research **38**: 359-370.

Sanchez-Velasco, L., Valdez-Holguin, J.E., Shirasgo, B., Cisneros-Mata, M.A., Zarate, A., 2002, *Changes in the spawning environment of* Sardinops sagax caerulus *in the Gulf of California during El Niño 1997-1998*; Estuarine, Coastal and Shelf Science **54**: 207-217.

Schrader, H., Kelts, K., Curray, J., Aguayo, E., Aubry, M.-P., Einsele, G., Fornari, D., Gieskes, J., Guerrero, J., Kastner, M., Lyle, M., Matoba, Y., Molina-Cruz, A., Niemitz, J., Rueda, J., Saunders, A., Simoneit, B., Vaquier, V., 1980, *Laminated diatomaceous sediments from Guaymas Basin slope (central Gulf of California): 250,000-year climate record*; Science **207**:1207-1209.

Schrader, H., 1982, *Diatom biostratigraphy and laminated diatomaceous sediments from the Gulf of California*; in Curray, J.R.; Blakeslee, J., Platt, L.W.,

Stout, L.N., Moore, D.G. Aguayo, J.E. Aubry, M.-P., Einsele, G. Fornari, D.J. Gieskes, J.M., Guerrero, G.J., Kastner, M., Kelts, K.R. Lyle, M. Matoba, Y., Molina-Cruz, A. Niemitz, J., Rueda-Gaxiola, J., Saunders, A.D., Schrader, H., Simoneit, B.R.T., Vacquier, V. (eds), *Initial Reports of the Deep Sea Drilling Project, Leg 64*: Washington DC, U.S. Government Printing Office, pp1313.

Seltzer, G.O., Rodbell, D.T., Baker, P.A., Fritz, S.C., Tapia, P.M., Rowe, H.D., Dunbar, R.B., 2002, *Early warming of tropical South America at the last glacial-interglacial transition*; Science **296**: 1685-1686.

Shackleton, N.J., Opdyke, N.D., 1973, *Oxygen isotope and palaeomagnetic stratigraphy of equatorial Pacific core V28-238: oxygen and isotope temperatures and ice volumes on a $10^5$- and $10^6$-year scale*; Quaternary Research **3**:39-55.

Shackleton, N.J., Hall, M.A., Line, J., Shuxi, C., 1983, *Carbon isotope data in core V19-30 confirm reduced carbon dioxide in the ice age atmosphere*; Nature **306**: 319-322.

Shackleton, N.J., Le, J., Mix, A.C., Hall, M.A., 1992, *Carbon isotope records from Pacific surface waters and atmospheric carbon dioxide*; Quaternary Science Reviews **11**: 387-400.

Shapiro, L., Brannock, W.W., 1962, *Rapid analysis of silicate, carbonate and phosphate rocks*, US Geological Survey Bulletin, A1-A56.

Simoneit, B.R., 1991, *Organic geochemistry of Deep Sea Drilling Project cores from Legs 63 to 66 – a synthesis of sources, preservation and maturation of organic matter in Quaternary and Neogene sediments from an active continental margin*; in Dauphin, J.P., Simoneit, B.R. (eds), *The Gulf and Peninsular Province of the Californias*, American Association of Petroleum Geologists Memoir **47**: 667-705.

Skinner, L.C., McCave, I.N., 2003, *Analysis and modelling of gravity- and piston-coring based on soil mechanics*, Marine Geology **199**: 181-204.

Smith, R.L., 1995, *The physical processes of coastal ocean upwelling systems*; in Summerhayes, C.P., Emeis, K.-C., Angel, M.V., Smith, R.L., Zeitschel, B. (eds), *Upwelling in the Ocean: modern processes and ancient records*; Report of the Dahlem Workshop, 1994; John Wiley & Sons, Chichester: 39-63.

Smith, G.I., Street-Perrott, F.A, 1984, *Pluvial lakes of the Western United States.* In Porter, S.C. (ed), *Late Quaternary environments of the United States*, Vol. **1** The Late Pleistocene, University of Minnesota Press, Minneapolis: 190-212.

Soutar, A., Crill, P.A., 1977, *Sedimentation and climatic patterns in the Santa Barbara Basin during the 19$^{th}$ and 20$^{th}$ centuries*; Geological Society of America Bulletin **88**: 1161-1172.

Stapp, P., Polis, G.A., Sanchez Pinero, F., 1999, *Stable isotopes reveal strong marine and El Niño effects on island food webs*; Nature **401**: 467-469.

Stott, L.D., Neumann, M., Hammond, D.E., 2000, *Intermediate water ventilation in the northeastern Pacific margin during the late Pleistocene inferred from benthic foraminiferal $\delta^{13}C$*; Paleoceanography **15**: 161-169.

Stuiver, M., Grootes, P.M., 2000, *GISP2 oxygen isotope ratios*; Quaternary Research **53**: 277-284.

Summerhayes, C.P., Emeis, K.-C., Angel, M.V., Smith, R.L., Zeitschel, B., 1995, *Upwelling in the ocean: modern processes and ancient records*; in Summerhayes, C.P., Emeis, K.-C., Angel, M.V., Smith, R.L., Zeitschel, B. (eds), *Upwelling in the Ocean: modern processes and ancient records*; Report of the Dahlem Workshop, 1994; John Wiley & Sons, Chichester: 1-37.

Taylor, S.R., McLennan, S.M., 1985, *The continental crust: its composition and evolution*, Blackwell, Malden, Massachusetts, pp312.

Tchakerian, V.P., Lancaster, N., 2002, *Late Quaternary arid/humid cycles in the Mojave Desert and western Great Basin of North America*; Quaternary Science Reviews **21**: 799-810.

Tertian, R., Claisse, C., 1982, *Principles of quantitative X-ray fluorescence*; Heydon, London, pp 320.

Thunell, R.C., 1998, *Seasonal and annual variability in particle fluxes in the Gulf of California: a response to climate forcing*; Deep-Sea Research I **45**: 2059-2083.

Thunell, R.C., Pride, C.J., Tappa, E.G., Muller-Karga, F.E., 1993, *Varve formation in the Gulf of California: insights from times series sediment trap sampling and remote sensing*, Quaternary Science Reviews **12**: 451-464.

Thunell, R.C., Pride, C.J., Tappa, E., 1994, *Biogenic fluxes and accumulation rates in the Gulf of California*; Geology **22**: 303-306.

Thunell, R.C., Tappa, E., Anderson, D.M., 1995, *Sediment fluxes and varve formation in Santa Barbara Basin, offshore California*; Geology **23**: 1083-1086.

Tomas, C.R., 1996, *Identifying marine diatoms and dinoflagellates*, Academic Press, San Diego, pp598.

van Andel, T.H, 1964, *Recent marine sediments of the Gulf of California*; in van Andel, T.H. & Shor, G.G. (eds), *Marine geology of the Gulf of California*, American Association of Petroleum Geologists Memoir **3**: 216-310.

van der Hammen, T., Absy, M.L., 1994, *Amazonia during the last glacial*; Palaeogeography, Palaeoclimatology, Palaeoecology **109**: 247-261.

van Devender, T.R., 1990a, *Late Quaternary vegetation and climate of the Chihuahuan Desert, United States and Mexico*. In *Packrat Middens*, Betancourt, J.L., van Devender, T.R., Martin, P.S. (eds), University of Arizona Press, Tucson, Arizona, 104-133.

van Devender, T.R., 1990b, *Late Quaternary vegetation and climate of the Sonoran Desert, United States and Mexico*. In *Packrat Middens*, Betancourt, J.L., van Devender, T.R., Martin, P.S. (eds), University of Arizona Press, Tucson, Arizona, 134-165.

van Geel, B., van der Hammen, T.,1973, *Upper Quaternary vegetational and climatic sequence of the Fuquene area (eastern Cordillera, Colombia)*; Palaeogeography, Palaeoclimatology, Palaeoecology **14**: 90-92.

van Geen, A., Zheng, Y., Bernhard, J.M., Cannariato, K.G., Carriquiry, J., Dean, W.E., Eakins, B.W., Ortiz, J.D., Pike, J., 2003, *On the preservation of laminated sediments along the western margin of North America*; Paleoceanography **18**: doi:1029/2003PA000911.

Wang, X., Auler, A.S., Edwards, R.L., Cheng, H., Cristalli, P.S., Smart, P.L., Richards, D.A., Shen, C-C., 2004, *Wet periods in northeastern Brazil over the past 210 kyr linked to distant climate anomalies*; Nature **432**: 740-743.

Watts, W.A., Bradbury, J.P., 1982, *Paleoecological studies at Lake Patzcuaro on the West-Central Mexican Plateau and at Chalco in the Basin of Mexico*; Quaternary Research **17**: 56-70.

Watts, W.A., Hansen B.S., 1988, *Environments of Florida in the Late Wisconsin and Holocene*. In Purdy, B. (ed), *Wet Site Archaeology*, Telford Press, New Jersey: 307-323.

Weaver, A.J., Bitz., C.M., Fanning, A.F., Holland, M.M., 1999, *Thermohaline circulation: high latitude phenomena and the difference between the Pacific and Atlantic*; Annual Reviews of Earth and Planetary Science **27**: 231-285.

Williams, J.W., 2002, *Variation in tree cover in North America since the Last Glacial Maximum*; Global and Planetary Change **35**: 1-23.

Winter, A., Seisser, W.G. (eds), 1994, *Coccolithophores,* Cambridge University Press, Cambridge NY, pp242.

Yarincik, K., Murray, R.W., Peterson, L.C., 2000, *Climatically sensitive eolian and hemipelagic deposition in the Cariaco Basin, Venezuela, over the past 587,000 years: results from Al/Ti and K/Al*, Paleoceanography **15**: 210-228.

Zhang, Y., Wallace, J.M., Battisti, D.S., 1997, *ENSO-like interdecadal variability: 1900-1993*; Journal of Climate **10**: 1004-1020.

Ziveri, P., Thunell, R.C., 2000, *Coccolithophore export production in Guaymas Basin, Gulf of California: response to climate forcing*; Deep-Sea Research II **47**: 2073-2100.